Implementation of Wavelet Based Damage Detection Methods Using Full-Scale Shaking Table Tests Data and Nonlinear Finite Element Models

By

DIEGO ARMANDO AGUIRRE REALPE

A thesis submitted in partial fulfillment of the requirements for the degree of

MASTER OF SCIENCE
IN
CIVIL ENGINEERING

UNIVERSITY OF PUERTO RICO
MAYAGÜEZ CAMPUS
MAYAGÜEZ, PUERTO RICO
2013

Approved by:

Luis E. Suárez Colche, Ph.D. Member, Graduate Committee	Date
Ricardo R. López Rodríguez, Ph.D. Member, Graduate Committee	Date
Luis A. Montejo Valencia, Ph.D. President, Graduate Committee	Date
Paul E. Castillo, Ph.D. Representative of Graduate Studies	Date
Ismael Pagán Trinidad, MSCE Chairperson of the Department	Date

ABSTRACT

Due to the scarce number of data available from instrumented buildings damaged during an earthquake, large scale shaking table tests of civil structures offer an invaluable opportunity to validate structural health monitoring (SHM) systems and their applicability to structures subjected to damaging earthquake loads.

The main goal of this research was to validate wavelet-based model-free methodologies for damage detection in reinforced concrete (RC) structures. For this purpose, signal processing algorithms were developed to perform time-frequency and system identification analyses, among others, using full-scale shaking table tests data along with results obtained from nonlinear finite element (FE) models. The experimental data used in this work was collected during two tests recently performed. First, a full-scale RC bridge column shaking table test performed at the University of California, San Diego (UCSD). Second, two full-scale RC 3D frame shaking table test performed at the National Laboratory for Civil Engineering (LNEC, by its initials in Portuguese) in Lisbon, Portugal. The structures were subjected to a sequence of earthquake excitations that induced different levels of inelastic demand on the structures. However, in the first case low-intensity white noise (WN) excitations were also applied between ground motions. The FE models developed in both cases were used only to obtain simulated responses (accelerations and/or displacements) in order to evaluate the feasibility of using numerical models for validation of the damage detection methodologies presented.

Wavelet analyses were capable of identifying rebar fracture episodes and partially identified the frequency shifts in the structures as the inelastic demand increased. It was also found that, depending on the methodology employed, the use of numerical models to validate damage detection techniques can oversimplify the actual problem and/or induce spurious irregularities.

RESUMEN

Debido a la escasa información proveniente de edificios instrumentados que hayan sufrido daño durante un sismo, los ensayos de mesa vibradora a gran escala de estructuras civiles ofrecen una oportunidad valiosa para validar sistemas de monitoreo de salud estructural y su aplicabilidad en estructuras sometidas a cargas sísmicas destructivas.

El objetivo principal de esta investigación consistió en validar metodologías basadas en wavelets, sin el uso de modelos estructurales, para detección de daño en estructuras de concreto reforzado. Para ello se desarrollaron algoritmos de procesamiento de señales con el fin de realizar análisis en el dominio del tiempo y la frecuencia así como también análisis de identificación del sistema entre otros, usando datos de ensayos de mesa vibradora a gran escala y resultados obtenidos de modelos no lineales de elementos finitos. La información experimental usada en esta investigación se obtuvo durante dos ensayos realizados recientemente. Primero, un ensayo de mesa vibradora a gran escala de una columna de un puente en concreto reforzado realizado en la universidad de California en San Diego (UCSD, por sus siglas en inglés). En segundo lugar, dos ensayos de mesa vibradora a gran escala de un pórtico tridimensional de concreto reforzado realizados en el laboratorio nacional para la ingeniería civil (LNEC, por sus siglas en portugués). Las estructuras fueron sometidas a una serie de movimientos sísmicos que generaron diferentes niveles de demanda inelástica en las estructuras. Sin embargo, en el primer caso también se aplicaron excitaciones de ruido blanco entre los sismos. Los modelos de elementos finitos que se realizaron fueron usados únicamente para obtener las respuestas simuladas (aceleraciones y/o desplazamientos) con el fin de evaluar la viabilidad de usar modelos numéricos para la validación de las metodologías de detección de daño presentadas.

El análisis con wavelets identificó episodios de ruptura de barras de refuerzo e identificó parcialmente los cambios de frecuencia en las estructuras a medida que la demanda inelástica aumentaba. También se encontró que, dependiendo de la metodología empleada, el uso de modelos numéricos para validar técnicas de detección de daño puede simplificar demasiado el problema real y/o generar irregularidades espurias.

Dedicated to my darling Angela,

who helped me get this achievement from the beginning...

Who was always there when I needed her, kept me strong, gave me her entire support and understanding during these two tough years far away from her...

To whom I owe the best moments and things I have...

You are the most important part of my life!

ACKNOWLEDGMENTS

I want to thank God for all the blessings I receive from him every day, especially at this time for letting me complete my master's degree. Also, thanks a lot to my family for all their unconditional support, essential to achieve this goal of my life and career: my darling Ángela Cárdenas, my parents, and my four sisters.

I would like to acknowledge not only the support and guidance, but also the opportunity and trust on my work, provided by my advisor Dr. Luis A. Montejo; his advice and teaching are greatly appreciated. Also, I want to thank my graduate committee: Dr. Luis E. Suárez, Dr. Ricardo López, and Prof. Ismael Pagan, for taking the time to review this research.

I want to thank Prof. Gilberto Areiza, a great teacher, and a friend who encouraged me to purse graduate studies. I also want to thank my graduate friends for making my stay more comfortable in Mayaguez.

This research is supported by the National Science Foundation Grant No. CMMI-1121146, which support I also acknowledge. Any opinion, findings and conclusions or recommendations expressed in this work are those of the author and do not necessarily reflect the views of the National Science Foundation.

The UCSD column's experimental data was obtained from the NEEShub Project Warehouse, a centralized data repository for sharing and publishing earthquake engineering research data from experimental and numerical studies https://nees.org/warehouse/project/987/. I would like to thank Dr. Matthew Schoettler and Professor Jose Restrepo for making the raw data for this set of tests publicly available in a timely manner. The Lisbon frames' experimental data was provided by the 15th World Conference on Earthquake Engineering (WCEE) Blind Test Committee.

TABLE OF CONTENTS

LIST OF FIGURES

LIST OF TABLES

CHAPTER I

1. INTRODUCTION

1.1. Problem Statement

Structural Health Monitoring (SHM) is a research field that has become one of major interest in civil engineering and it is increasing its importance in modern structural engineering practice. SHM aims to provide a diagnosis of the state of a structure in terms of the behavior and condition of its structural components at every moment along its lifetime (Balageas et al., 2006). In general terms, the health of a structure can be affected by normal aging due to usage, by the action of the environment, or extraordinary events such as an earthquake.

Thanks to recent developments in sensor, communication, computational, and signal processing technologies; now it is possible to monitor the structural behavior continuously in order to assess damage and implement effective remediation efforts. SHM has the potential to indicate if a structure is in need of repairs, or if a catastrophic failure could occur (Huston, 2011). SHM can then play a very important role on preventing and mitigating the course of structural damage, improving the safety and reliability of current civil infrastructure.

Traditionally, visual inspection in combination with heuristic assumptions and mathematical models has been used as the default method for SHM purposes for many years (Huston, 2011). Nowadays, modern sensing systems are used to increase the benefits of using SHM methods. Besides the safety issues, more knowledge about the structural behavior of a structure can lead to an improved, more rational, design of structures.

SHM is divided into four category levels: (1) damage detection; (2) damage localization; (3) quantification of the degree of damage; and (4) estimation of the remaining service life (Curadelli et al., 2008). This research is focused in damage detection and quantification in reinforced concrete (RC) structures. For this purpose, simultaneous time-frequency and system identification analyses will be employed. This is one of the existing methods extensively studied over the last years in the SHM field (Michel and Gueguen, 2010).

1.2. Justification and Previous Research

Perhaps the strongest motivation for developing damage detection techniques is not only the improvement of safety during or after a seismic event, but also the prevention of premature structural failure. Some accidents have taken place in the past due to: (1) unsatisfactory maintenance, for instance, the 1983 collapse of the Mianus River Bridge at Greenwich, CT, USA, in which 3 people died; and (2) a poorly controlled construction process, for example, the 1998 collapse of the Injak Bridge at Bushbuckridge, Mpumalanga, South Africa, in which 14 people died (Balageas et al., 2006). Premature structural failure could result on severe safety and economic consequences. Damage detection methodologies would help to avoid and decrease such catastrophic results. The economic aspect is also a motivation. It has been found that the maintenance costs and reliability are constant for structures with SHM systems, in contrast with the increasing maintenance costs and decreasing reliability for conventional structures (Balageas et al., 2006).

As mentioned before, visual inspection is the most common method for damage detection purposes; however, it is an arduous and time-consuming task. Thus, it is desirable to develop techniques that enable the immediate assessment of the safety of a structure. Several techniques have been developed for damage detection purposes based on the dynamic response of the structure, and they are classified basically into two groups: (1) signal-based methods; and (2) model-based methods. Robust model-free signal processing techniques to analyze/process sensors data have the potential to detect, quantify, and localize damage of a civil structure in a timely manner. Therefore this type of methods could play a very important role on any SHM system. However, most of the available methods have limitations that have not been solved yet (Montejo, 2011). In the case of signal-based approaches, for instance, some methodologies use the changes in the mode shapes. This requires a dense sensor network with a large spatial resolution, and for some complex structures this could be a serious issue. In the case of model-based approaches, most techniques depend on the updating of a detailed finite element (FE) model. This is a serious limitation because the resulting FE models might be of high complexity and still not able to capture the intricate nonlinear localized behavior of a civil structure undergoing a damage process. Other simpler approaches focus on comparing the dynamic properties of the pristine and damaged structure (e.g. before and after the damaging event). This

has two serious drawbacks: (1) the information of the pristine structure is not always available and (2) significant information regarding the system changes during the damaging process is lost.

Many of the signal-based techniques are based on the vibration characteristics of a structure. They are based on the premise that changes in the physical properties of a structure (i.e., mass, energy dissipation mechanisms, and stiffness) are directly related to changes in the modal properties, such as the natural frequencies, mode shapes, and modal damping (Curadelli et al., 2008). Therefore, the fundamental basis of these methods is that a local or global, stiffness, damping, or mass shift will induce changes in the modal parameters, and these changes can be used for damage identification. The aforementioned parameters can be measured by performing time domain analyses, frequency domain analyses, or simultaneous time-frequency domain analyses. In this research, time-frequency analyses will be performed using Wavelet Transform (WT) and Hilbert Transform (HT) analyses to estimate the dynamic properties of the structures at different levels of inelastic seismic demand.

Several authors have explored the use of wavelet analysis and system identification for SHM. Hera and Hou (2004) used simulated data generated by the ASCE Task Group on Health Monitoring for a four-story prototype building structure subjected to simulated stochastic wind loading. They found that structural damage due to sudden breakage of structural elements and the time when it occurred can be clearly detected by spikes in the wavelet details and that the damaged region can be determined by the spatial distribution pattern of the observed spikes. A similar approach was presented by Ovanesova and Suarez (2004) to detect cracks in frame structures from the wavelet analysis of the static deflected shape. The methodology was validated using numerically simulated data. Hou et al. (2006) introduced a wavelet-based methodology to extract the instantaneous modal parameters to assess the structural health condition of structures subjected to base accelerations; the proposed methodology was validated using the simulated response of a 3 story shear building. Todorovska and Trifunac (2007) analyzed data recorded from an instrumented six-story building severely damaged by the Imperial Valley earthquake in 1979. They found changes (drops) in the instantaneous frequencies of the building which were calculated by performing a time-frequency analysis; this means that the changes they found occurred during the earthquake excitation. Todorovska and Trifunac (2010) used experimental data collected in their previous research (Todorovska and

Trifunac, 2007). They found that the irregularities detected in the wavelet details correlate well with the observed damage. Nevertheless, the building was severely damaged during the earthquake and an assessment of the level of damage that can be identified is not possible through this data. Loh et al. (2011) analyzed shaking table test data from six RC frames using, among others, a signal processing-based approach and performing a system identification to support the damage detection methodologies. While they were able to correlate the change in frequency with the inelastic demand in the structure, it should be noticed that the level of damage induced during the test remained at the serviceability level (e.g. no core crushing, no rebar buckling or rupture). Noh et al. (2011) proposed three wavelet-based damage-sensitive features (DSFs) extracted from structural responses recorded during earthquakes to diagnose structural damage. The methodology was validated using simulated data as well as shake-table experiments of a 30% scaled model of a reinforced concrete bridge column and a 1:8 scale model of a four-story steel moment-resisting frame. The results obtained were very encouraging and affirmed once more the appropriateness of wavelet analysis to study non-stationary signals. It was noticed also that for practical applications a predefined system needs to map the values of the DSFs to different damage states of the structure. For this purpose, Noh et al. (2012) developed fragility functions that define the probabilistic relationship between the DSFs and the damage state of steel moment resisting frame structure.

The purpose of this research is to validate wavelet-based model-free methodologies for damage detection in RC structures, by developing algorithms to perform time-frequency and system identification analyses using data collected during full-scale shaking table tests of RC structures.

1.3. Objectives

The specific objectives of this research can be summarized as follows:

- ✓ Evaluate the feasibility and possible limitations of using output-only model-free wavelet-based methodologies to detect damage in RC structures subjected to base accelerations using data collected during full-scale shaking table tests.

- ✓ Evaluate the suitability of using numerical models for the validation of damage detection techniques for RC structures. For this purpose nonlinear FE models capable of replicating the shaking table tests results will be generated.
- ✓ Assess the feasibility of employing changes in the natural frequencies and damping ratios of RC structures to identify different levels of seismic induced damage. Perform signal processing-based system identification analyses to investigate the changes in the aforementioned dynamic properties.
- ✓ Examine the correlation between damage detected by using signal-based methodologies, and damage observed during full-scale tests of RC structures. Use different techniques to measure the degree of damage detected to compare it with the severity of damage reported during the tests.

1.4. Data Used in This Research

The data used in this research was collected during two large scale shaking table tests of reinforced concrete structures performed in San Diego, USA and Lisbon, Portugal:

(1) Full-scale RC bridge column shaking table tests were recently performed at the Network for Earthquake Engineering Simulation (NEES) Large High Performance Outdoor Shake Table (LHPOST) at the University of California, San Diego (UCSD). Ten ground motions, starting with low-intensity motions, were applied to the column leaving it near collapse conditions. One of the safety columns was struck by the superstructure during the last Earthquake (EQ) load, and so this motion will not be considered. In addition to earthquake loads, low-intensity White Noise (WN) excitations were applied to the column between earthquakes. The column had a height (cantilever length) of 7.32m (24ft) with a circular cross section of 1.22m (4ft) diameter, and it also had a reinforced concrete block at the top with a total weight of 2245kN (250ton). A total of 18 No. 11 bars were provided as the longitudinal reinforcement, and butt-welded double No. 5 hoops spaced 152mm (6in) center to center were used as the transverse reinforcement. Further details of the test, material properties, and specimen geometry were presented by Schoettler et al. (2012). Figure 1-1 shows some pictures of the test setup.

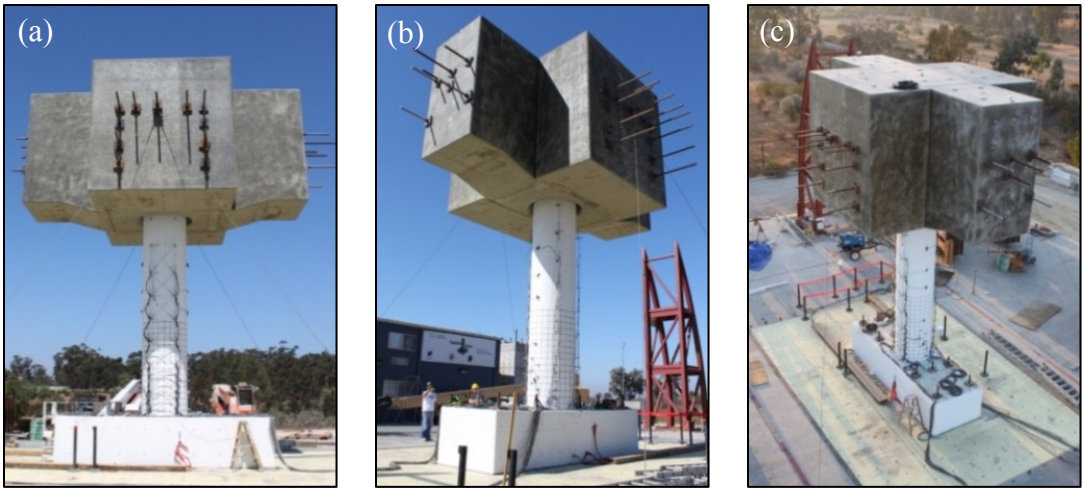

Figure 1-1: Full-scale bridge column test setup (a) front view, (b) 3D view from bottom, and (c) 3D view from top (photos taken from: https://nees.org/warehouse/project/987/)

(2) Two full-scale RC 3D frame shaking table tests recently performed at the National Laboratory for Civil Engineering (LNEC) 3D shaking table in Lisbon, Portugal. Both structures were geometrically identical, but they were designed for low and high ductility levels, according to the Eurocode 8 (EC8) provisions, so that the steel reinforcement detailing was different. The structure displacement response and design data were provided by the 15th World Conference on Earthquake Engineering (WCEE) Blind Test Committee (2012). Both 3D frames were subjected to four EQ loads with increasing intensity levels, that is, low, moderate, reference, and high. Both structures had one bay in each horizontal direction; one story; four columns of 3m (9.84ft) height with a square cross section of 20cm (7.87in) x 20cm (7.87in); four beams with a square cross section of 20cm (7.87in) x 40cm (15.75in) from which two of them had a 3.5m (11.48ft) length on one direction and the other two had a 4m (13.12ft) length on the perpendicular direction. A slab extended 2m (6.6ft) from one edge to the beam in the perpendicular direction. Also both structures had nine additional masses of 1200kg (2645.6lb) each one placed on top of the slab. Steel reinforcement detailing, as well as further details of the test, material properties, and specimens' geometry were presented in the 15th WCEE Blind Test Challenge Design Report (2012). Figure 1-2 presents some pictures of the test setup.

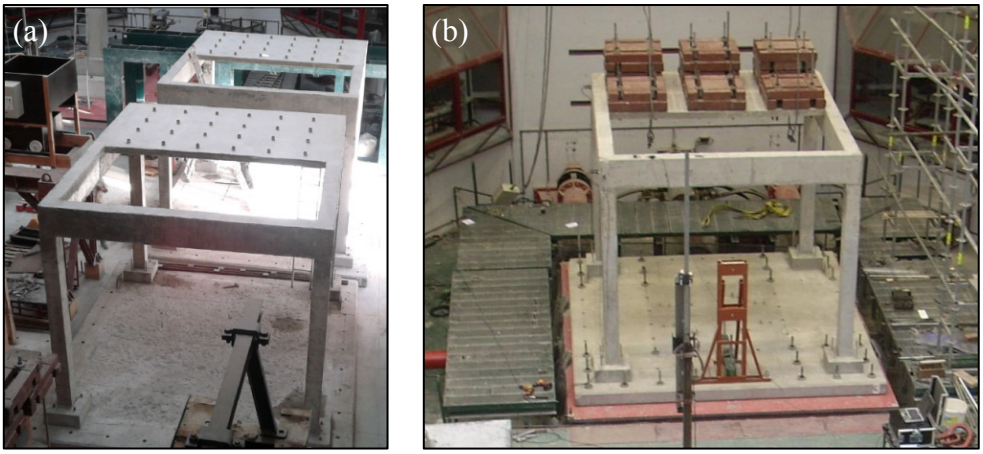

Figure 1-2: Full-scale 3D frame structure tests setup (a) 3D view from top, and (b) front view (photos taken from: 15th WCEE Blind Test Challenge, 2012)

1.5. Scope of the Research Work

The activities to be performed as part of this research work include:

(1) Perform Continuous Wavelet Transform (CWT) and Discrete Wavelet Transform (DWT) analyses on the structure response signals, to extract frequency ridges and detect any shift in the vibration frequency, and to detect irregularities in the high frequency response of the structure, respectively.

(2) Develop FE models using different approaches representative of current design/assessment practice, (multilinear hysteresis, Takeda like) and RC seismic research (distributed plasticity - fiber based sections). These models are used only to obtain the simulated response of the structure in order to evaluate the suitability of using this type of models for validation of SHM methodologies.

(3) Perform signal processing-based system identification analyses to determine damping ratio and natural frequency changes after each EQ (UCSD column only): (1) using the final part of the structure response to EQ records (free decay) and CWT analysis; and (2) using the structure response to WN excitations and the Random Decrement Technique (RDT) in combination with the Hilbert Transform (HT).

(4) Determine the maximum displacement ductilities and damage indexes (DI) for each EQ load to correlate them with the damage observed, and the changes in the dynamic properties computed previously in activity 3.

1.6. Thesis Organization

1.6.1. Damage detection methodologies

The theoretical basis of the methodologies employed in this research is presented in Chapter II. The signal processing based techniques for simultaneous time-frequency and system identification analyses are described. Also, the mathematical tools that allow performing the analyses, like Wavelet or Hilbert Transforms, are briefly described in this chapter.

1.6.2. Development and calibration of nonlinear finite element models

Chapter III describes the numerical models developed during this work for the UCSD RC column and the Lisbon 3D RC frame. The models will be calibrated based on available experimental data from shaking table tests and by performing analysis of lateral monotonic and cyclic load. In the case of the Lisbon 3D frame model only a lateral monotonic load analysis will be applied for calibration purposes. In addition, dynamic earthquake analyses will be performed by applying the same WN excitations and EQ records used during the tests, respectively.

1.6.3. Damage detection using the UCSD column experimental and simulated data

Chapter IV presents and analyzes the results of applying the wavelet-based and the system identification methodologies for damage detection using the available experimental data and the simulated data obtained from the developed models in Chapter III for the UCSD column.

1.6.4. Damage detection using the Lisbon 3D frame experimental and simulated data

Based on the results obtained in Chapter IV, Chapter V presents and analyzes the results of applying the wavelet-based methodologies for damage detection using the available experimental data and the simulated data obtained from the developed models in Chapter III for the Lisbon 3D RC frame.

1.6.5. Conclusions and recommendations

In Chapter VI, final conclusions and recommendations for future works are developed, according to the results obtained on Chapters III through V.

1.7. References

15th WCEE Blind Test Challenge Design Report, (2012), "15th World Conference on Earthquake Engineering", Lisbon, Portugal.

Balageas, D., Fritzen C.-P., and Guemes, A. (2006), Structural Health Monitoring, ISTE Ltd., London, United Kingdom.

Curadelli, R. O., Riera, J. D., Ambrosini, D., and Amani, M. G. (2008), "Damage Detection by Means of Structural Damping Identification", Engineering Structures 30, 3497-3504.

Hera, A. and Hou, Z. (2004), "Application of Wavelet Approach for ASCE Structural Health Monitoring Benchmark Studies", ASCE Journal of Engineering Mechanics 130(1), 96-104.

Hou, Z., Hera, A. and Shinde, A. (2006), "Wavelet–Based Structural Health Monitoring of Earthquake Excited Structures", Computer Aided Civil and Infrastructure Engineering 21, 268–279.

Huston, D. (2011), Structural Sensing, Health Monitoring, and Performance Evaluation, Taylor & Francis, Boca Raton, FL.

Michel, C. and Gueguen, P. (2010), "Time-Frequency Analysis of Small Frequency Variations in Civil Engineering Structures Under Weak and Strong Motions Using a Reassignment Method", Structural Health Monitoring 9, 159–171.

Montejo, L. A. (2011), "Signal Processing Based Damage Detection in Structures Subjected to Random Excitations", Structural Engineering and Mechanics 4(6), 745-763.

Ovanesova, A. V. and Suarez, L. E. (2004), "Applications of Wavelet Transforms to Damage Detection of Frame Structures," Engineering Structures 26, 39-49.

Schoettler, M.J., Restrepo, J. I., Guerrini, G., Duck, D.E. and Carrea, F. (2012), "A Full-Scale, Single-Column Bridge Bent Tested by Shake-Table Excitation" Center for Civil Engineering Earthquake Research, Department of Civil Engineering, University of Nevada, Reno.

Todorovska, M. I. and Trifunac, M. D. (2007), "Earthquake Damage Detection in The Imperial County Services Building I: The Data and Time Frequency Analysis", Soil Dynamics and Earthquake Engineering 27, 564-576.

Todorovska, M. I. and Trifunac, M. D. (2010), "Earthquake Damage Detection in The Imperial County Services Building II: Analysis of Novelties Via Wavelets", Structural Control and Health Monitoring 17(8), 895-917.

Loh, C. H., Mao C. H., Huang, J. R. and Pan, T. C. (2011), "System Identification and Damage Evaluation of Degrading Hysteresis of Reinforced Concrete Frames", Earthquake Engineering and Structural Dynamics 40, 623–640.

Noh, H. Y., Nair, K. K., Lignos, D. G. and Kiremidjian, A. S. (2011), "Use of Wavelet–Based Damage–Sensitive Features for Structural Damage Diagnosis Using Strong Motion Data", ASCE Journal of Structural Engineering 137(10), 1215–1228.

Noh, H. Y., Lignos, D. G., Nair, K. K. and Kiremidjian, A. S. (2012), "Development of Fragility Functions as a Damage Classification/Prediction Method for Steel Moment–Resisting Frames Using a Wavelet–Based Damage Sensitive Feature", Earthquake Engineering and Structural Dynamics 41(4), 681–696.

CHAPTER II

2. DAMAGE DETECTION METHODOLOGIES

2.1. Introduction

Signal processing based techniques might play an important role in any SHM system as they allow near-real time identification of structural parameters and damage episodes from the analysis of the nonlinear-nonstationary characteristics of the dynamic response of the structure (usually accelerations) to the damaging event.

In this chapter, two methodologies for model-free output-only wavelet based damage detection are described, that is, methodologies that only use the accelerations/displacements recorded on the structure will be presented. The methodologies presented in this chapter will be implemented in the following chapters using data collected during full-scale shaking table tests of RC structures.

2.2. Wavelet-Based Time-Frequency Analysis

Information about how the frequency content of a signal evolves with time can be provided by performing a time-frequency analysis. This kind of analysis can be performed using recently developed methodologies like Wavelet and Hilbert-Huang transforms. These methods are able not only to detect certain slow varying phenomena of a signal but also permit the detection of sudden discontinuities (Montejo, 2011).

Two types of analyses are performed, one at low frequencies using the Continuous Wavelet Transform, i.e. in the frequency range of the structure modes of vibration. The second analysis is performed at high frequencies using the Discrete Wavelet Transform, i.e. well above the natural structural frequencies and close to the signal Nyquist frequency. The aims of the two methodologies can be summarized as follows:

(1) Detect shifts in the vibration frequency as the structure responds to the seismic accelerations by extracting the frequency ridges from the wavelet map obtained via

the CWT. This is based on the premise that the damaging process during earthquakes produces a permanent loss of structural stiffness and thus a decrease of the fundamental frequency (Michel and Gueguen, 2010). This is an elementary approach of SHM methods studied by several authors. Todorovska and Trifunac (2007), for instance, analyzed the inter-story drifts and changes in the first frequencies of a six-story RC structure severely damaged by the 1979 Imperial Valley earthquake. They found a decrease in the system frequencies which correlated well with the observed damage. Similar results have been reported by Zembaty et al. (2006) using shaking table data of two RC frames subjected to different levels of earthquake intensities.

(2) Detect irregularities in the high frequency response of the structure by investigating the detail function obtained via the DWT. This is based on the premise that an abrupt change in stiffness will be reflected on the high frequency acceleration response of the structure. To study the high frequency response of the structure, past research efforts have used high-pass filters (e.g. Montejo 2011, Bisht and Singh 2012) or the DWT to obtain the detail functions (e.g. Pan and Lee 2002, Hera and Hou 2004, Todorovska and Trifunac 2010). Regardless of the approach used, the irregularities (damage episodes) are reflected as spikes on the high frequency response.

2.2.1. Continuous Wavelet Transform

The Continuous Wavelet Transform (CWT) of a function *x(t)* of a real variable is defined as a function of two variables *W(a,b)*, which is the convolution of the signal and a scaled, shifted versions of the mother wavelet *ψ(t)*:

$$W(a,b) = \frac{1}{\sqrt{a}} \int_{-\infty}^{+\infty} x(t)\, \psi\left(\frac{t-b}{a}\right) dt \tag{2-1}$$

The wavelet coefficients *W(a,b)* are a measure of the similitude between the shifted mother wavelet and the signal at the time position *b* and scale *a* which can be related with frequency (Kijewski and Kareem, 2003). A modified version of the Complex Morlet Wavelet (Grossman and Morlet, 1990; Yan and Miyamoto, 2006) is used in this research:

$$\psi(t) = \frac{1}{\sqrt{\pi\, f_b}}\, e^{i\, 2\, \pi\, f_c\, t}\, e^{-t^2/f_b} \tag{2-2}$$

where f_b is a bandwidth parameter that controls the shape of the mother wavelet and f_c is the central frequency of the mother wavelet. Figure 2-1 and Figure 2-2 show the effect of changing the parameter values on the time and frequency characteristics of the mother wavelet. It is seen that increasing the localization in the frequency domain (by increasing the value of f_b) decreases the localization in the time domain, and vice versa. In this case, the time and frequency resolutions for this wavelet at a frequency f_i, using the Heisenberg uncertainty principle, are given by:

$$\Delta t_i = \frac{f_c}{f_i}\, \frac{\sqrt{f_b}}{2} \tag{2-3}$$

$$\Delta f_i = \frac{f_i}{f_c}\, \frac{1}{2\, \pi\, \sqrt{f_b}} \tag{2-4}$$

Figure 2-3 and Figure 2-4 show the effect of changing the parameter values, f_b and f_c, on the time and frequency resolutions computed using Equations (2-3) and (2-4), respectively.

Another critical point in wavelet analyses are the edge effects. Such phenomena can significantly affect the quality of the wavelet coefficients. The end-effect zone depends on the time resolution and can be estimated using Equation (2-5) (Kijewski and Kareem, 2003; Yan et al., 2006):

$$\Delta\, T_i = \beta\, \frac{f_c}{f_i}\, \frac{\sqrt{f_b}}{2} \tag{2-5}$$

where the value for β is determined according to the desired accuracy level; a value of $\beta = 4$ is usually large enough.

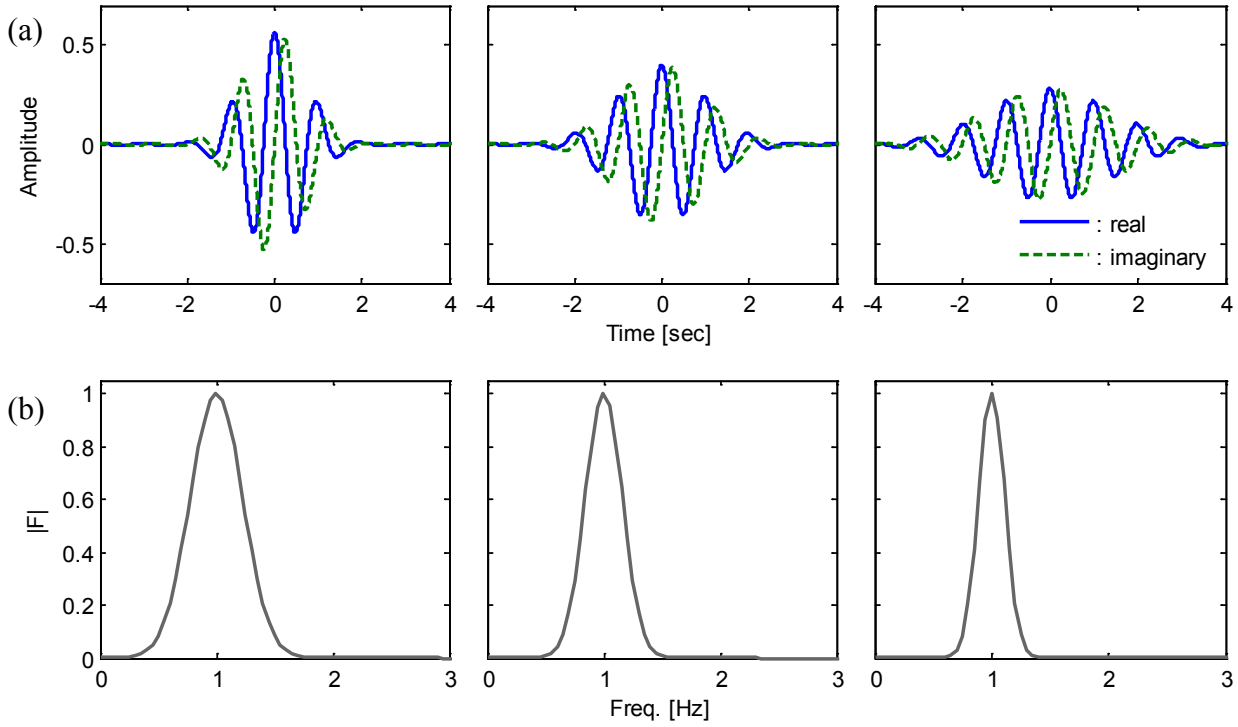

Figure 2-1: The Modified Complex Morlet Wavelet in (a) the time and (b) frequency domains for $f_c=1$ and different values of the parameter f_b. From left to right: $f_b=1$; $f_b=2$; $f_b=4$

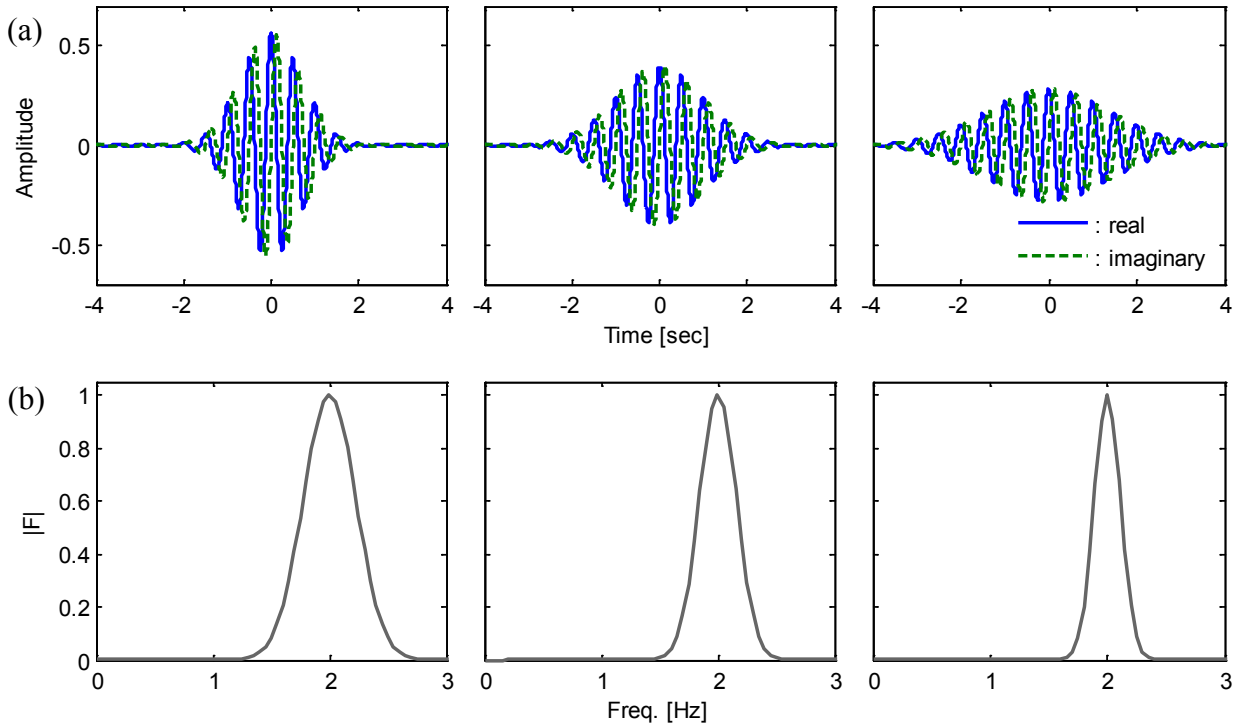

Figure 2-2: The Modified Complex Morlet Wavelet in (a) the time and (b) frequency domains for $f_c=2$ and different values of the parameter f_b. From left to right: $f_b=1$; $f_b=2$; $f_b=4$

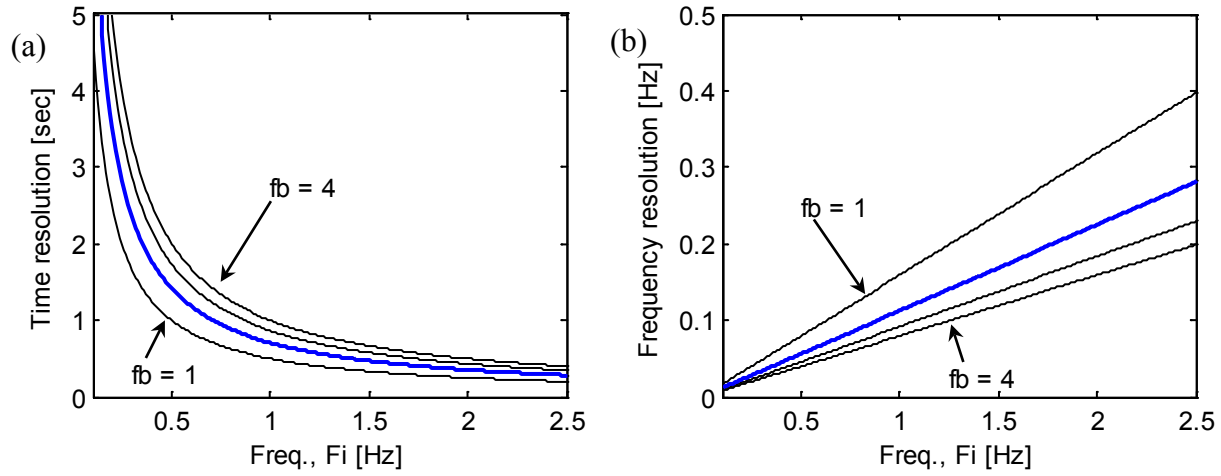

Figure 2-3: (a) Time and (b) frequency resolutions for the Modified Complex Morlet Wavelet for different values of f_b and f_c=*1*

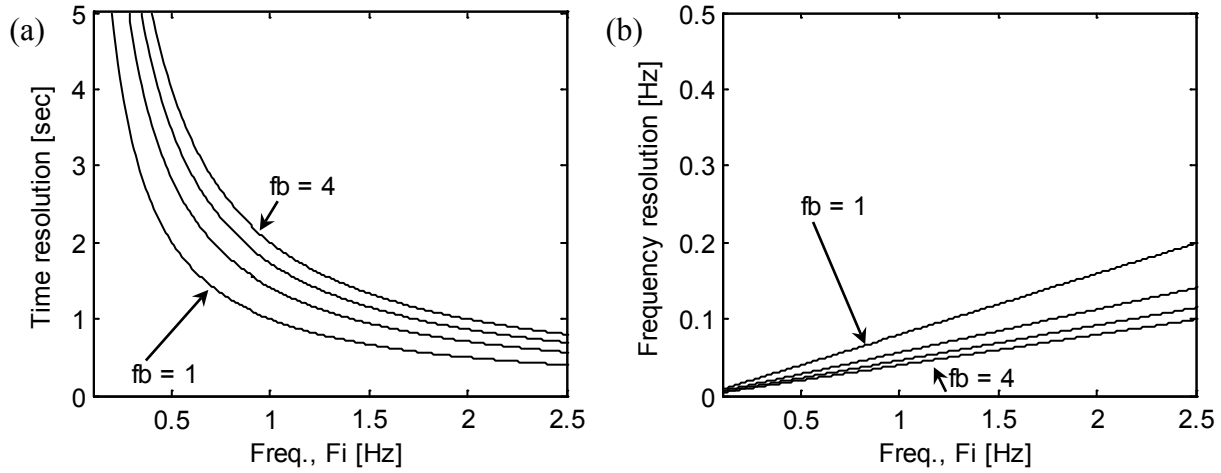

Figure 2-4: (a) Time and (b) frequency resolutions for the Modified Complex Morlet Wavelet for different values of f_b and f_c=*2*

Usually, the wavelet coefficients *W(a,b)* are illustrated in a two-dimensional graph as shown in Figure 2-5b. This graph is called a wavelet map, and it is a representation of the response function *x(t)* in the time-frequency domain. The darker colors indicate higher values of the wavelet coefficients. The estimation of the instant frequency is done by identifying a ridge in the time-frequency plane which can be obtained by locating the local maxima at each time instant (Montejo, 2011). The ridge can be obtained according to:

$$W(a_r, b) = \max[W(a, b)] \tag{2-6}$$

where a_r are the scales (that can be related to frequencies) corresponding to the ridge and $W(a_r,b)$ is a complex function that represents the ridge that evolves with time. The real and imaginary components along the ridge are directly proportional to the response function content at that frequency and its corresponding Hilbert Transform (HT) (Kijewski and Kareem, 2003).

As an example, a CWT analysis was performed using an artificially generated signal with two sinusoidals. First, from 0 to 5 seconds, a sinusoidal with frequency of 2.0 Hz, then from 5 to 10 seconds, a sinusoidal with frequency of 1.0 Hz. Notice that at 5 seconds a discontinuity is induced in the signal due to the change of the frequency.

Figure 2-5a illustrates the aforementioned signal in the time domain. Figure 2-5b shows the results of the analysis (CWT wavelet map) which is the representation of the signal in the time-frequency domain. Dotted lines on the sides of the figure denote the end-effects zone (Equation (2-5)). The darker colors in the image indicate higher values of the wavelet coefficients and are an indicator of the frequency content of the signal at any time instant. The instantaneous dominant frequencies (wavelet ridges) were obtained using Equation (2-6) (red dashed line). It can be clearly seen that the CWT analysis allows identifying how the frequency of the signal evolves in the time domain. The parameters f_c and f_b required to define the modified Morlet wavelet were defined as 1 and 2 respectively. The time and frequency resolutions for these parameters are illustrated in Figure 2-3 (thick blue line).

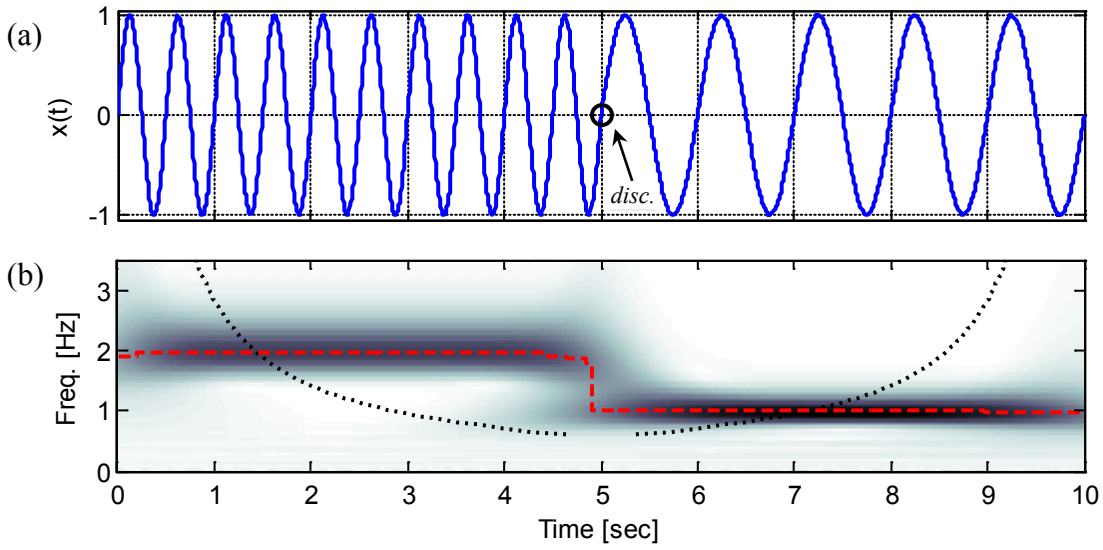

Figure 2-5: (a) Artificially generated signal and (b) CWT wavelet map

2.2.2. Discrete Wavelet Transform

In the CWT the wavelet coefficients are calculated at scale values that vary continuously resulting in a highly redundant and computationally demanding representation of the signal. Using values of scale and position based on a dyadic scale one can define the Discrete Wavelet Transform (DWT) to represent a signal. For some special mother wavelets $\psi(t)$ the corresponding discretized wavelets $\psi_{a,b}(t)$ constitute an orthonormal basis. Mallat (1989) developed a fast wavelet decomposition and reconstruction algorithm (FWT) using a two-channel subband coder. In the FWT, a signal can be represented (Equation (2-7)) by its approximations (A) and details (D) at different levels of decomposition (j). The approximations contain the high-scale (low-frequency) components of the signal, while the details contain the low-scale (high-frequency) components.

$$x(t) = A_j + \sum_{i \le j} D_i \tag{2-7}$$

In this work we are concerned about the detail functions as sudden damage episodes are usually echoed in the high frequency response of the structure. The wavelet used to perform the FWT is the Biorthogonal (Bior) 6.8 wavelet (Cohen et al., 1992). Notice that the Morlet wavelet used for the CWT does not allow carrying out a FWT. Biorthogonal wavelets are compactly supported biorthogonal spline wavelets for which symmetry and exact reconstruction are possible. The Bior 6.8 has been successfully used in the past to uncover discontinuities (Ovanesova and Suarez 2004, Todorovska and Trifunac 2010, Montejo 2011, Montejo et al. 2012a, 2012b). Contrary to the Morlet wavelet, Bior wavelets do not have an explicit expression for the wavelet function.

Figure 2-6 presents an example of a DWT analysis using the same artificially generated signal than in section 2.2.1 (Figure 2-5a). Notice how the approximations (Figure 2-6b) replicate the original signal. Figure 2-6c presents the details of the signal and it is clearly seen that a spike (discontinuity/irregularity) appears when the frequency in the signal changes. In this particular example the artificially generated signal is clean, in other words, it does not include any noise.

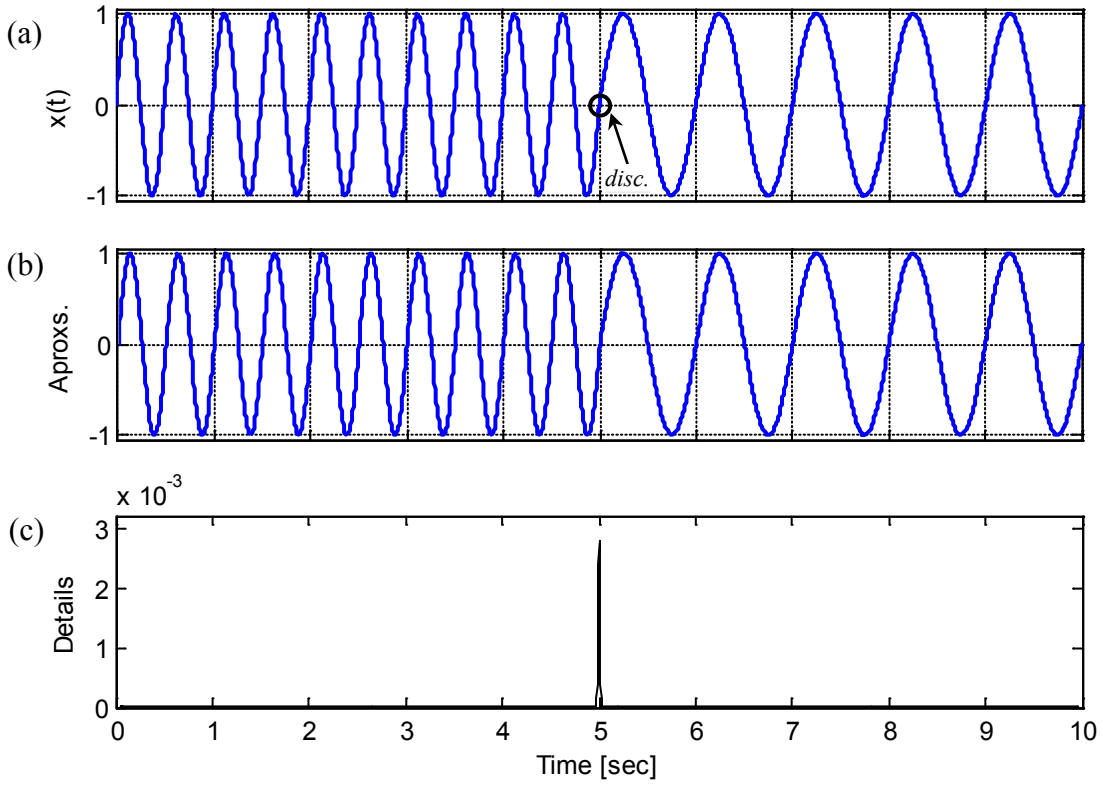

Figure 2-6: (a) Artificially generated signal, (b) DWT aproximations, and (c) DWT details

2.3. Signal Processing Based System Identification

System identification is an important and very useful tool to identify the dynamic properties of any structural system. In this work system identification will be used to determine such properties at different levels of seismic induced damage.

During a seismic event, a civil structure can be subjected to high inelastic demand and its dynamic properties can change depending on the resulting damage. If damage occurs, a decrease in its natural frequencies and an increase in its damping ratios are expected. The aim of this methodology is to assess the feasibility of employing the two aforementioned dynamic properties to identify different levels of seismic induced damage. The use of system identification for damage detection has been extensively studied in previous works in the field of SHM. However, research using real scenario data is not found so often. One of the few studies using this type of data is presented in Todorovska and Trifunac (2007). They analyzed data recorded from an instrumented six-story building severely damaged by the 1979 Imperial Valley EQ. They found changes (drops) in the instant frequencies of the building which were calculated by performing a

time-frequency analysis, this means, the changes they found were determined during the EQ excitation. Unlike the mentioned reference, we focus on natural frequency and damping ratio computation before and after the ground motions are applied. One of the most recent studies was presented by Loh et al. (2011). They analyzed shaking table test data from six RC frames using a signal processing-based approach, among others, performing a system identification to support damage detection methodologies. While they were able to correlate the change in frequency with the inelastic demand in the structure, it should be noticed that the level of damage induced during the test remained at the serviceability level (e.g. no core crushing, no rebar buckling or rupture).

Two different approaches are implemented to identify the first structure's vibration frequency and damping ratio at the different test stages. In the first one, free decay response is obtained by applying the Random Decrement Technique (RDT) to the system acceleration response to white noise (WN) excitations to generate a Random Decrement Signature (RDS). The Hilbert Transform (HT) is then applied to find the analytical signal. In the second approach, free decay response is obtained after each EQ from the end portion of the structure acceleration response to ground motions. In this case, the analytical signal is obtained by performing a Continuous Wavelet Transform (CWT) analysis.

2.3.1. The complex analytical signal

The complex analytical signal (Gabor, 1946) can be described by an exponential function as follows:

$$z(t) = a(t)\, e^{i\,\theta(t)} \tag{2-8}$$

where $a(t)$ and $\theta(t)$ are the amplitude and phase, respectively, which vary in the time domain. The concept of instantaneous frequency as the time-varying derivative of the phase was proposed by Ville (1948) as:

$$IF(t) = \frac{1}{2\,\pi}\,\frac{d}{dt}\big(\theta(t)\big) \tag{2-9}$$

Thus, the identification of the time-varying frequency of the system is provided by the phase of the complex analytical function. In this case, since the analyzed signal corresponds to a

free decay, the damped natural frequency (ω_d) is identified, and the amplitude term takes the form of an exponential which decays based on the natural frequency of the system (ω_n) and damping ratio (ξ). Equation (2-8) then becomes:

$$z(t) = \left(A_0\, e^{-\xi\, \omega_n\, t}\right) e^{i\,(\omega_d\, t + \phi)} \tag{2-10}$$

where A_0 is an initial amplitude value, and ϕ is a phase shift. This complex analytical signal can also be written as:

$$z(t) = x(t) + i\, y(t) = \; a(t)\, e^{i\,\theta(t)} \tag{2-11}$$

where:

$$a(t) = \sqrt{x^2 + \; y^2} \tag{2-12}$$

$$\theta(t) = arctan\left(\frac{y}{x}\right) \tag{2-13}$$

This means that the analytical signal decomposes a signal into its components, namely, their instant amplitude (IA) $a(t)$ and instant phase *θ(t)*. The instant frequency (IF) was defined mathematically in Equation (2-9), but if the IF is computed directly by using this equation with numerical differentiation of instant phase values, the results obtained will show discontinuities at the same instants in which the instant phase presents discontinuities (Ramirez and Montejo, 2011). This problem can be solved by using several techniques. One of them was proposed by Feldman (2011a, 2011b) and it consists of computing the phases of the differences instead of computing the differences of the phases:

$$IF(t) = \frac{1}{2\,\pi}\; arctan\left(z_n\; conj(z_{n+1})\right) \tag{2-14}$$

In both the RDT in combination with HT approach and the CWT approach the complex analytical signal in Equation (2-11) can be obtained. The process to do this is explained in sections 2.3.3 and 2.3.4. Having the analytical signal defined, the IF and the IA are calculated

using Equations (2-12), (2-13), and (2-14), enabling the identification of the dynamic properties. For the scope of this work, the natural frequency is a constant obtained directly from the mean value of the IF as:

$$f_d = \frac{1}{N}\sum_{i=1}^{N} IF(t_i) \tag{2-15}$$

where *N* is the number of points in the IF function. The damping ratio is obtained by applying a linear fit to the natural logarithm of the amplitude as:

$$Ln(IA) = -m \cdot t + Ln(A_0) \tag{2-16}$$

$$m = \xi\, \omega_n \tag{2-17}$$

where the resulting line slope *(m)* in Equation (2-17) is computed from the mean-squares linear fit. By definition, the damped natural frequency (ω_d) is:

$$\omega_d = \omega_n \sqrt{1-\xi^2} \tag{2-18}$$

Using Equations (2-17) and (2-18), the damping ratio *(ξ)* is computed as:

$$\xi = \sqrt{\frac{(m)^2}{{\omega_d}^2 + (m)^2}} \tag{2-19}$$

where ω_d is computed using the result from Equation (2-15) as follows:

$$\omega_d = 2\,\pi\, f_d \tag{2-20}$$

Once the damped natural frequency (ω_d) and damping ratio (ξ) are computed, the natural frequency can be calculated from Equation (2-18) as:

$$\omega_n = \frac{\omega_d}{\sqrt{1-\xi^2}} \tag{2-21}$$

2.3.2. Random Decrement Technique

The Random Decrement Technique (RDT) is used to obtain the characteristic free decay of the structure from its response to white noise (WN), so that Equation (2-10) can be applied. RDT is a fast-converging method to extract information from random data. This method can be applied to any system which is subjected to an unknown random excitation in which only the system response is measured (e.g., the acceleration response). The fundamental concept of the RDT is based on the fact that the response of a damped structure is composed of two parts: a deterministic part and a random part (Al Sanad et al., 1983). Segments of the random vibration response of a system are ensemble averaged to form a signature that is representative of the free vibration modal response of the system. By averaging enough segments of the same random response, the random part will be averaged out, leaving the deterministic part (i.e., impulse and/or step function). The deterministic part that remains is the free vibration response from which the dynamic properties (i.e., the natural frequency and the damping ratio) can be measured.

In order to explain the principles of the RDT, a linear single degree of freedom (SDOF) system will be analyzed. The displacement response $x_i(t)$ of a SDOF system that is subjected to an arbitrary load is governed by the following equation of motion:

$$m\,\ddot{x}(t) + c\,\dot{x}(t) + k\,x(t) = f(t) \tag{2-22}$$

where $x(t)$, $\dot{x}(t)$, and $\ddot{x}(t)$ are the displacement, velocity, and acceleration responses, respectively. The parameters m, c, and k correspond to the mass, damping coefficient, and stiffness, respectively. Finally, $f(t)$ is an arbitrary excitation force which, in this particular case, must be of random nature. For linear systems the response $x_i(t)$ can be decomposed into three parts: response to initial displacement $x_d(t)$, response to initial velocity $x_v(t)$, and response to the random excitation force $x_f(t)$. The response can then be written as:

$$x_i(t) = x_d(t) + x_v(t) + x_f(t)$$

(2-23)

The RDT consists of dividing the time history of a system response (i.e., displacement, velocity, or acceleration) into N equal length segments of duration τ_{max} possibly overlapping as shown in Figure 2-7.

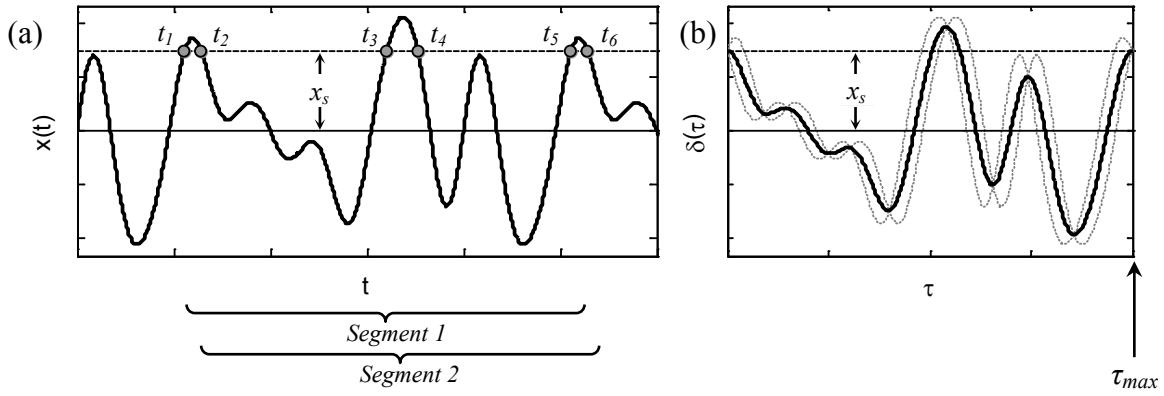

Figure 2-7: (a) Selection of the initial points of equal length segments and (b) extraction of the RDS (continuous dark line) using only segments 1 and 2 (doted light lines)

The starting time t_i of each segment is selected such that each one begins at a selected amplitude x_s. This means that $x_i\ (t_i) = x_s = constant$ and that the slope $\dot{x}_i(t_i)$ alternates between positive and negative. Segments are chosen such that half of them have initial positive slopes and half of them have initial negative slopes. These segments are then ensemble averaged to obtain a signature of length τ_{max} whose initial amplitude is x_s and which can be written as:

$$\delta(\tau) = \frac{1}{N}\sum_{i=1}^{N} x_i(t_i + \tau)$$

(2-24)

where N is the number of segments, and $\delta(\tau)$ is a function called "the Random Decrement Signature" (RDS), which is defined in the time interval $0 \leq \tau \leq \tau_{max}$. Because the initial slopes alternate between positive and negative values, the average responses due to initial velocity cancel out. In addition, if the parts caused by the excitation force are averaged, they also disappear because the excitation is random with zero mean Gaussian distribution by definition. The responses caused by initial displacement are left and their average is the random decrement signature which, for a linear SDOF system, represents the free vibration modal response of the

system caused by an initial displacement, which corresponds to the initial value x_s. The required number of segments N to be averaged depends on the signal shape, but usually 400 to 500 segments are enough to obtain good results (Al Sanad et al., 1983).

One of the main advantages of this method is that it does not require any knowledge of the excitation force *f(t)*, as long as it exhibits white noise characteristics. As an example, Figure 2-8 shows a WN excitation and the corresponding simulated acceleration response of a damped SDOF system with natural frequency 2Hz and damping ratio 2.5%. The RDT is applied to the acceleration response and the extracted RDS is illustrated in Figure 2-9 as a continuous dark line.

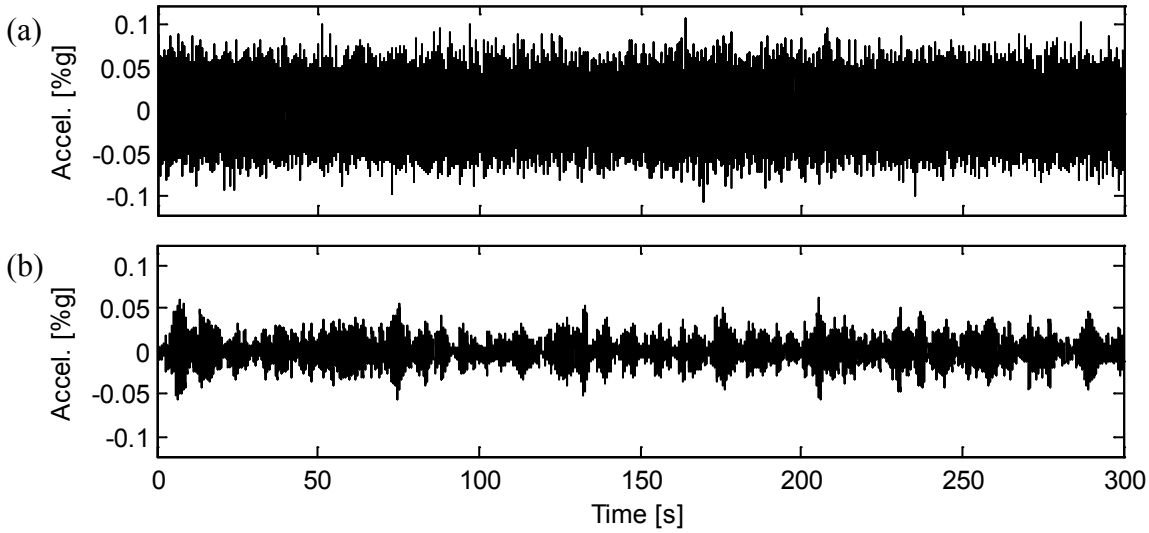

Figure 2-8: (a) Generated low-intensity white noise excitation and (b) simulated acceleration response of a damped SDOF system

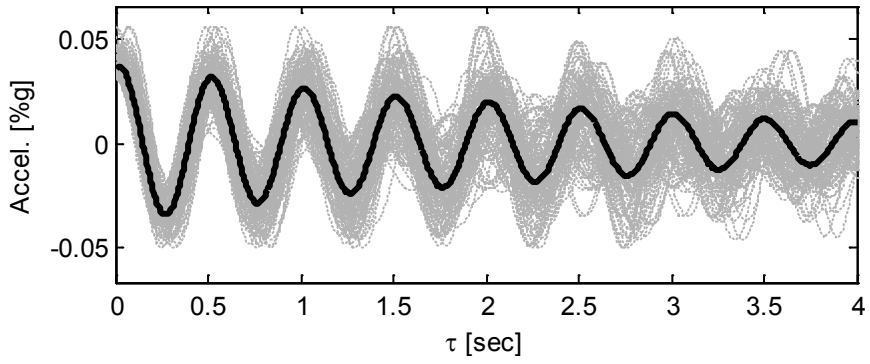

Figure 2-9: Extracted RDS (continuous dark line) from the segments (doted light lines) after applying the RDT to the simulated acceleration response of a damped SDOF system

For multiple degrees of freedom systems, the signature obtained is a combination of modes and it represents the free vibration response to an initial condition. In this case, the response needs to be pre-processed to isolate all the modes in the response, which can be done by using methodologies like the Empirical Mode Decomposition (Huang et al., 1998), the Hilbert Vibration Decomposition (Feldman, 2006), the Synchrosqueezed Transform (Daubuchies et al., 2011; Montejo and Vidot, 2012) or band-pass filtering. The dynamic properties can then be estimated for each mode.

2.3.3. Hilbert Transform

The Hilbert Transform (HT) of a function *x(t)* is defined by an integral transform (Hahn, 1996):

$$H[x(t)] = \frac{1}{\pi}\int_{-\infty}^{+\infty}\frac{x(\tau)}{t-\tau}d\tau \tag{2-25}$$

The HT is the convolution integral of the function *x(t)* and the inverse of time, the result is the original signal with phase shift of π/2. The HT can then be used to generate the analytical signal (Equation (2-11)) of the function *x(t)*:

$$z(t) = x(t) + i\,y(t) = x(t) + i\,H[x(t)] = a(t)\,e^{i\,\theta(t)} \tag{2-26}$$

If the HT is known, it is possible to compute the IF and IA of a mono-component signal, allowing the identification of the natural frequency and damping ratio. Nevertheless, if the HT is applied to a multi-component signal it will still identify only one IF, which represents a weighted average of the frequencies occurring in the signal. Hence, for multi-component signals it is necessary to decompose them first into their mono-component constituents, using the methodologies mentioned in section 2.3.2. Figure 2-10 shows the calculation of the dynamic properties via HT from the free decay response of the damped SDOF system presented in Figure 2-9. The natural frequency and the damping ratio identified were 2.01Hz and 2.52%, respectively, by using 232 segments with 4 seconds of duration. In this case, the error in the estimation of the parameters is less than 1%. Notice the edge effects at the beginning and the end, an expected feature for any transform.

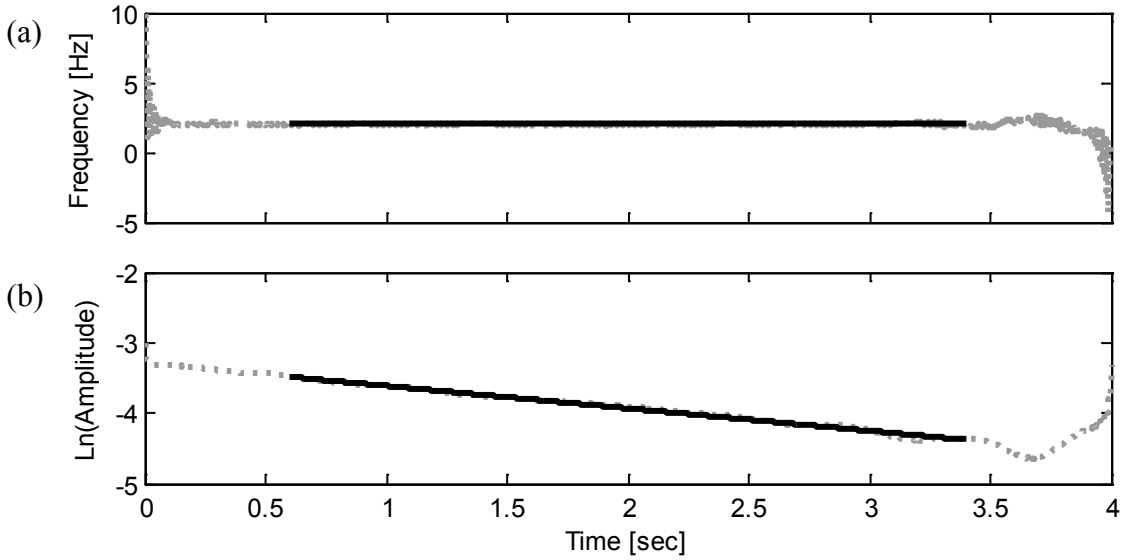

Figure 2-10: (a) Instant frequency and (b) natural logarithm of the instant amplitude

2.3.4. Continuous Wavelet Transform

As explained in section 2.2.1, the CWT allows performing a simultaneous time-frequency analysis of a signal that can provide information about how the frequency content of the signal evolves with time (e.g., Montejo, 2011). In this case, the CWT is used to define the IF and IA by computing the wavelet ridge. The wavelet coefficients, computed using Equation (2-6), are a complex function that represents the ridge that evolves with time. The real and imaginary components along the ridge are directly proportional to the response function content at that frequency and its corresponding HT (Kijewski and Kareem, 2003). The analytical signal in Equation (2-11) can be formed as:

$$z(t) = W(a_r, b) = x(t) + i\, y(t) = a(t)\, e^{i\,\theta(t)} \tag{2-27}$$

Once the analytical signal is constructed, IF and IA can be computed to estimate the dynamic properties, as explained in section 2.3.1.

Figure 2-11 shows the calculation of the dynamic properties via CWT of the simulated free decay response of a damped SDOF system with a damping ratio of 2.50% and a natural frequency of 2Hz. The calculated natural frequency and damping ratio identified were 1.94Hz

and 2.49%, respectively. In this case, the error in the estimation of the parameters is less than 3%. Edge effects appear at the beginning and the end as in the HT approach.

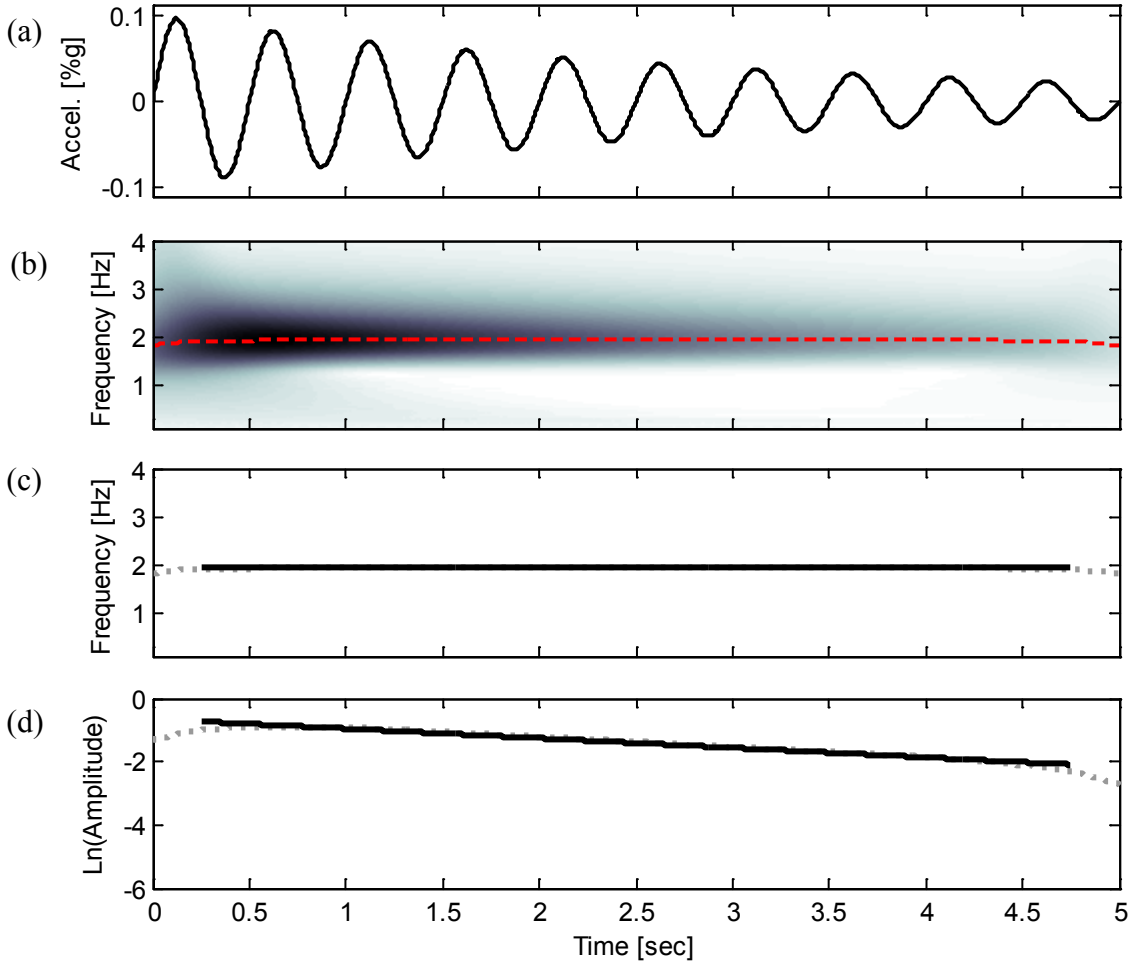

Figure 2-11: (a) Free vibration modal response, (b) wavelet map and extracted ridges, (c) instant frequency, and (d) natural logarithm of the instant amplitude

2.4. References

Al Sanad, H., Aggour, M.S. and Yang, J.C.S. (1983), "Dynamic Shear Modulus and Damping Ratio from Random Loading Tests", Geotechnical Testing Journal 6(3), 120-127.

Bisht, S.S. and Singh, M.P. (2012), "Detecting Sudden Changes in Stiffness Using High-Pass Filters", Structural Control and Health Monitoring 19 (3), 319-331.

Cohen, A., Daubechies, I. and Feauveau, J.C. (1992), "Biorthogonal Basis of Compactly Supported Wavelets", Communications on Pure and Applied Mathematics 45, 485-560.

Daubuchies, I., Lu, J. y Wu, H.T. (2011), "Synchrosqueezed Wavelet Transforms: An Empirical Mode Decomposition-Like Tool", Applied and Computational Harmonic Analysis 30, 243-261.

Feldman, M. (2006), "Time Varying Vibration Decomposition and Analysis Based on The Hilbert Transform", Journal of Sound and Vibration 295, 518-530.

Feldman, M. (2011a), "Hilbert Transform in Vibration Analysis", Mechanical Systems and Signal Processing 25, 735-802.

Feldman, M. (2011b), Hilbert Transform Applications in Mechanical Vibration, John Wiley & Sons Ltd., Chichester, United Kingdom.

Gabor, D. (1946), "Theory of Communication". Proceedings of the IEEE 93(III), 429-457.

Grossman, A. and Morlet, J. (1990), "Decompositions of Functions into Wavelets of Constant Shape and Related Transforms", Mathematics and Physics – Lecture on Recent Results, World Scientific, Singapore, 135-65.

Hahn, S.L. (1996), Hilbert Transforms in Signal Processing, Artech House (print-on-demand).

Hera, A. and Hou, Z. (2004), "Application of Wavelet Approach for ASCE Structural Health Monitoring Benchmark Studies", ASCE Journal of Engineering Mechanics 130(1), 96-104.

Huang, N.E., Shen, Z., Long, S.R., Wu, M.C., Shih, H.H., Zheng, Q., Yen, N.C., Tung, C.C. and Liu, H.H. (1998), "The Empirical Mode Decomposition and the Hilbert Spectrum for Nonlinear and Non-Stationary Time Series Analysis", Philosophical Transactions of the Royal Society of London, Series A: Mathematical, Physical and Engineering Sciences A454, 903-995.

Kijewski, T. and Kareem, A. (2003), "Wavelets Transforms for System Identification in Civil Engineering", Computer Aided Civil and Infrastructure Engineering 18, 339-355.

Loh, C.H., Mao C.H., Huang, J.R. and Pan, T.C. (2011), "System Identification and Damage Evaluation of Degrading Hysteresis of Reinforced Concrete Frames", Earthquake Engineering and Structural Dynamics 40, 623-640.

Mallat, S.G. (1989), "Theory for Multiresolution Signal Decomposition: The Wavelet Representation", IEEE Transactions on Pattern Analysis and Machine Intelligence 11(7), 674–693.

Michel, C. and Gueguen, P. (2010), "Time-Frequency Analysis of Small Frequency Variations in Civil Engineering Structures Under Weak and Strong Motions Using a Reassignment Method", Structural Health Monitoring 9, 159–171.

Montejo, L.A. (2011), “Signal Processing Based Damage Detection in Structures Subjected to Random Excitations”, Structural Engineering and Mechanics 4(6), 745-763.

Montejo, L.A. and Vidot, A.L. (2012), “Synchrosqueezed Wavelet Transform for Frequency and Damping Identification from Noisy Signals”, Smart Structures & Systems 9(5).

Montejo, L.A., Velazquez, L.R, Ramirez, R.I., and Jang, S. (2012a), “Wavelet and HHT Based Identification of Different Levels of Inelastic Action in RC Structures”, 15th World Conference on Earthquake Engineering, Lisbon, Portugal.

Montejo, L.A., Velazquez, L.R, Ramirez, R.I., Jiang, Z., and Christenson, R.E. (2012b), “Frequency Content Effect on the Efficiency of Wavelet and Hilbert-Huang Transforms for Health Monitoring”, 15th World Conference on Earthquake Engineering, Lisbon, Portugal.

Ovanesova, A.V. and Suarez, L.E. (2004), “Applications of Wavelet Transforms to Damage Detection of Frame Structures”, Engineering Structures 26, 39-49.

Pan, T.C. and Lee, C.L. (2002), “Application of Wavelet Theory to Identify Yielding in Seismic Response of Bi-Linear Structures”, Earthquake Engineering and Structural Dynamics 31, 379-398.

Ramirez-Castro, R.I. and Montejo, L.A. (2011), "Hilbert Transform, Empirical Mode Decomposition and its Applications to Free Vibration Analysis (in Spanish)", Revista Internacional de Desastres Naturales, Accidentes e Infraestructura Civil 11(2), 123-134.

Todorovska, M. I. and Trifunac, M. D. (2007), “Earthquake Damage Detection in The Imperial County Services Building I: The Data and Time Frequency Analysis”, Soil Dynamics and Earthquake Engineering 27, 564-576.

Todorovska, M.I. and Trifunac, M.D. (2010), “Earthquake Damage Detection in the Imperial County Services Building II: Analysis of Novelties via Wavelets”, Structural Control and Health Monitoring 17(8), 895-917.

Ville, J. (1948), “Theorie et Application de la Notion de Signal Analytical (in French)”, Cables et Transmissions 2A(1), 61-74.

Yan, B.F. and Miyamoto, A. (2006), “A Comparative Study of Modal Parameter Identification Based on Wavelet and Hilbert–Huang Transforms”, Computer-Aided Civil and Infrastructure Engineering 21, 9-23.

Yan, B.F., Miyamoto, A. and Bruhlier, E. (2006), “Wavelet Transform-Based Model Parameter Identification Considering Uncertainty”, Journal of Sound and Vibration 291, 285-301.

Zembaty, Z., Kowalski, M. and Pospisil, S. (2006), “Dynamic Identification of a Reinforced Concrete Frame in Progressive States of Damage”, Engineering Structures 28, 668-681.

CHAPTER III

3. DEVELOPMENT AND CALIBRATION OF NONLINEAR FINITE ELEMENT MODELS

3.1. Introduction

This chapter describes the modeling and calibration processes of the structural models. FE models were developed using two different approaches, representative of current design/assessment practice (multilinear hysteresis) and RC seismic research (fiber based sections). However, as explained later the hysteretic approach will be used only for the UCSD column model.

The FE models generated are used only to obtain a simulated response (e.g., acceleration or displacement) of the structure to evaluate the adequacy of using this type of approach for validation of SHM methodologies. At no point the FE models are used to aid in the identification of damage. Each structural model was generated using the OpenSees software framework system (McKenna et al., 2000). The models were subjected to cyclic pushover and dynamic analyses. The acceleration/displacement responses obtained with the numerical models are compared with the actual experimental results and the theoretical moment-curvature based monotonic prediction (i.e., CUMBIA: Montejo and Kowalsky, 2007).

As reported by other researchers (e.g., Velázquez, 2011; Huang, 2012; among others), it will be verified that the fiber-based approach allows a realistic RC member representation which results in accurate predictions of structures responses. This is really helpful in terms of the SHM techniques validation.

3.2. Development of Structural Models

Distributed plasticity force-based FE models were developed, two for the UCSD column and one for the Lisbon 3D frames. For the UCSD column the difference between the two models is in the way the behavior at the section level is described. One of the models uses a fiber

approach while the other uses a more traditional multilinear hysteretic rule. For the Lisbon 3D frame only one distributed plasticity force-based model was developed, considering that, as explained later in Chapter IV, the results after applying the damage detection techniques (described earlier) are not good enough for the hysteretic approach.

In the force-based formulation the internal force fields are expressed as functions of the nodal force and it has been shown that force-based elements are exact within the framework of classical beam theory (Spacone et al., 1996a and 1996b). Because of its precision, the main advantage of using force-based elements over displacement-based elements is the ability to use one force-based element per structural member to simulate the non-linear behavior of a frame structure. However, it has been shown that both, force-based and displacement-based approaches, cause localization of the response when the structural members exhibit elastic-plastic or strain-softening type behaviors, which is usually the case in RC members (Bazant and Planas, 1998; Coleman and Spacone, 2001). In the displacement-based approach inelastic curvatures are concentrated over a single displacement based element; in the case of force-based element the inelastic curvatures are located at a single integration point. To circumvent this problem the number of integration points and element lengths, in both UCSD column models, were chosen so that the integration weight of the fixed node matched the expected plastic hinge length (L_p). The value for L_p is calculated using Equation (3-1) (Priestley et al., 2007):

$$L_p = kL + 0.022 f_y d_{bl} \geq 2 * 0.022 f_y d_{bl}, \quad k = 0.2\left(\frac{f_u}{f_y} - 1\right) \leq 0.08 \tag{3-1}$$

In the above equation, d_{bl} is the diameter of longitudinal bars, L is the length of the member and; f_y and f_u are the yielding and ultimate stress of the longitudinal steel, respectively.

In the Lisbon 3D frame the beams and columns of the structure were modeled using the OpenSees *BeamWithHinges* element (Scott and Fenves, 2006). This kind of element has a force-based definition but considers plasticity to be concentrated over specified hinge lengths at the element ends. The element is divided in three parts: (1) two hinges, one at each end; and (2) a linear-elastic region in the middle. In this case the hinge lengths are also specified using Equation (3-1).

3.3. Calibration of Structural Models

This section presents the calibration process of the three analytical models developed, which is done by direct comparison with the actual experimental results. Moreover, for the UCSD column theoretical moment-curvature based monotonic prediction (i.e., CUMBIA, Montejo and Kowalsky, 2007) is performed in order to compare the results with the cyclic pushover results. As mentioned earlier, for the Lisbon 3D frame only a fiber based model is performed and the results are compared with the experimental response (i.e., displacements).

A structure description including the geometric properties and the input accelerations at the base of the structure will be presented in both examples. Different values are assigned to the required parameters in order to calibrate the models until the simulated responses (i.e., acceleration or displacements) closely resemble the actual experimental ones. For the sake of brevity, only the final values of the required parameters will be presented. In addition, for a better understanding of the models' generation, flowcharts are presented, in which the basic process of modeling in OpenSees is illustrated.

3.3.1. UCSD Column

3.3.1.1. Description

The UCSD column is a full-scale, circular RC bridge column built and tested for a blind prediction contest in 2010. The column was tested under uniaxial seismic excitation on the Network for Earthquake Engineering Simulation (NEES) Large High Performance Outdoor Shake Table (LHPOST) at the University of California, San Diego (UCSD). The column had a height (cantilever length) of 7.32m (24ft) with a circular cross section of 1.22m (4ft) diameter, and it also had a reinforced concrete block at the top with a total weight of 2245kN (250ton). A total of 18 No. 11 bars were provided as the longitudinal reinforcement and butt-welded double No. 5 hoops spaced 152mm (6in) center to center were used as the transverse reinforcement. The geometric dimensions and other properties of the column are summarized in Figure 3-1 and Table 3-1. Figure 3-2 presents schematic pictures of the test setup. Further details of the test, material properties, and specimen geometry were presented by Schoettler et al. (2012).

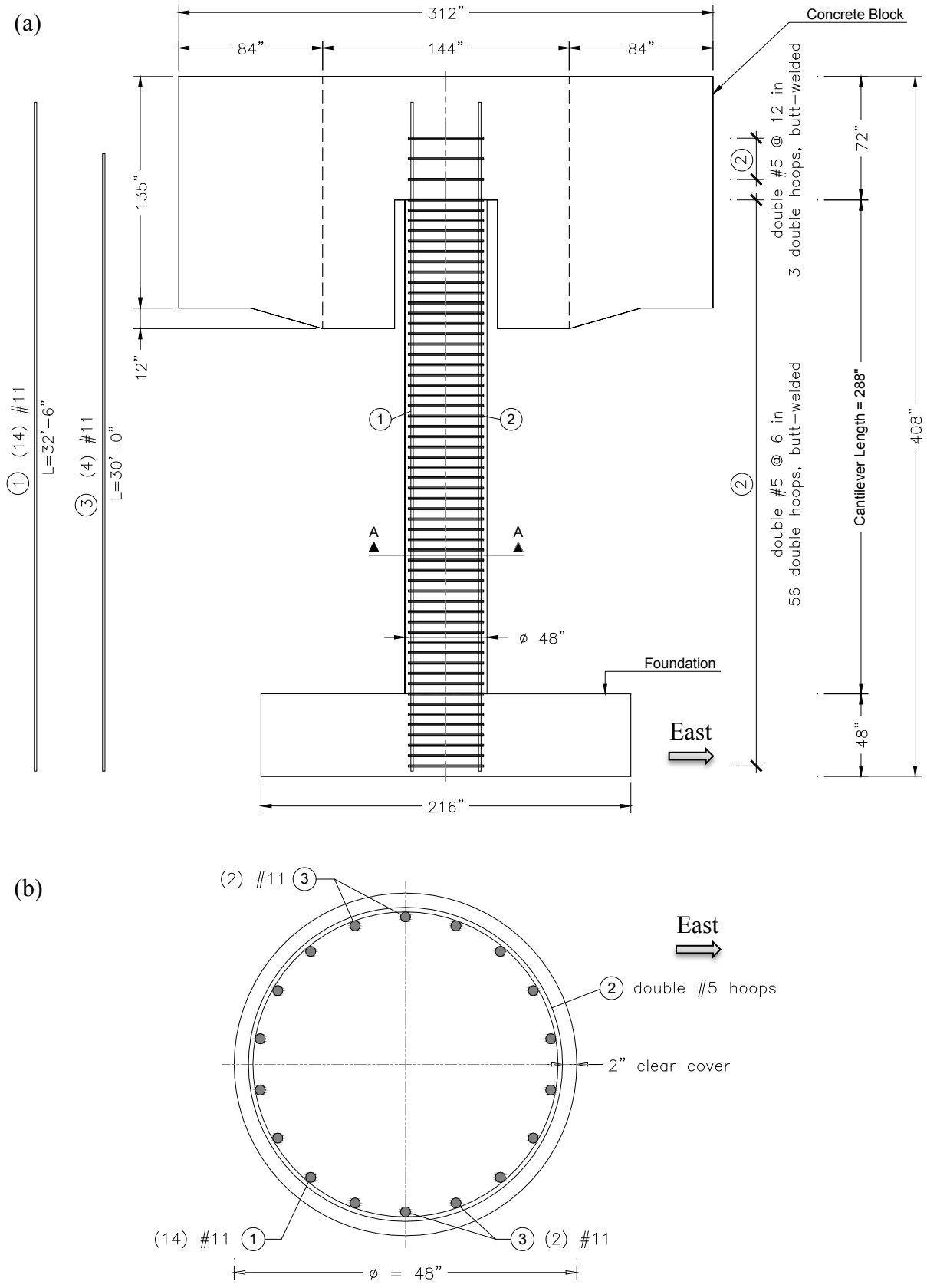

Figure 3-1: Geometric properties and details (a) vertical section and (b) section A-A

Table 3-1: Geometric properties and details summary

Property	Measure	Units
Column length (L) =	288	in
Column diameter (D) =	48	in
Plastic hinge length (Lp) =	36.89	in
Bar clear cover =	2	in
Longitudinal bar diameter (#11) =	1.41	in
Longitudinal bar area (#11) =	1.56	in^2
Number of longitudinal bars =	18	-
Equivalent transverse bar diameter (2#5) =	0.889	in
Transverse bar spacing (s) =	6	in
Column area (A) =	1810	in^2
Moment of inertia (Iz) =	88252	in^4
Modulus of elasticity (E) =	4411	ksi
Concrete block weight =	521.9	kips

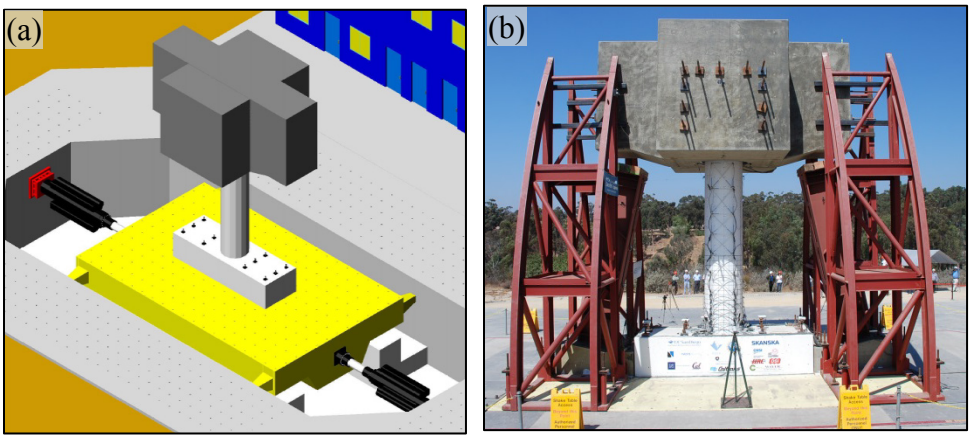

Figure 3-2: Full-scale bridge column test setup (a) 3D view scheme from top and (b) front view (photo taken from: https://nees.org/warehouse/project/987/)

During the experimental test, the column was subjected to a sequential load of 10 ground motions with different levels of intensity, starting with low-intensity motions and progressively bringing the column to near-collapse conditions. No attempts were made to straighten or repair the column between tests. One of the safety columns was struck by the superstructure during the last EQ load, and so this motion will not be considered in this work. The test protocol also included low-intensity WN excitations in-between ground motions for dynamic properties identification purposes. The condition of the column after EQ9 is illustrated in Figure 3-3.

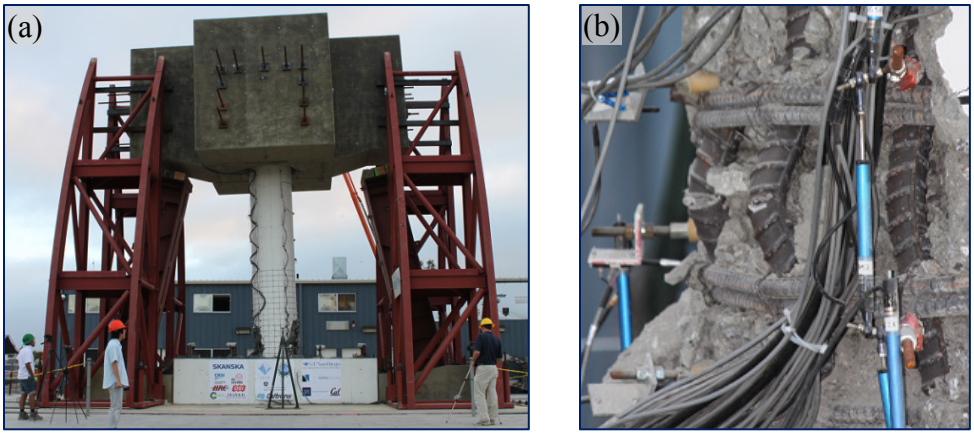

Figure 3-3: Condition of the column after EQ9 (a) front view and (b) rebar fracture close-up (photos taken from: https://nees.org/warehouse/project/987/)

Four historical EQ records were selected as input ground motions for the test: the 1989 Loma Prieta EQ (at different stations) and the 1995 Kobe EQ (at Takatori station). These records and their properties are summarized in Table 3-2. Figure 3-4 to Figure 3-12 present the acceleration time-histories of the aforementioned records.

Table 3-2: Input ground motions applied to the UCSD column

Test	Earthquake	Scale	Magnitude	Station Name	Component
EQ1	Loma Prieta	100%	6.9	Agnew State Hospital	090
EQ2	Loma Prieta	100%	6.9	Corralitos	090
EQ3	Loma Prieta	100%	6.9	LGPC	000
EQ4	Loma Prieta	100%	6.9	Corralitos	090
EQ5	Kobe	-80%	6.9	Takatori	000
EQ6	Loma Prieta	100%	6.9	LGPC	000
EQ7	Kobe	100%	6.9	Takatori	000
EQ8	Kobe	-120%	6.9	Takatori	000
EQ9	Kobe	120%	6.9	Takatori	000

* The negative sign in EQ5 and EQ8 indicates that the earthquake's polarity has been inverted.

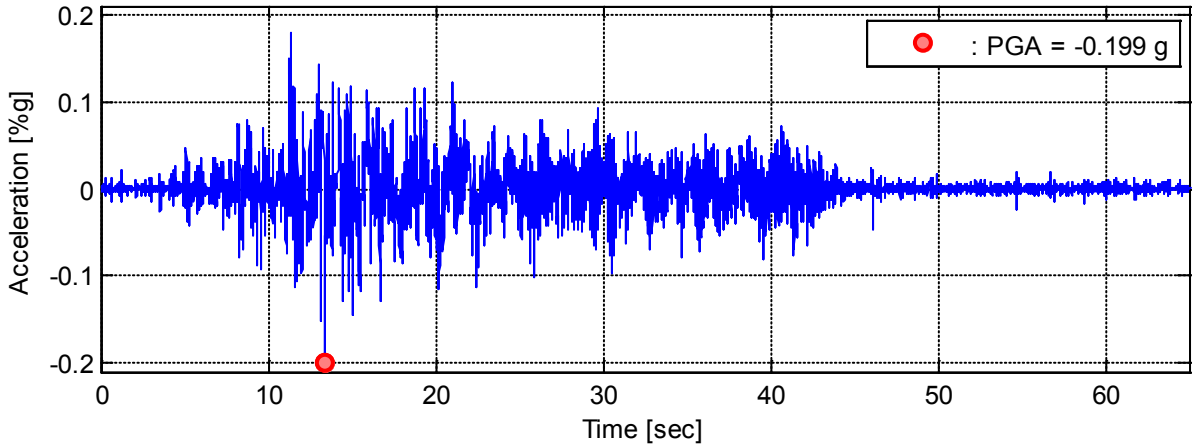

Figure 3-4: 1989 Loma Prieta input ground motion at Agnew State Hospital station (EQ1)

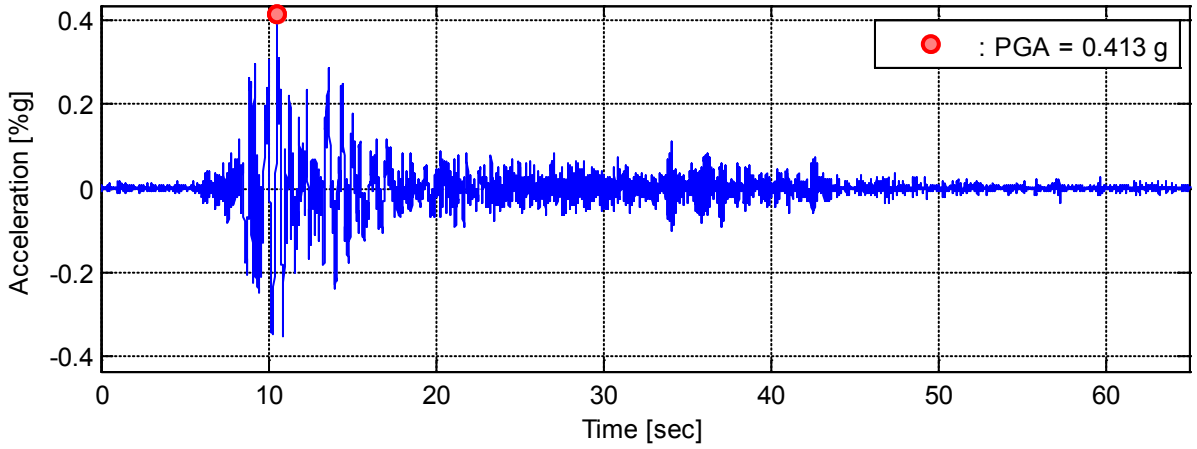

Figure 3-5: 1989 Loma Prieta input ground motion at Corralitos station (EQ2)

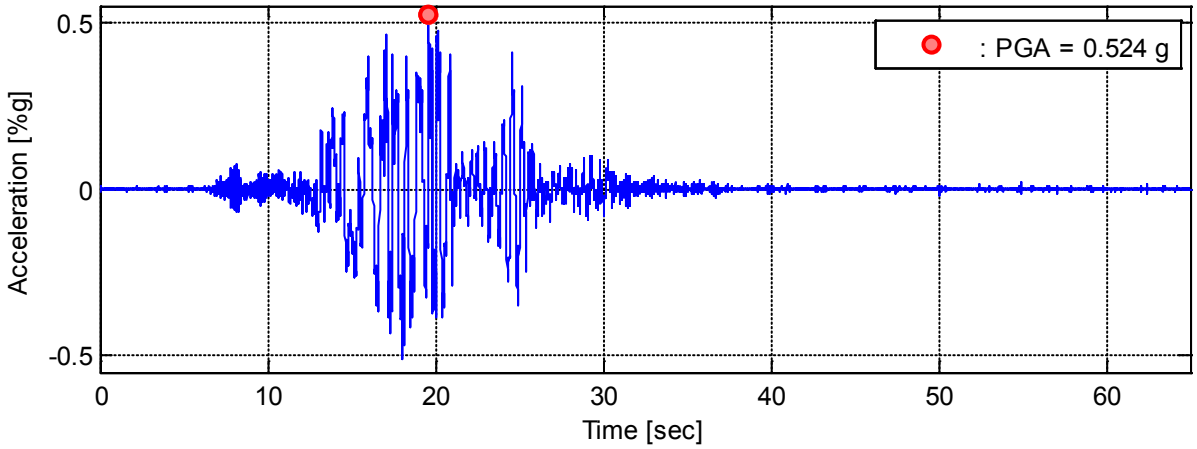

Figure 3-6: 1989 Loma Prieta input ground motion at LGPC station (EQ3)

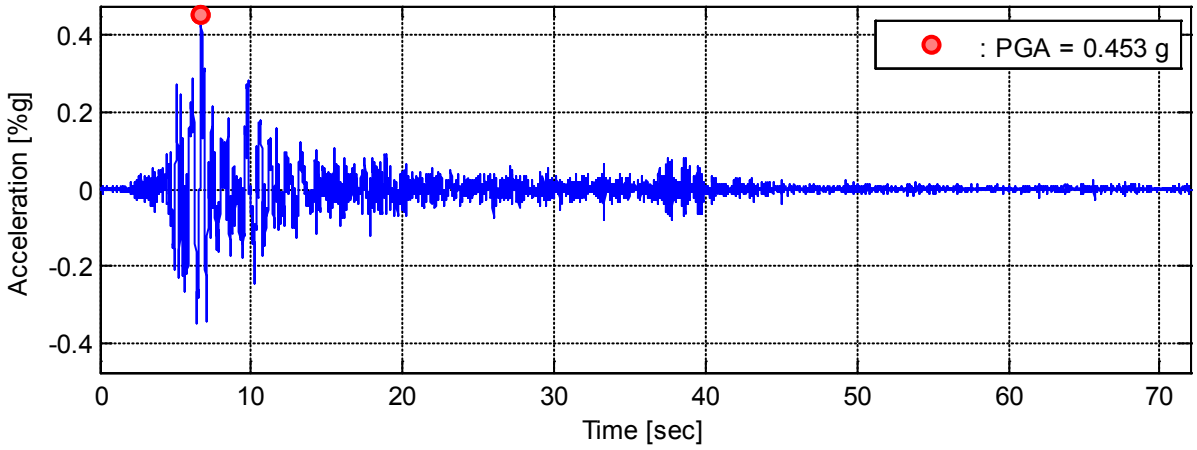

Figure 3-7: 1989 Loma Prieta input ground motion at Corralitos station (EQ4)

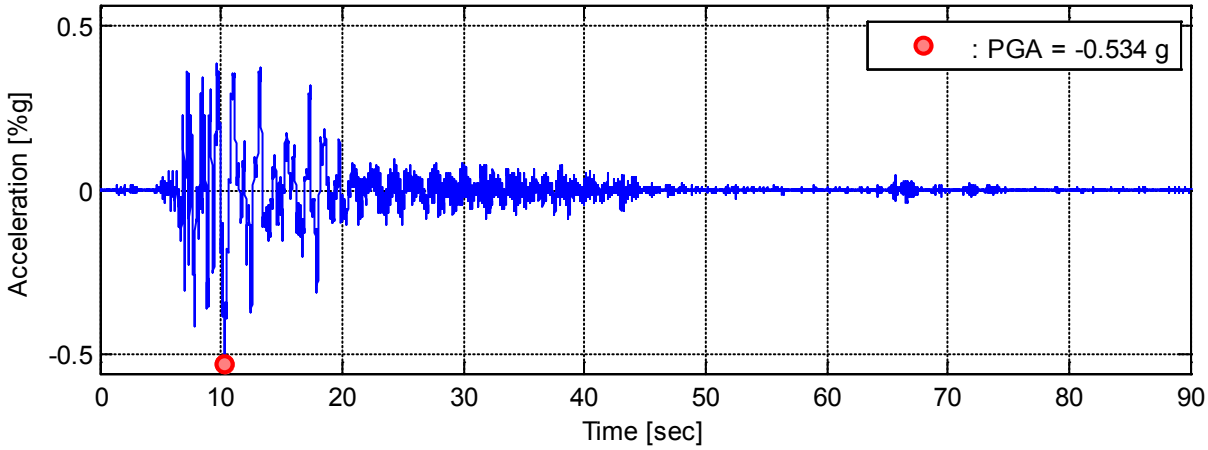

Figure 3-8: 1995 Kobe input ground motion at Takatori station (EQ5)

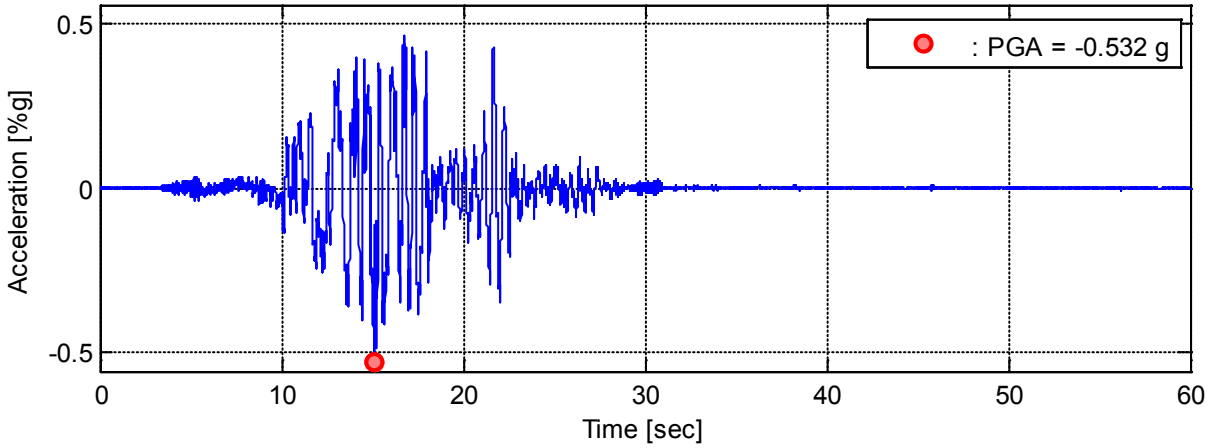

Figure 3-9: 1989 Loma Prieta input ground motion at LGPC station (EQ6)

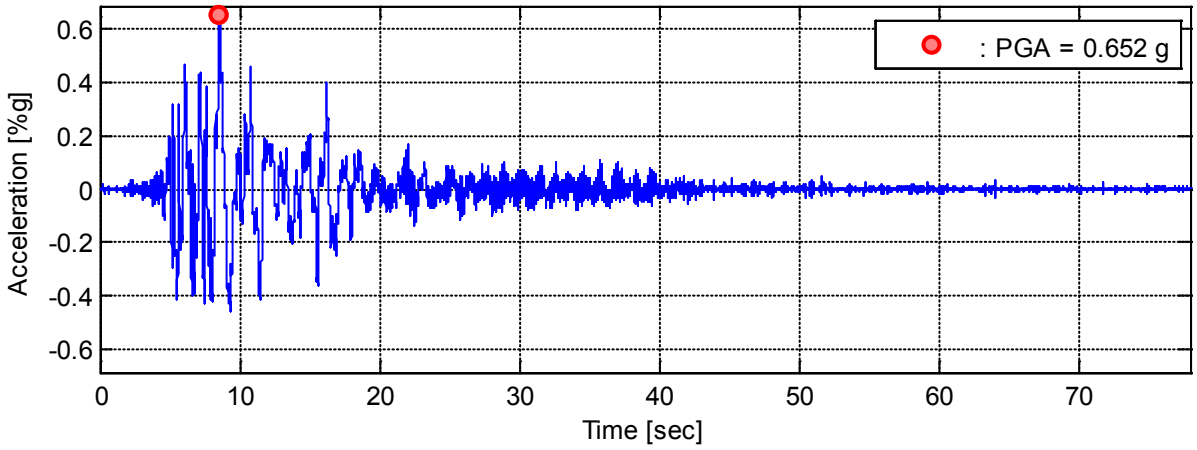

Figure 3-10: 1995 Kobe input ground motion at Takatori station (EQ7)

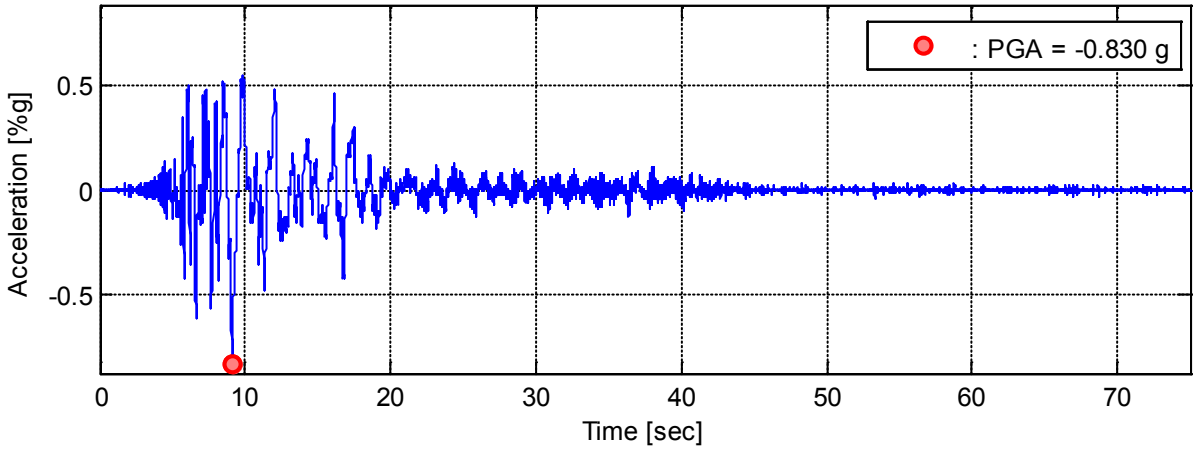

Figure 3-11: 1995 Kobe input ground motion at Takatori station (EQ8)

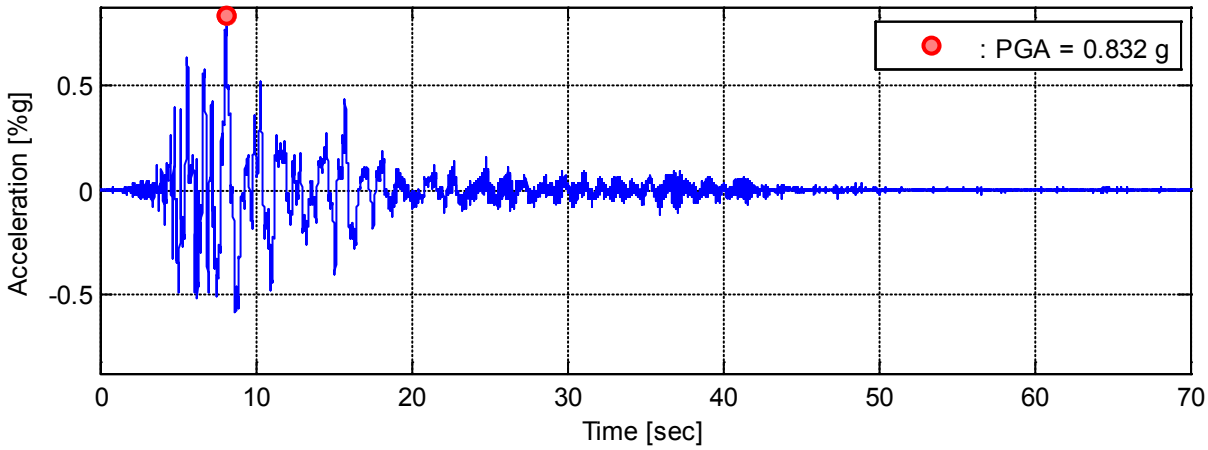

Figure 3-12: 1995 Kobe input ground motion at Takatori station (EQ9)

Table 3-3 summarizes the main results registered during the experimental tests (Schoettler et al., 2012). In this table, *Abot* and *Atop* are the maximum absolute acceleration registered in the shaking table and column, respectively. *Duct* is the maximum absolute displacement ductility reached by the column during the tests.

Table 3-3: Main response parameters of the ground motions applied

Test	Abot (g)	Duct.	Atop (g)	Observations
EQ1	0.20	0.68	0.21	Hairline cracks
EQ2	0.43	1.44	0.29	Rebar first yield
EQ3	0.53	4.07	0.38	Concrete cover spalling
EQ4	0.43	1.88	0.17	No significant changes
EQ5	0.53	6.28	0.37	Deep concrete spalling / onset of rebar buckling
EQ6	0.53	5.44	0.34	No significant changes
EQ7	0.66	6.27	0.37	Initial concrete core crushing / rebar buckling
EQ8	0.83	6.77	0.34	Rebar fracture (2)
EQ9	0.83	7.13	0.29	Rebar fracture (3)

Based on the column geometry ($L=7315mm$, $d_{bl}=35.8mm$) and the experimental results for the rebar tension tests ($f_y=503MPa$, $f_u=689MPa$), the calculated value for L_p is 937mm (36.89in). For both approaches (i.e., hysteretic and fiber based) the column was then modeled using two force-based elements with three Gauss-Lobatto integration points each (integration weights: 0.333, 1.333, 0.333). To match the plastic hinge length, the length for the first element (next to the fixed node) was set as 5622mm (221.3 in).

The cyclic pushover analysis was performed based on the results obtained from a theoretical moment-curvature prediction using CUMBIA and the yield displacement defined as 89.92mm (3.54in) (displacement ductility $\mu=1$) by Schoettler et al. (2012). The displacement loading history (Figure 3-13) was then divided in a sequence of five stages as follows: (1) 2 cycles up to 1.77in ($\mu=0.5$); (2) 2 cycles up to 3.54in ($\mu=1$); (3) 2 cycles up to 10.62in ($\mu=3$); (4) 2 cycles up to 17.70in ($\mu=5$); and (5) 2 cycles up to 24.78in ($\mu=7$).

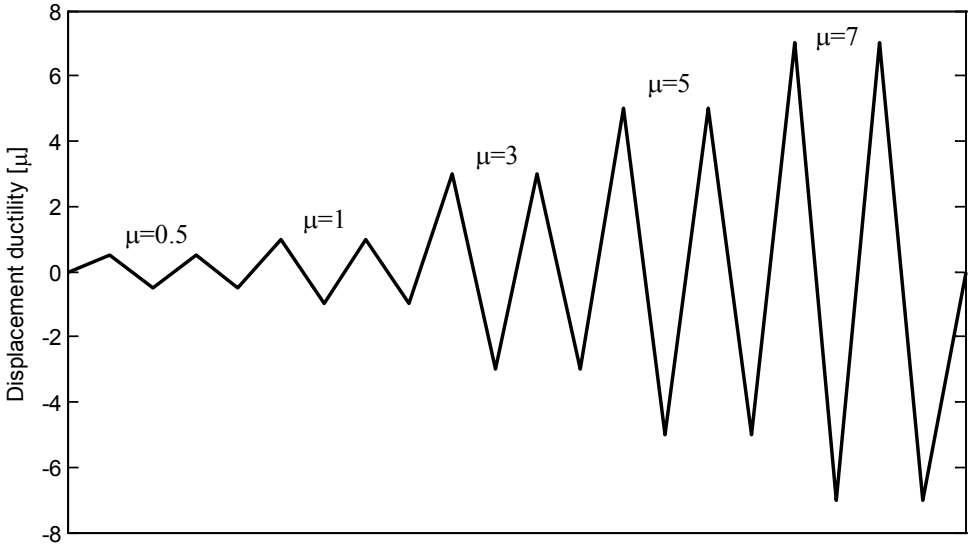

Figure 3-13: UCSD cyclic pushover analysis: displacement ductility loading history

3.3.1.2. Fiber-based model

In the fiber approach the section is represented by unidirectional fibers and constitutive-material relationships are specified to each type of fiber. No prior moment-curvature analysis is required because the hysteretic response of the section is defined by the material properties. To model the UCSD column using this approach we have fibers representing the reinforcing steel, cover concrete (unconfined) and core concrete (confined). Concrete fibers were modeled using the *Conc*rete01 material with parameters based on the Mander et al. model (1988) along with the concrete cylinder results. Longitudinal steel bars were modeled using the *ReinforcingSteel* material (Mohle and Kunnath, 2006), this model accounts for degradation of strength and stiffness due to cyclic loads according to a Coffin and Manson fatigue model through the factors α, C_f and C_d. The damage strain range constant, α, is used to relate damage from one strain range to an equivalent damage at another strain range and it is constant for a material type. The ductility constant, C_f, is used to adjust the number of cycles to failure and the strength reduction constant, C_d, controls the amount of degradation per cycle. Values of $\alpha=0.505$, $C_f=0.187$ and $C_d=0.357$ were used for this model, these values were determined so that rebar fracture occurred at the same earthquake load (EQ8 and EQ9) than in the shake table test. Second order effects were included using the OpenSees P-Delta coordinate transformation command and elastic damping was included as 2% tangent-stiffness-proportional damping (Petrini et al., 2008). Figure 3-14 presents a scheme of the model's generation in OpenSees.

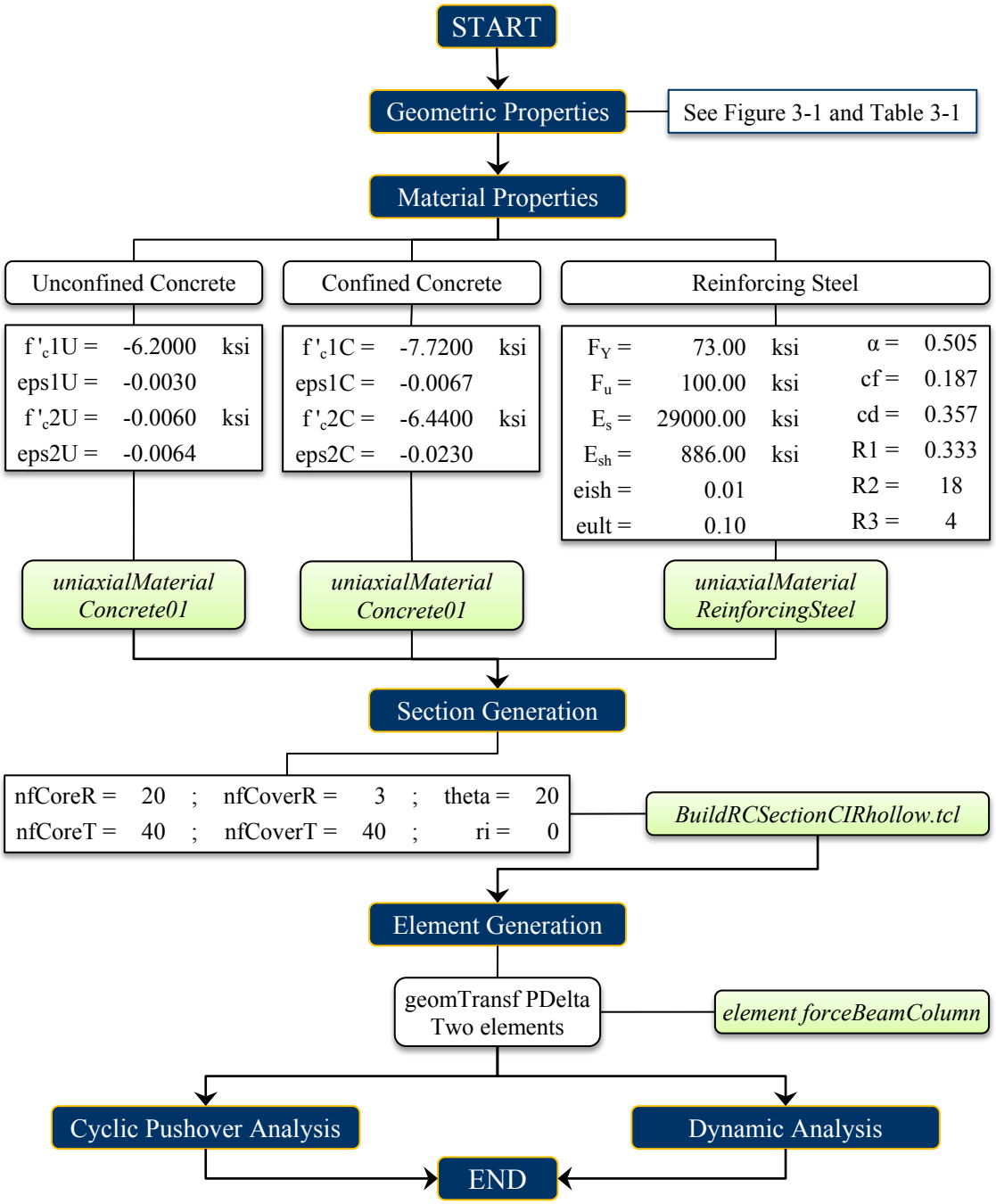

Figure 3-14: UCSD column fiber-based model generation scheme

3.3.1.3. Hysteretic model

The multilinear hysteretic model, represented in Figure 3-15, was developed using the *Hysteretic* material available in Opensees with parameters defined following the modified Takeda rules (Saiidi and Sozen, 1979). The model is defined by (1) the yield deformation, (2) the

initial stiffness, (3) the post-yield flexural stiffness and (4) the unloading stiffness parameter. The first three parameters were obtained from a moment-curvature analysis using the computer code CUMBIA (Montejo and Kowalsky, 2007); the unloading stiffness was taken as 0.5.

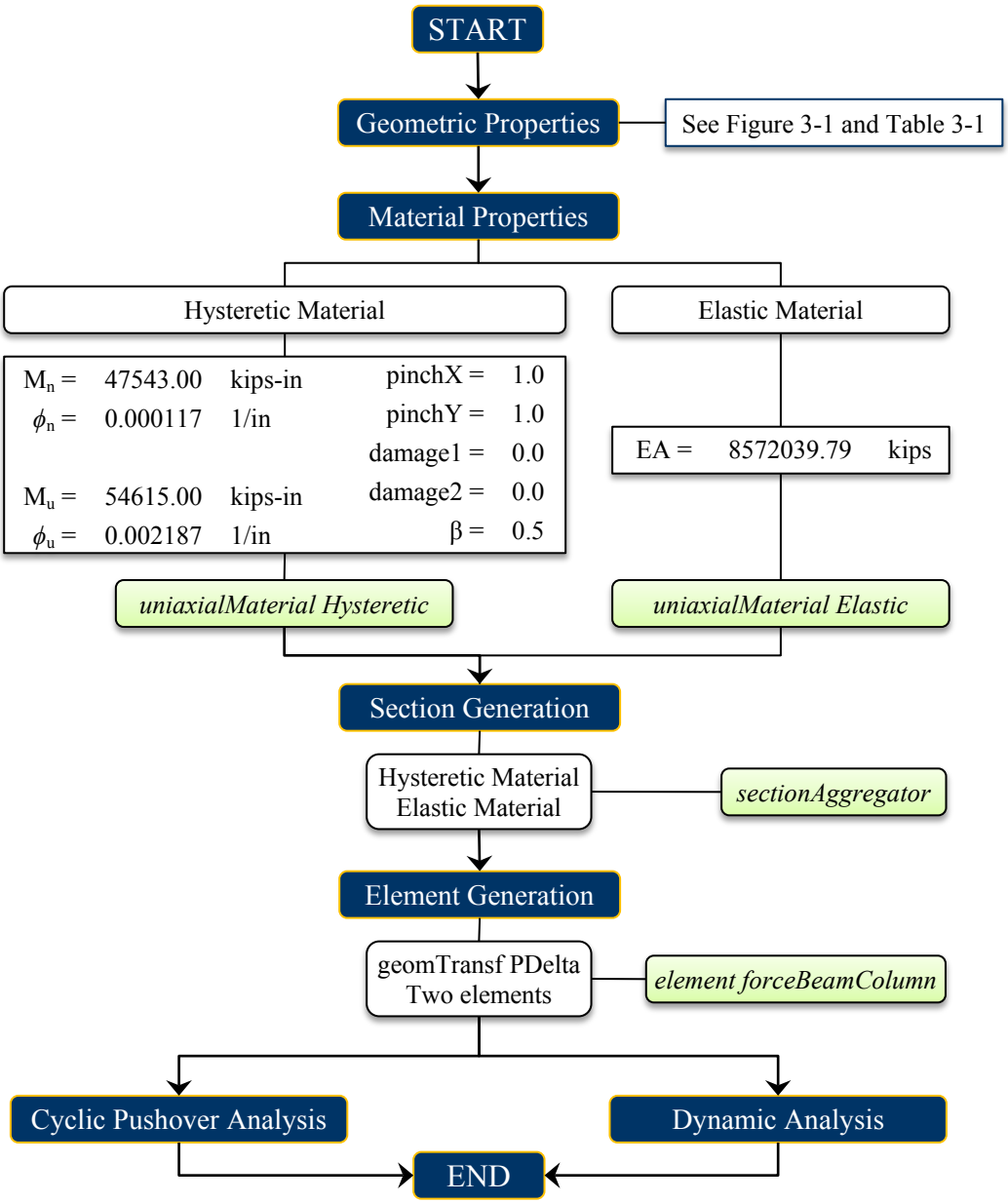

Figure 3-15: UCSD column hysteretic model generation scheme

3.3.1.4. Cyclic pushover test results

For FE models validation and calibration purposes, material behavior is presented using the results from CUMBIA (i.e., moment-curvature monotonic prediction), from model

simulation (i.e., fiber-based and hysteretic approach), and from available experimental results (i.e., material tests). In addition, section behavior (i.e., moment-curvature response) and member behavior (i.e., force-displacement response) are presented.

Notice that there is a good correlation in terms of the material behavior between the simulated and experimental results for the concrete (Figure 3-16) and reinforcing steel (Figure 3-17) strain-stress relationships. Nevertheless, in both cases there is a difference as the strain increase. This is expected because in the cyclic analysis fatigue and material degradation are taken into account, while in the monotonic analysis they are not. Also notice, since the model definition is based on a RC section as a unit in the hysteretic approach, that is, the material stress-strain behavior is not considered to define the cross section; it is not possible to display material behavior results for this approach.

Figure 3-18 and Figure 3-19 present the simulated moment-curvature response and simulated force-displacement response for both models, respectively, along with the theoretical monotonic envelope obtained based on the moment-curvature analysis and equivalent plastic hinge method (Priestley et al., 2007). Ductility values (μ) were calculated based on the reported experimental yield drift: 1.23% (89.97mm/3.54in) (Schoettler et al., 2012). The yield force was taken from the moment-curvature prediction as 683.76kN (53.72kips).

While there is no experimental data available to compare the results from the simulated cyclic reversal loads, the results displayed in Figure 3-19 are useful to understand the limitations of numerical modeling for validation of damage detection methodologies. From this figure it is seen that P-Delta effects are important for this structure causing the post-yield response of the column to have a negative slope. Moreover, the fiber-based model predicts rebar fracture after the second cycle of load at μ7, which matches well with the dynamic experimental results presented on Table 3-3. The rebar fracture prediction performed by the fiber-based model depends on the Opensees material type selected for modeling the longitudinal steel bars. As mention earlier, the *ReinforcingSteel* material was used for this purpose. In this model, rebar rupture is determined by the ultimate stress F_u, its corresponding strain e_{ult}, and the material degradation due to the cyclic load according to a Coffin and Mason Fatigue model whose parameters were explained in section 3.3.1.2.

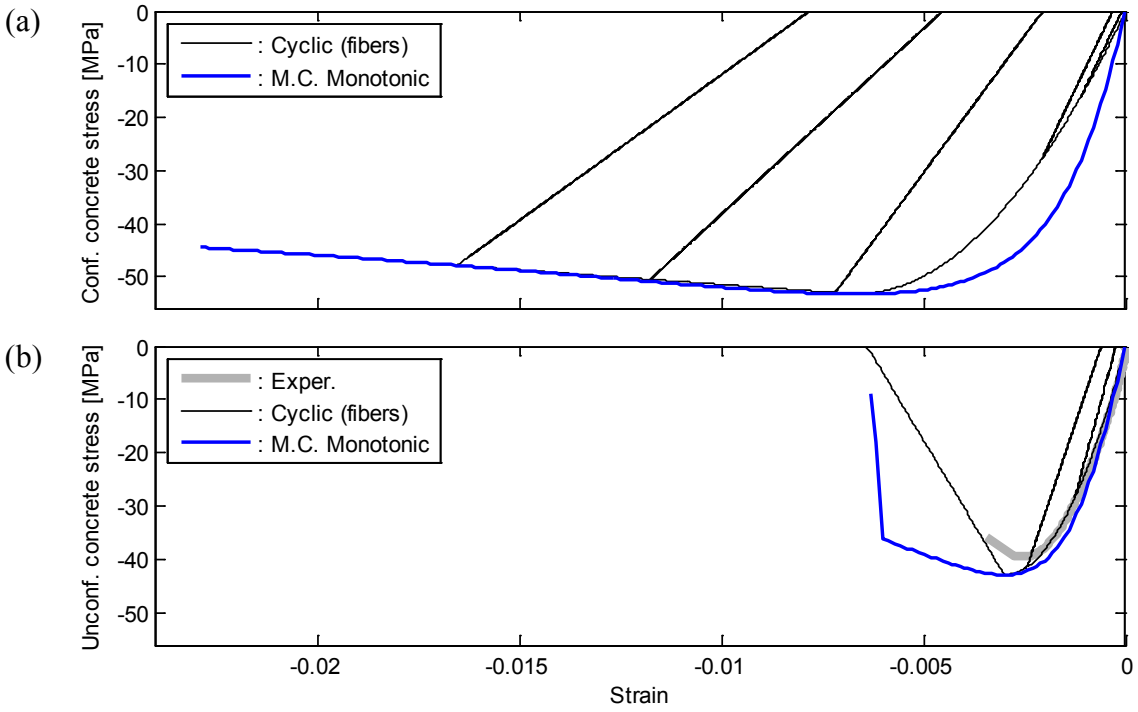

Figure 3-16: Stress-strain behavior for the (a) confined concrete and (b) unconfined concrete

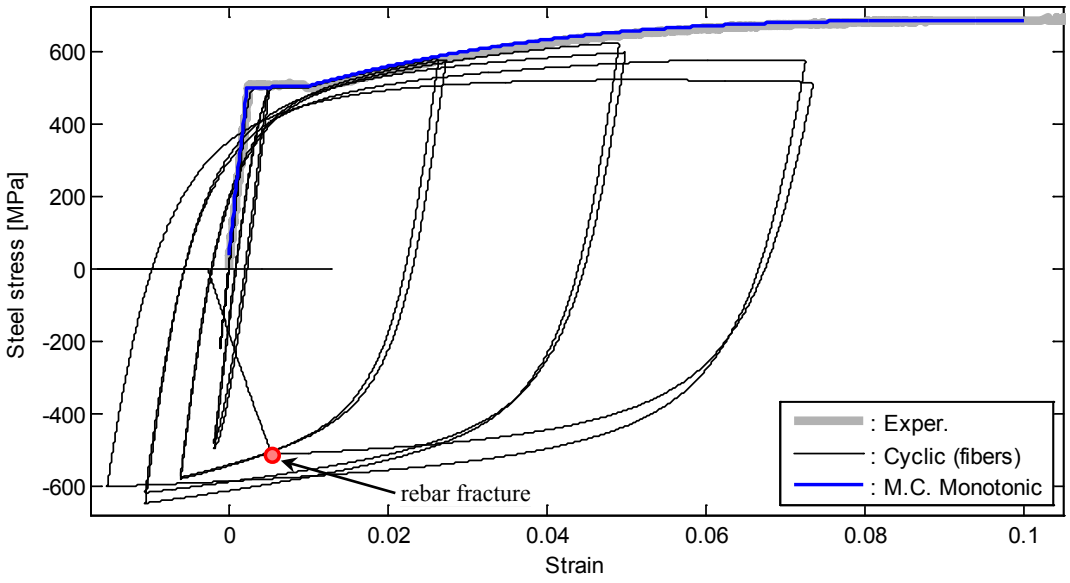

Figure 3-17: Stress-strain behavior for the reinforcing steel

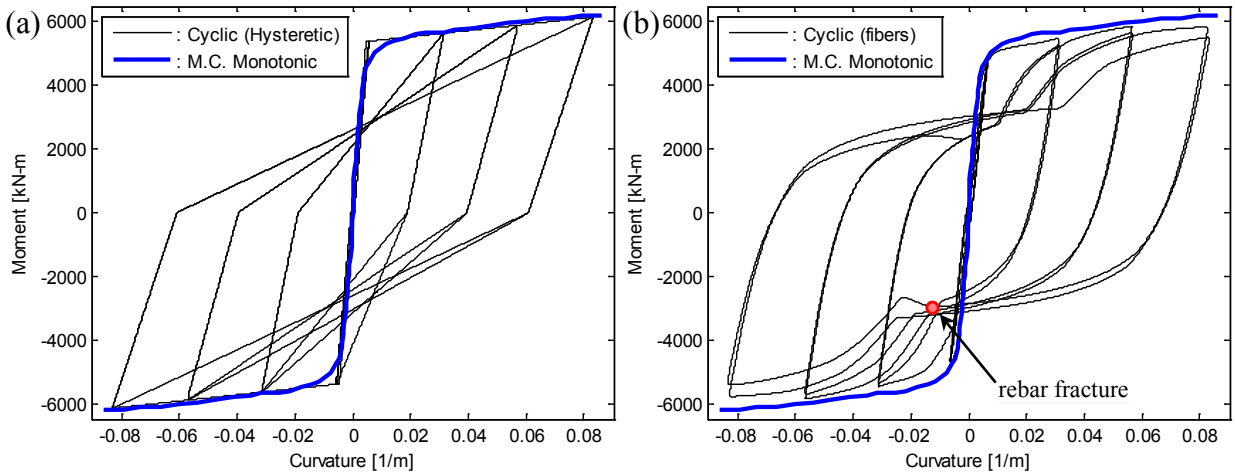

Figure 3-18: Cyclic moment-curvature response for the (a) modified Takeda model and (b) fiber-based model along with the monotonic envelope extrapolated from the moment curvature analysis

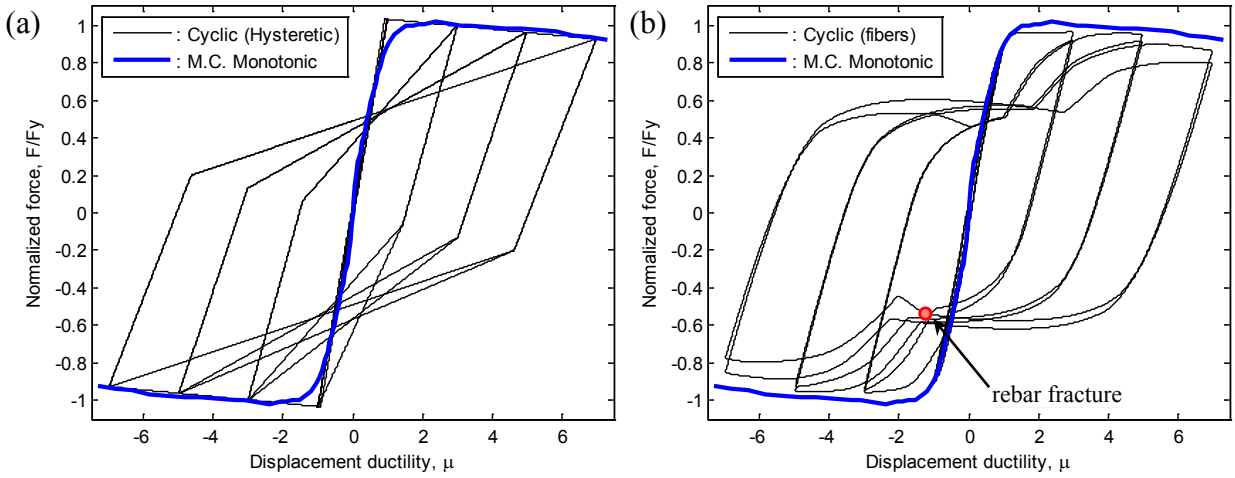

Figure 3-19: Cyclic force-displacement response for the (a) modified Takeda model and (b) fiber-based model along with the monotonic envelope extrapolated from the moment curvature analysis

3.3.1.5. Dynamic analysis test results

Figure 3-20 to Figure 3-28 compare the results from the shaking table tests with the results obtained using the numerical models. Notice in these figures that the time duration does not match the actual length of the EQs. Only the results for the strong motion part are displayed to allow for a better observation of the results.

The results are representative of the different levels of damage in the structure: column in the linear range (i.e. no rebar yield or concrete spalling), first significant inelastic excursion, rebar buckling and rebar fracture. It is seen that the accelerations obtained at the top of the column are in close agreement with the experimental results. In the case of the displacement ductility time histories the agreement in the maximum peaks is also close; however capturing the column residual displacements is more challenging. As a result, it is seen that in some cases the displacements from the simulation are similar to the experimental results but shifted by some value. This phenomenon is more critical for the modified Takeda model and at the last motions of the sequential load program, where the residual displacement errors have accumulated (e.g., EQ6 to EQ9, Figure 3-25 to Figure 3-28). Similar observations has been reported by other researchers (e.g., Yazgan and Dazio, 2011).

Note that the success of the numerical models in replicating the overall seismic response of the structure does not necessarily guarantee their adequacy for validation of damage detection methodologies; this aspect is explored in Chapter IV.

Table 3-4 and Table 3-5 summarize the maximum positive and negative peak values for the experimental and simulated, column acceleration and displacement ductility responses. Notice that the maximum values are in close agreement.

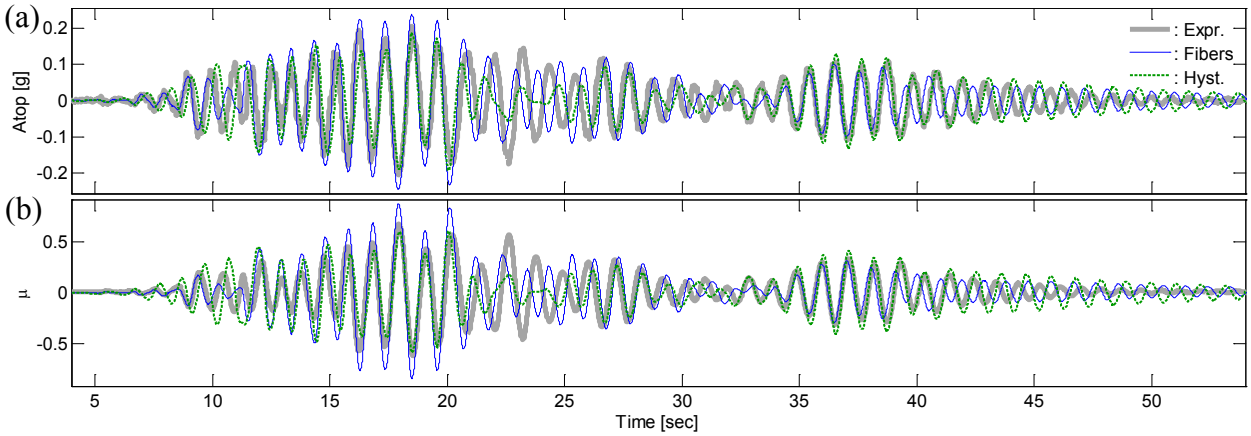

Figure 3-20: Comparison of experimental and numerical models results for EQ1: (a) column accelerations and (b) displacement ductilities

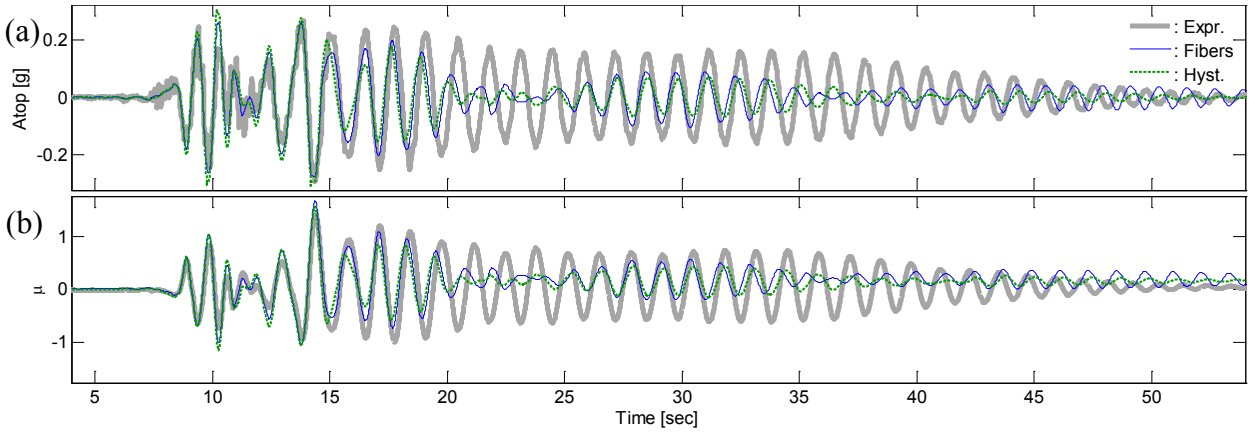

Figure 3-21: Comparison of experimental and numerical models results for EQ2: (a) column accelerations and (b) displacement ductilities

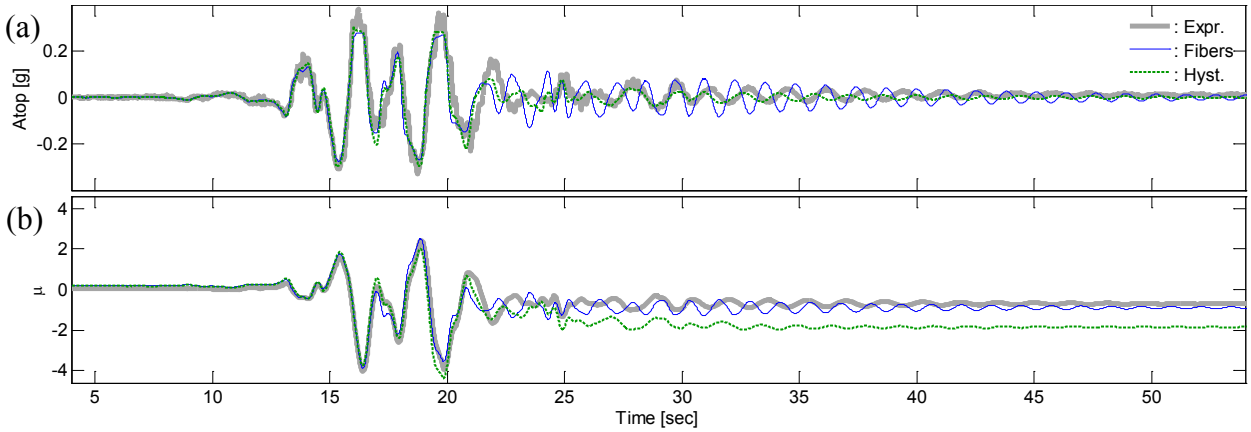

Figure 3-22: Comparison of experimental and numerical models results for EQ3: (a) column accelerations and (b) displacement ductilities

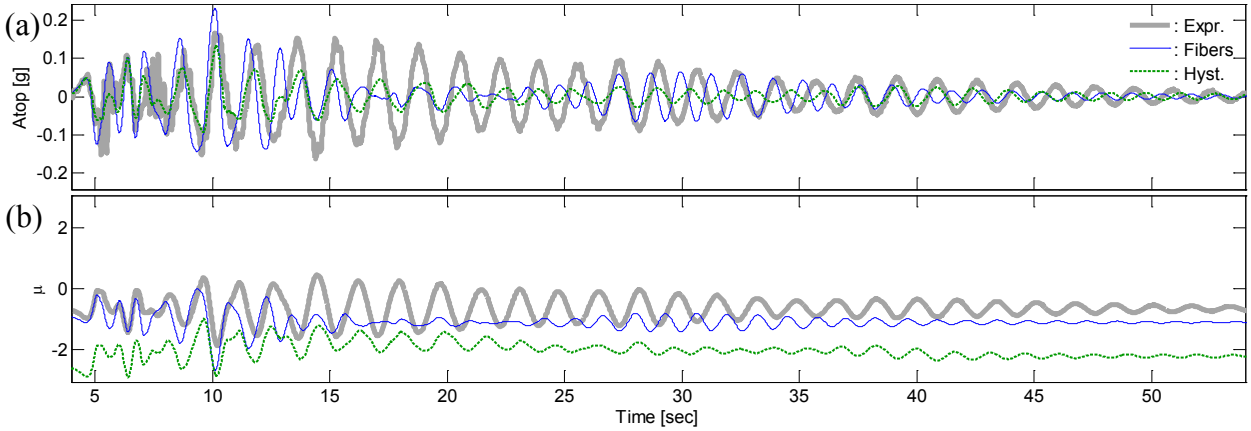

Figure 3-23: Comparison of experimental and numerical models results for EQ4: (a) column accelerations and (b) displacement ductilities

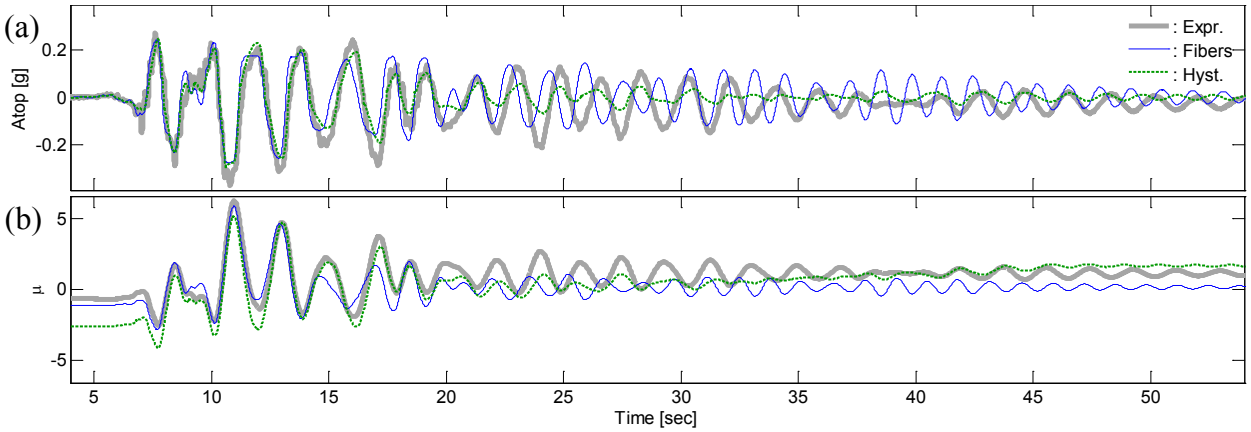

Figure 3-24: Comparison of experimental and numerical models results for EQ5: (a) column accelerations and (b) displacement ductilities

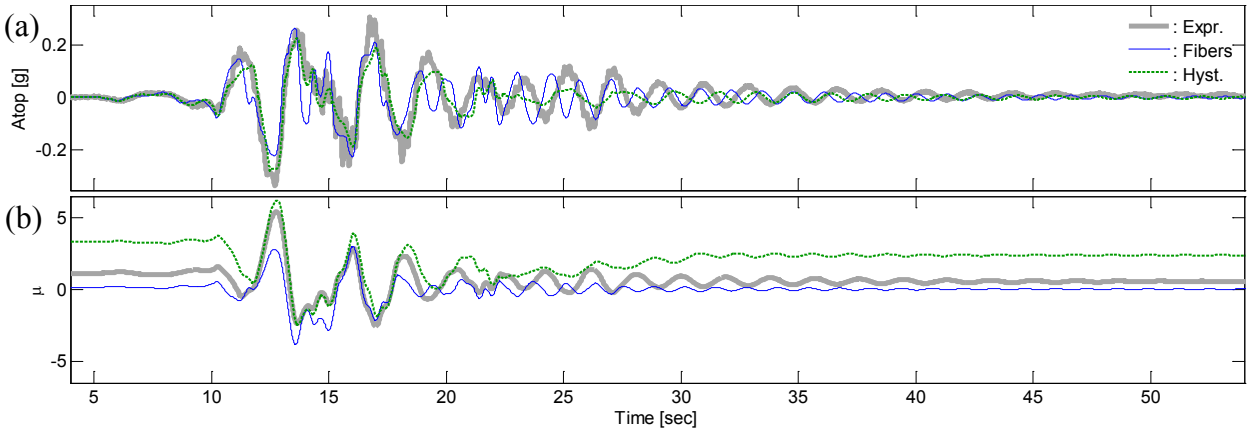

Figure 3-25: Comparison of experimental and numerical models results for EQ6: (a) column accelerations and (b) displacement ductilities

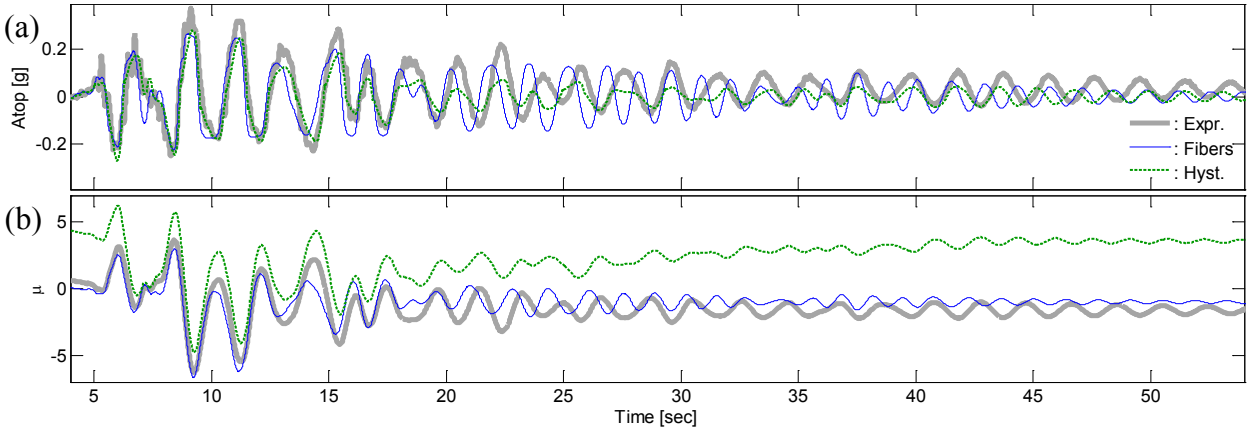

Figure 3-26: Comparison of experimental and numerical models results for EQ7: (a) column accelerations and (b) displacement ductilities

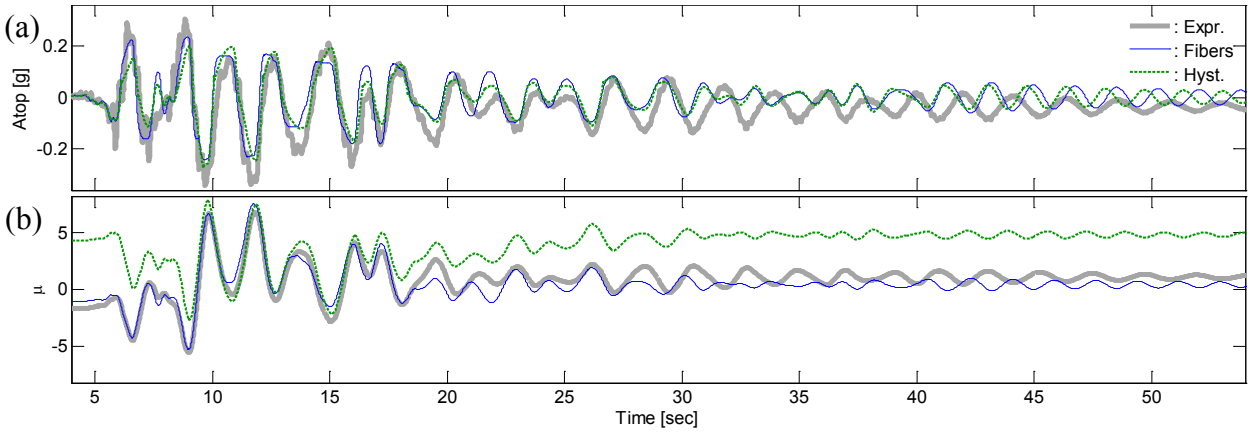

Figure 3-27: Comparison of experimental and numerical models results for EQ8: (a) column accelerations and (b) displacement ductilities

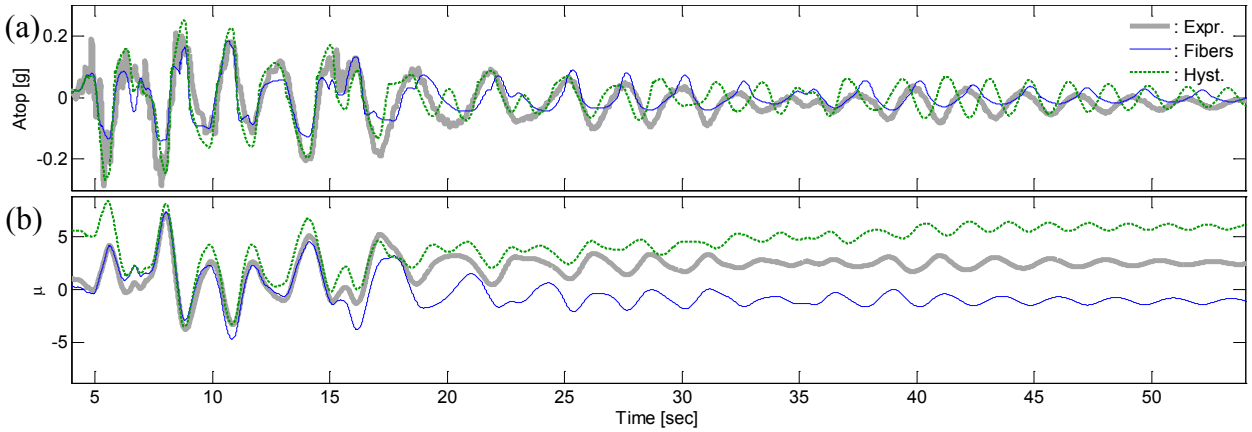

Figure 3-28: Comparison of experimental and numerical models results for EQ9: (a) column accelerations and (b) displacement ductilities

Table 3-4: Comparison of experimental and numerical peak accelerations

Test	Max. Positive Accelerations [g]			Max. Negative Accelerations [g]		
	Exper.	Fibers	Hysteretic	Exper.	Fibers	Hysteretic
EQ1	0.21	0.24	0.19	-0.21	-0.25	-0.19
EQ2	0.26	0.26	0.31	-0.29	-0.27	-0.31
EQ3	0.38	0.28	0.31	-0.33	-0.27	-0.30
EQ4	0.17	0.23	0.13	-0.16	-0.14	-0.09
EQ5	0.27	0.24	0.24	-0.37	-0.27	-0.30
EQ6	0.30	0.26	0.23	-0.34	-0.23	-0.28
EQ7	0.37	0.26	0.28	-0.25	-0.23	-0.27
EQ8	0.31	0.24	0.20	-0.34	-0.24	-0.27
EQ9	0.21	0.19	0.25	-0.29	-0.14	-0.27

Table 3-5: Comparison of experimental and numerical peak displacement ductilities

Test	Max. Positive Displacement Ductility			Max. Negative Displacement Ductility		
	Exper.	Fibers	Hysteretic	Exper.	Fibers	Hysteretic
EQ1	0.68	0.87	0.61	-0.61	-0.84	-0.59
EQ2	1.44	1.69	1.58	-1.00	-1.04	-1.15
EQ3	2.44	2.53	2.01	-4.07	-3.89	-4.39
EQ4	0.46	0.00	-0.99	-1.88	-2.70	-2.94
EQ5	6.28	5.90	5.17	-2.55	-2.85	-4.14
EQ6	5.44	3.04	6.22	-2.60	-3.84	-2.45
EQ7	3.65	3.01	6.27	-6.27	-6.68	-4.80
EQ8	6.77	7.54	7.80	-5.58	-5.24	-2.64
EQ9	7.13	7.37	8.40	-3.81	-4.69	-3.54

3.3.2. Lisbon 3D Frames

3.3.2.1. Description

Lisbon 3D frames are two full-scale, RC 3D frame structures geometrically identical, designed for low and high ductility levels (i.e., different steel reinforcement detailing), models A and B respectively, according to the Eurocode 8 (EC8) provisions. Both structures were built and tested for the 15th World Conference on Earthquake Engineering (WCEE) Blind Test Challenge. Both 3D frames were tested under biaxial seismic excitation at the National Laboratoty for Civil Engineering (LNEC) 3D shaking table in Lisbon, Portugal, during the 15th WCEE. Both structures had one bay in each horizontal direction; one story; four columns of 3m (9.84ft) height with a square cross section of 20cm (7.87in) x 20cm (7.87in); four beams with a square cross section of 20cm (7.87in) x 40cm (15.75in) from which two of them had a 3.5m (11.48ft) length on EW direction and the other two had a 4m (13.12ft) length on the perpendicular NS direction. A slab extended 2m (6.6ft) from one edge to the beam in the perpendicular NS direction. General dimensions of the 3D frame structures are presented in Figure 3-29.

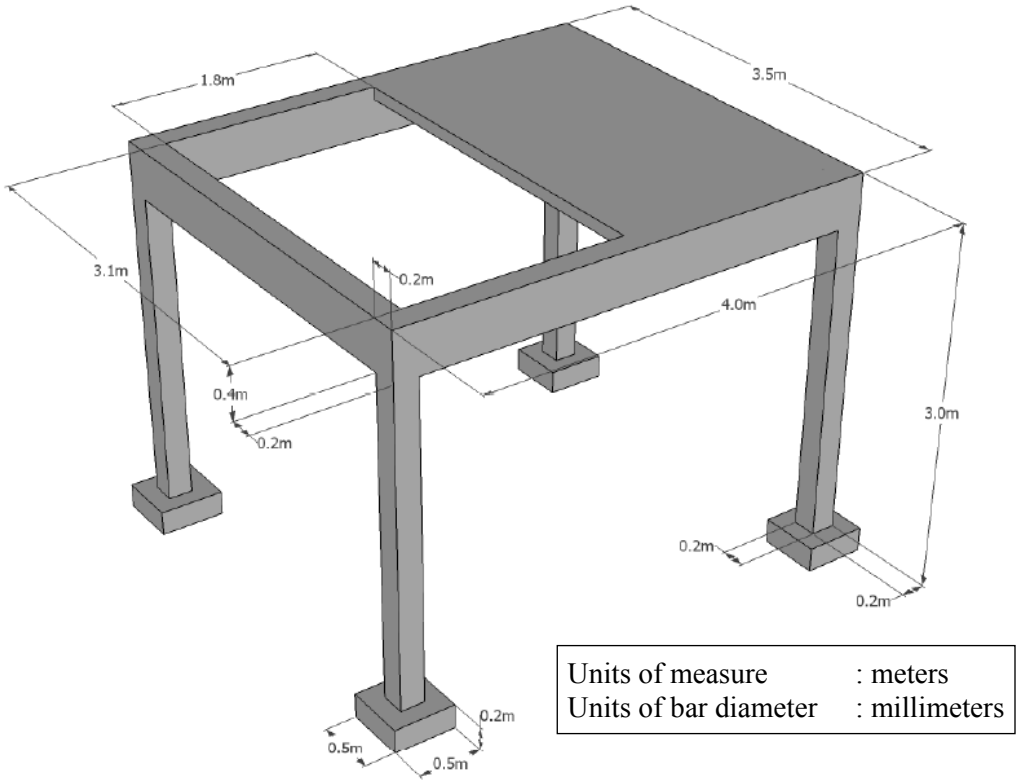

Figure 3-29: 3D scheme with general dimensions of the Lisbon RC 3D frame structures (taken from: 15th WCEE Blind Test Challenge Report, 2012)

Model A is characterized by having a constant stirrup/hoop spacing of 15cm (5.9in) along the columns, of 20cm (7.87in) in the mid-span of the beams, and of 10cm (3.94in) near the beam-column joints on the beams. Figure 3-30 through Figure 3-32 illustrate some details. Table 3-6 summarizes the geometric properties and some reinforcement details of this model.

Model B is characterized by having a stirrup/hoop spacing of 15cm (5.9in) in the mid-span of the columns, of 10cm (3.94in) in the mid-span of the beams, and of 5cm (1.97in) near the beam-column joints and the foundations. Figure 3-33 through Figure 3-35 illustrate some details. The geometric properties and some reinforcement details of this model are summarized in Table 3-7.

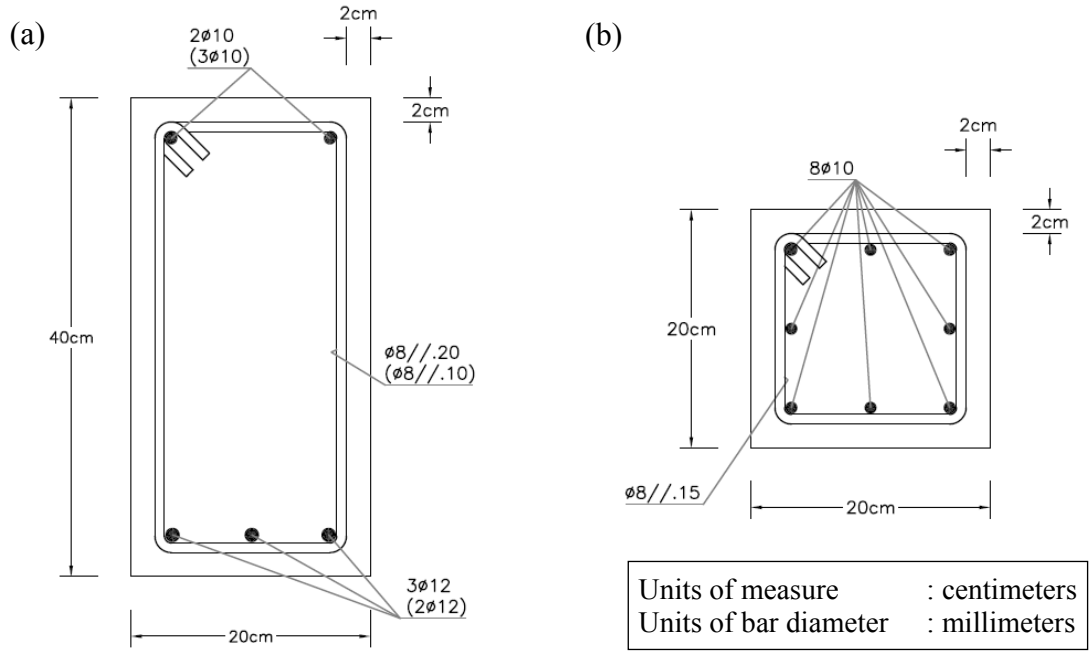

Figure 3-30: (a) Beam and (b) column section details of Lisbon 3D frame model A (taken from: 15th WCEE Blind Test Challenge Report, 2012)

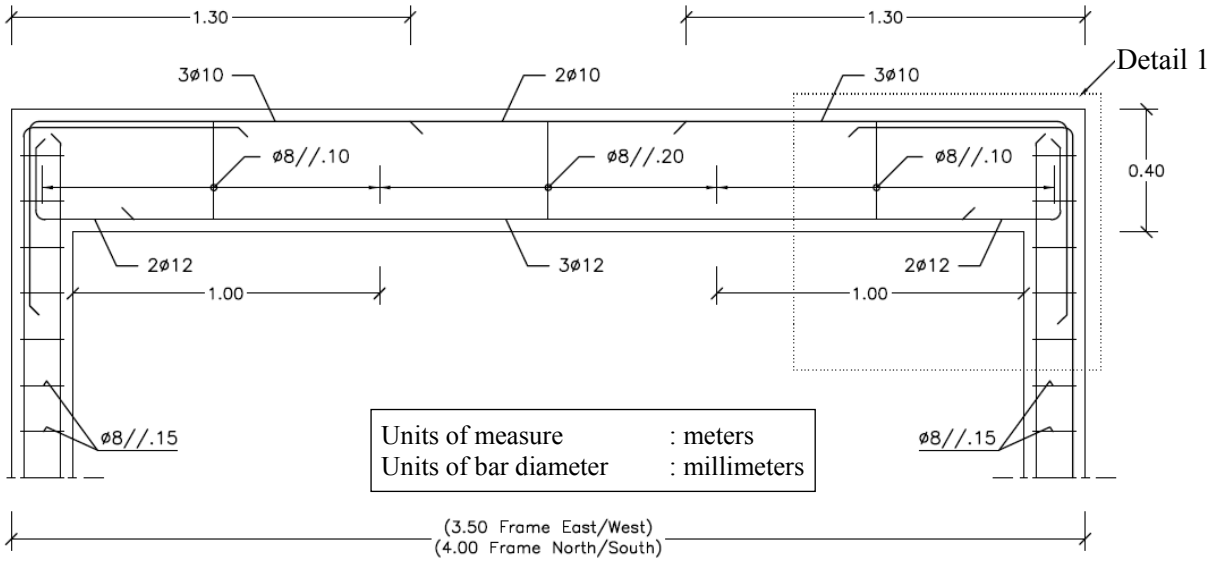

Figure 3-31: Reinforcement details of Lisbon 3D frame model A (taken from: 15th WCEE Blind Test Challenge Report, 2012)

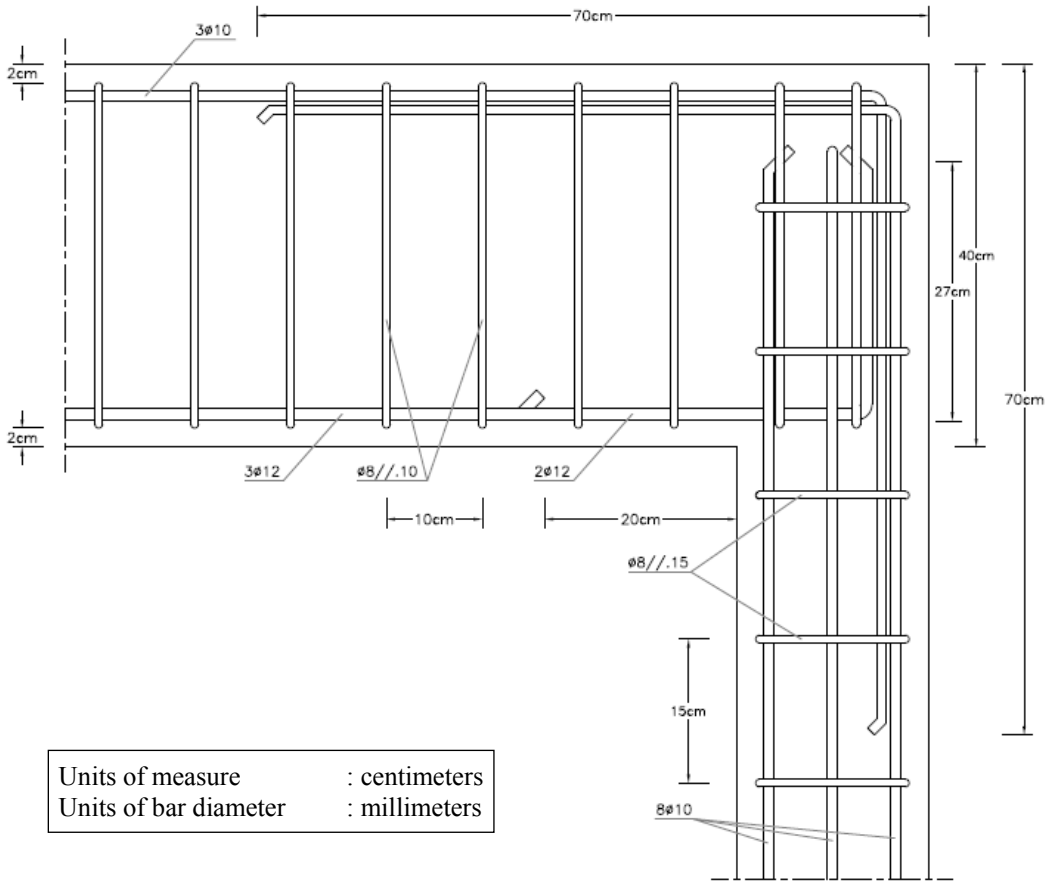

Figure 3-32: Lisbon 3D frame model A: detail 1 (taken from: 15th WCEE Blind Test Challenge Report, 2012)

Table 3-6: Geometric properties and details summary of model A

Property	Measure	Units
Columns height (H) =	3.0	m
Columns plastic hinge length (Lpc) =	24.42	cm
Beams length EW (Lx) =	3.5	m
Beams length NS (Ly) =	4.0	m
Beams plastic hinge length (Lpb) =	14.65	cm
Bar clear cover =	2	cm
Beam and column section details :	Figure 3-30	
Additional reinforcement details :	Figures 3-31 and 3-32	
Total weight of additional masses =	10.80	ton

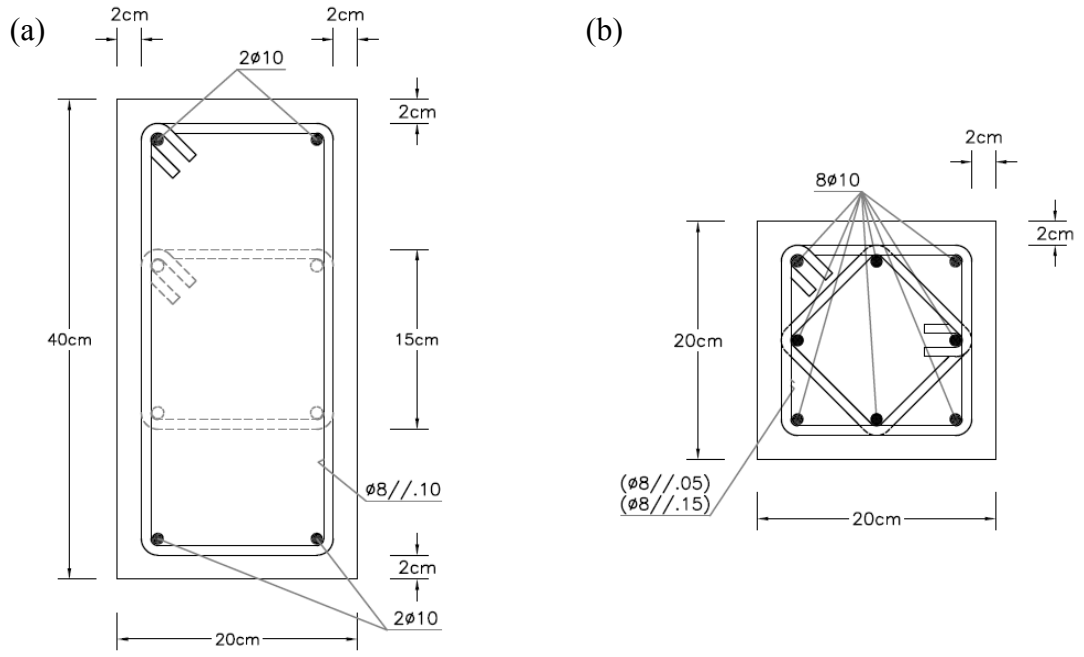

Figure 3-33: (a) Beam and (b) column section details of Lisbon 3D frame model B (taken from: 15th WCEE Blind Test Challenge Report, 2012)

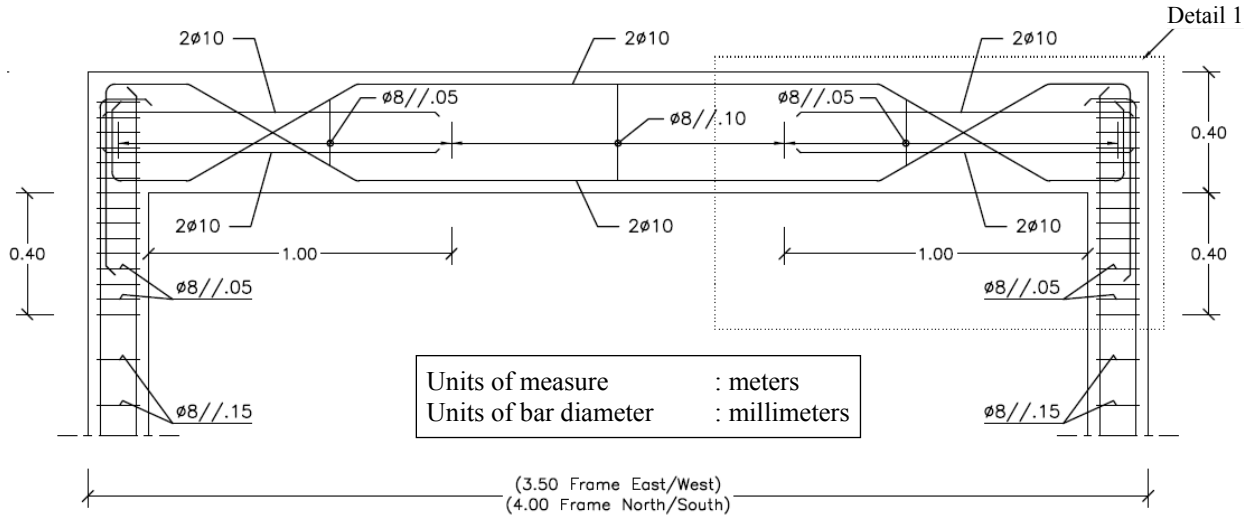

Figure 3-34: Reinforcement details of Lisbon 3D frame model B (taken from: 15th WCEE Blind Test Challenge Report, 2012)

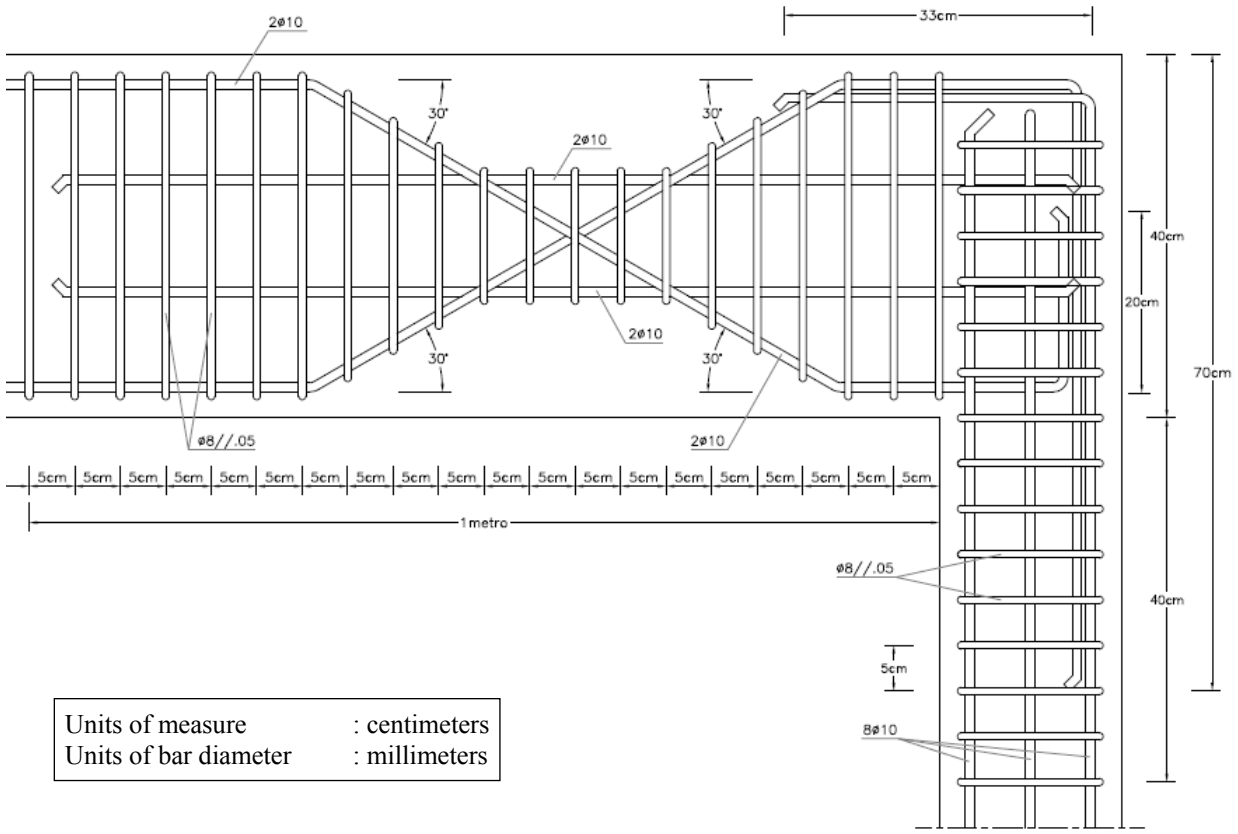

Figure 3-35: Lisbon 3D frame model B: detail 1 (taken from: 15th WCEE Blind Test Challenge Report, 2012)

Table 3-7: Geometric properties and details summary of Lisbon 3D frame model B

Property	Measure	Units
Columns height (H) =	3.0	m
Columns plastic hinge length (Lpc) =	24.42	cm
Beams length EW (Lx) =	3.5	m
Beams length NS (Ly) =	4.0	m
Beams plastic hinge length (Lpb) =	14.65	cm
Bar clear cover =	2	cm
Beam and column section details :	Figure 3-33	
Additional reinforcement details :	Figures 3-34 and 3-35	
Total weight of additional masses =	10.80	ton

Both structures had nine additional masses of 1200kg (2645.6lb) each one placed on top of the slab (Figure 3-36). Pictures of the test setup are presented in Figure 3-37. Steel reinforcement detailing, as well as further details of the tests, material properties, and specimens' geometry were presented in the 15th WCEE Blind Test Challenge Design Report (2012).

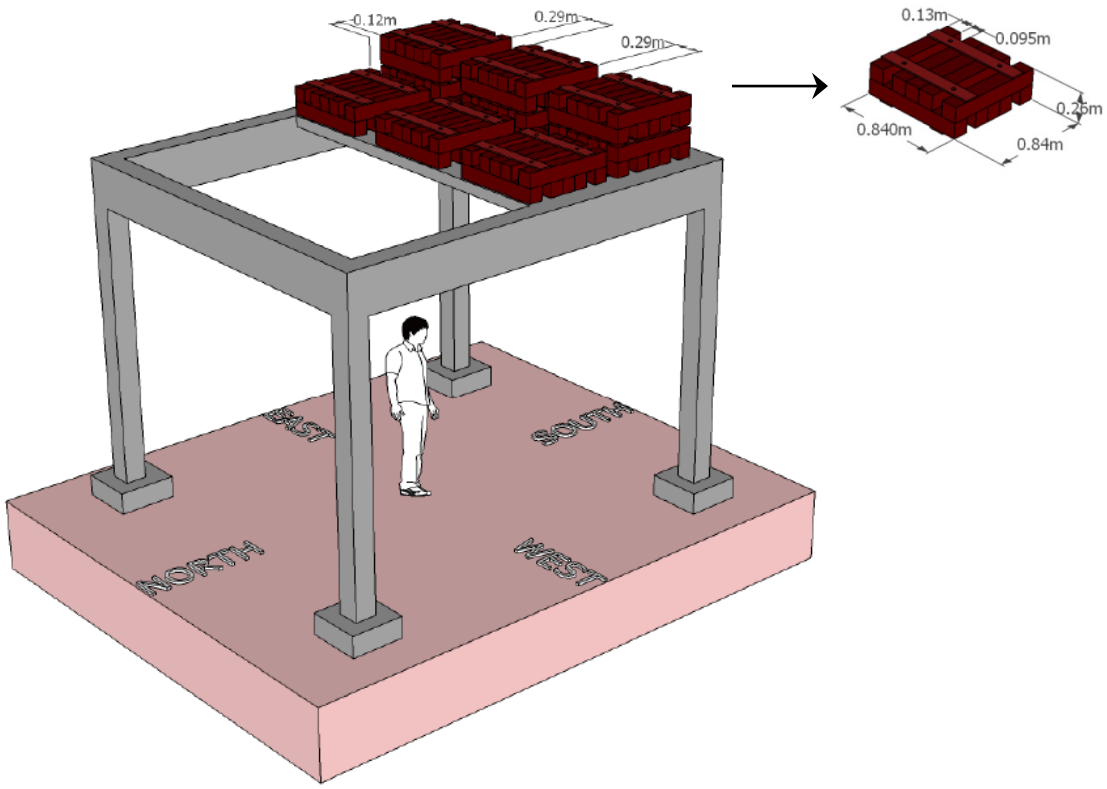

Figure 3-36: Position of the masses on the slab and dimensions of one mass (taken from: 15th WCEE Blind Test Challenge Report, 2012)

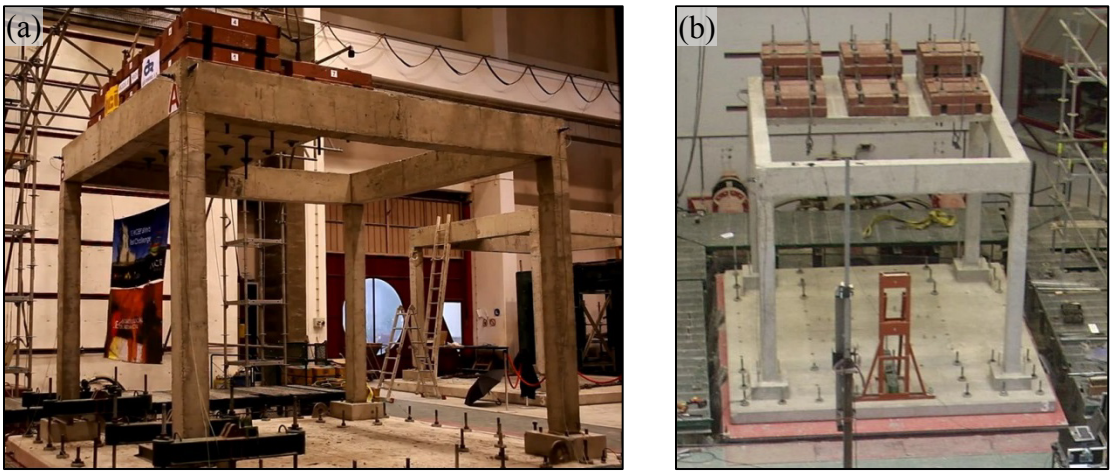

Figure 3-37: Full-scale 3D frame structure tests setup (a) 3D view from bottom, and (b) 3D front view from top (photos taken from: 15th WCEE Blind Test Challenge, 2012)

Both 3D frames were subjected to a sequential seismic load of 4 biaxial ground motions with increasing intensity levels, namely, low, moderate, reference, and high, which for the

purpose of this work will be called EQ1, EQ2, EQ3, and EQ4, respectively. Unlike the UCSD column, both structures were not taken to near-collapse conditions. Also, no attempts were made to straighten or repair the 3D frames between tests. Displacements in two selected control points (i.e., points A and B in Figure 3-38) were the only data provided from the organizers.

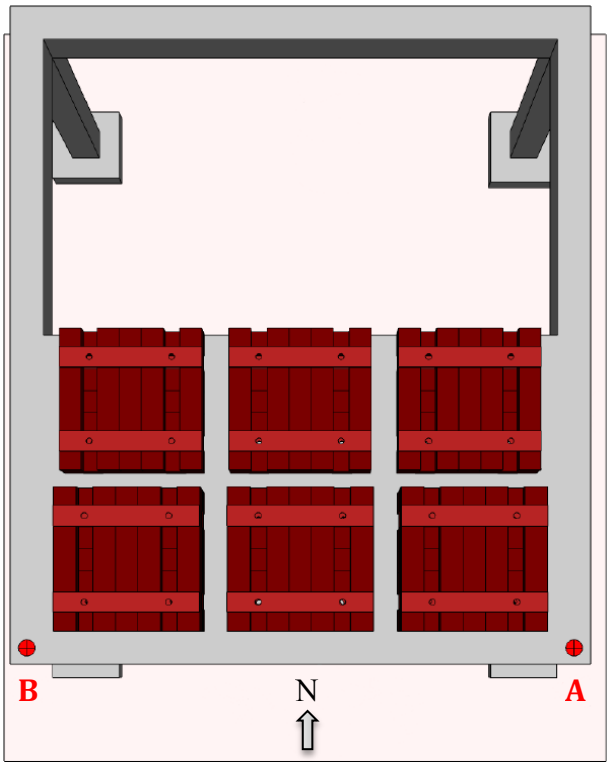

Figure 3-38: General top view of 3D frame models: points A and B where the experimental data was collected (taken from: 15th WCEE Blind Test Challenge Report, 2012)

Considering the scarce information from the experimental tests (no test report was provided), only Root-Mean-Square (RMS) error values (Equation (3-2)) between the experimental and simulated displacements in the aforementioned control points will be computed for model calibration purposes.

In Equation (3-2), *sim* and *exp* are related to the simulated and experimental data respectively. *N* is the number of sampling points. LA, TA, and LB, TB belong to the longitudinal and transversal displacements of points A and B respectively.

$$error_{RMS} = \sqrt{\frac{1}{N}\cdot\sum_{i=1}^{N}(LA_{sim(i)} - LA_{\exp(i)})^2} + \sqrt{\frac{1}{N}\cdot\sum_{i=1}^{N}(TA_{sim(i)} - TA_{\exp(i)})^2} + \sqrt{\frac{1}{N}\cdot\sum_{i=1}^{N}(LB_{sim(i)} - LB_{\exp(i)})^2} + \sqrt{\frac{1}{N}\cdot\sum_{i=1}^{N}(TB_{sim(i)} - TB_{\exp(i)})^2} \quad (3\text{-}2)$$

Both components of the input ground motions were synthetic time series, compatible with the EC8 standard elastic response spectra format for 5% damping. A time segment of two horizontal orthogonal components of the 2011 Tohoku earthquake at Japan were used in the artificial signals generation process. The target ground motion (two orthogonal components) generated matches the reference intensity level (EQ3) and the other EQs used during the tests are simply scaled versions of the target record as follows: (1) EQ1 corresponds to 20% EQ3; (2) EQ2 corresponds to 70% EQ3; and (3) EQ4 corresponds to 200% of EQ3. Figure 3-39 to Figure 3-42 show both components (i.e., East-West and North-South) of the artificially generated input ground motions.

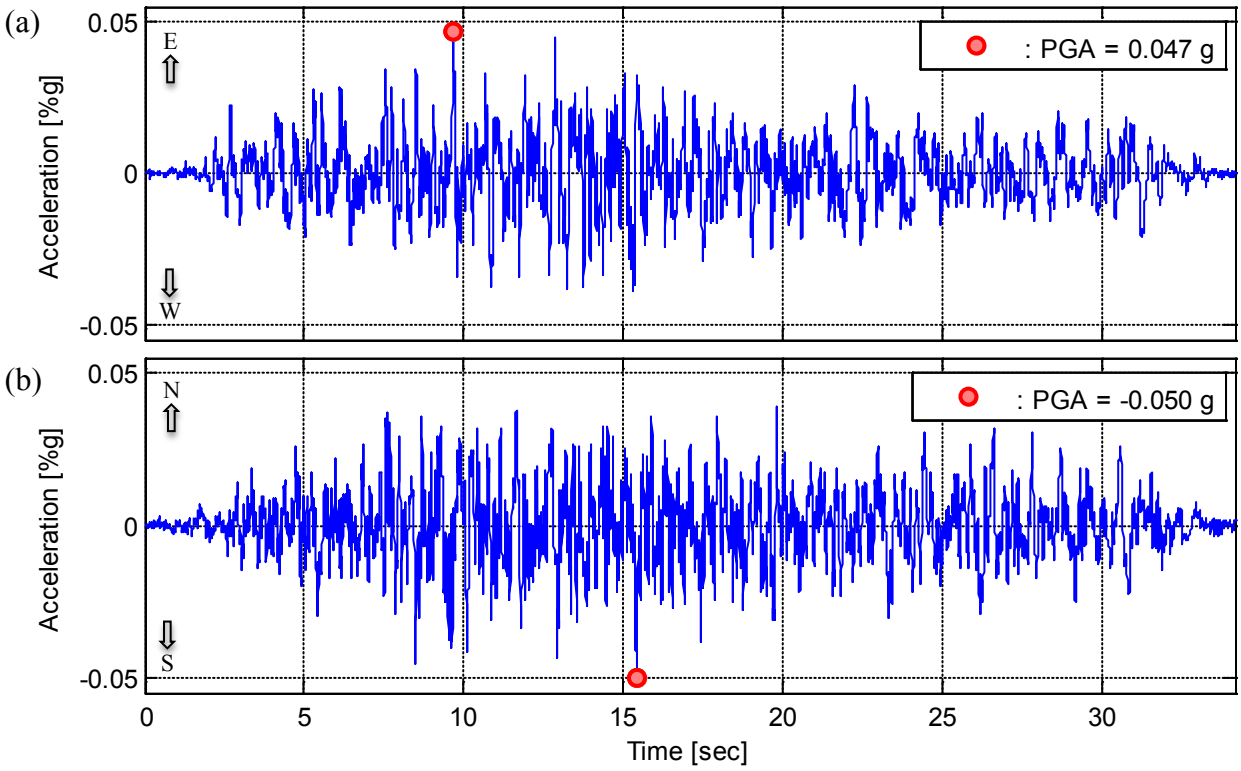

Figure 3-39: Input ground motion EQ1: (a) component EW and (b) component NS

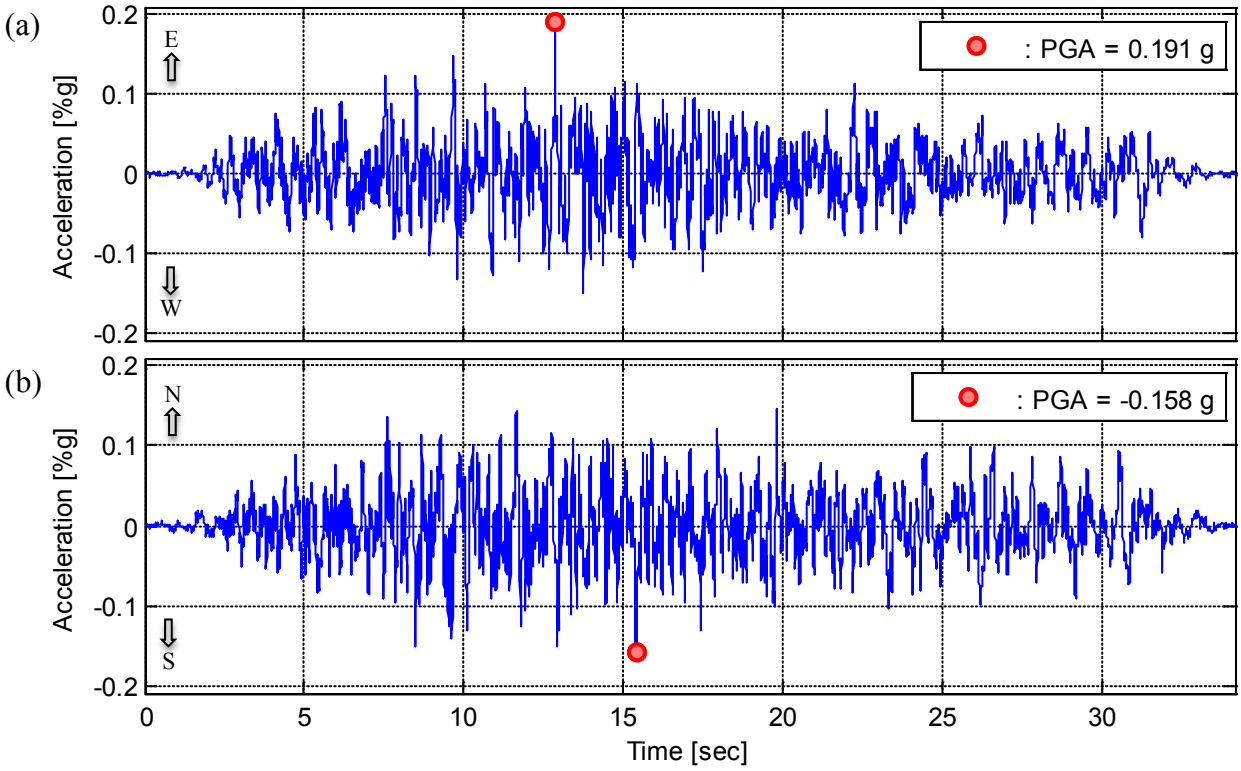

Figure 3-40: Input ground motion EQ2: (a) component EW and (b) component NS

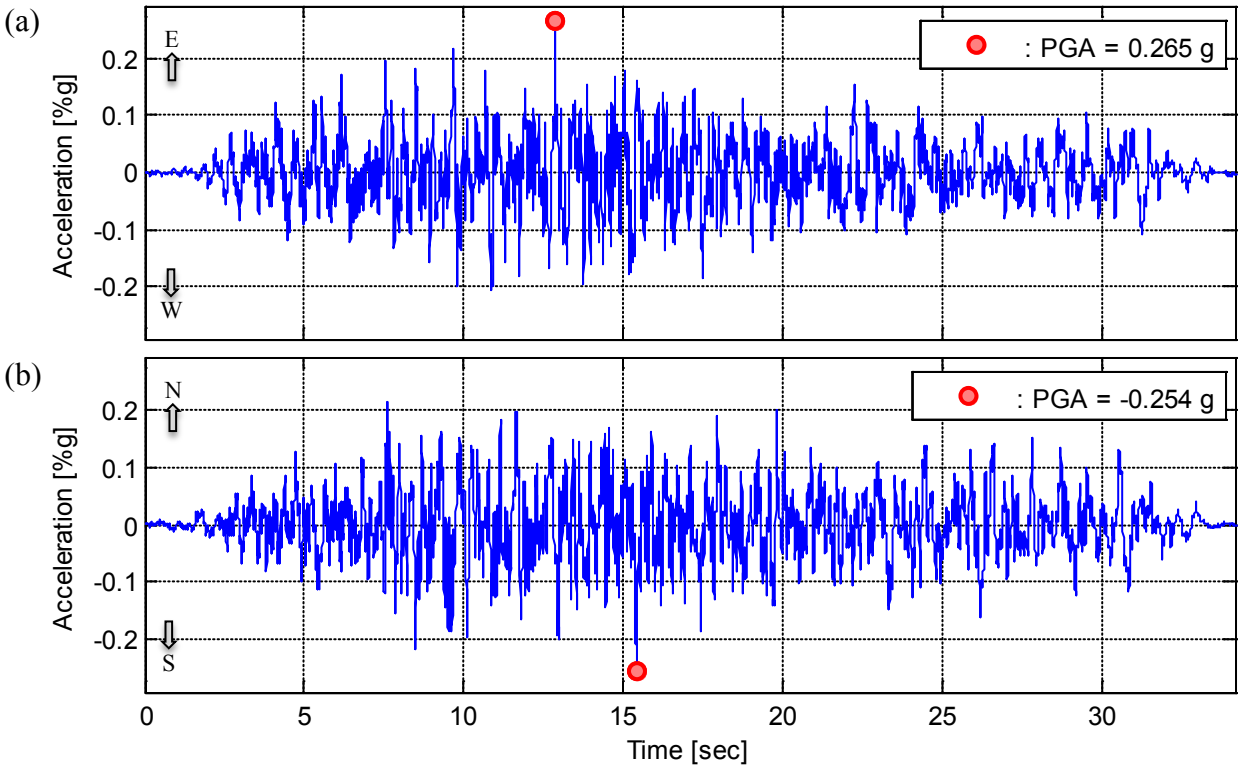

Figure 3-41: Input ground motion EQ3: (a) component EW and (b) component NS

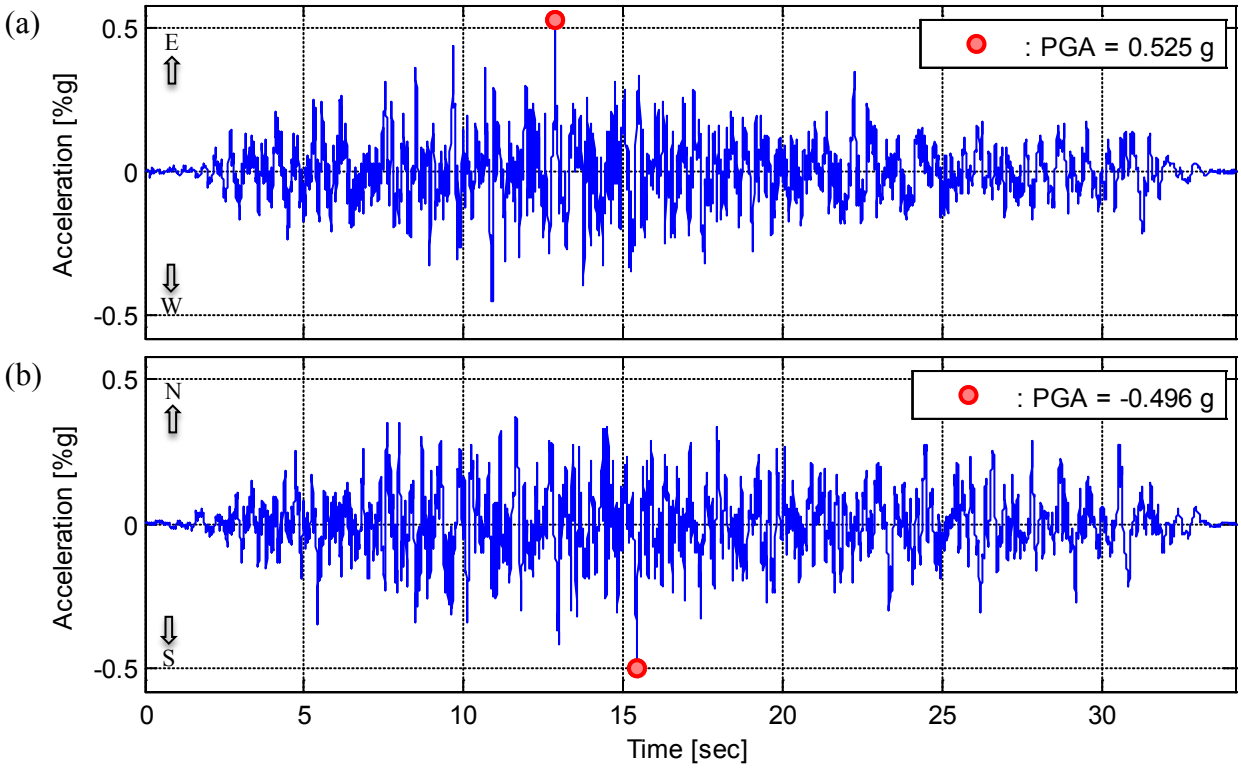

Figure 3-42: Input ground motion EQ4: (a) component EW and (b) component NS

Considering that both structures are quite similar, only one nonlinear finite element model will be developed. The structure selected to perform the model is the one in which more damage occurred, that is, the structure that experienced the larger relative displacements. Total displacements are computed using the experimental data collected in the two aforementioned control points and the following equation:

$$Total_{displ} = \sqrt{(d_{EW})^2 + (d_{NS})^2} \tag{3-3}$$

where d_{EW} and d_{NS} correspond to the relative displacements on the EW and NS directions respectively. The total displacements at both points (A and B) for both structures are computed using Equation (3-3) and the results are presented in Figure 3-43 and Figure 3-45. In addition, the maximum displacement ratio for both points between structures A and B is computed (Equation (3-4)) and then illustrated in Figure 3-44 and Figure 3-46.

$$Max.Displ._{ratio} = \frac{Max.Displ_{S1}}{Max.Displ_{S2}} \quad (3\text{-}4)$$

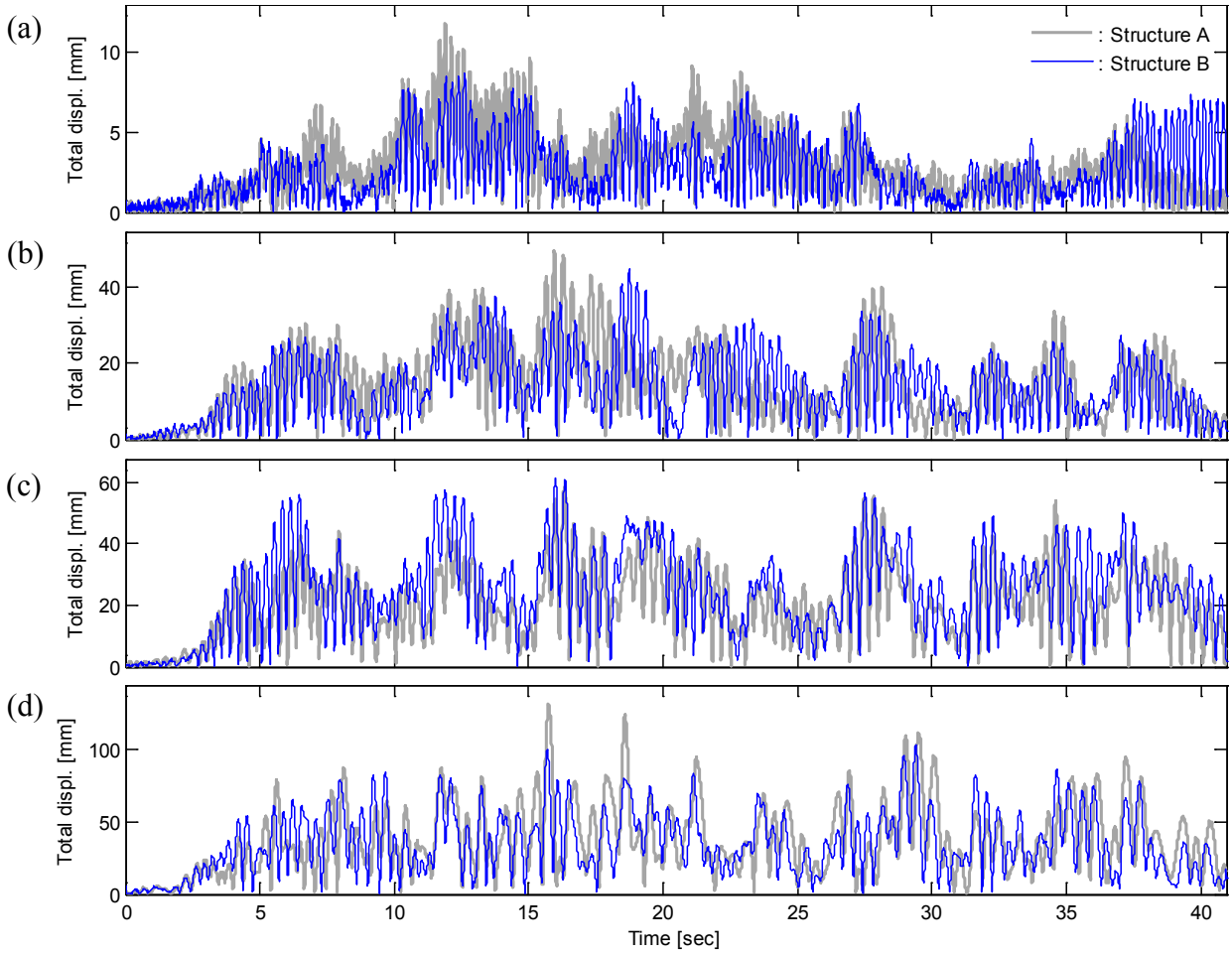

Figure 3-43: Total displacements of point A during: (a) EQ1, (B) EQ2, (c) EQ3, and (d) EQ4

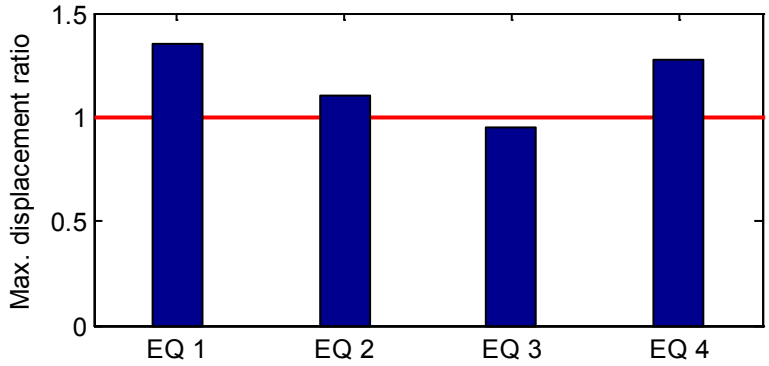

Figure 3-44: Maximum displacement ratio between structures A and B for point A

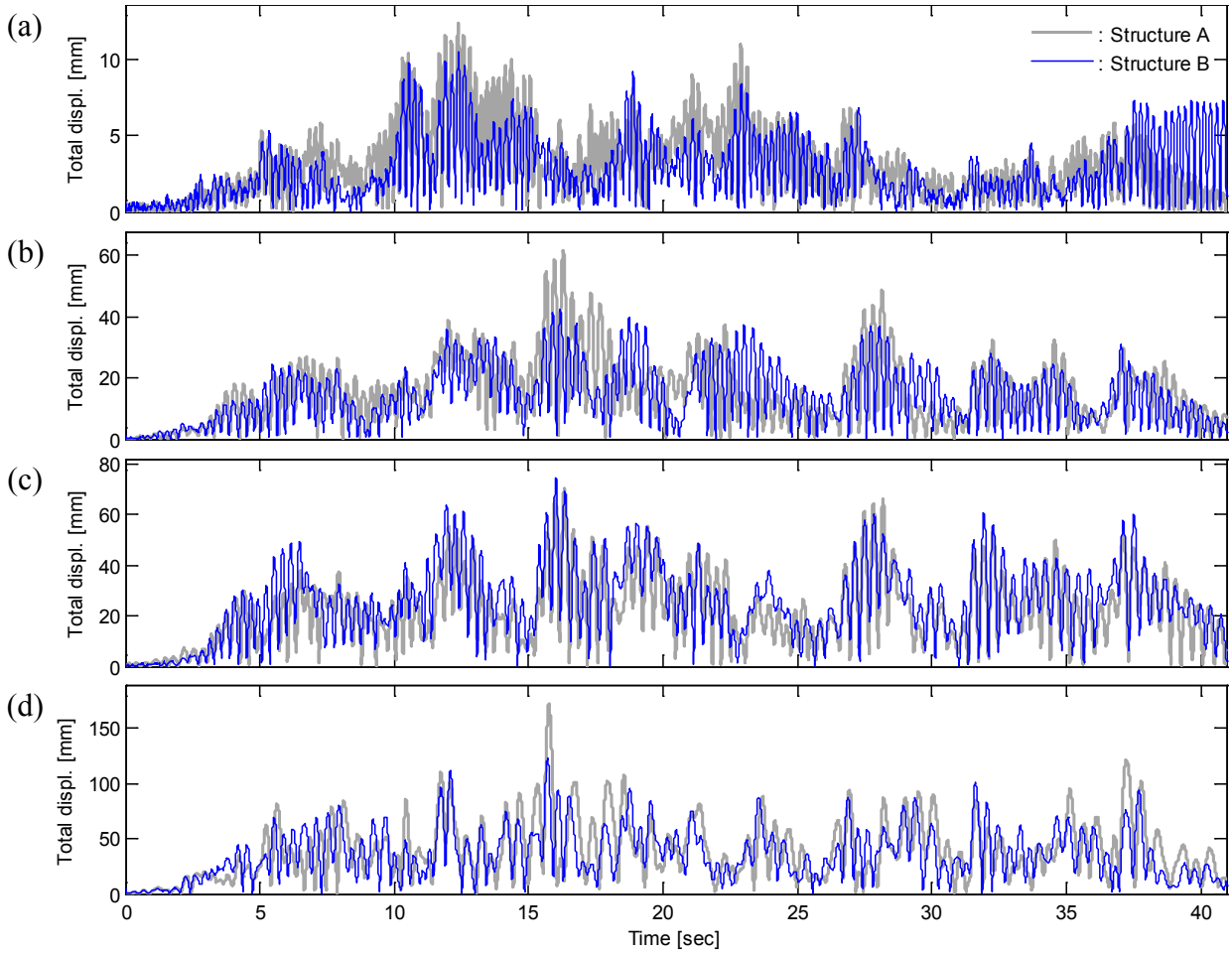

Figure 3-45: Total displacements of point B during: (a) EQ1, (B) EQ2, (c) EQ3, and (d) EQ4

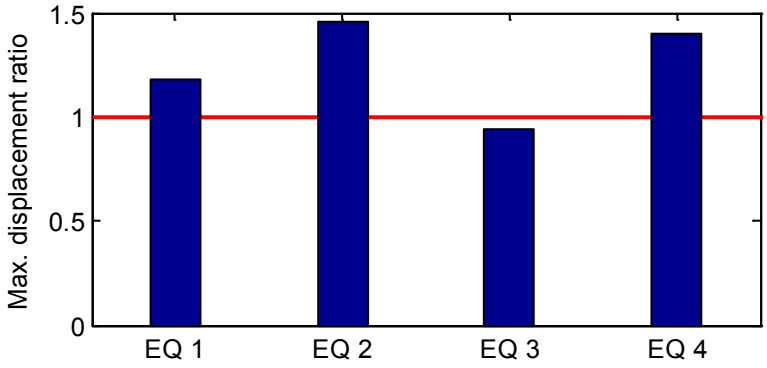

Figure 3-46: Maximum displacement ratio between structures A and B for point B

It can be clearly seen that the structure which undergoes the larger displacements is the Lisbon 3D frame model A, which means there was more damage in this one than in model B. In

some way this was expected since model A was the structure designed for low ductility levels, which is reflected in the poor steel reinforcement detailing.

Table 3-8 and Table 3-9 summarize the peak displacement ductilities in both orthogonal directions (EW and NS) registered during the experimental tests for the structure A.

Table 3-8: Experimental peak displacement ductilities in EW direction

Test	Max. Positive		Max. Negative	
	Point A	Point B	Point A	Point B
EQ1	0.37	0.39	-0.40	-0.41
EQ2	1.43	1.45	-1.48	-1.44
EQ3	1.91	1.90	-1.90	-1.87
EQ4	4.41	4.29	-3.89	-3.78

Table 3-9: Experimental peak displacement ductilities in NS direction

Test	Max. Positive		Max. Negative	
	Point A	Point B	Point A	Point B
EQ1	0.20	0.26	-0.21	-0.28
EQ2	1.23	1.71	-1.24	-1.68
EQ3	1.31	1.74	-1.23	-1.82
EQ4	3.21	4.33	-2.47	-3.23

Based on the model A geometry and the experimental results for the rebar tension tests (f_y=*80.3ksi,* f_u=*90.43ksi*), two values of *Lp* are computed using Equation (3-1), that is, one for the beams and another one for the columns. The calculated values are *Lpb = 146.5mm* (5.77in) and *Lpc = 244.2mm* (9.61in), respectively.

Unlike the UCSD column, there is no report of the yield displacement in this case. Moreover, it is not possible to use CUMBIA for a moment curvature prediction since in this case the structure is a 3D frame. For this reason, in addition to a cyclic pushover analysis, a monotonic pushover analysis was performed to define the displacement ductility μ=1. Notice that it is necessary to perform each analysis (monotonic and cyclic) twice due to the spatial nature of the structure. Nevertheless, due to the symmetry of the structure the results will be quite similar for both directions. The differences will be a result of the eccentricity induced by

the slab and the different beam length on each direction. Then, the process consists in performing the monotonic analysis first and based on these results the cyclic pushover analysis is then performed. Based on the peak experimental displacement ductilities, the maximum ductility to reach during the cyclic analyses was set up as μ=6.

For the EW direction the yield displacement is calculated as 28.45mm (1.12in) (displacement ductility μ_{EW}=1). Based on this result, the displacement loading history for the cyclic pushover on EW direction (Figure 3-47) was divided in a sequence of 7 stages as follows: (1) one cycle up to 0.56in (μ_{EW}=0.5); (2) one cycle up to 1.12in (μ_{EW}=1) ; (3) one cycle up to 2.24in (μ_{EW}=2) ; (4) one cycle up to 3.36in (μ_{EW}=3) ; (5) one cycle up to 4.48in (μ_{EW}=4) ; (6) one cycle up to 5.6in (μ_{EW}=5); and (7) one cycle up to 6.72in (μ_{EW}=6).

For the NS direction the yield displacement is calculated as 28.19mm (1.11in) (displacement ductility μ_{NS}=1). Based on this result, the displacement loading history for the cyclic pushover on NS direction (Figure 3-47) was divided in a sequence of 7 stages as follows: (1) one cycle up to 0.55in (μ_{NS}=0.5); (2) one cycle up to 1.11in (μ_{NS}=1) ; (3) one cycle up to 2.22in (μ_{NS}=2) ; (4) one cycle up to 3.33in (μ_{NS}=3) ; (5) one cycle up to 4.44in (μ_{NS}=4) ; (6) one cycle up to 5.55in (μ_{NS}=5); and (7) one cycle up to 6.66in (μ_{NS}=6).

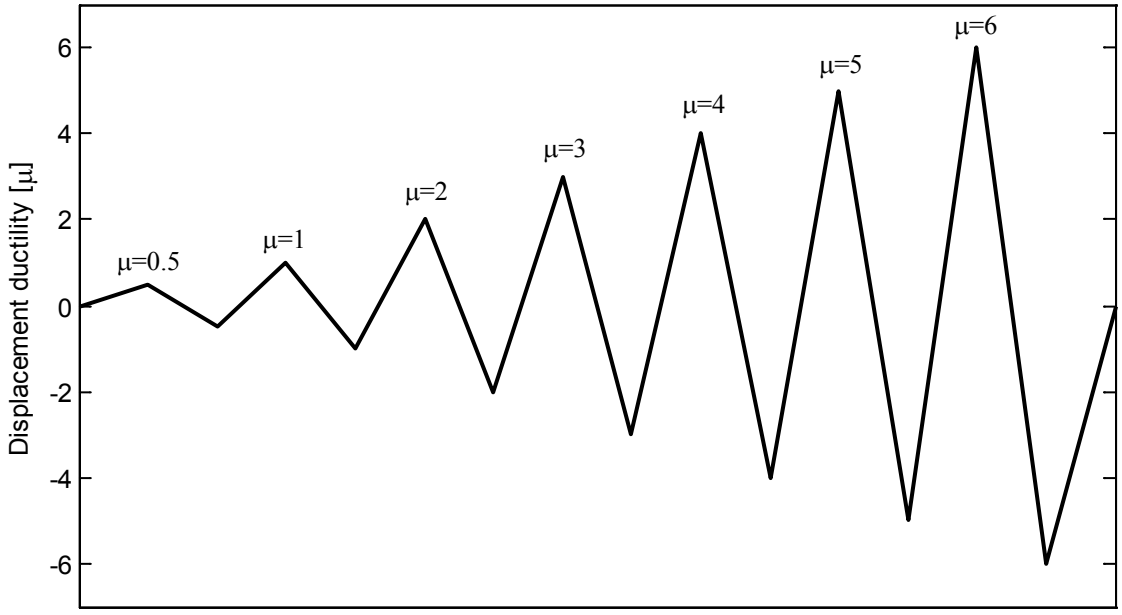

Figure 3-47: Lisbon model A cyclic pushover analysis: displacement ductility loading history

3.3.2.2. Fiber-based model

In this model, the parameters for the *ReinforcingSteel* material were defined as: $\alpha=0.505$, $C_f=0.250$ and $C_d=0.075$. These values were determined based on the minimization of the RMS error value (RMS_{error} = 190.38) by using the Equation (3-2). Using the P-Delta coordinate transformation command, second order effects were included considering that the total weight of the additional masses exceeds the structure's self-weight. Figure 3-48 presents a scheme of the model's generation in OpenSees.

3.3.2.3. Monotonic and cyclic pushover test results

In this case, the monotonic and cyclic pushover test results are obtained once the model has been calibrated and validated based only on the RMS_{error} value as mentioned before. Figure 3-49 and Figure 3-50 present the monotonic and cyclic force-displacement response for the EW direction and NS direction respectively. Notice in both figures the negative slope in the post yield response of the structure. This means that P-Delta effects are important in this case, which was anticipated considering the huge weight of the additional masses on the slab. Also notice that in both cases the results of the cyclic analysis are not symmetric, this happens because of the geometric eccentricity generated by the slab and the load eccentricity created by the over-imposed load distribution. The yield force was taken from the monotonic analyses as 393.87kN (18.25kips) for the EW direction and as 388.91kN (18.02kips) for the NS direction.

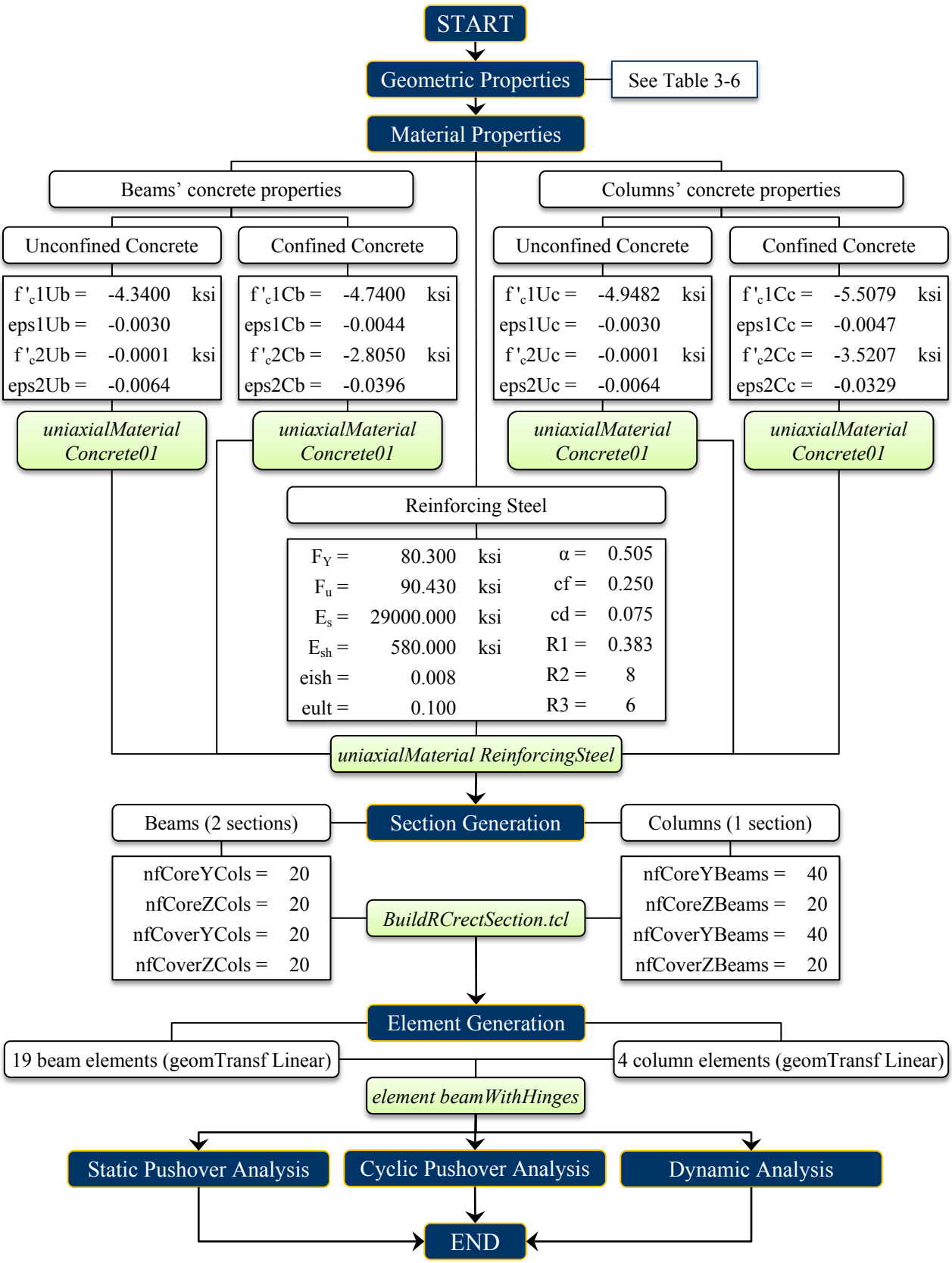

Figure 3-48: Lisbon 3D frame fiber-based model A generation scheme

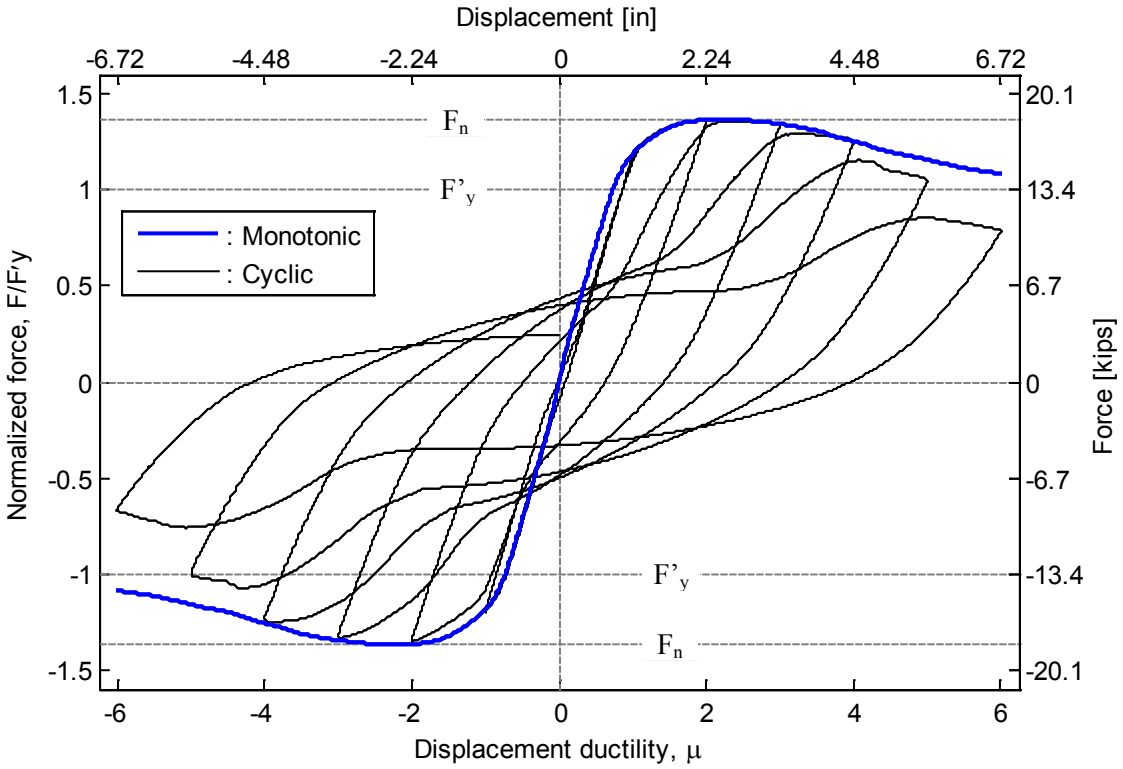

Figure 3-49: Monotonic and Cyclic force-displacement response on EW direction of model A

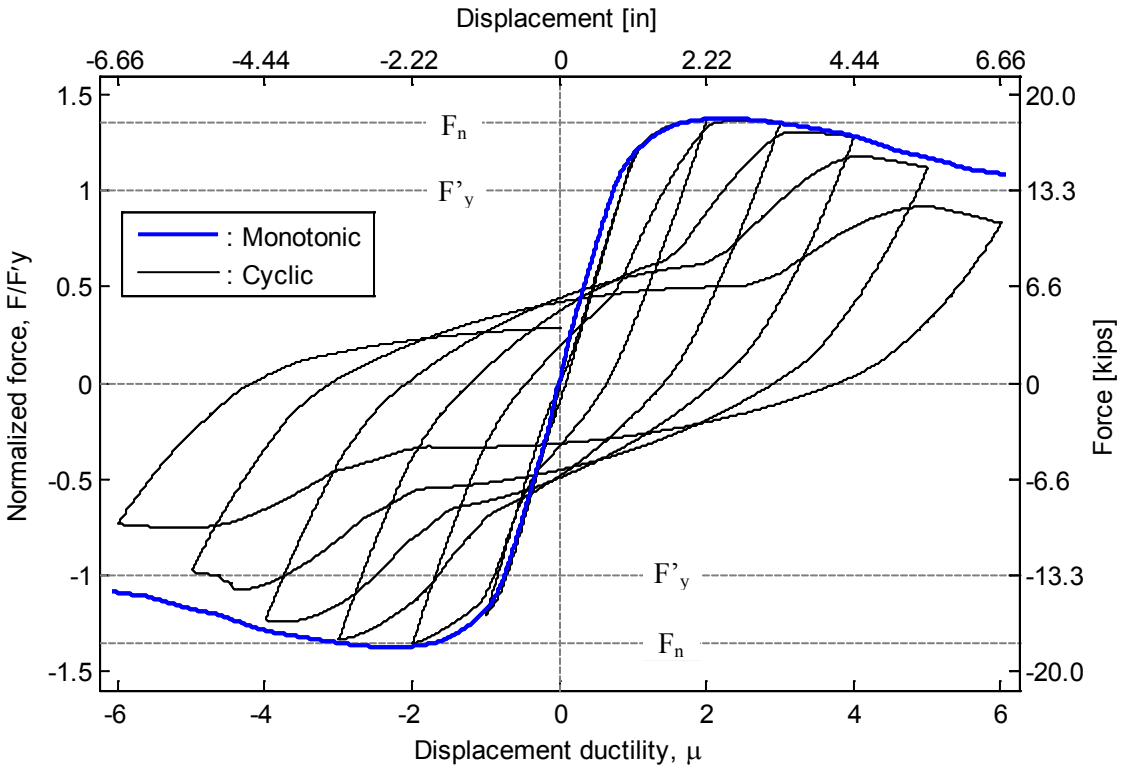

Figure 3-50: Monotonic and Cyclic force-displacement response in NS direction of model A

3.3.2.4. Dynamic analysis test results

Figure 3-51 to Figure 3-58 compare the results from the shaking table tests for model A with the results obtained with the numerical model. Notice that in this case, unlike the UCSD column, the acceleration responses are not displayed since there is no experimental data available in terms of acceleration. In general, the results are in close agreement. In terms of the displacement ductility maximum peaks the agreement is also close. This can also be observed in Table 3-10 and Table 3-11, which summarize the maximum positive and negative displacement ductility peak values for the experimental and simulated results for both control points.

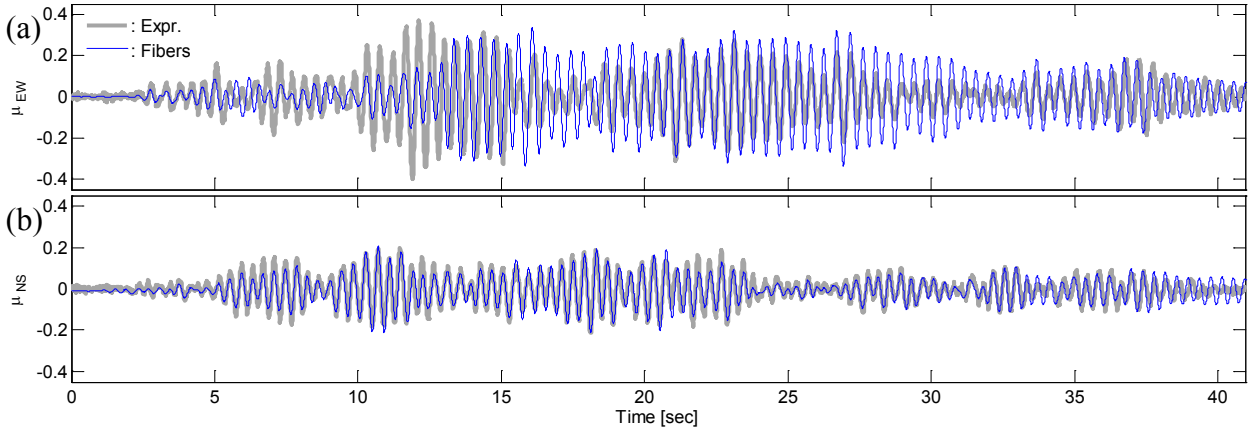

Figure 3-51: Comparison of experimental and numerical model A displacement ductilities of point A for EQ1: (a) EW direction and (b) NS direction

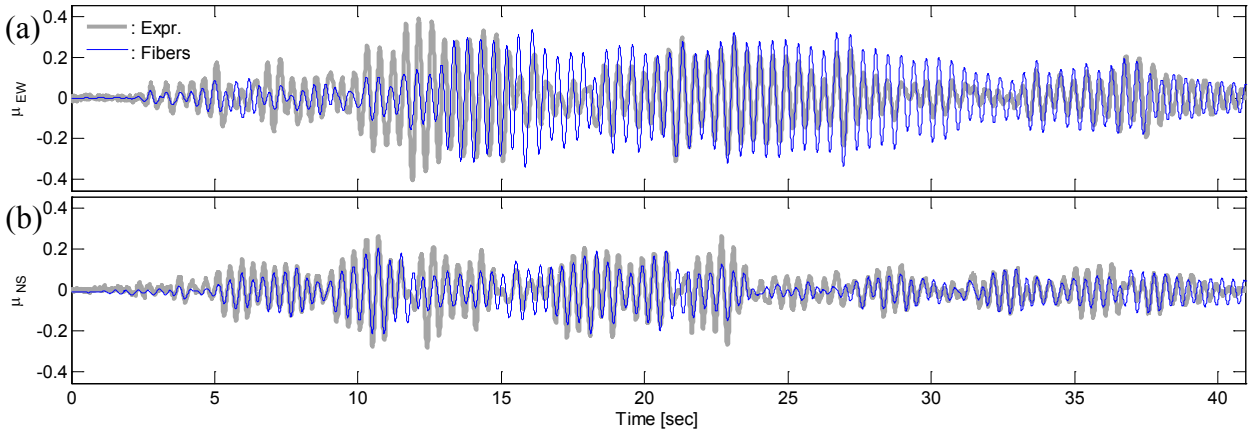

Figure 3-52: Comparison of experimental and numerical model A displacement ductilities of point B for EQ1: (a) EW direction and (b) NS direction

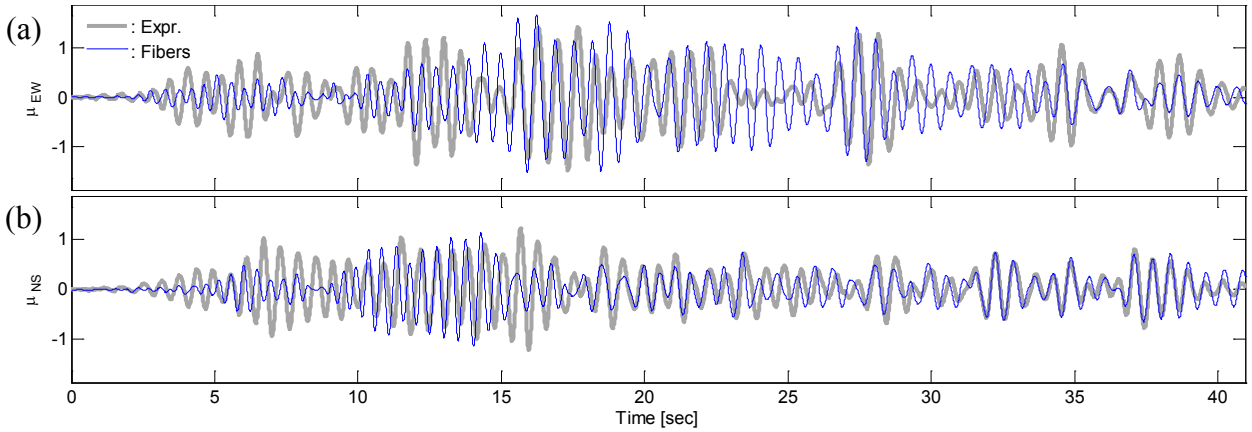

Figure 3-53: Comparison of experimental and numerical model A displacement ductilities of point A for EQ2: (a) EW direction and (b) NS direction

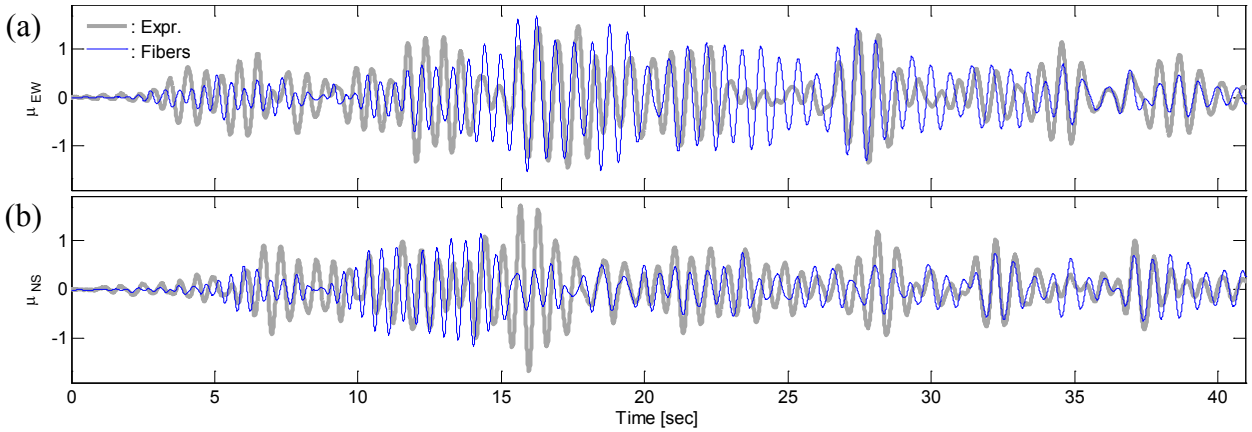

Figure 3-54: Comparison of experimental and numerical model A displacement ductilities of point B for EQ2: (a) EW direction and (b) NS direction

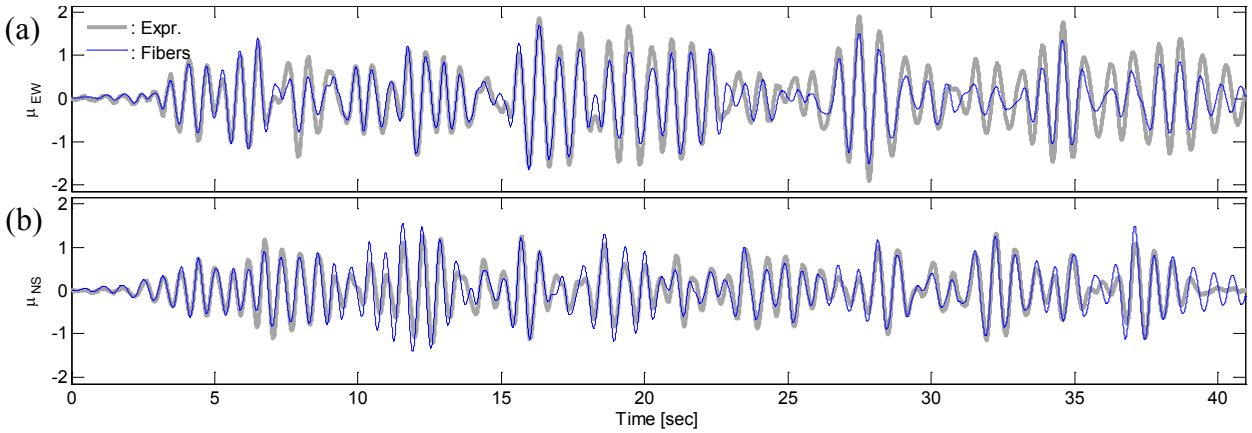

Figure 3-55: Comparison of experimental and numerical model A displacement ductilities of point A for EQ3: (a) EW direction and (b) NS direction

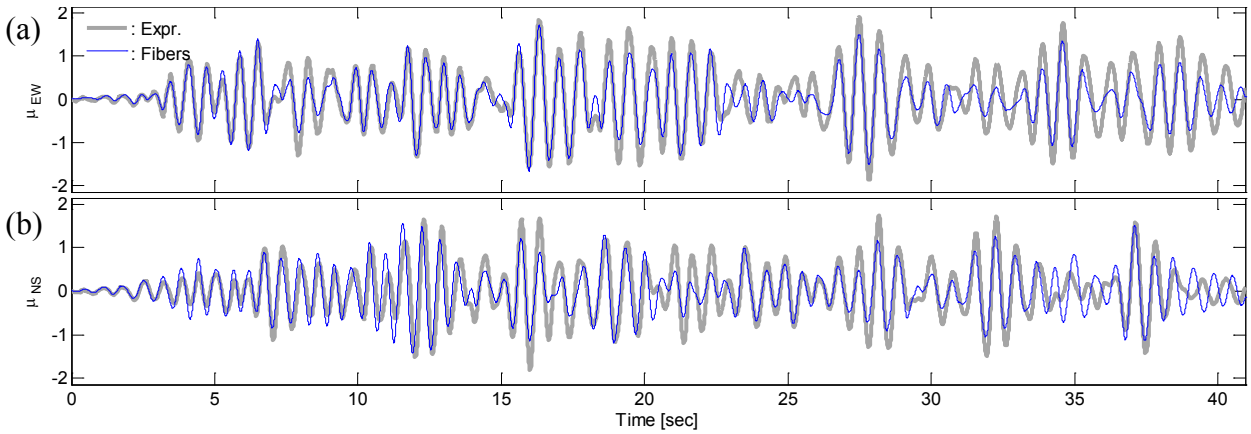

Figure 3-56: Comparison of experimental and numerical model A displacement ductilities of point B for EQ3: (a) EW direction and (b) NS direction

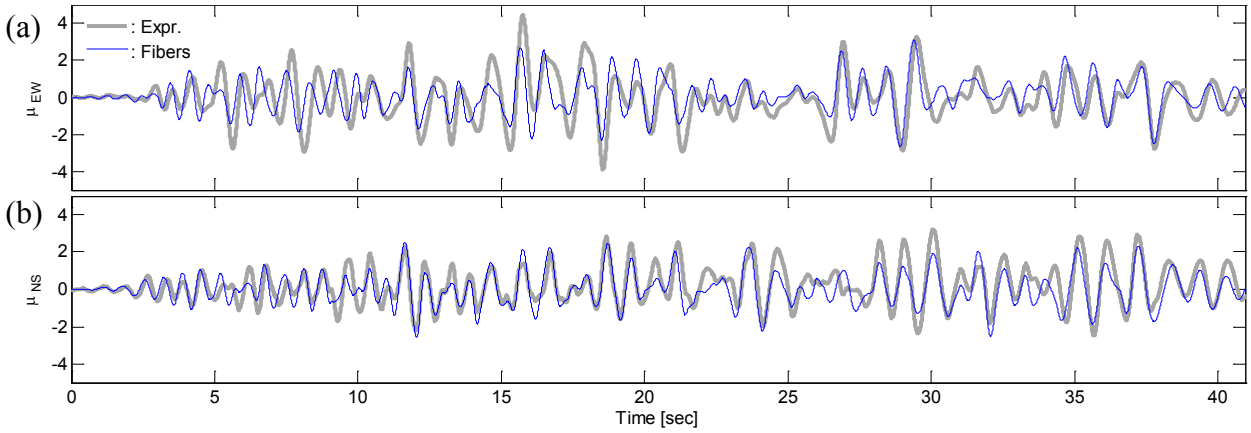

Figure 3-57: Comparison of experimental and numerical model A displacement ductilities of point A for EQ4: (a) EW direction and (b) NS direction

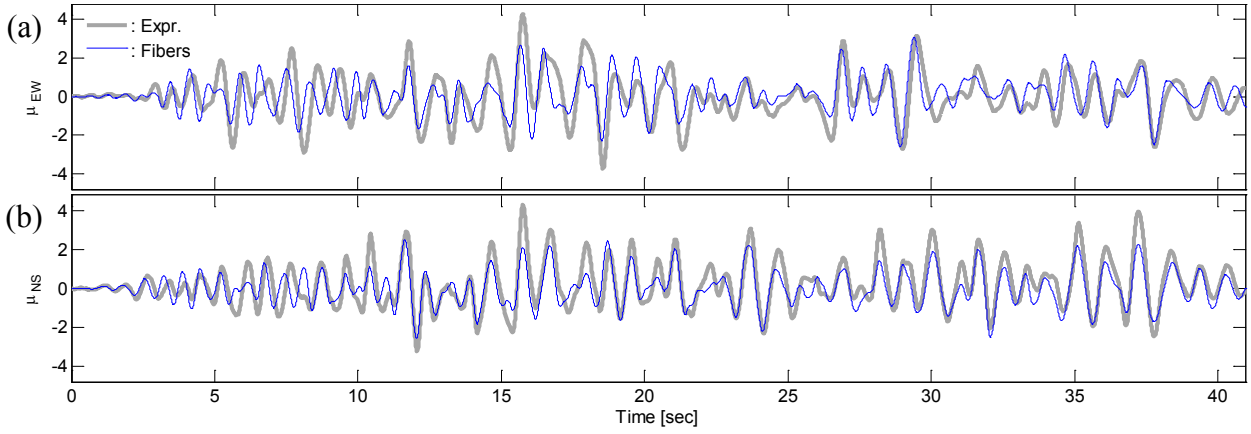

Figure 3-58: Comparison of experimental and numerical model A displacement ductilities of point B for EQ4: (a) EW direction and (b) NS direction

Table 3-10: Experimental and numerical peak displacement ductilities on EW direction

	Test	Max. Positive		Max. Negative	
		Exper.	Fibers	Exper.	Fibers
Point A	EQ1	0.37	0.34	-0.40	-0.34
	EQ2	1.43	1.67	-1.48	-1.52
	EQ3	1.91	1.71	-1.90	-1.65
	EQ4	4.41	3.08	-3.89	-2.62
Point B	EQ1	0.39	0.34	-0.41	-0.34
	EQ2	1.45	1.67	-1.44	-1.53
	EQ3	1.90	1.71	-1.87	-1.66
	EQ4	4.29	3.08	-3.78	-2.62

Table 3-11: Experimental and numerical peak displacement ductilities on NS direction

	Test	Max. Positive		Max. Negative	
		Exper.	Fibers	Exper.	Fibers
Point A	EQ1	0.20	0.21	-0.21	-0.21
	EQ2	1.23	1.15	-1.24	-1.15
	EQ3	1.31	1.54	-1.23	-1.41
	EQ4	3.21	2.52	-2.47	-2.57
Point B	EQ1	0.26	0.20	-0.28	-0.22
	EQ2	1.71	1.15	-1.68	-1.15
	EQ3	1.74	1.55	-1.82	-1.43
	EQ4	4.33	2.52	-3.23	-2.59

3.4. Chapter Summary and Conclusions

- ✓ Second order effects largely influence the behavior of both structures, which are reflected in the negative slope of the post-yield response in Figure 3-19, Figure 3-49 and Figure 3-50. They are significant in terms of the entire response of the structures (e.g., accelerations and displacements) especially if large inelastic excursions are expected.
- ✓ Currently, the use of fiber-based sections is perhaps the best alternative for section representation for a FE model element as confirmed by other researchers (e.g., Spacone, 1996b and 1996b; Scott and Fenves, 2006; Velázquez, 2011; Huang, 2012). In this work, fiber-based sections in combination with *forceBeamColumn* and *beamWithHinges* elements give the best results in terms of the structural response.

One of the main advantages of the *beamWithHinges* element is that it is not necessary to define any integration points which make easier its use for structures with several elements since only plastic hinge lengths need to be defined.

- ✓ Having experimental and simulated results in close agreement has a great significance since it allows comparing simulated and experimental results with more reliability when damage detection methodologies are applied. Indubitably, the more experimental data is available (e.g., material tests, acceleration and displacement responses, observations during the tests like rebar fracture and concrete spalling, among others), the better the calibration and validation that can be performed. Nevertheless, it will be shown in the following chapter that the close match obtained in the global response of the structures does not necessarily means that the numerical model is appropriate for validation of health monitoring algorithms.

3.5. References

15th WCEE Blind Test Challenge Design Report, (2012), "15th World Conference on Earthquake Engineering", Lisbon, Portugal.

Bazant, Z.P. and Planas, J. (1998), Fracture and Size Effect in Concrete and Other Quasibrittle Materials, CRC Press, Boca Raton, FL.

Coleman, J. and Spacone, E. (2001), "Localization Issues in Force-Based Frame Elements", ASCE Journal of Structural Engineering 127(11), 1257-1265.

Huang, X. (2012), "Applicability Criteria of Fiber-Section Elements for the Modelling of RC Columns Subjected to Cyclic Loading", ME report, University of Toronto.

Mander, J.B., Priestley, M.J.N. and Park, R. (1988), "Theoretical Stress-Strain Model for Confined Concrete", ASCE Journal of Structural Engineering 114(8), 1804-1826.

Mazzoni S., McKenna, F., Scott M.H., Fenves, G.L. et al. (2007). "The OpenSees Command Language Manual", Pacific Earthquake Engineering Research Center, University of California at Berkeley.

McKenna, F., Fenves, G.L., Scott, M.H. and Jeremic, B. (2000), "Open System for Earthquake Engineering Simulation – OpenSees", http://opensees.berkeley.edu

Mohle, J. and Kunnath, S (2006), Reinforcing Steel Material, http://opensees.berkeley.edu

Montejo, L.A and Kowalsky, M.J. (2007), “CUMBIA – Set of Codes for the Analysis of Reinforced Concrete Members”, CFL Technical Report No. IS-07-01, Department of Civil, Construction and Environmental Engineering, North Carolina State University, Raleigh, NC.

Petrini, L., Maggi, C., Priestley, M.J.N. and Calvi, G.M. (2008), “Experimental Verification of Viscous Damping Modeling for Inelastic Time History Analyzes”, Journal of Earthquake Engineering 12(S1), 125-145.

Priestley, M.J.N., Calvi G.M. and Kowalsky, M.J. (2007), Direct Displacement Based Seismic Design of Structures, IUSS Press, Pavia, Italy.

Saiidi, M. and Sozen, M. (1979), “Simple and Complex Models for Nonlinear Seismic Response of Reinforced Concrete Structures”, Tech. Rep. UILU-ENG-79-2031, Department of Civil Engineering, University of Illinois, Urbana, IL.

Scott, M.H. and G.L. Fenves (2006), "Plastic Hinge Integration Methods for Force-Based Beam-Column Elements", Journal of Structural Engineering, ASCE, 132(2), 244-252.

Schoettler, M.J., Restrepo, J. I., Guerrini, G., Duck, D.E. and Carrea, F. (2012), “A Full-Scale, Single-Column Bridge Bent Tested by Shake-Table Excitation” Center for Civil Engineering Earthquake Research, Department of Civil Engineering, University of Nevada, Reno.

Spacone, E., Filipou, F.C. and Taucer, F.F. (1996a), “Fibre Beam-Column Model for Non-Linear Analysis of RC Frames: Part I. Formulation”, Earthquake Engineering and Structural Dynamics 25, 711-725.

Spacone, E., Filipou, F.C. and Taucer, F.F. (1996b), “Fibre Beam-Column Model for Non-Linear Analysis of RC Frames: Part II. Applications”, Earthquake Engineering and Structural Dynamics 25, 727-742.

Velázquez-Carrasquillo, L.R. (2011), “Wavelet Based Damage Detection in Civil Structures Subjected to Earthquake Loads”, MSc dissertation, University of Puerto Rico at Mayaguez.

Yazgan, U. and Dazio, A. (2011), “Simulating Maximum and Residual Displacements of RC Structures: I. Accuracy”, Earthquake Spectra 27(4), 1187-1202.

CHAPTER IV

4. DAMAGE DETECTION USING THE UCSD COLUMN EXPERIMENTAL AND SIMULATED DATA

4.1. Introduction

Using the available experimental data and the simulated data generated in Chapter III by developing nonlinear FE models for the UCSD bridge column, a complete damage detection analysis is performed in this chapter. Wavelet-based time-frequency and signal processing based system identification analyses are performed based on the methodologies previously described in Chapter II. In this particular case, the experimental acceleration and displacements responses are available. However, the aforementioned damage detection methodologies are applied to the acceleration response only. The displacement data is used to compute the displacement ductilities for a better understanding and explanation of the analyses results.

This chapter is organized in two parts. First, wavelet-based analyses (i.e., CWT and DWT analysis) at low and high frequencies are performed for each ground motion using the experimental response, the simulated response using the modified Takeda model, and the simulated data using the fiber-based model. Second, system identification analyses using two approaches (i.e., RDT in combination with HT and CWT) are performed using the experimental response. In addition, a damage index is computed based on experimental observations and using some results from the fiber-based model.

4.2. Wavelet-Based Time-Frequency Analysis

Before applying the wavelet procedures previously described in section 2.2, it is important to have a preliminary idea of the characteristics of the signal being analyzed, for SHM purposes knowing the range of structural frequencies is desired. In this particular case, the first natural frequency of the column at each load stage can be identified from the Fourier spectrum of the column acceleration response to the white noise (WN) excitations performed in-between

earthquake loads. Figure 4-1 shows the Fourier spectra for the response to the WN excitations applied before EQ1 and after EQ8. The frequency shift in the column vibration frequency due to induced levels of damage is quite evident (from 1.1 Hz for the pristine column, to 0.44Hz to the column near to collapse).

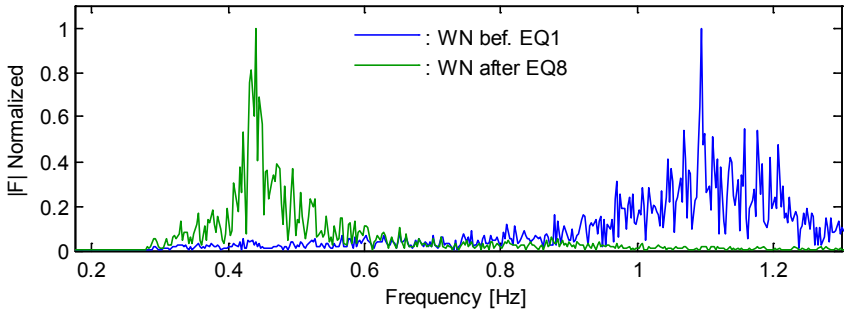

Figure 4-1: Normalized Fourier spectra of the column acceleration response to low amplitude WN excitations before EQ1 was applied and after EQ8 was applied

Figure 4-2 summarizes the results obtained for each load stage and includes the results obtained from the numerical models. It is seen that while there are some differences in the frequency values calculated from the recorded accelerations and the frequency values obtained from the simulated accelerations using both numerical models, the frequency shift pattern is the same: the largest frequency shifts occurred at the beginning of the sequential loads when the first inelastic excursions occur in the column (EQ2 and EQ3). After this point the reduction in the frequency of vibration is less noticeable, independent of the increasing values of inelastic demand and induced damage.

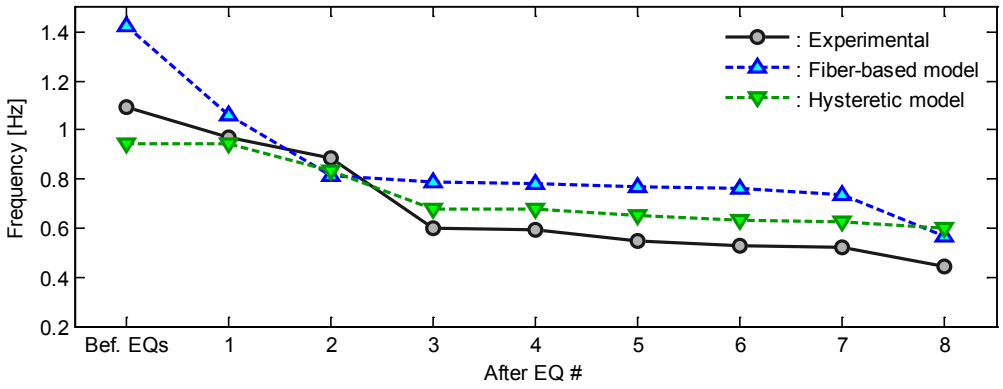

Figure 4-2: Summary of the identified first column frequencies at each load stage

4.2.1. Low frequency analysis (CWT)

Based on the identified range of structural frequencies, the parameters f_c and f_b required to define the modified Morlet wavelet were defined as 1 and 2, respectively. Figure 4-3 (thick line) shows the time and frequency resolutions for the CWT analysis on the frequency range of interest.

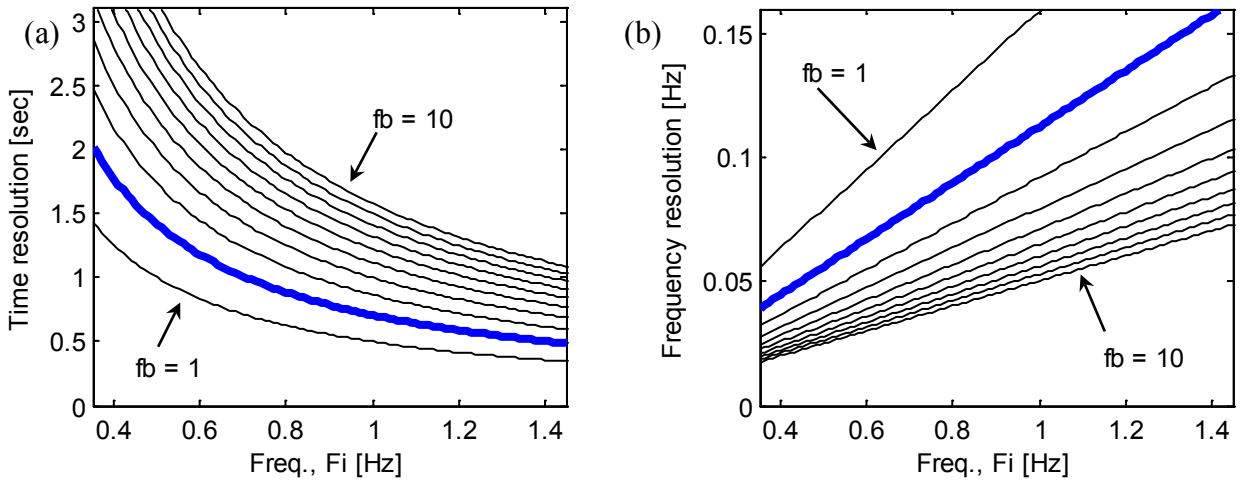

Figure 4-3: (a) Time and (b) frequency resolutions for the modified Morlet Wavelet for different values of f_b and using $f_c = 1$

The CWT results for the experimental data, modified Takeda and fiber based model are displayed in Figure 4-4 to Figure 4-9. Dotted lines on the sides of the figures denote the edge-effects zone (Equation (2-5)). The horizontal thick continuous lines denote the target frequency values at the beginning and end of the motion. For the experimental results the frequencies were obtained from a Fourier analysis and for the simulated results the frequencies were determined from an eigenvalue analysis with the FE models. In those cases where only one line appears, it is because the frequency shift was minimum and the two lines cannot be distinguished. The darker colors in the images indicate higher values of the wavelet coefficients and are an indicator of the frequency content of the signal at any time instant. A more precise estimation of the instantaneous dominant frequencies can be obtained by identifying a ridge in the time-frequency plane. In this work, the instantaneous dominant frequencies (wavelet ridges) were obtained by locating the local maxima at each time instant (continuous thin gray line). As expected, the identified ridges tend to be unstable close to the end regions, which is a reflection of the poor

quality of the wavelet coefficients in this zone. A smoothed version of the identified ridges obtained by applying a 1-second window running average is also displayed in these figures (dashed blue lines).

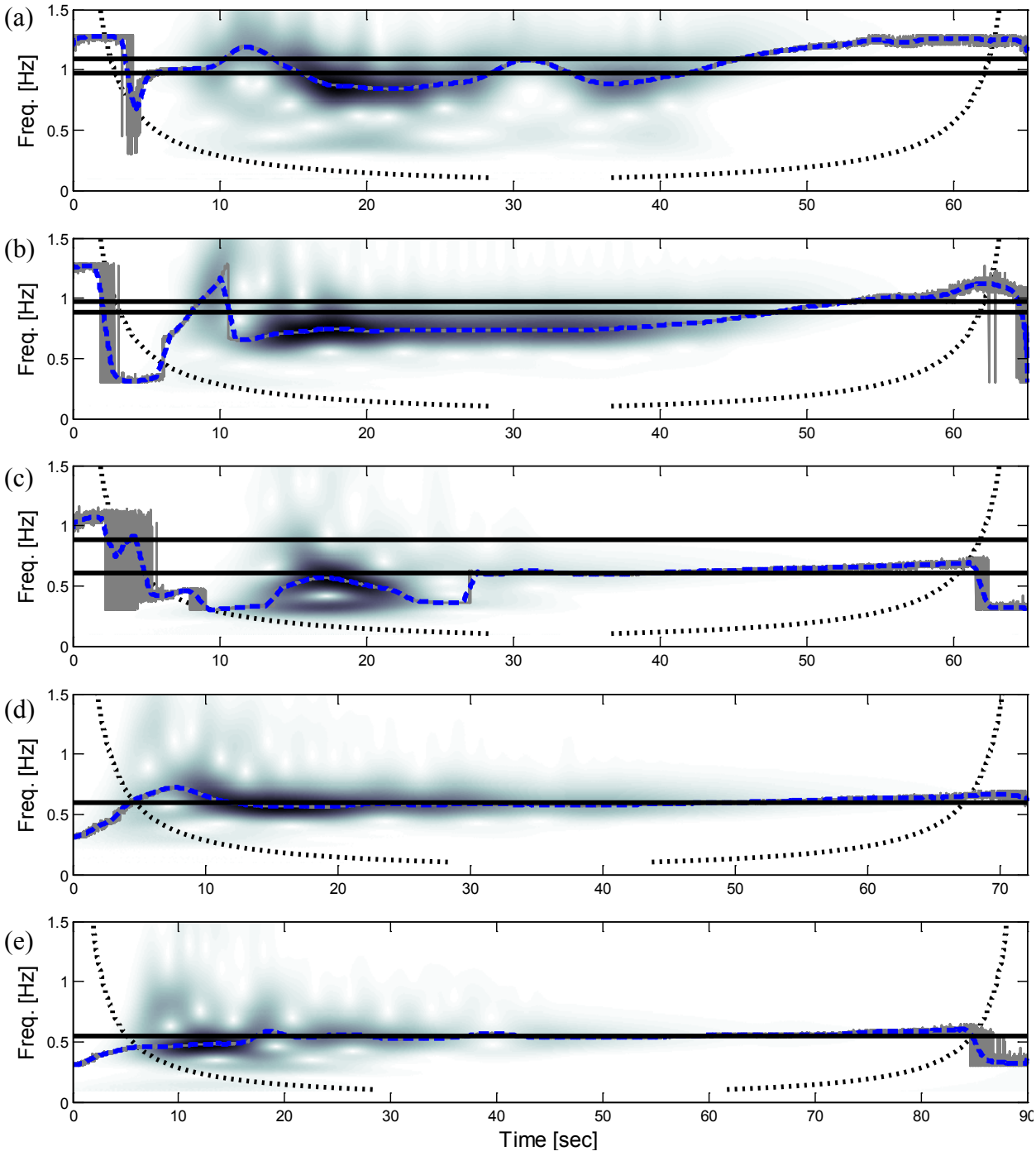

Figure 4-4: Low frequency CWT analysis results for the recorded column accelerations for (a) EQ1, (b) EQ2, (c) EQ3, (d) EQ4, and (e) EQ5

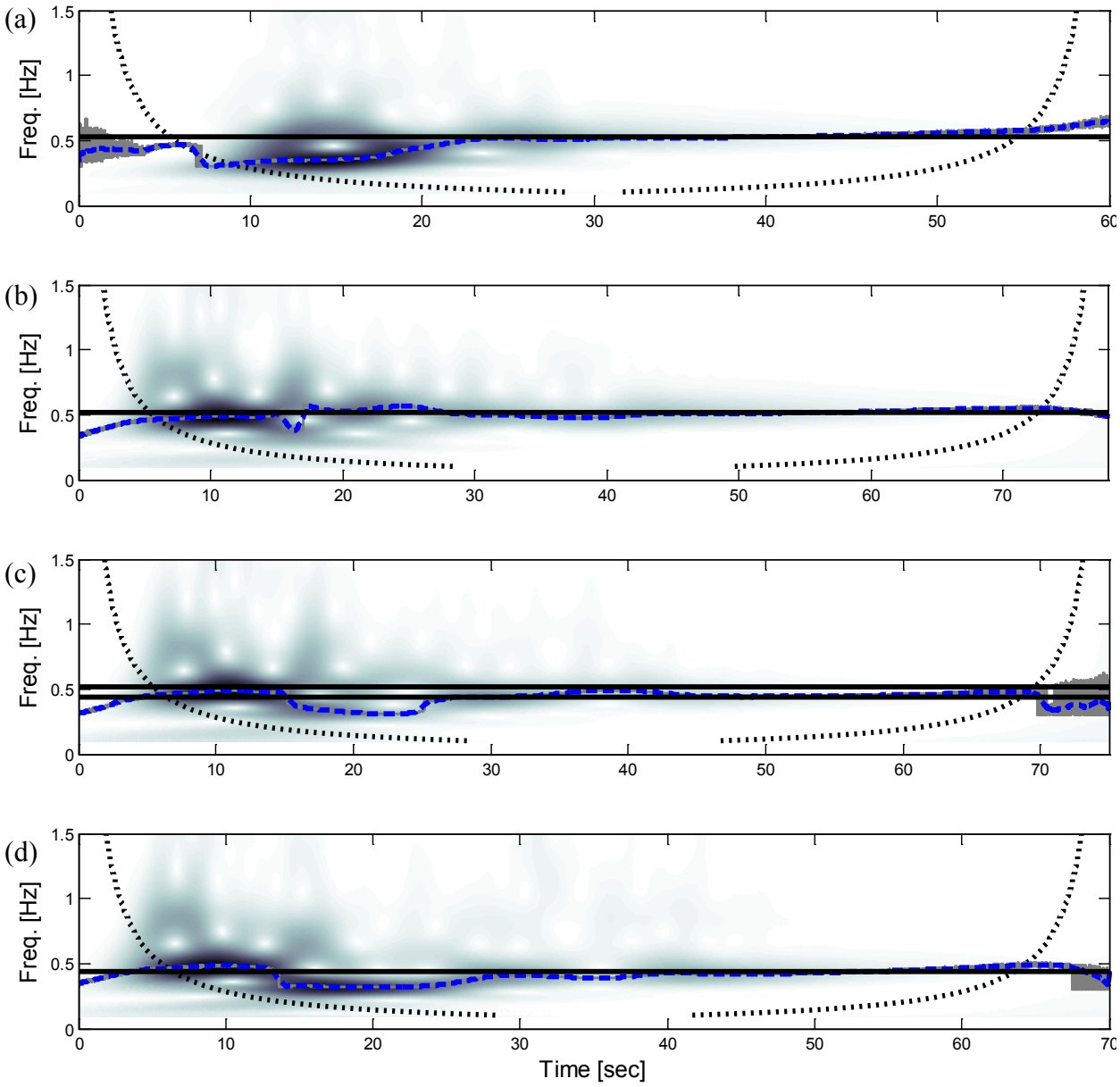

Figure 4-5: Low frequency CWT analysis results for the recorded column accelerations for (a) EQ6, (b) EQ7, (c) EQ8, and (d) EQ9

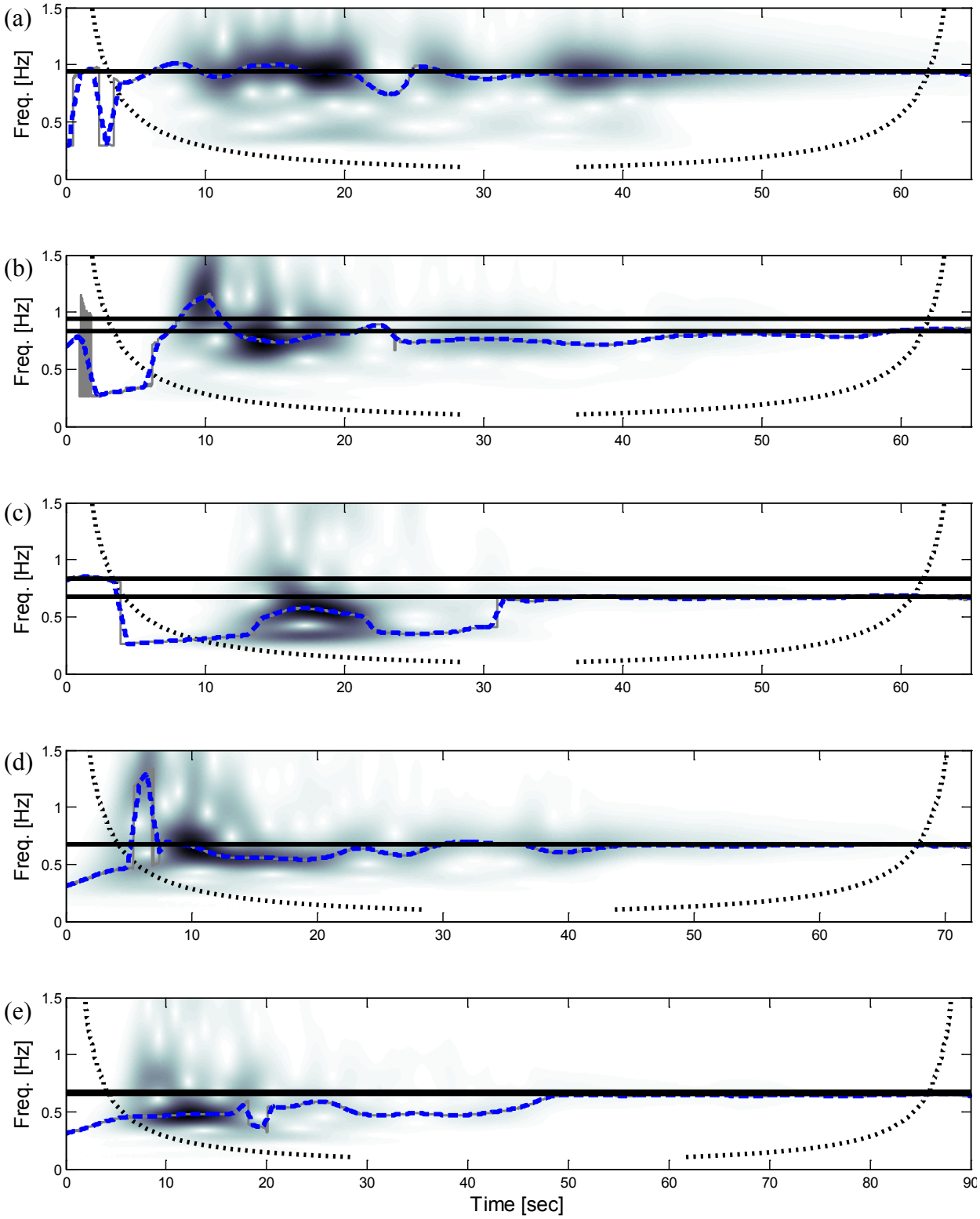

Figure 4-6: Low frequency CWT analysis results for the simulated column accelerations using the modified Takeda model for (a) EQ1, (b) EQ2, (c) EQ3, (d) EQ4, and (e) EQ5

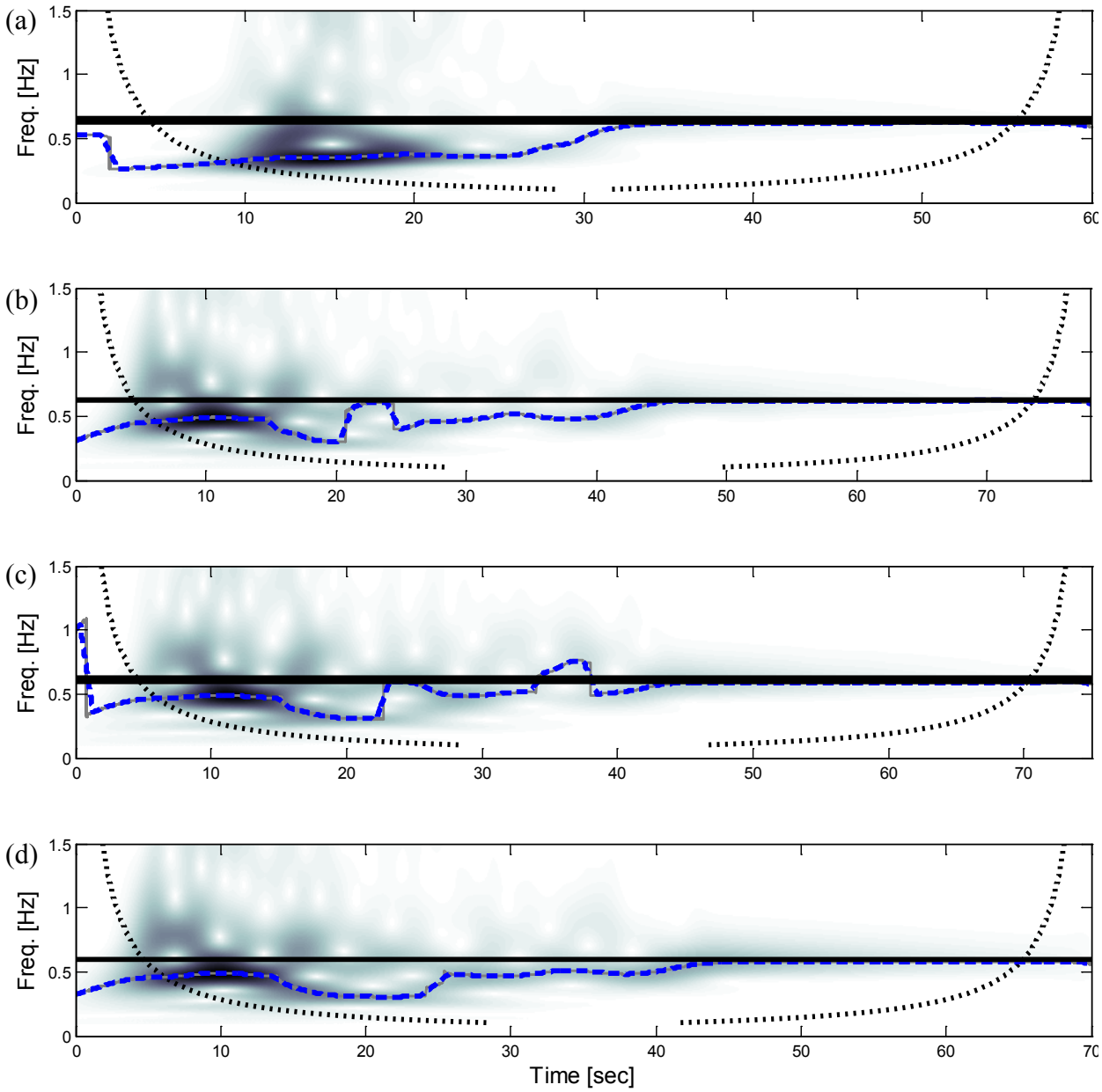

Figure 4-7: Low frequency CWT analysis results for the simulated column accelerations using the modified Takeda model for (a) EQ6, (b) EQ7, (c) EQ8, and (d) EQ9

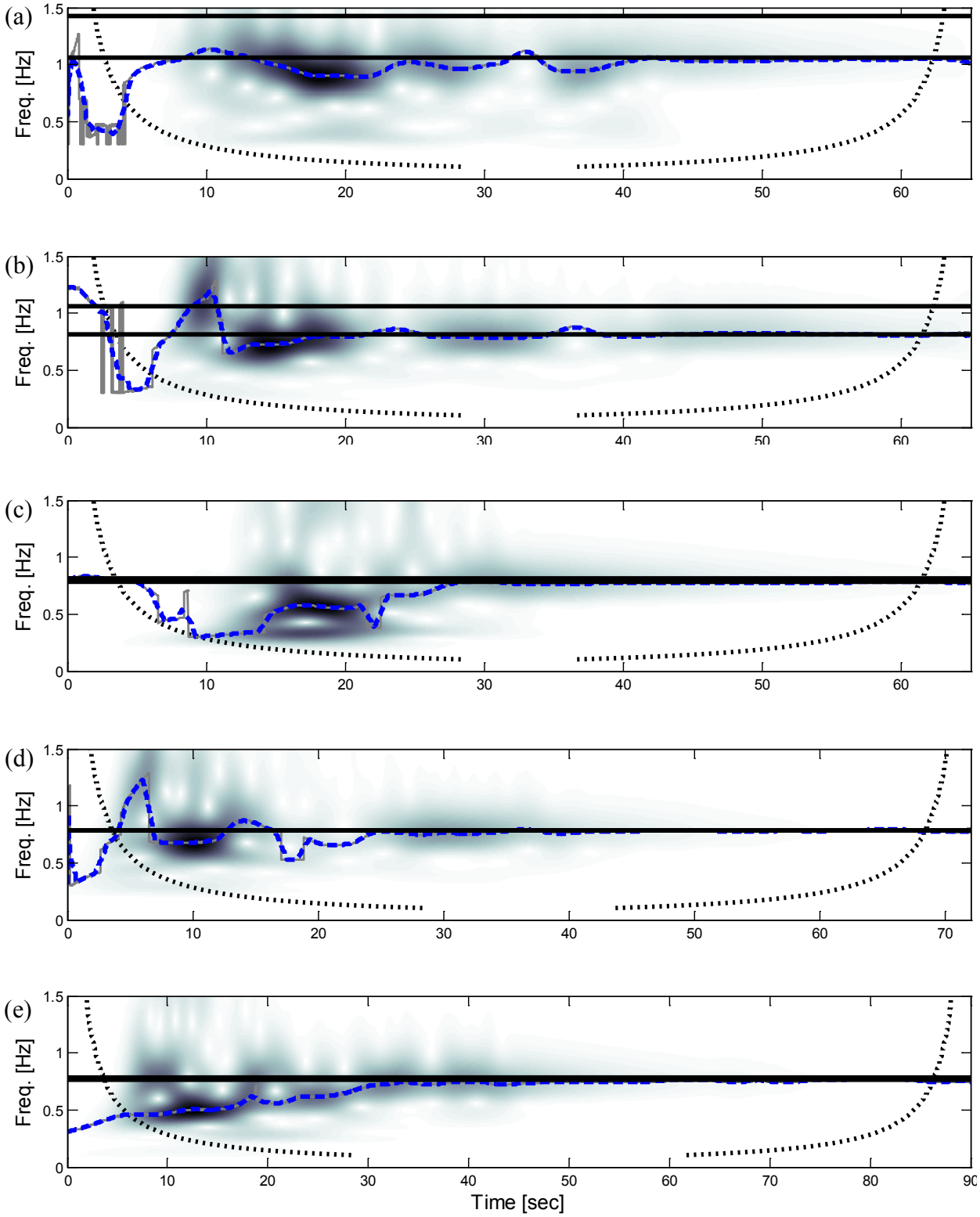

Figure 4-8: Low frequency CWT analysis results for the simulated column accelerations using the fiber-based model for (a) EQ1, (b) EQ2, (c) EQ3, (d) EQ4, and (e) EQ5

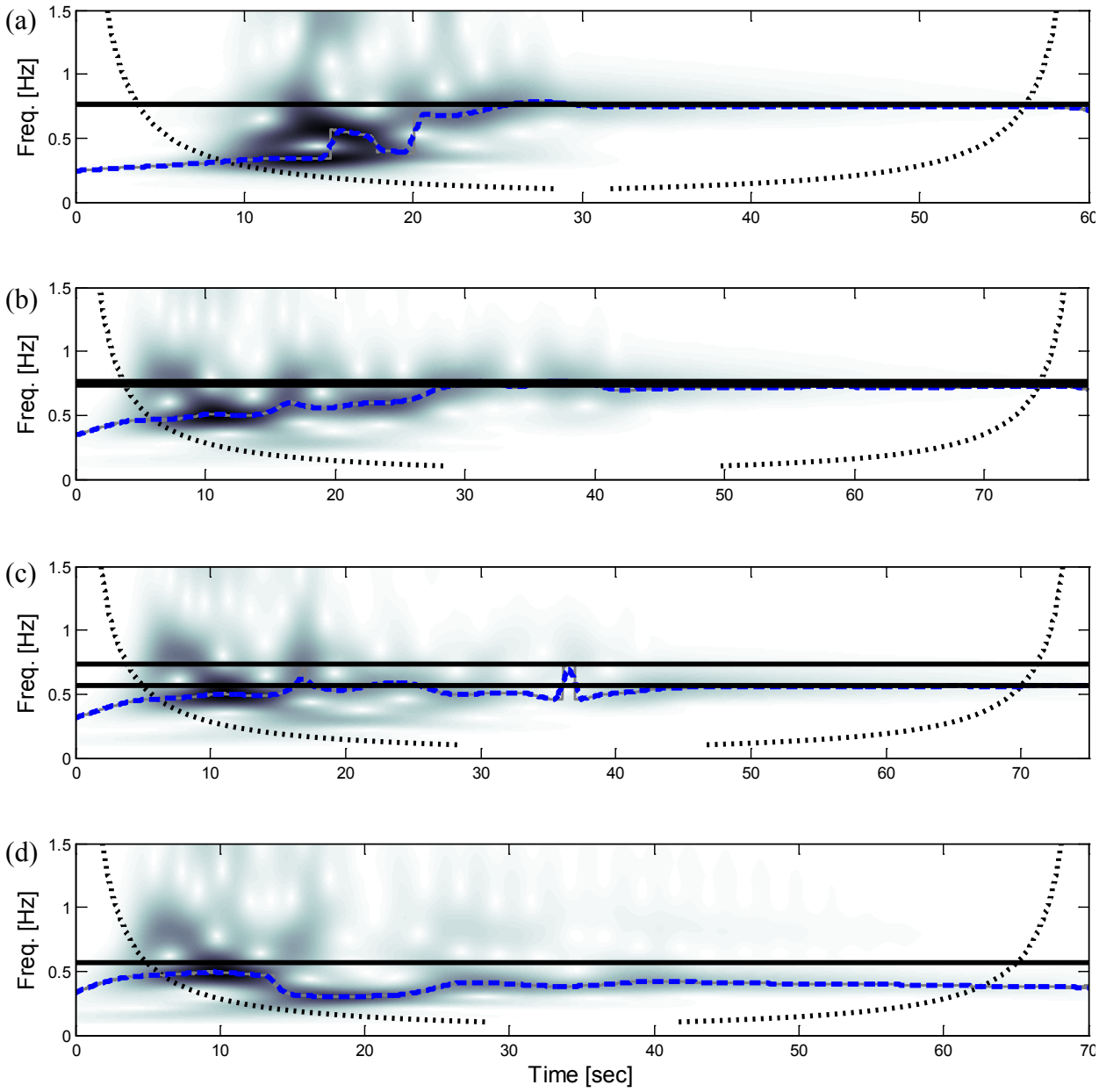

Figure 4-9: Low frequency CWT analysis results for the simulated column accelerations using the fiber-based model for (a) EQ6, (b) EQ7, (c) EQ8, and (d) EQ9

In general for all three scenarios (experimental and the two numerical models) the identified variation patterns in the column vibration frequency are quite similar. While this is encouraging in regards to the use of numerical models for validation and/or calibration of this type of damage detection methodologies, it also exposes a serious limitation of the method when the structure is subjected to earthquake loads. It is seen that for most cases the structure frequency at the end of the motion is successfully identified; however, identification of the initial

frequency is not that evident. Furthermore, there are time instants where the identified frequency drops substantially below the final target frequency, see for example the results for EQ3 in Figure 4-4c. A more detailed analysis of this case is presented in Figure 4-10, where only the first 40 seconds of the analysis are displayed along with CWT results for the shaking table accelerations (bottom figure). Notice that the dominant frequencies distribution between 10 and 25 seconds (i.e. the strong motion part of the load, see Figure 3-22) are strongly related. That is, at these instants the structure is responding in tune with one of the dominant frequencies in the excitation load and the observed frequency shift is not necessarily related to stiffness degradation in the structure.

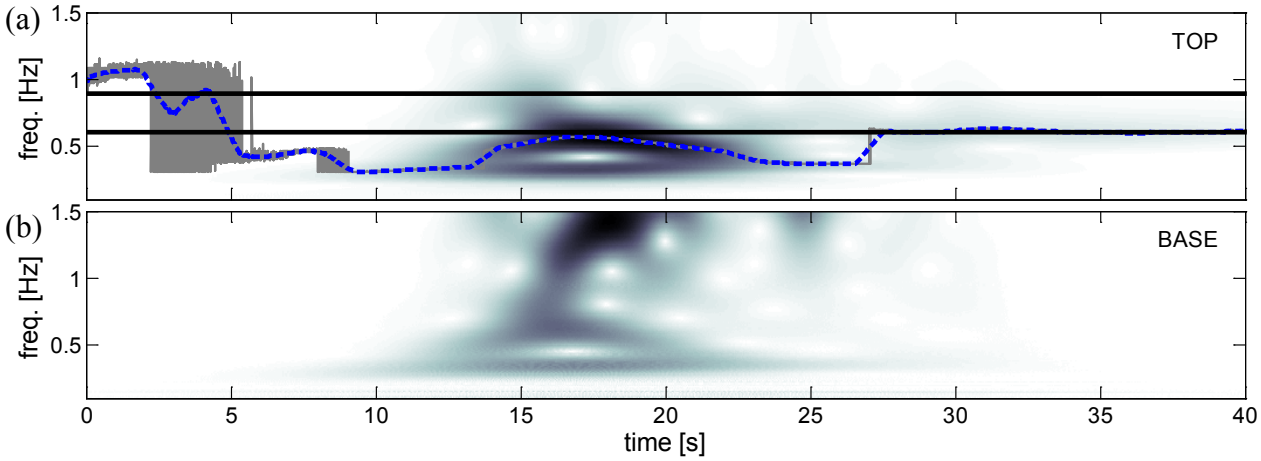

Figure 4-10: Low frequency CWT analysis results (first 40 seconds only) for the recorded column accelerations for EQ3 at (a) the column top and (b) shaking table. Notice input signal frequency interference in the identification of the column instant frequency

Notice that the same trend was captured by the modified Takeda and fiber based models (EQ3: Figure 4-6c and Figure 4-8c). Such phenomenon is more likely to occur if the frequency content of the input load is within the range of the structural frequencies. Figure 4-11, for example, shows the results obtained when the fiber based model is subjected to a modified version of EQ3 where the frequencies below 1.8 HZ have been removed (the motion was also amplified to 1.5g to increase the level of inelastic demand and was applied to the pristine structure). It is seen that in this case the identified structural frequency is not influenced by the dominant frequencies of the base motion and the observed frequency shift can be certainly

related to increasing levels of inelastic demand causing stiffness degradation (the sudden drop to 0.4Hz around 5 seconds should be disregarded as it is within the end-effect region).

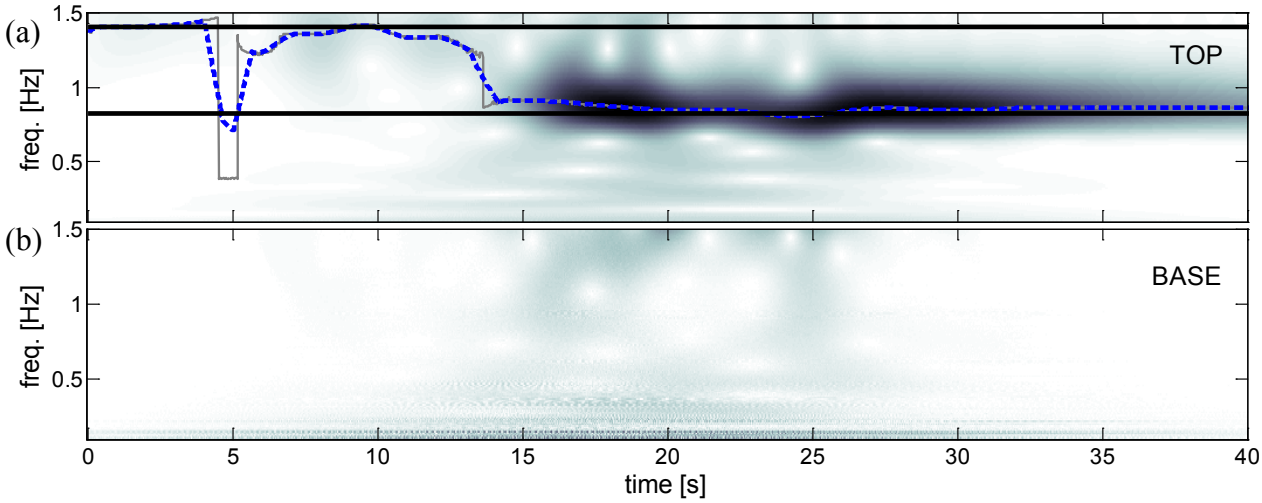

Figure 4-11: Low frequency CWT analysis results (first 40 seconds only) for the simulated response using the fibers based model EQ3 filtered to remove frequencies lower than 1.8 Hz and scaled to 1.5g

4.2.2. High frequency analysis (DWT)

Once the signal is processed via FWT, a number of spikes will appear in the detail functions. To avoid the identification of spurious spikes, a threshold criterion is adopted. First, the details (D) are normalized at each time instant (i) according to the rule:

$$z_i = \frac{D_i - \mu}{\sigma} \tag{4-1}$$

where μ and σ are the mean and standard deviation of the detail values, respectively. The normalized absolute values of the detail functions from the experimental, modified Takeda and fiber based model column accelerations are displayed in Figure 4-12 to Figure 4-17. Any instant (i) where the normalized absolute value (z) is larger than 6, i.e. where the normalized details with absolute amplitude deviates more than 6 standard deviations (horizontal thick blue line) from the mean value, is treated as a damage instant. The confidence level using a threshold at z=6 is 99.99%. This value was determined by inspection of the results obtained. It should be noticed

that past research has used a threshold value of 2 when working with simulated data from simplified models subjected to elastic damage (Montejo, 2011). The increase in this value is a direct reflection of the more realistic and complex nature of the data being analyzed.

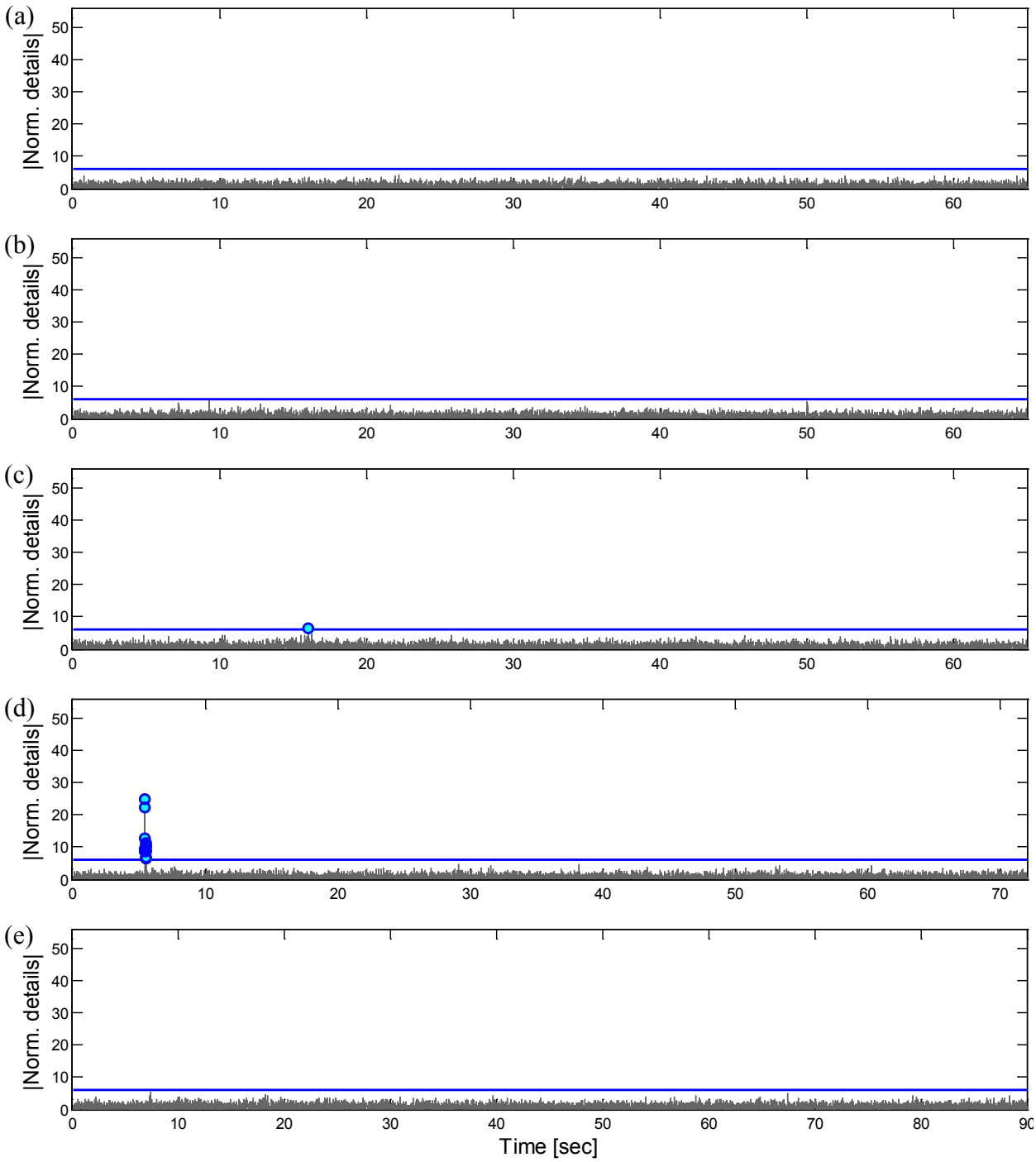

Figure 4-12: DWT analysis results (normalized detail functions) for the recorded column accelerations for (a) EQ1, (b) EQ2, (c) EQ3, (d) EQ4, and (e) EQ5

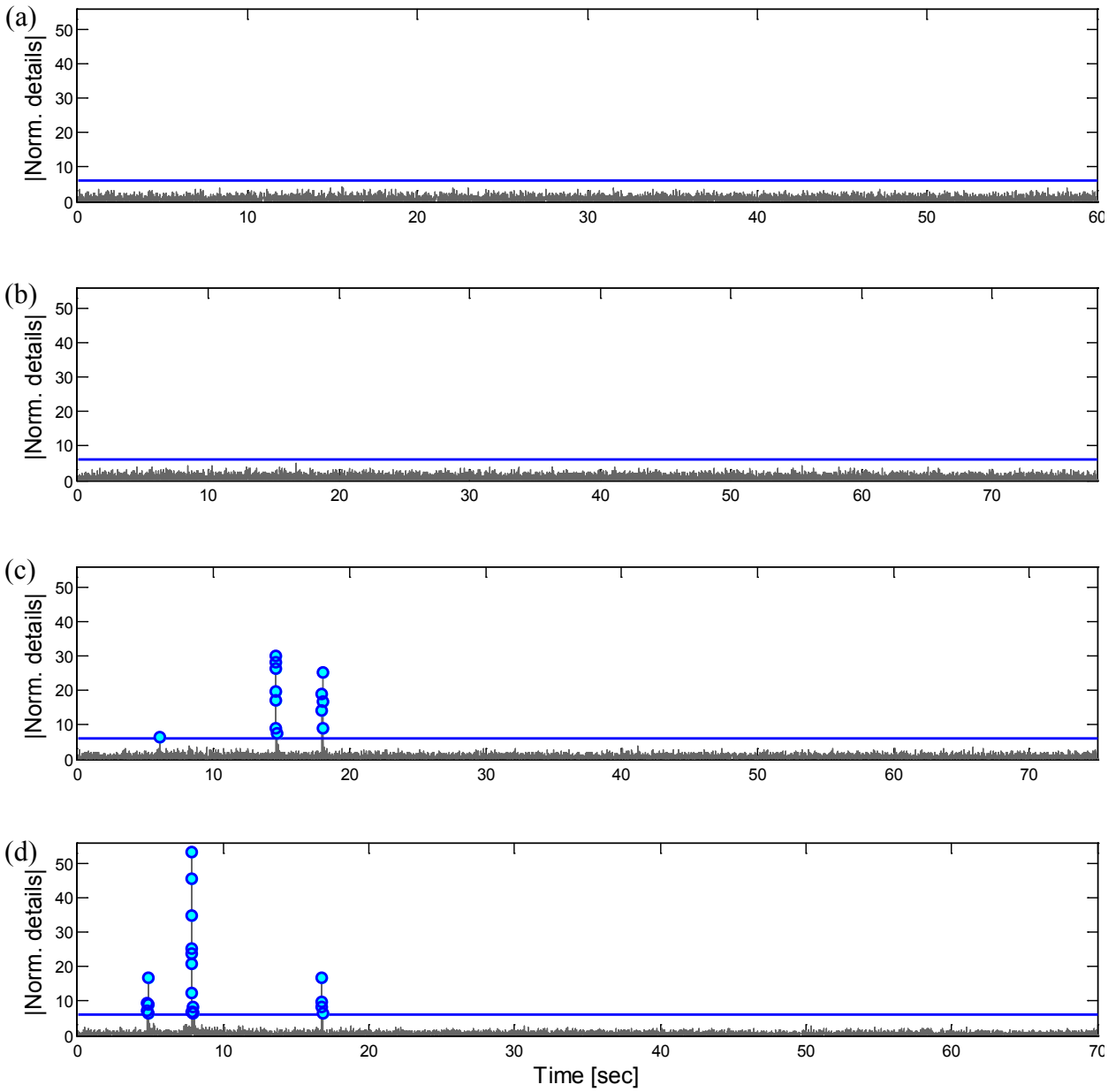

Figure 4-13: DWT analysis results (normalized detail functions) for the recorded column accelerations for (a) EQ6, (b) EQ7, (c) EQ8, and (d) EQ9

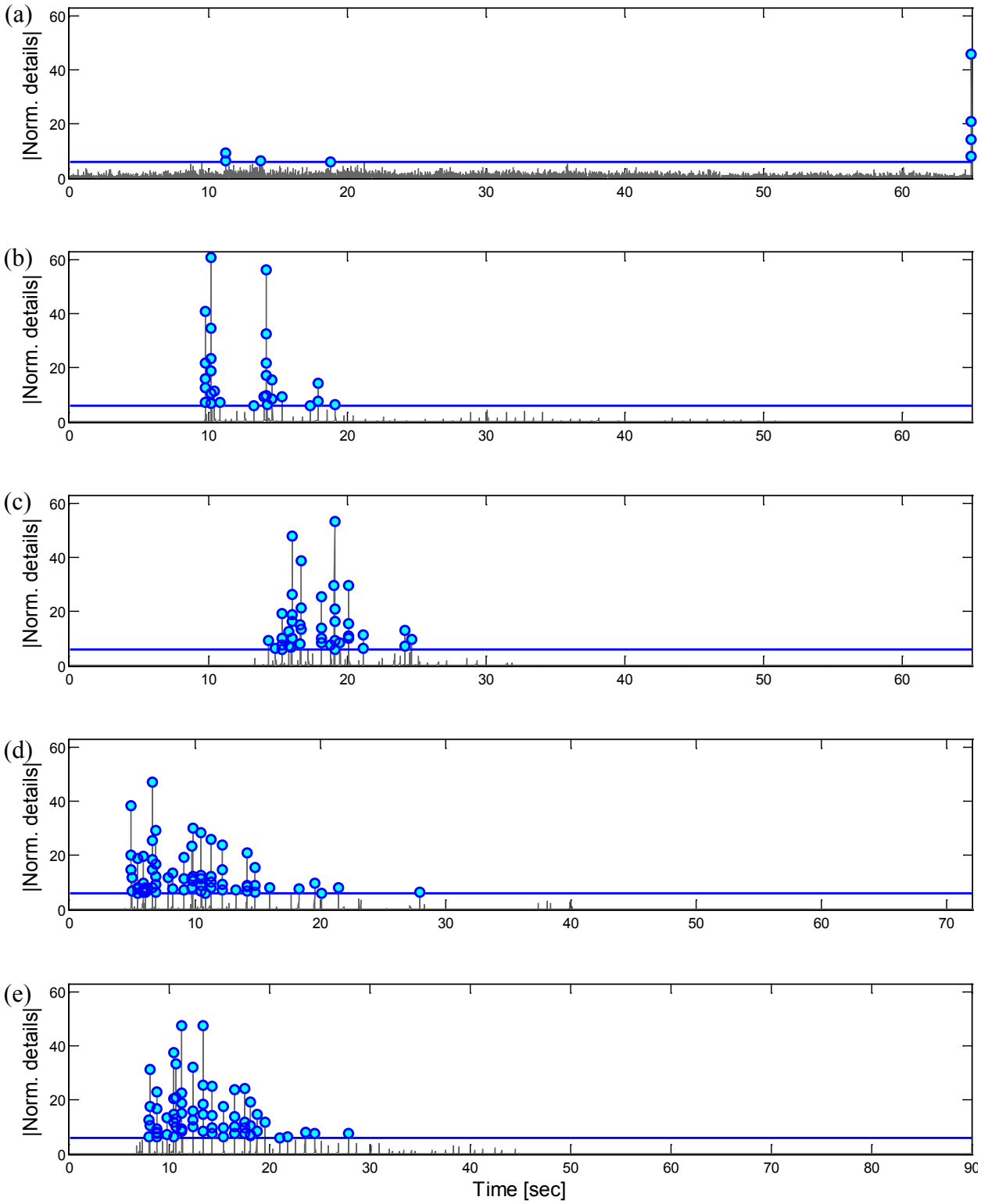

Figure 4-14: DWT analysis results (normalized detail functions) for the simulated column accelerations using the modified Takeda model for (a) EQ1, (b) EQ2, (c) EQ3, (d) EQ4, and (e) EQ5

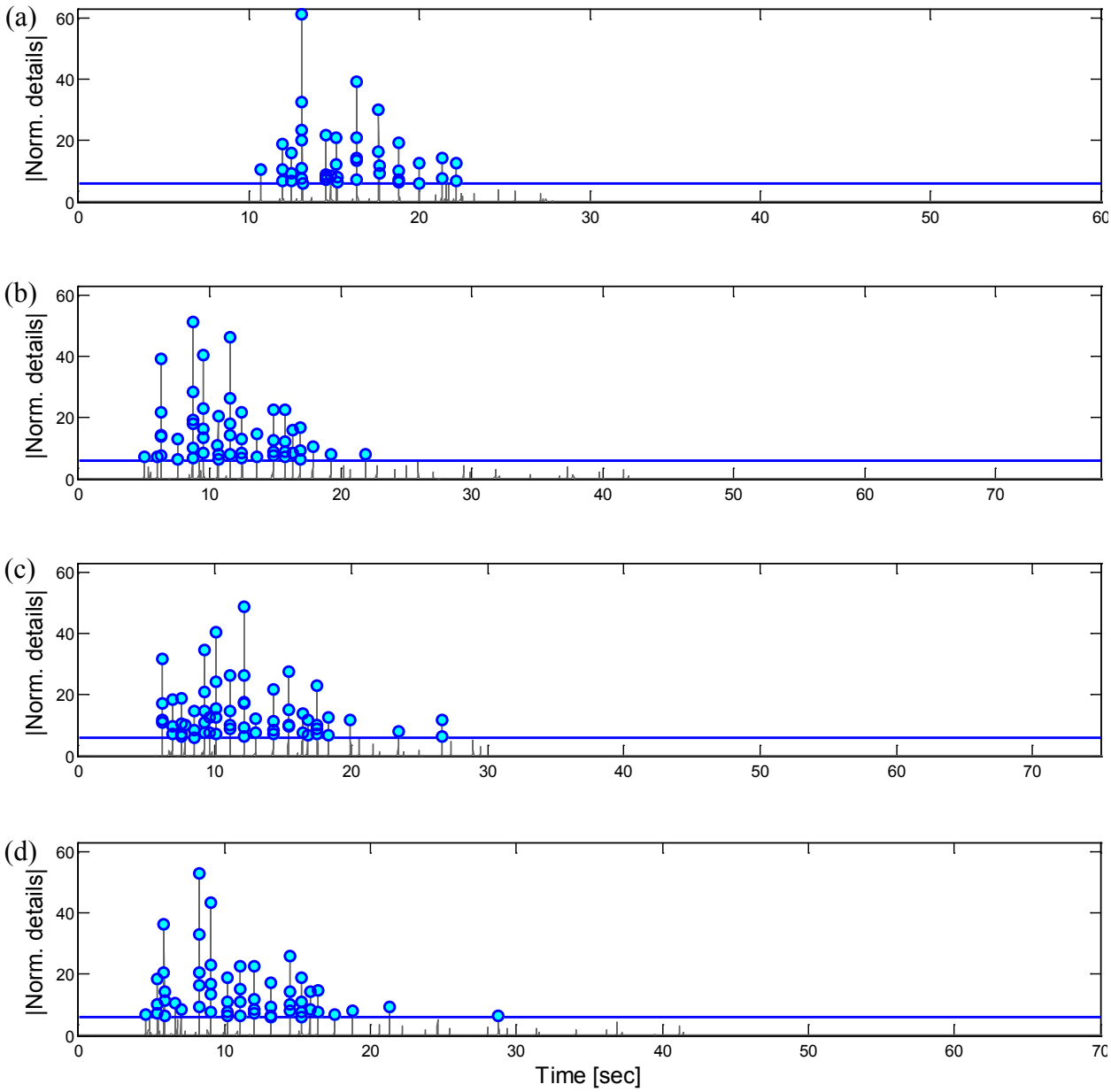

Figure 4-15: DWT analysis results (normalized detail functions) for the simulated column accelerations using the modified Takeda model for (a) EQ6, (b) EQ7, (c) EQ8, and (d) EQ9

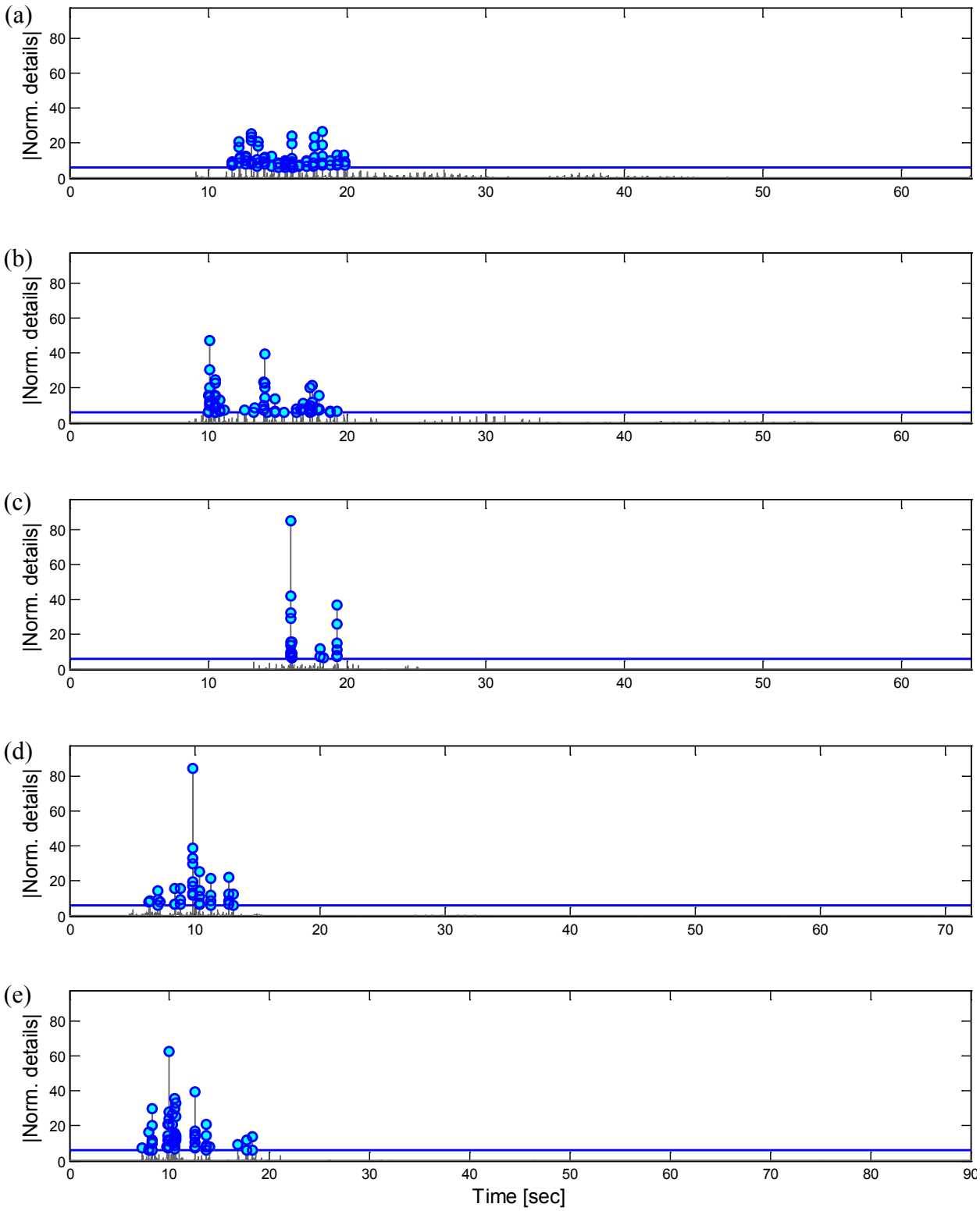

Figure 4-16: DWT analysis results (normalized detail functions) for the simulated column accelerations using the fiber-based model for (a) EQ1, (b) EQ2, (c) EQ3, (d) EQ4, and (e) EQ5

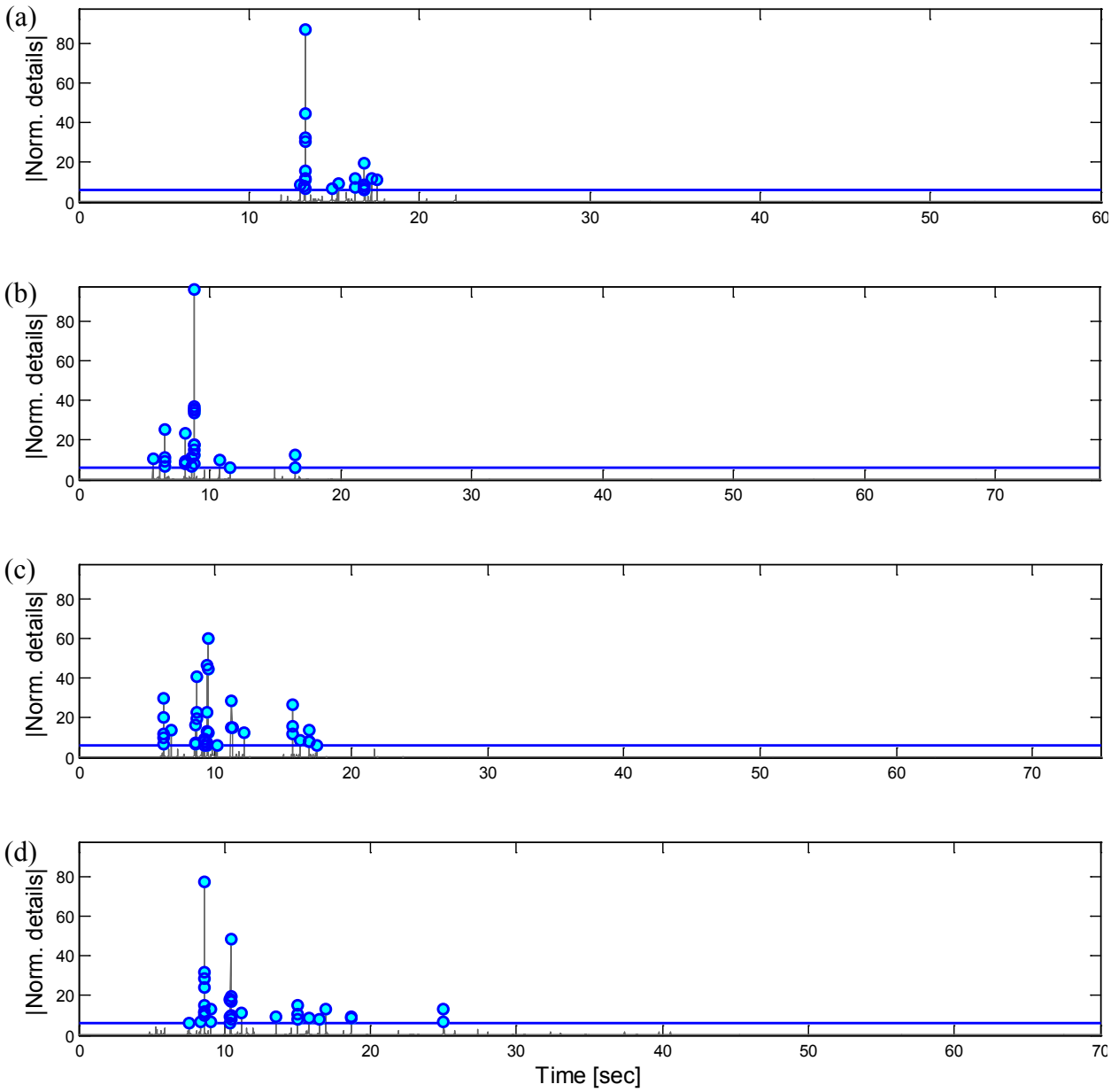

Figure 4-17: DWT analysis results (normalized detail functions) for the simulated column accelerations using the fiber-based model for (a) EQ6, (b) EQ7, (c) EQ8, and (d) EQ9

It is seen that the results obtained differ significantly within the 3 different scenarios (experimental data and the two numerical models). Moreover, the results obtained for the modified Takeda model exhibit the larger number of irregularities detected (Figure 4-14 and Figure 4-15), followed by the fiber based model (Figure 4-16 and Figure 4-17). In the results from the experimental accelerations (Figure 4-12 and Figure 4-13) only few irregularities were

identified. During EQ1 no irregularities were detected from the experimental data: this was expected since the column remained within the elastic range during this load (Figure 4-12a). In spite of a low normalized amplitude, a number of spikes were identified from the results of the numerical models. As it will be explained from the results of EQ3, these spikes are likely to arise from limitations in the numerical models rather than from actual induced damage.

The first irregularity detected from the experimental data occurred during EQ3 (Figure 4-12c). Figure 4-18 presents a more detailed analysis of these results, the detail functions are shown along with the displacement ductility time history and the column hysteretic response in terms of absolute acceleration vs. displacement ductility (since the structure response is highly dominated by its first mode, this plot is strongly correlated with the column force-displacement hysteretic response). It is seen that the irregularity detected coincides with the first large excursion of the column into the inelastic range; however, further inelastic excursions occurring during the same earthquake load are not detected.

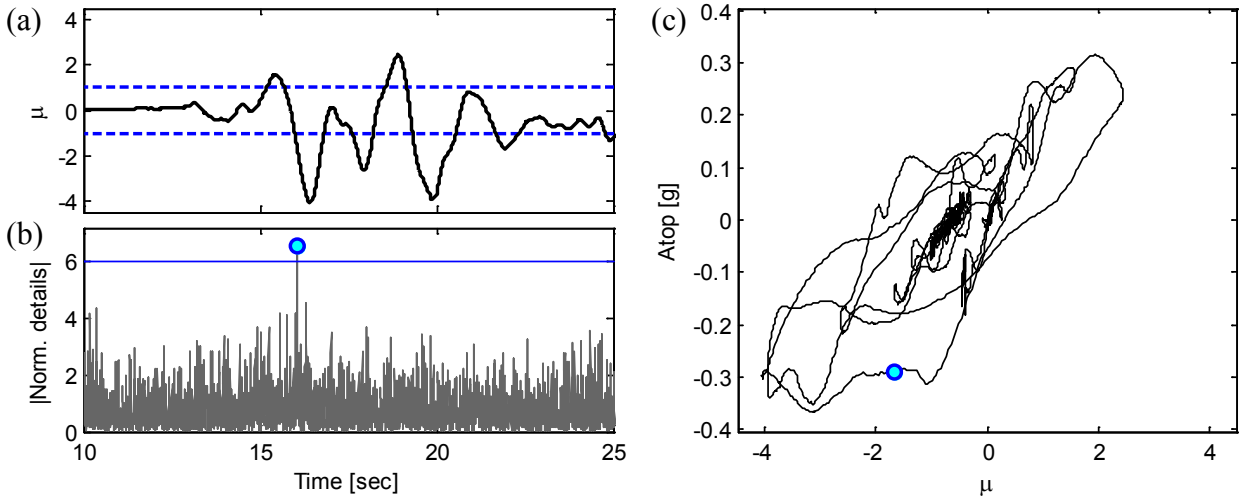

Figure 4-18: DWT analysis of the experimental results for EQ3: (a) time history of ductility demand, (b) detail function, and (c) column hysteretic response along with the location of the discontinuity detected

Figure 4-19 shows the same type of analysis, this time for the results obtained using the modified Takeda model. Note that while all of the inelastic excursions are identified, there are also a large number of irregularities that arise from the drastic change in stiffness occurring close to the static equilibrium point, i.e. the additional irregularities detected are proper of the

multilinear nature of the hysteresis rule used in the numerical model and not really related to induced damage in the column. The results obtained for the fiber based model during EQ3 (Figure 4-20) show that basically three irregularities instants were detected, with two of them clearly related to large inelastic excursions.

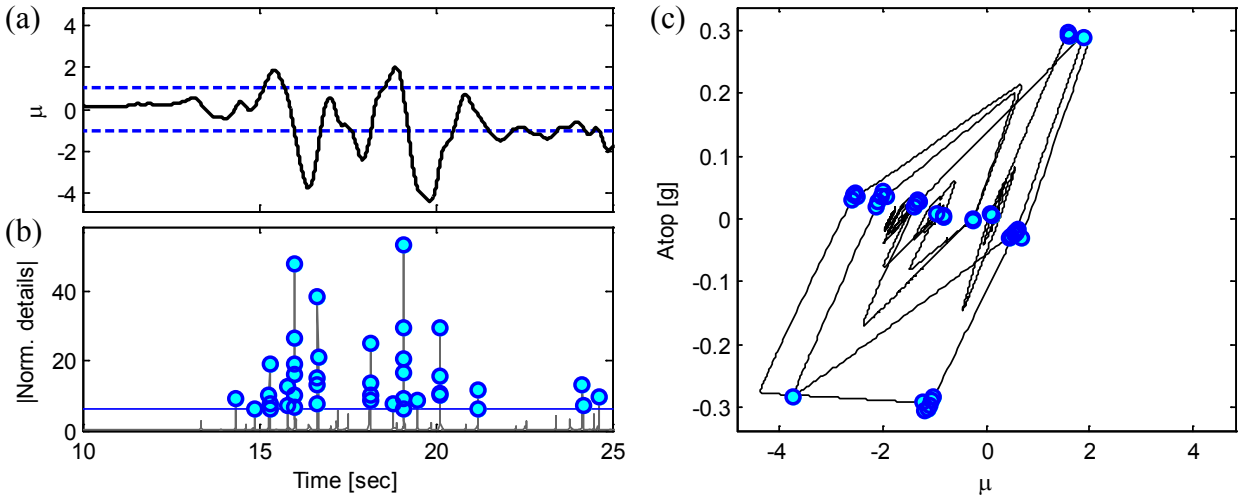

Figure 4-19: DWT analysis of the modified Takeda model results for EQ3: (a) time history of ductility demand, (b) detail function, and (c) column hysteretic response along with the location of the discontinuities detected

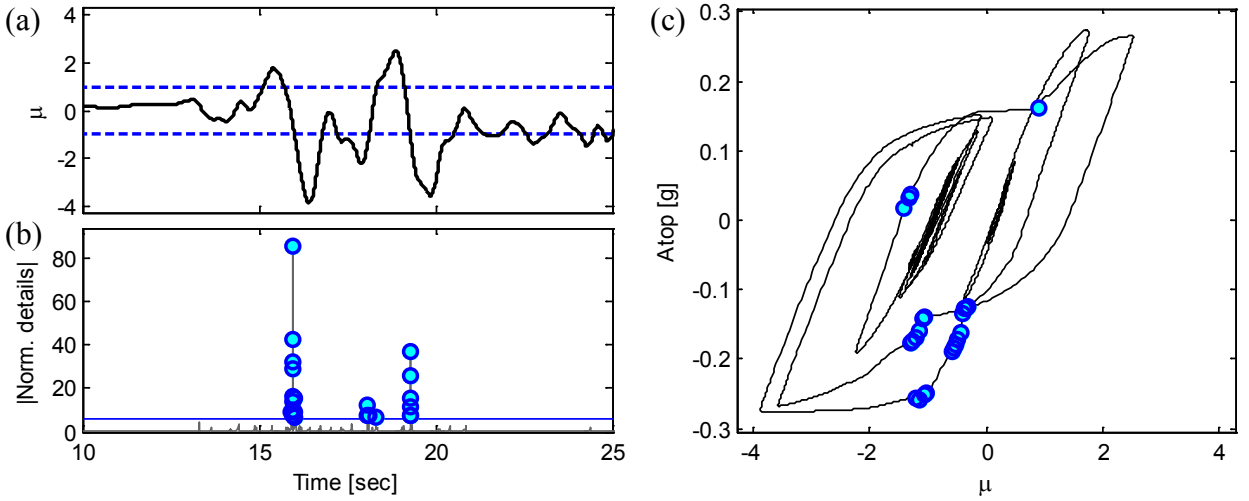

Figure 4-20: DWT analysis of the fiber-based model results for EQ3: (a) time history of ductility demand, (b) detail function, and (c) column hysteretic response along with the location of the discontinuities detected

No spikes were detected from the column experimental acceleration at EQ7 (Figure 4-13b), i.e. the occurrence of rebar buckling was not identified by this methodology. Although the results from the numerical models exhibit a number of spikes at EQ7 (Figure 4-15b and Figure 4-17b), these spikes are related to other phenomena, inelastic excursions or numerical spurious spikes, as the developed models do not allow for the modeling of rebar buckling.

Of special interest are the results obtained for EQ8 and EQ9 since during these motions two and three of the longitudinal bars fractured, respectively. From the results of EQ8 presented in Figure 4-13c, it is seen that two large spikes emerge in the detail function for this earthquake motion. Furthermore, notice that the normalized magnitudes of the spikes are about 4 times larger than the spike in EQ3 (related to the first large inelastic excursion of the column, Figure 4-12c), therefore it is inferred that each spike is pinpointing a rebar fracture episode. Analysis of the ductility demand time history and hysteresis response of the column for EQ8 (Figure 4-21) reveals that fracture of the longitudinal bars took place at 14.6 and 18 seconds at intermediate levels of ductility after the two large excursions at ~μ7 occurred. Analysis of the column accelerations during EQ9 (Figure 4-22) identified three rupture episodes at ~ 4.8, 7.8 and 16.8 seconds.

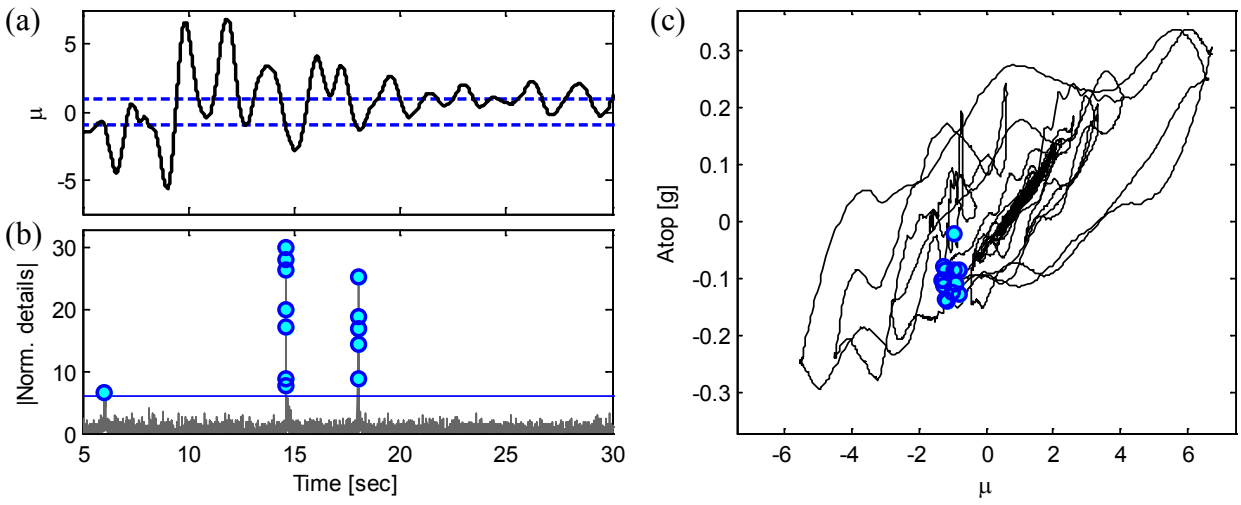

Figure 4-21: DWT analysis of the experimental results for EQ8: (a) time history of ductility demand, (b) detail function, and (c) column hysteretic response along with the location of the discontinuities detected

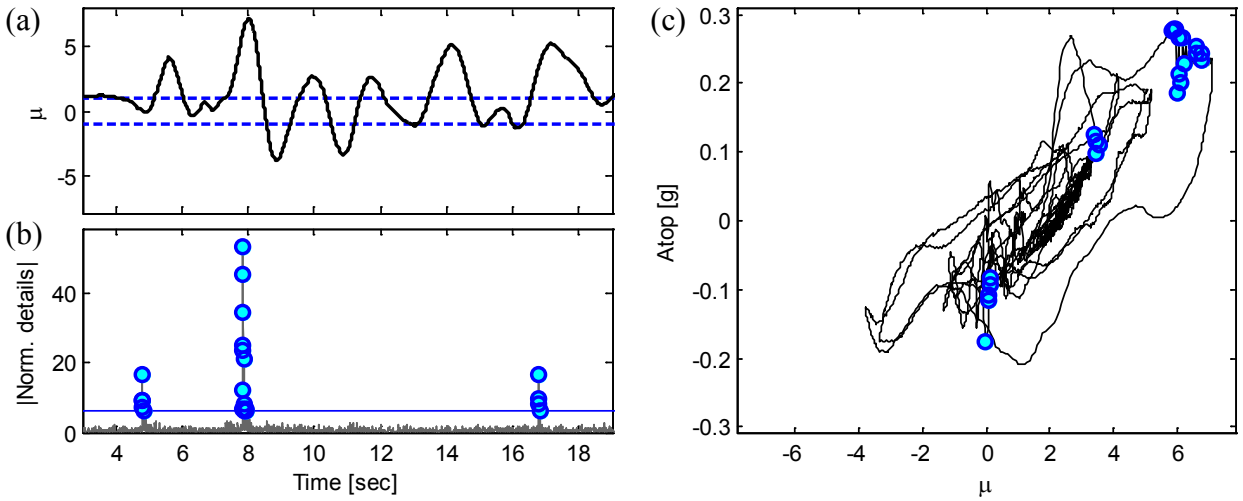

Figure 4-22: DWT analysis of the experimental results for EQ9: (a) time history of ductility demand, (b) detail function, and (c) column hysteretic response along with the location of the discontinuities detected

A detailed analysis of the EQ8 results obtained for the fiber model is presented in Figure 4-23. It is seen that all of the irregularities detected in the detail functions can be related to inelastic excursions in the column. To examine if the rebar fracture episodes were also identified, Figure 4-24 presents the stress time history for the first rebar that fracture during the simulation (at 12.5 seconds). This instant is also identified in the stress-strain plot and at the isolated hysteresis loop where the rebar fractured (dashed line). It is seen that the closest spike to the fracture instant is identifying the inelastic excursion rather than the rupture of the rebar. Note also from the hysteretic loop that the discontinuity in the simulated structural response, caused by the fracture of the rebar, is minimal when compared to the discontinuity in the experimental response (loop with solid line). By looking at the rebar stress history and stress-strain behavior it is noticed that once the rebar fractures the stress is quickly, but not drastically, driven to zero. Therefore, the immediate effect on the global structural response is reduced. The second fracture episode during the simulation was neither identified, as it occurred at 25.9 seconds and there were no spikes around this time. The results from the modified Takeda model for EQ8 are no further studied as this approach does not allow for modeling of the rebar fracture.

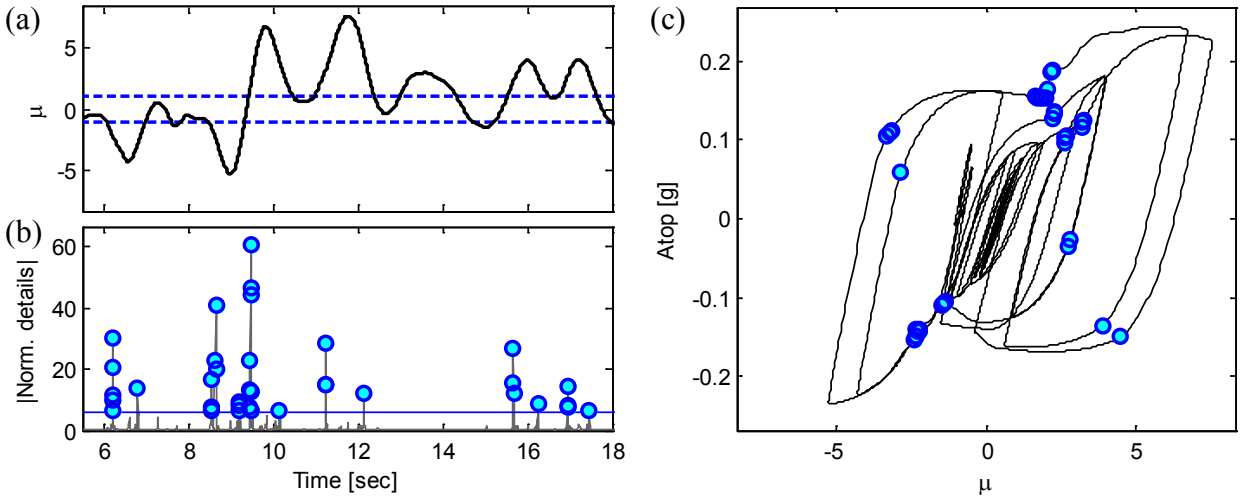

Figure 4-23: DWT analysis of the fiber-based model results for EQ8: (a) time history of ductility demand, (b) detail function, and (c) column hysteretic response along with the location of the discontinuities detected

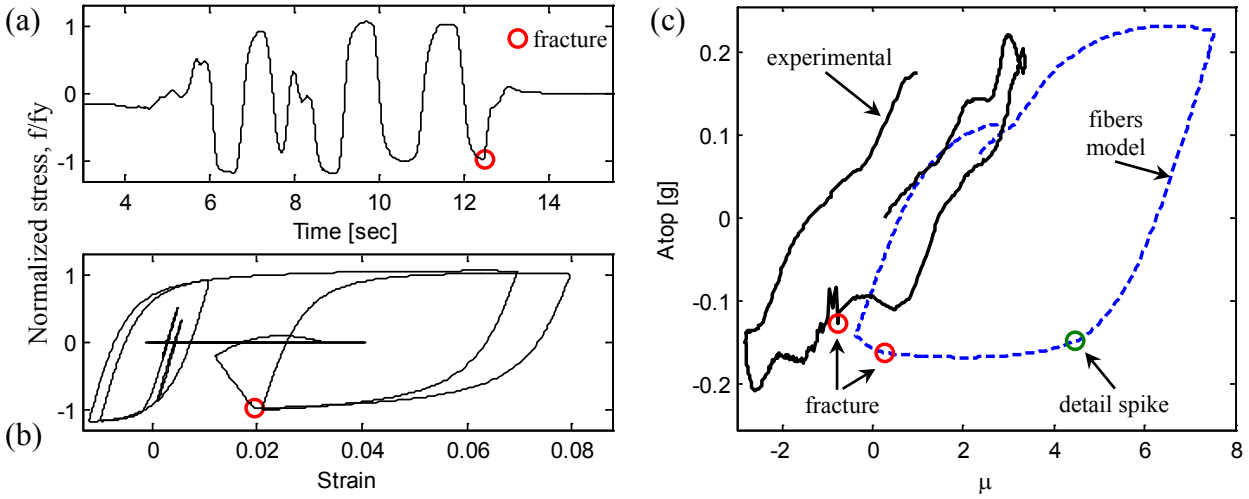

Figure 4-24: Detailed results for EQ8: (a) stress time history, (b) stress-strain relation from the fiber-based model, and (c) hysteresis loops where rebar fracture occurred

In an effort to improve the results obtained using the experimental column acceleration response, an alternative DWT analysis was explored. For this purpose, the first derivative of the acceleration signal (known as jerk) was computed using a backward numerical differentiation expressed mathematically as follows:

$$f'(a_i) = \frac{a_i - a_{i-1}}{t_i - t_{i-1}} \tag{4-2}$$

where $f'(a_i)$ is the first derivative of the acceleration (a) with respect to the time (t), at a time instant (i). a_{i-1} and t_{i-1} are the acceleration and time at the previous instant (i-1).

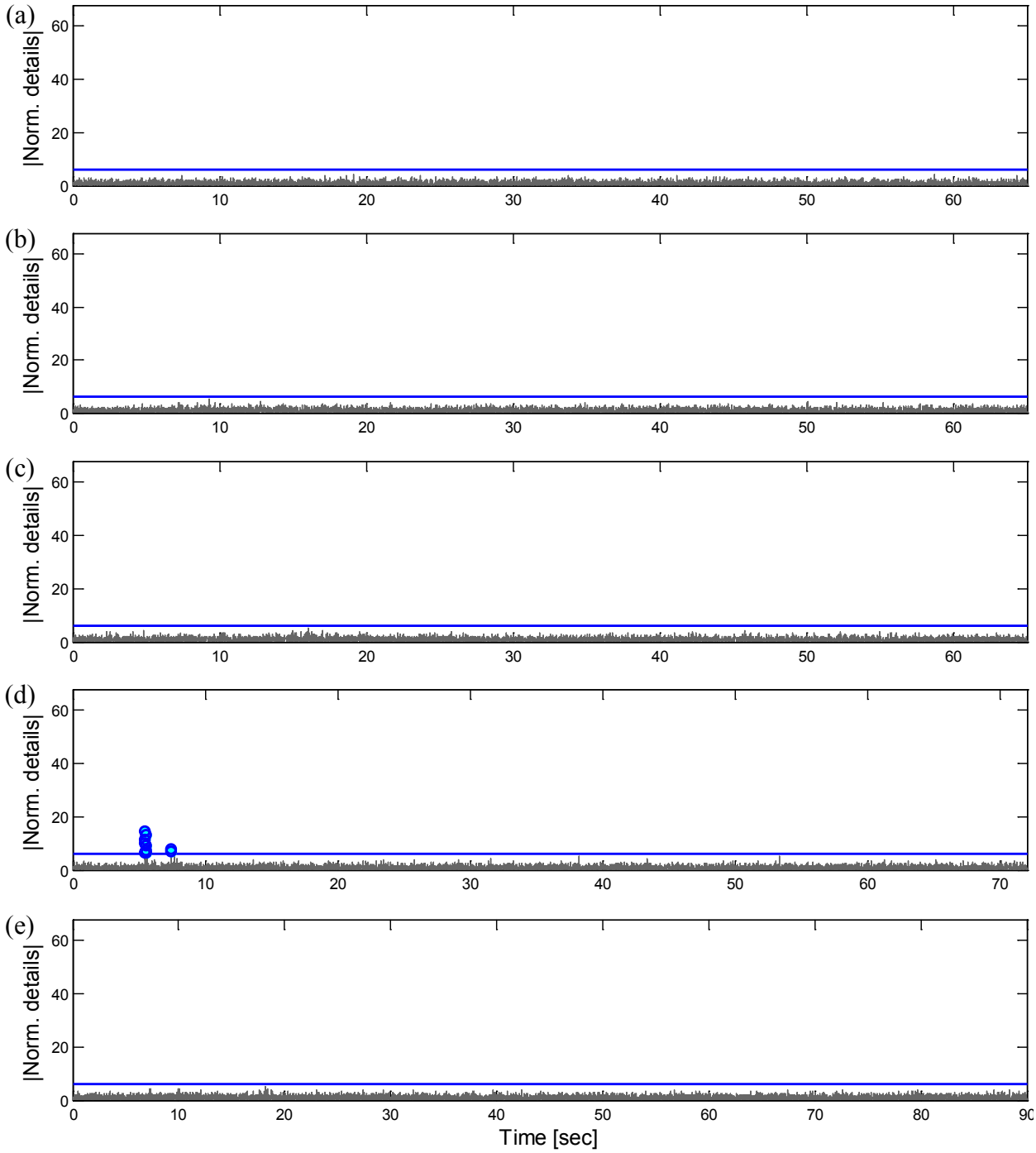

Figure 4-25: DWT analysis results (detail functions) for the experimental column jerk for (a) EQ1, (b) EQ2, (c) EQ3, (d) EQ4, and (e) EQ5

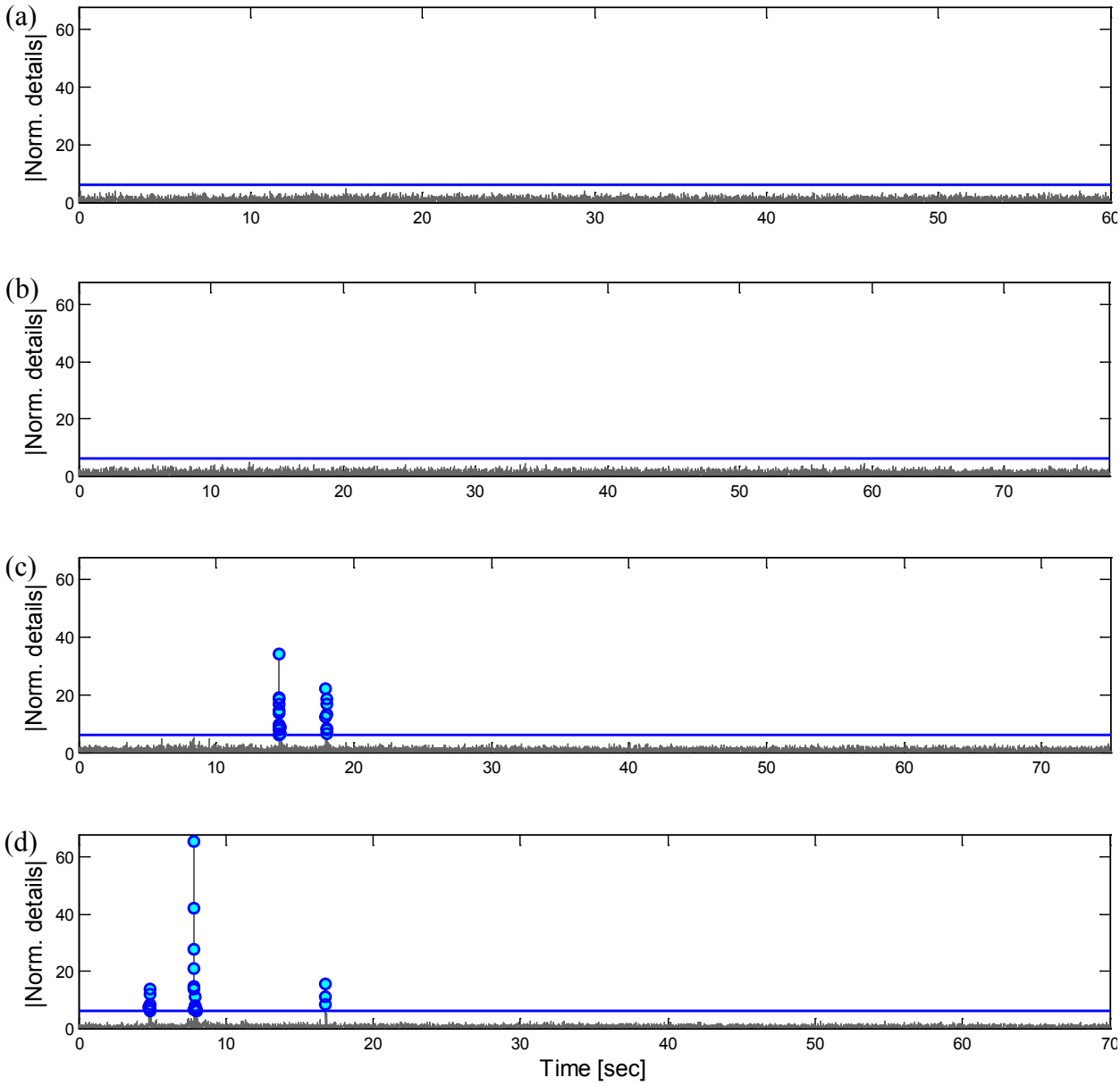

Figure 4-26: DWT analysis results (detail functions) for the experimental column jerk for (a) EQ6, (b) EQ7, (c) EQ8, and (d) EQ9

The normalized absolute values of the detail functions from the computed column jerk are displayed in Figure 4-25 and Figure 4-26. Similar to the DWT analyses using the acceleration response, the spikes from the normalized details with absolute amplitude that deviate more than 6 standard deviations (horizontal thick blue line) from the mean value, are treated as damage episodes.

It is seen that the results are in close agreement with the ones obtained using the experimental acceleration response (Figure 4-12 and Figure 4-13). However, the spikes in the results of EQ3 using the accelerations (Figure 4-12c) do not appear this time in the results using the jerk data (Figure 4-25c). In the case of EQ8 and EQ9 (Figure 4-26c and Figure 4-26d, respectively), the normalized absolute values of the detail functions seem to have a little increase with respect to the results using the acceleration data (Figure 4-13c and Figure 4-13d).

Figure 4-27 presents a detailed analysis of the results for EQ3. The detail functions are shown along with the jerk time history and the column ductility vs. jerk response (a similar analysis was presented in Figure 4-18). As mentioned earlier, no irregularity was detected during EQ3, unlike the irregularity detected using the results from the experimental accelerations during EQ3 (Figure 4-18).

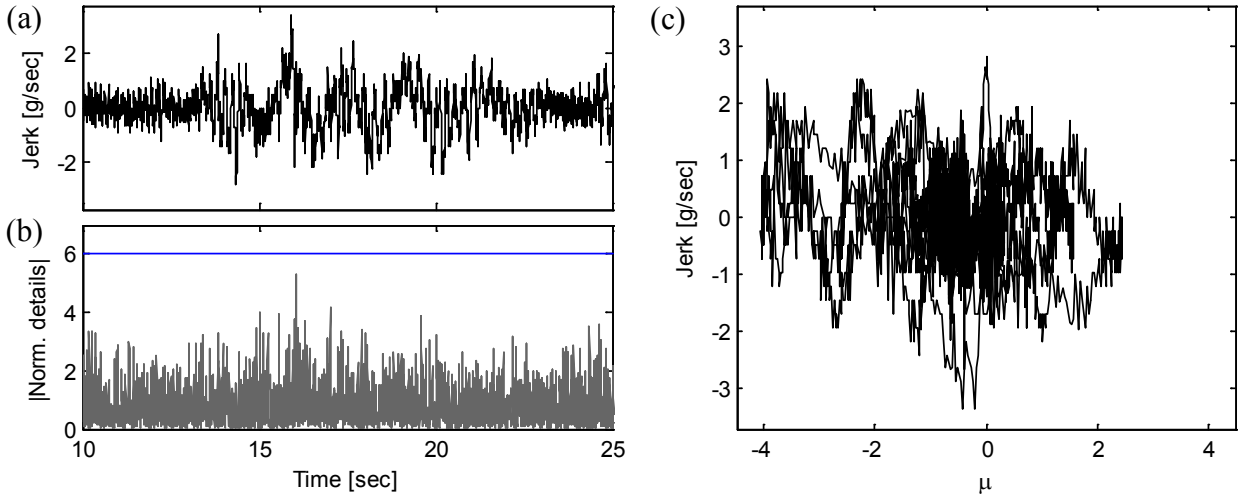

Figure 4-27: DWT analysis of the experimental jerk for EQ3: (a) time history of jerk, (b) detail function, and (c) column ductility vs. jerk response

The same type of analysis was performed for EQ8 and EQ9 (Figure 4-28 and Figure 4-29, respectively). For EQ8, the results presented previously in Figure 4-21 displayed a small irregularity at ~ 6 seconds, which is not observed this time. Fracture of the longitudinal bars were detected at the same instants (~ 14.6 and 18 seconds). For EQ9 the three rupture fracture episodes were well identified at ~ 4.8, 7.8 and 16.8 seconds. Notice that for the rupture episodes, the normalized absolute values of the detail functions are larger than in the results using the column acceleration response. It is also observed that the irregularities of the detail function for

EQ8 and EQ9 (Figure 4-28b and Figure 4-29b) correlated well with the peak values of the jerk response (Figure 4-28a and Figure 4-29a). It is inferred that rupture episodes can be detected by simply looking at the jerk response.

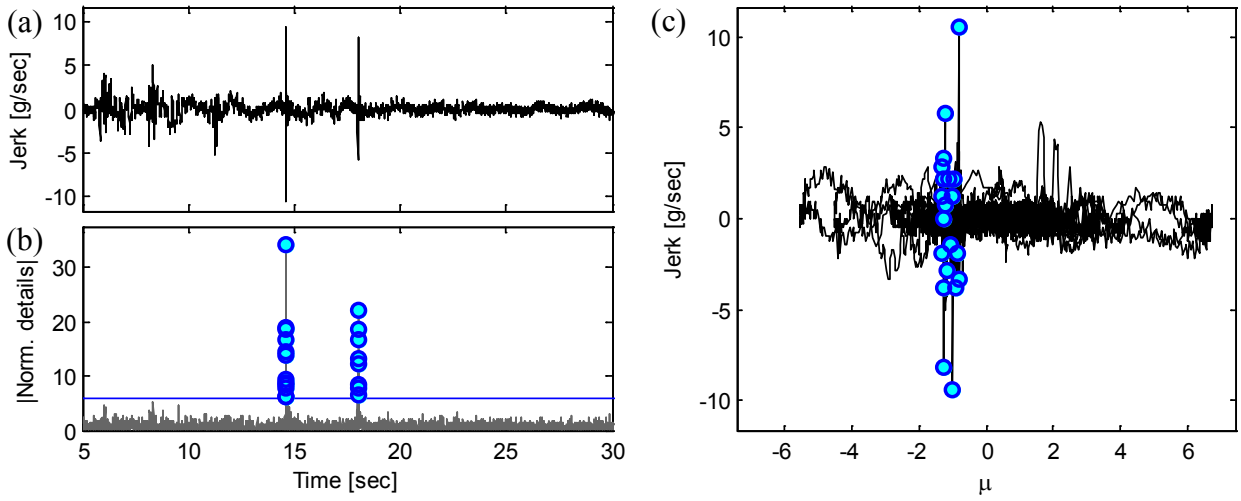

Figure 4-28: DWT analysis of the experimental jerk for EQ8: (a) time history of jerk, (b) detail function, and (c) column ductility vs. jerk response along with the location of the discontinuities detected

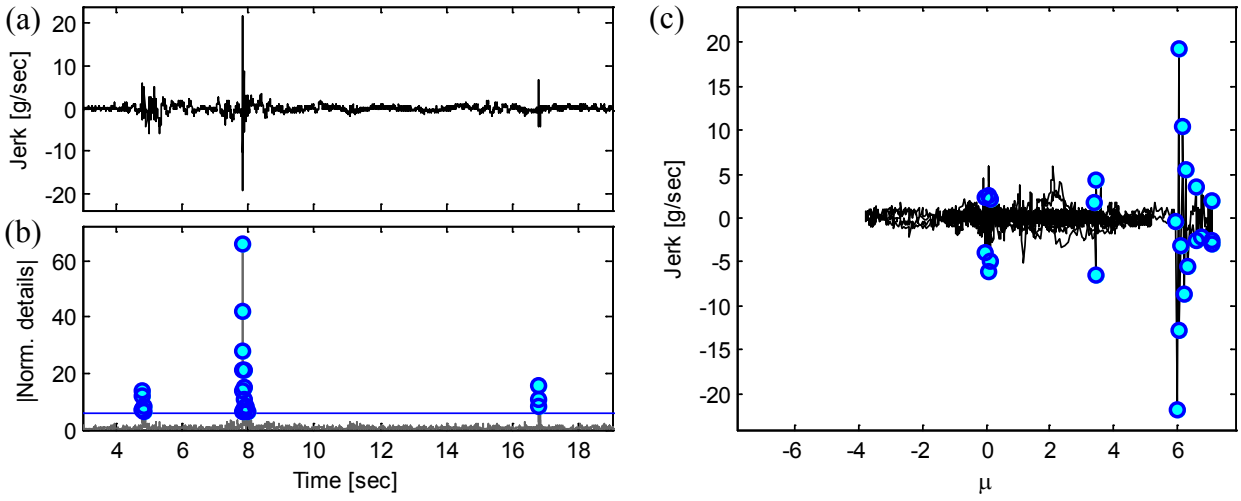

Figure 4-29: DWT analysis of the experimental jerk for EQ9: (a) time history of jerk, (b) detail function, and (c) column ductility vs. jerk response along with the location of the discontinuities detected

A detail analysis with a time frame of 0.1 seconds on each bar rupture episode was performed in order to have a measure of the disturbance caused by the bar fracture in the acceleration response of the structure. The disturbance at the irregularities detected is computed, that is, changes in the instant acceleration and jerk response are measured at the instants where the irregularities were detected. For this purpose, the mean value is removed from the acceleration and jerk responses and then values of acceleration and jerk are computed. Figure 4-30 to Figure 4-34 present the acceleration and jerk response, detail functions, and disturbance along with the irregularities detected using both responses (acceleration and jerk). Maximum positive and negative values of acceleration and jerk are illustrated for the disturbance and they are also summarized in Table 4-1. Notice again in Figure 4-30 to Figure 4-34 how, in some way, the bar rupture episodes are predictable from the jerk response. In fact, in this case it is not necessary to remove the mean value in order to compute the disturbance.

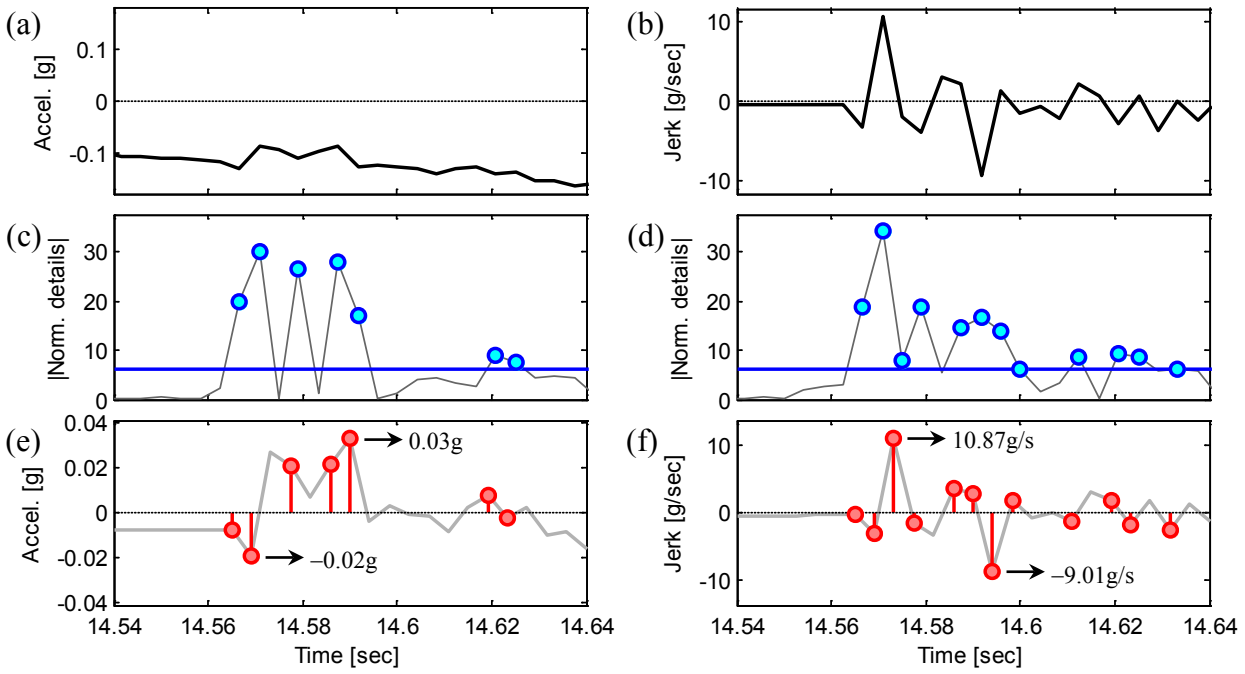

Figure 4-30: Analysis of first rebar fracture (t=14.57 seconds) during EQ8 using experimental data: (a) acceleration and (b) jerk time history; detail function using (c) acceleration and (d) jerk; (e) acceleration and (f) jerk disturbance at the discontinuities detected

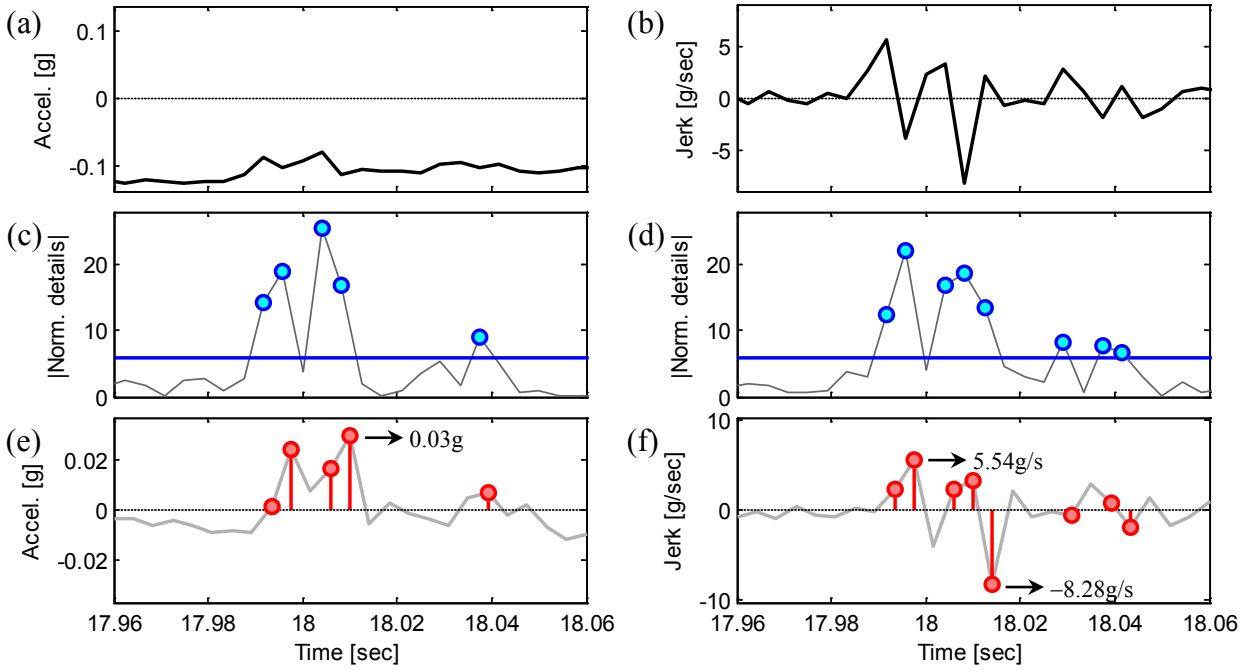

Figure 4-31: Analysis of second rebar fracture (t=18.01 seconds) during EQ8 using experimental data: (a) acceleration and (b) jerk time history; detail function using (c) acceleration and (d) jerk; (e) acceleration and (f) jerk disturbance at the discontinuities detected

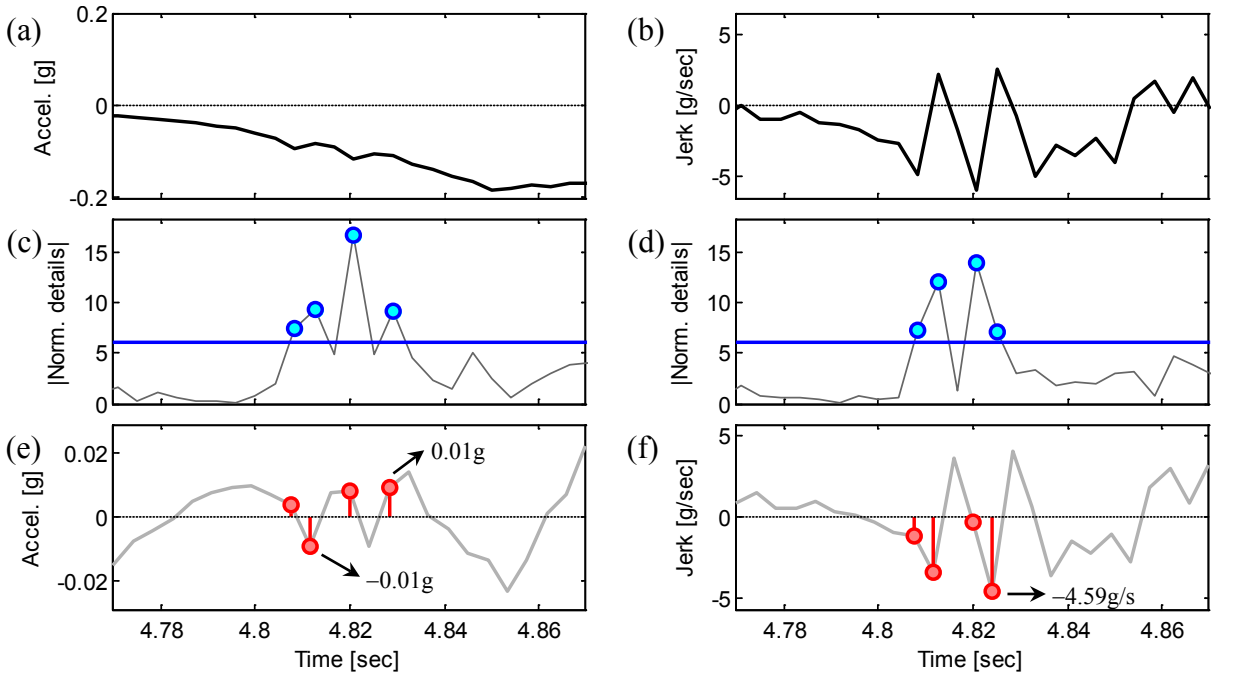

Figure 4-32: Analysis of first rebar fracture (t=4.82 seconds) during EQ9 using experimental data: (a) acceleration and (b) jerk time history; detail function using (c) acceleration and (d) jerk; (e) acceleration and (f) jerk disturbance at the discontinuities detected

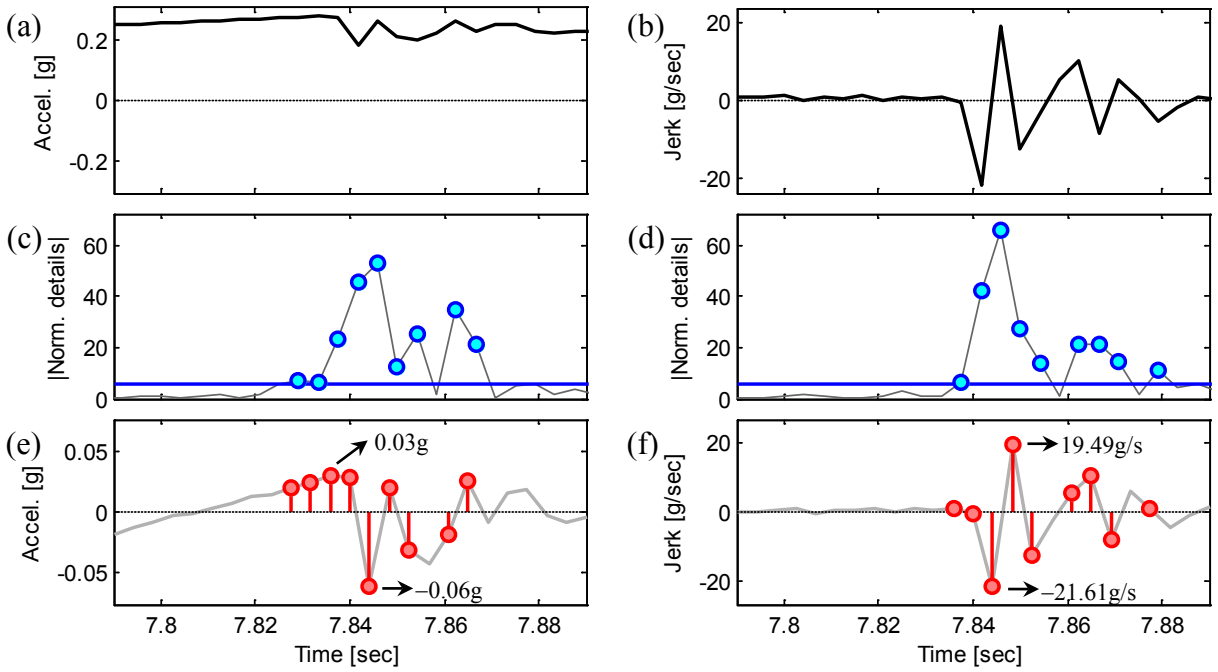

Figure 4-33: Analysis of second rebar fracture (t=7.84 seconds) during EQ9 using experimental data: (a) acceleration and (b) jerk time history; detail function using (c) acceleration and (d) jerk; (e) acceleration and (f) jerk disturbance at the discontinuities detected

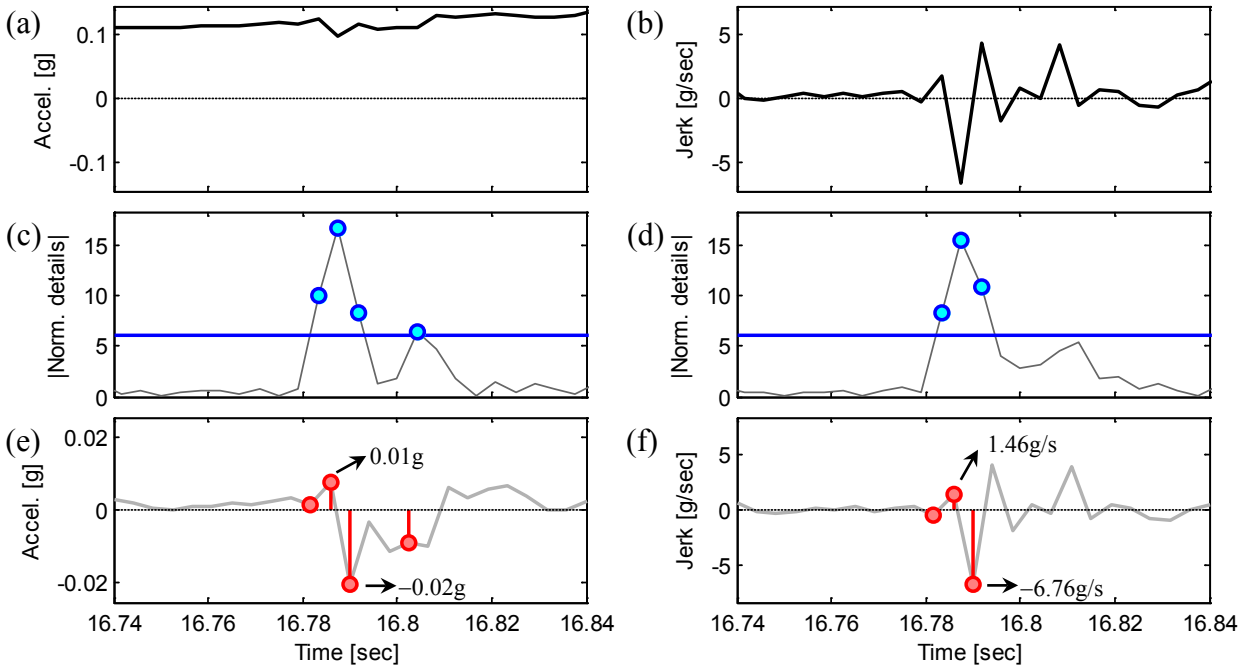

Figure 4-34: Analysis of third rebar fracture (t=16.79 seconds) during EQ9 using experimental data: (a) acceleration and (b) jerk time history; detail function using (c) acceleration and (d) jerk; (e) acceleration and (f) jerk disturbance at the discontinuities detected

Table 4-1: Comparison of acceleration and jerk peak disturbances

Test	Rebar Fracture	Accel. Disturbance [g]		Jerk Distrubance [g/sec]	
		Max. Positive	Max. Negative	Max. Positive	Max. Negative
EQ8	First	0.03	-0.02	10.87	-9.01
	Second	0.03	-	5.54	-8.28
EQ9	First	0.01	-0.01	-	-4.59
	Second	0.03	-0.06	19.49	-21.61
	Third	0.01	-0.02	1.46	-6.76

4.3. Signal Processing Based System Identification

In order to determine the changes on the dynamic properties, two approaches are used in this methodology. They are the RDT in combination with HT (described in sections 2.3.2 and 2.3.3) using the acceleration response to WN excitations, and the CWT (explained in section 2.3.4) using the end portion of the acceleration response to EQ excitations.

4.3.1. Identification using the response to white noises (RDT+HT)

As mentioned before, in this approach the identification is made using the response to low-intensity WN excitations. For the sake of brevity, only graphic results for WN1 and WN9 are displayed in Figure 4-35 and Figure 4-36, respectively. For all cases the segment duration varies in order to generate the RDS with the same number of cycles; a total of four cycles were used.

In the case of WN1, the natural frequency and damping ratio identified were 1.07Hz and 3.26%, respectively, and a total of 206 segments with 3.66 seconds of duration were used to obtain the RDS. For the WN9, the natural frequency was 0.44Hz, the damping ratio was 3.10%, and 186 segments with 9.09 seconds of duration were used. Figure 4-44 and Figure 4-45 show the changes of frequency and damping of all the WNs analyzed. Notice that in some way the results in frequency changes are as expected, but the damping ratios seem to remain constant.

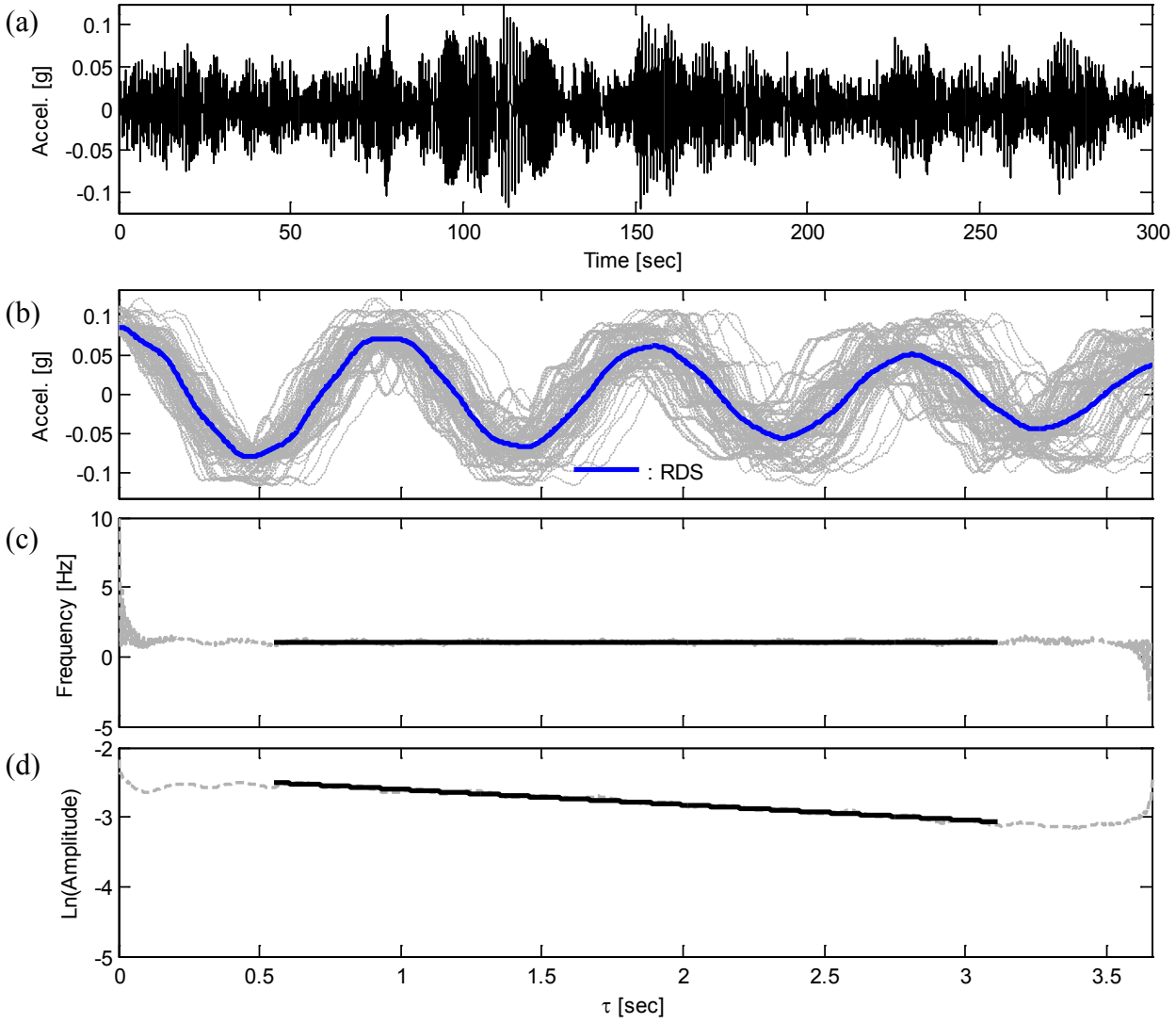

Figure 4-35: Results of approach 1 (RDT+HT) for WN1: (a) column acceleration response to WN1, (b) RDS extracted from response, (c) instant frequency, and (d) natural logarithm of the instant amplitude calculated from the free decay response obtained via RDS

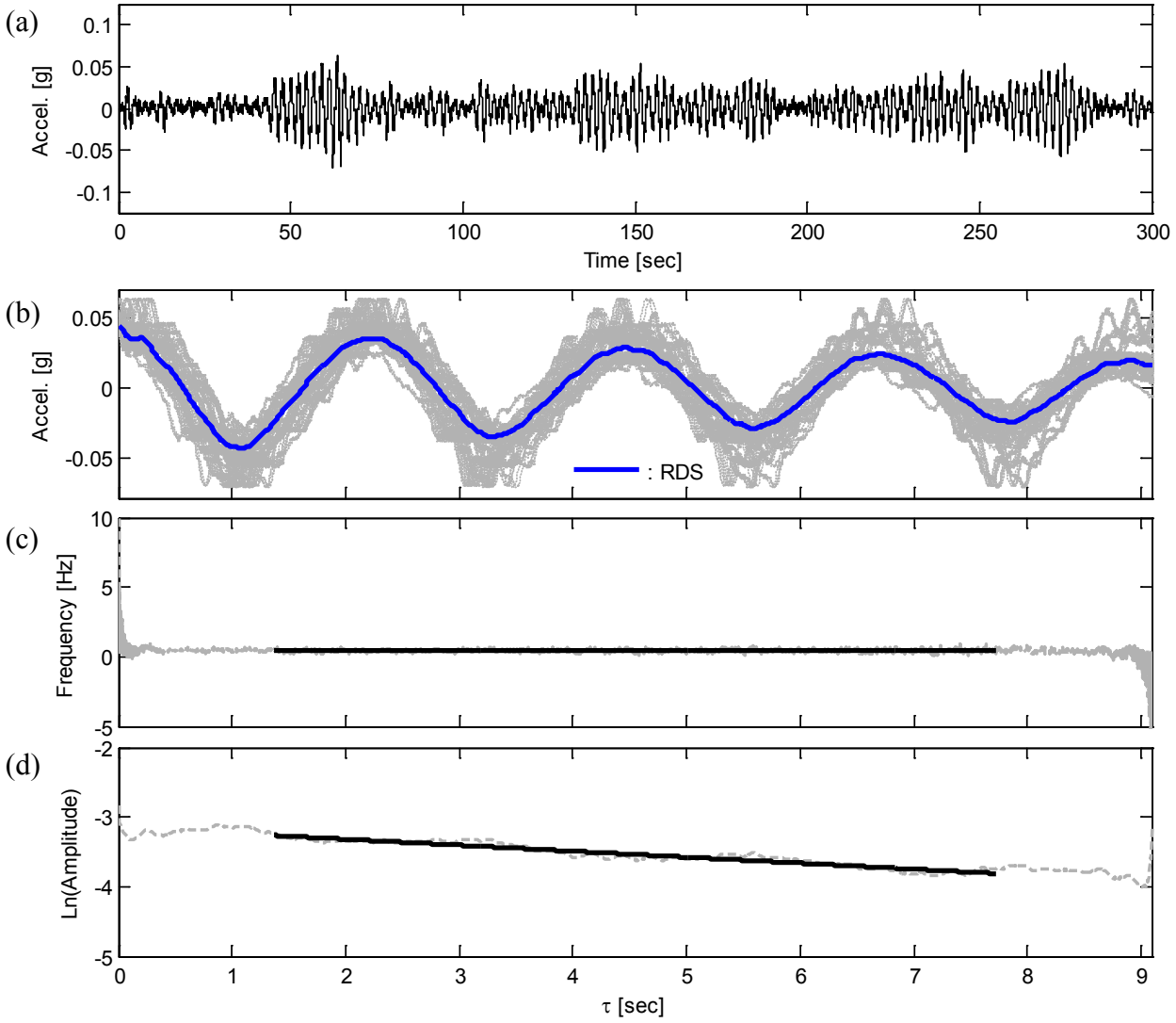

Figure 4-36: Results of approach 1 (RDT+HT) for WN9: (a) column acceleration response to WN9, (b) RDS extracted from response, (c) instant frequency, and (d) natural logarithm of the instant amplitude calculated from the free decay response obtained via RDS

4.3.2. Identification using the response to earthquakes (CWT)

Before applying the CWT to the free decay portion of the column acceleration response to EQ loads, it is necessary to define the frequency ranges for the analysis and define the wavelet parameters (i.e., the central frequency f_c, and bandwidth parameter f_b). From the other approach (i.e., RDT in combination with HT) it is known that the frequencies to identify vary from 1.1Hz to 0.44Hz before applying EQ9. Hence, the analyses were performed from 0.10Hz to 1.90Hz.

Figure 4-37 shows time and frequency resolutions as functions of frequency to be identified using the Heisenberg uncertainty principle. The selected parameters were f_b=f_c=1 for all cases.

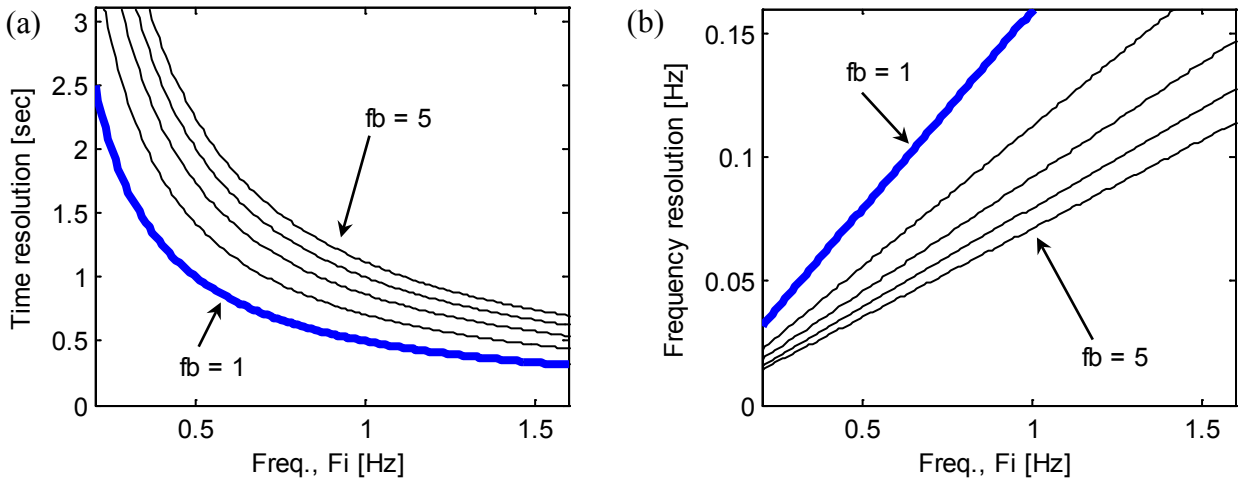

Figure 4-37: (a) Time and (b) frequency resolutions for the modified Morlet Wavelet for different values of f_b and using f_c = 1

Figure 4-38 shows the results for the free decay portion after EQ1, and Figure 4-39 presents the results for the free decay portion from EQ9. After EQ1 the natural frequency and damping ratio identified were 1.18Hz and 2.83%, respectively. The natural frequency was 0.43Hz and the damping ratio was 4.94% after EQ9 was applied. Figure 4-44 and Figure 4-45 show the changes in the frequency and damping for all the EQs analyzed.

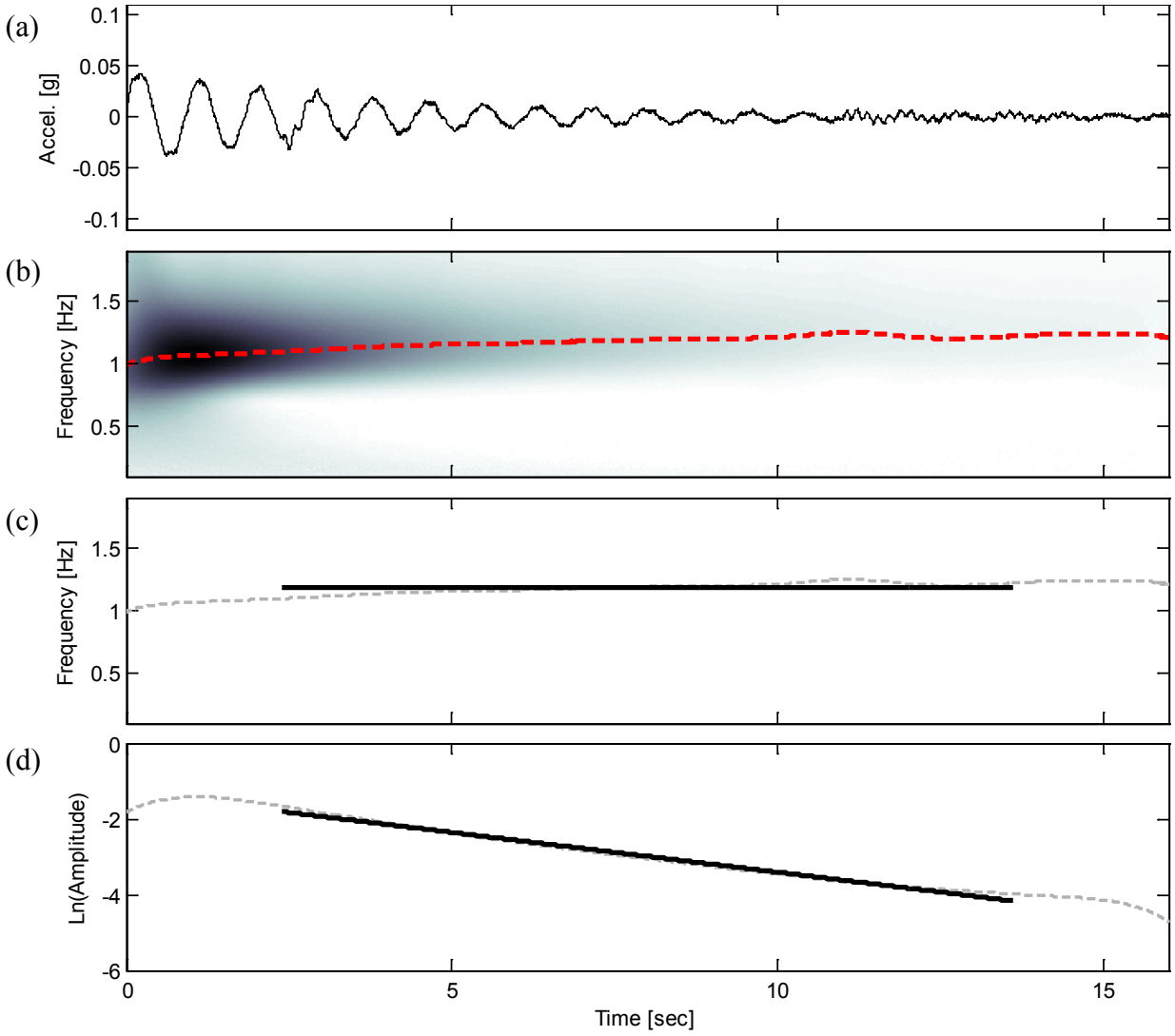

Figure 4-38: Results of approach 2 (CWT) for EQ1: (a) free decay portion of EQ1, (b) wavelet map and extracted ridges (dashed red line), (c) instant frequency, and (d) natural logarithm of instant amplitude

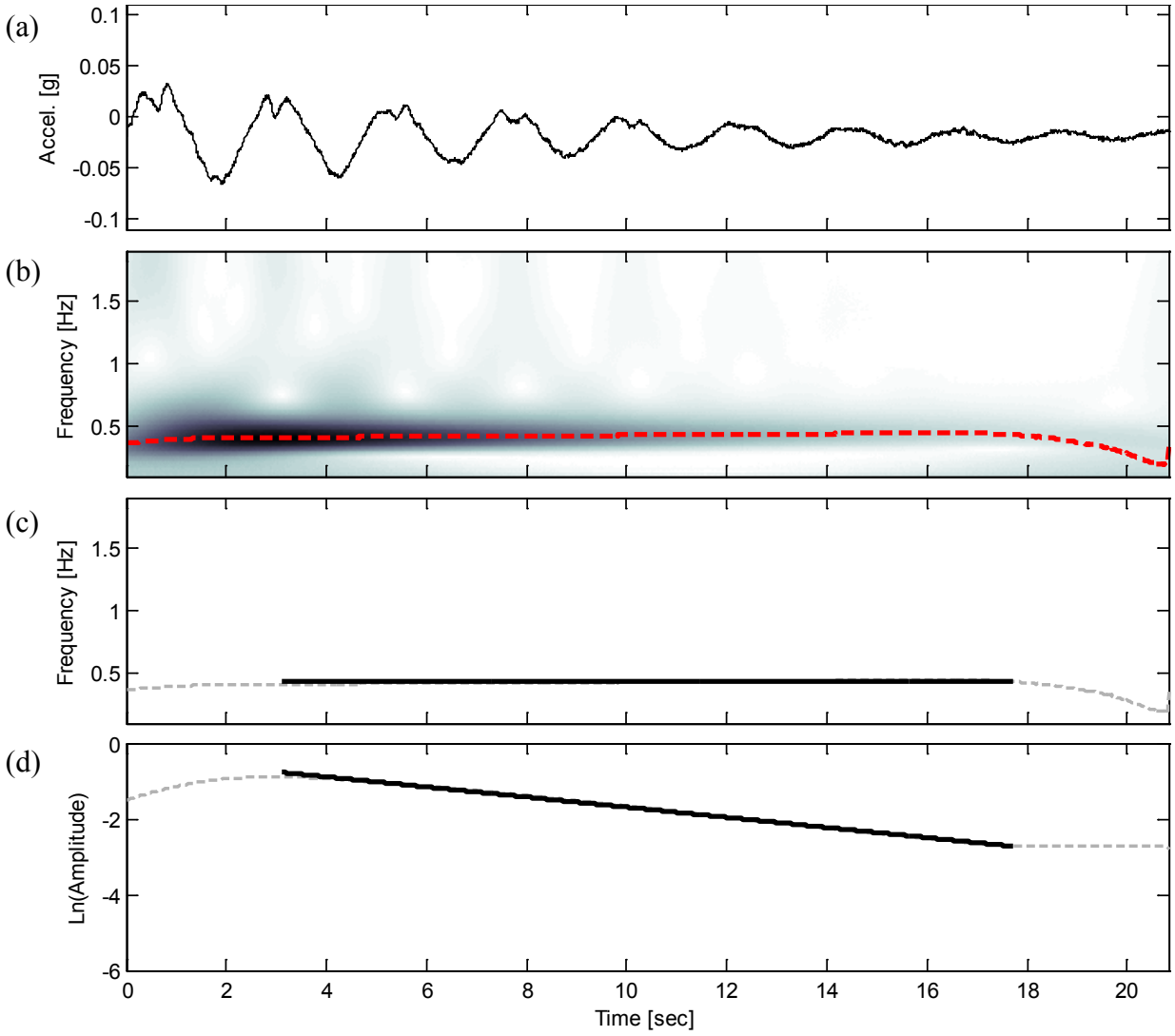

Figure 4-39: Results of approach 2 (CWT) for EQ9: (a) free decay portion of EQ9, (b) wavelet map and extracted ridges (dashed red line), (c) instant frequency, and (d) natural logarithm of instant amplitude

4.3.3. Damage index computation

A RC structure can be weakened or damaged when it is subjected to a combination of stress reversals and high stress excursions. Park and Ang (1985) proposed a damage model which includes not only the maximum response, but also the effect of repeated cyclic loadings. The seismic structural damage can be estimated as a Damage Index (DI) which is expressed as a linear combination of the damage caused by excessive deformation and that contributed by the repeated cyclic loading. Mathematically the DI can be calculated as follows:

$$DI = \frac{\delta_M}{\delta_U} + \frac{\beta}{Q_Y \cdot \delta_U} \int dE \tag{4-3}$$

where δ_M is the maximum deformation during an earthquake (i.e., a dynamic load), δ_U is the ultimate deformation, β is a non-negative parameter that represents the effect of cyclic loading on structural damage, dE is the incremental absorbed hysteretic energy, and Q_Y is the calculated yield strength. If the maximum strength Q_U is smaller than Q_Y, then Q_Y is replaced by Q_U. The result of the integral in Equation (4-3) is the total absorbed hysteretic energy (E) which can be determined by using the load-deformation time history.

Figure 4-40 illustrates the load, deformation, and load-deformation time history for the first ground motion (EQ1) applied during the full-scale test. The sum of the area of all hysteresis cycles from Figure 4-40c, allows calculating the total absorbed energy (E). Notice that the area of the hysteresis cycles is small which means that E will be also small, and therefore, the DI will be low for the EQ1. The dashed lines in Figure 4-40a and Figure 4-40b represent the yield strength and yield displacement, respectively. It can be observed, that neither the lateral force nor the displacement exceed the yield limits aforementioned. The displacement and force time histories were obtained from the detailed distributed plasticity-fiber based FE model, developed in Chapter III, which closely resembled the behavior of the column (Aguirre at al., 2013).

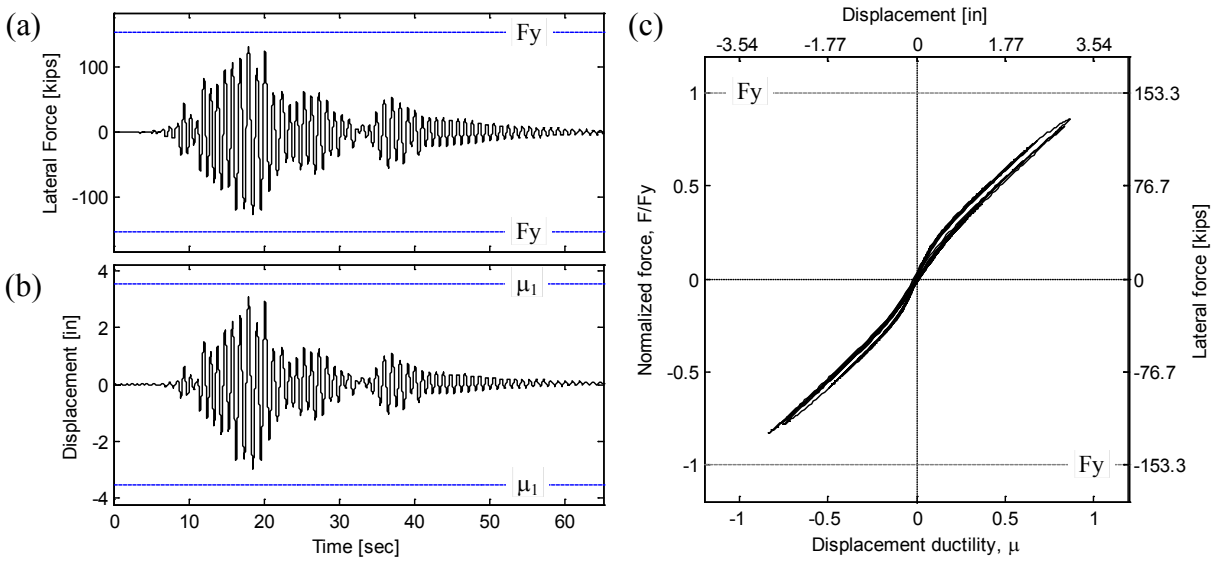

Figure 4-40: Structure response during EQ1: (a) lateral force time history, (b) displacement time history, and (c) force-displacement time history

Structural damage is then a function of the responses δ_M and dE that are dependent of the load-deformation time history, while the parameters β, δ_U, and Q_Y are independent of it. The parameters δ_U, Q_Y, and Q_U can be obtained by performing a monotonic pushover analysis. Figure 4-41 shows the simulated force-deformation curve for the column from which the ultimate deformation, yield strength, and maximum strength were δ_U = 41.76 in, Q_Y = 137.18 kip, and Q_U = 108.28 kip. Notice that $Q_U < Q_Y$, hence, Q_Y = 108.28 kip.

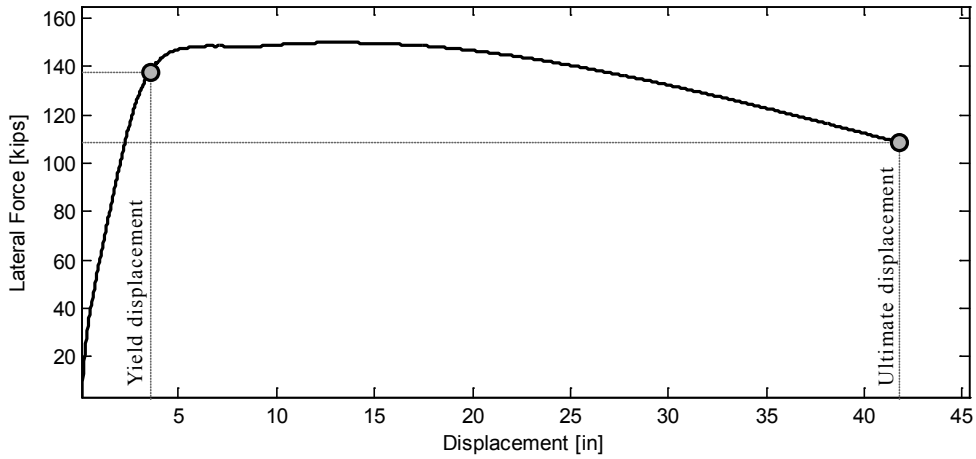

Figure 4-41: Simulated monotonic force-displacement curve

The value of β can be obtained through a trial and error process by identifying different levels of performance. For example, if damage is induced such that the structure cannot be repaired then $DI \geq 1.0$. In this study, the load-deformation time history is known from the pristine structure up to near-collapse conditions, in other words, from $DI = 0.0$ to $DI \geq 1.0$. Moreover, the point of failure of the column was well-identified after the application of EQ7 due to the rebar buckling and the initial concrete core crushing.

The maximum deformation (δ_M) and the parameter E, which is the integral in Equation (4-3), need to be computed for each earthquake. Figure 4-42 presents the maximum response and maximum displacement ductility for each ground motion. In the case of E, notice that it must be accumulated along all ground motions, for instance, for the EQ2 the total energy (E) is the sum of the hysteresis cycles of EQ2 and the energy (E) previously calculated for EQ1, and so forth.

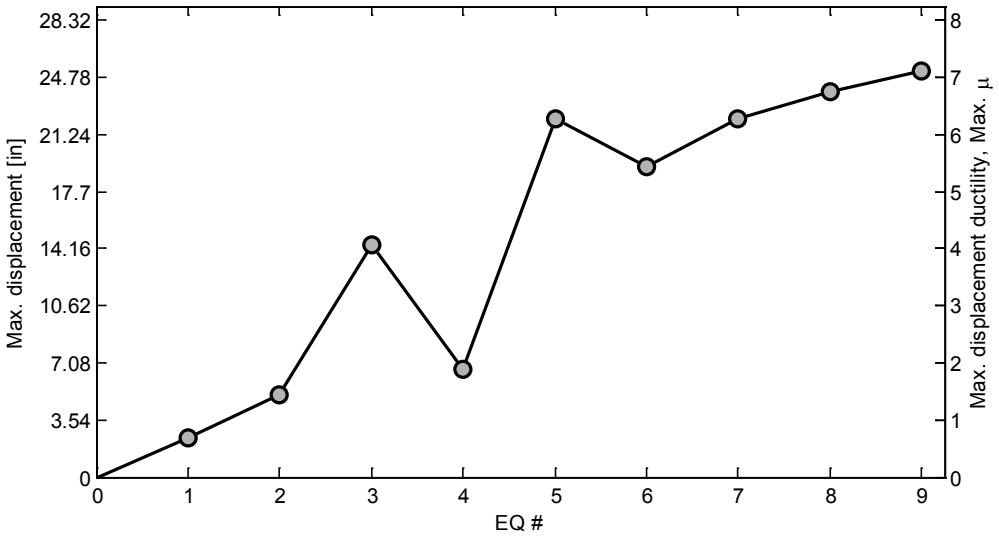

Figure 4-42: Maximum response during each earthquake

The value for the parameter beta ($\beta = 0.06$) was set so that the DIs obtained correlate well with the damage observed during the test. For example, after EQ7 when multiple rebar buckling and core crushing was observed, DI should be close to 1. On the other hand, for the first two records DI should be below 0.3 because the induced damage was negligible. The DI values computed after each EQ are presented in Figure 4-43.

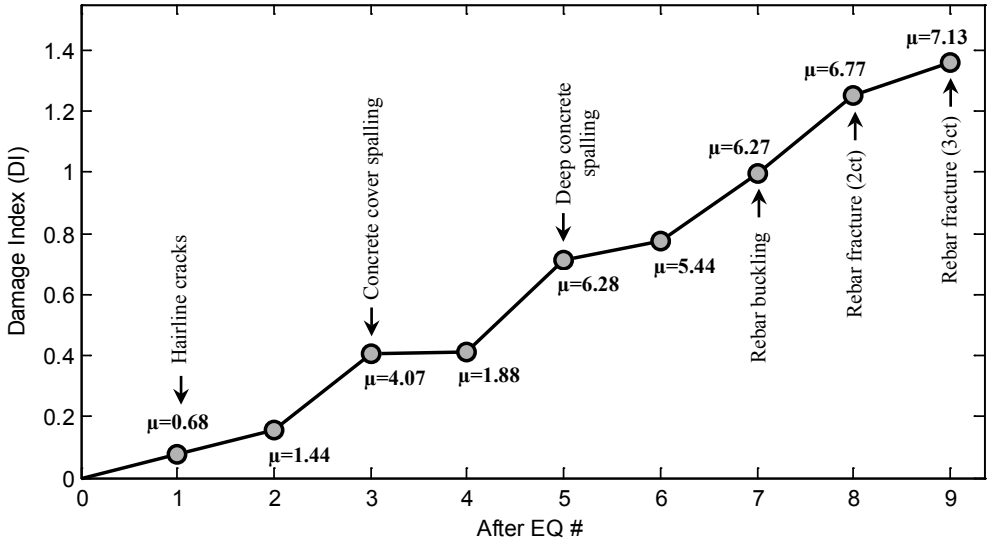

Figure 4-43: Calculated damage index (DI) after each earthquake

4.3.4. Analysis of results from system identification

Figure 4-44 summarizes the frequency shifts the structure experienced during the tests. It can be seen that the changes in the first natural frequency are in close agreement for both approaches. There is some difference in the frequency values obtained for the structure after the first earthquake, but thereafter the frequencies identified are very similar. The largest frequency shift occurred for EQ3, just when the first substantial inelastic excursions occurred. From this point forth, the changes are less noticeable despite the increasing inelastic demand and induced damage during the following ground motions. The next observed frequency shifts (though much less significant) occurred for EQ5 which coincides with the observed deep concrete spalling and the on-set of buckling and during EQ8, which coincides with the first rebar fractures. Table 4-2 summarizes and correlates the computed frequency changes with the observed damage.

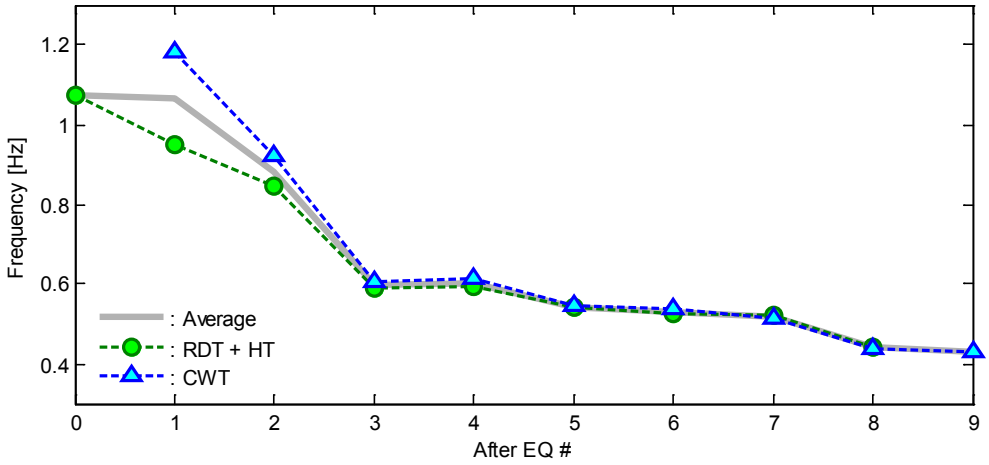

Figure 4-44: Frequency changes after each earthquake for both approaches

Table 4-2: Significant performance levels and frequency shifts

Test	Damage	Relative Freq. Shift (%)	Absolute Freq. Shift (%)	Max. Ductility Reached
EQ1	Hairline cracks	0.82	0.82	0.68
EQ2	No significant changes	17.08	17.76	1.44
EQ3	Concrete cover spalling	32.11	44.17	4.07
EQ4	No significant changes	0.62	43.82	1.88
EQ5	Deep concrete spalling	10.02	49.45	6.28
EQ6	No significant changes	2.09	50.51	5.44
EQ7	Rebar buckling	2.59	51.79	6.27
EQ8	Rebar fracture (2)	15.04	59.04	6.77
EQ9	Rebar fracture (3)	2.17	59.93	7.13

The frequency shifts presented in Table 4-2 are computed so that the relative shift measures the frequency change after each EQ and the absolute shift measures the cumulative change with respect to the initial frequency of vibration before applying any EQ.

As it can be seen from Figure 4-45, the differences in the results of the damping ratios identified by the two methodologies employed are larger than in the case of the natural frequencies. There is not a clear trend for the results presented in Figure 4-45. A minimum of 200 segments and initial amplitude (*Xs*) equal to the maximum value of each WN acceleration response were used to compute the RDS in the first approach (RDT+HT).

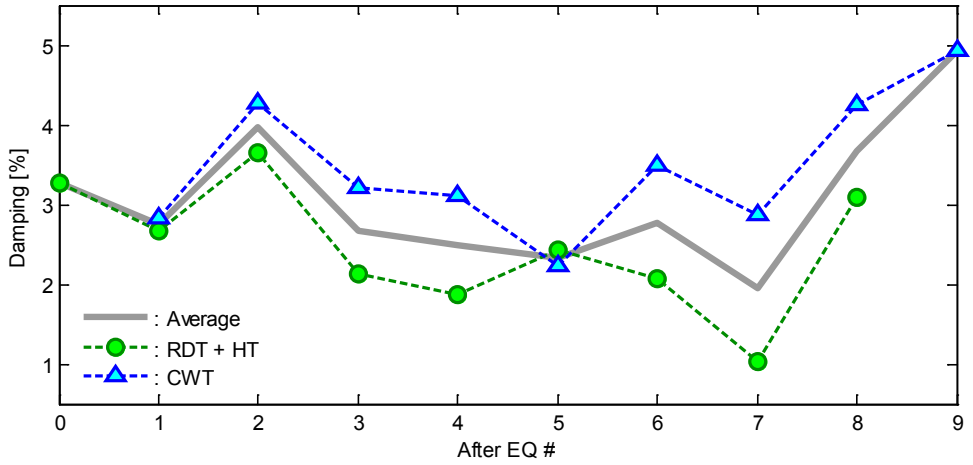

Figure 4-45: Damping changes after each earthquake for both approaches

Figure 4-46 presents once more the frequency changes, but this time as function of the maximum displacement ductility reached during each EQ. The results for EQ4, EQ6, and EQ7 are not shown since these ground motions were not applied with increasing intensity levels. It is seen from Figure 4-46 that there is a clear tendency on the natural frequency to decrease as the inelastic demand increases, and this behavior is almost asymptotic. That is, the changes in frequency are more notorious at the early stages of ductility demand ($\mu<4$) and then tend to saturate unless a major sudden damage occur for the first time (in this case rebar fracture around ductility 6-7).

Frequency changes as function of the damage index (DI) are presented in Figure 4-47. In this case, all the ground motions were considered because the induced damage is accumulated for each event. Similar to Figure 4-44, the frequency decrease rapidly at the early stages but it

tends to saturate before DI ≈ 0.5 that corresponds to moderate/reparable damage (Park and Ang, 1985).

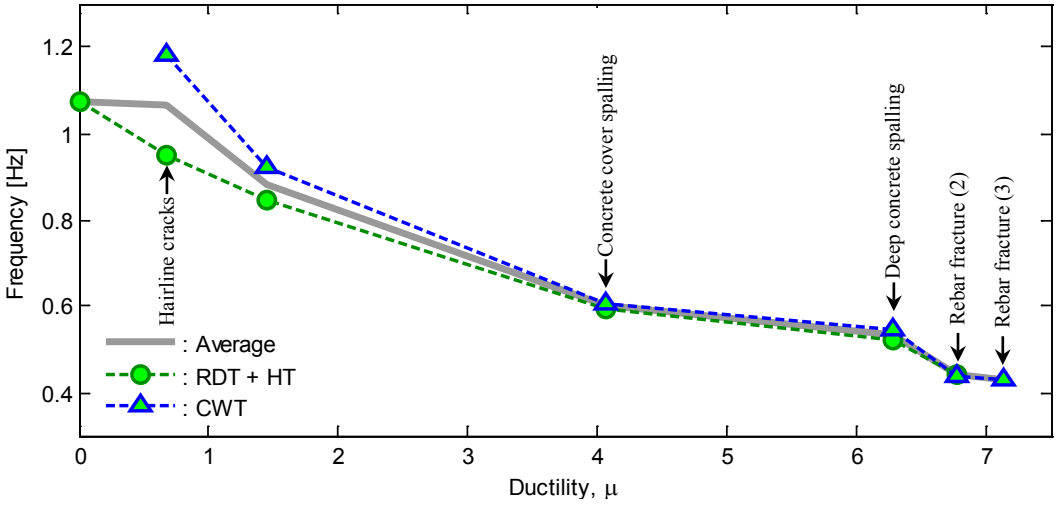

Figure 4-46: Frequency changes vs. ductility demand for both approaches

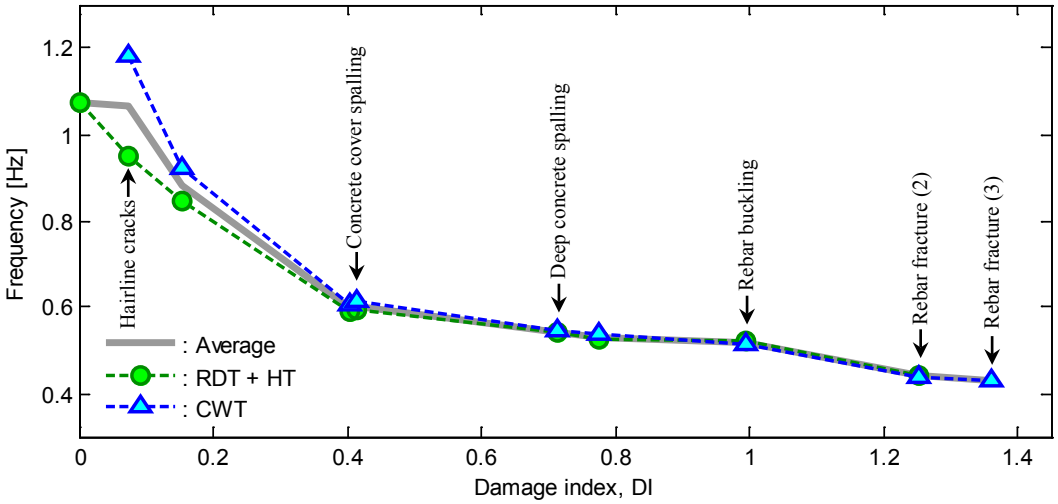

Figure 4-47: Frequency changes vs. damage index (DI) for both approaches

4.4. Chapter Summary and Conclusions

- ✓ The CWT analysis in the low frequency range was partially successful in identifying the changes in the structure's natural frequency of vibration. It was found that when the dominant frequencies in the strong motion part of the excitation are close to the structure's natural frequency, the structure may respond in tune with the excitation

and the identified frequency shift is not necessarily related to damage induced in the structure.

- ✓ Analysis of the detail functions obtained via DWT allowed the identification of the rebar rupture episodes during EQ8 and EQ9 and they are in agreement with reported test observations (Table 3-3). Such type of information is not easy to extract from conventional instrumentation and analyses, since at this level of inelastic deformation the strain gages on the bars have stopped working. Nevertheless, the buckling of the longitudinal rebar was not identified.
- ✓ The use of Takeda-like models for validation of damage detection techniques based on the analysis of discontinuities in the high frequency response of the structure (DWT analysis) is not adequate. This is due to the unrealistic abrupt change in stiffness typical of multi-linear hysteretic models which results in a large number of spurious spikes. The fiber-based model is more appropriate for this purpose as this type of approach more closely reproduced the actual non-linear hysteretic response of the structure, including the effect of local damage like rebar rupture.
- ✓ The Random Decrement Technique (RDT) in combination with the Hilbert Transform (HT) and the Continuous Wavelet Transform (CWT) were the two approaches used in order to investigate the changes in dynamic properties in the RC bridge column. The results obtained show that a clear trend in damping ratio changes is not observed and thus this dynamic parameter does not seem to be a good damage indicator. In regards to the natural frequency, decreasing values were observed as the lateral demand in the column increased. However, the observed frequency shifts tend to saturate at large levels of ductility demand.

4.5. References

Aguirre, D.A., Gaviria, C.A., and Montejo, L.A. (2013), "Wavelet Based Damage Detection in Reinforced Concrete Structures Subjected to Seismic Excitations", Journal of Earthquake Engineering (in press).

Montejo, L.A. (2011), "Signal Processing Based Damage Detection in Structures Subjected to Random Excitations", Structural Engineering and Mechanics 4(6), 745-763.

Park, Y.J. and Ang, A.H.S. (1985), "Mechanistic Seismic Damage Model for Reinforced Concrete", Journal of Structural Engineering 111, 722-739.

CHAPTER V

5. DAMAGE DETECTION USING THE LISBON 3D FRAME EXPERIMENTAL AND SIMULATED DATA

5.1. Introduction

Based on the simulated and experimental results of the Lisbon 3D frame model A, a complete damage detection analysis is performed using the same wavelet-based methodologies used in the previous chapter. The wavelet analyses are performed using the displacement responses of point B (Figure 3-38) since this point is the one which undergoes the larger displacements. Figure 5-1 and Figure 5-2 present the ductility displacement response for the EW and NS directions, respectively. Ductility values were computed using the recorded displacements and the yield displacements obtained on section 3.3.2.3 (Monotonic and cyclic pushover analysis).

Unlike the UCSD column, signal processing based system identification analyses are not performed in this example for three reasons. First, during the test only earthquake excitations were applied while for system identification purposes it is necessary to use low intensity WN excitations. Second, both components of the earthquake records used during the test were obtained from the strong motion part of an earthquake, so there is not a free decay portion at the end of the recorded displacements. Third, in this case it is not possible to perform a damage index analysis since information about induced damage (in terms of rebar buckling, rebar fracture, or concrete cracking) is not provided, so that there are no damage episodes to correlate with a damage index.

While not shown here for the sake of brevity, analyses of the experimental data of frame B showed similar results to those obtained for model A. However, due to the slightly smaller displacements and the steel reinforcement detailing, smaller frequency shifts were detected in model B than in model A analyses.

Wavelet analyses at low and high frequencies are performed to the simulated and experimental displacement response along each direction of point B of model A. The results are presented in the next section.

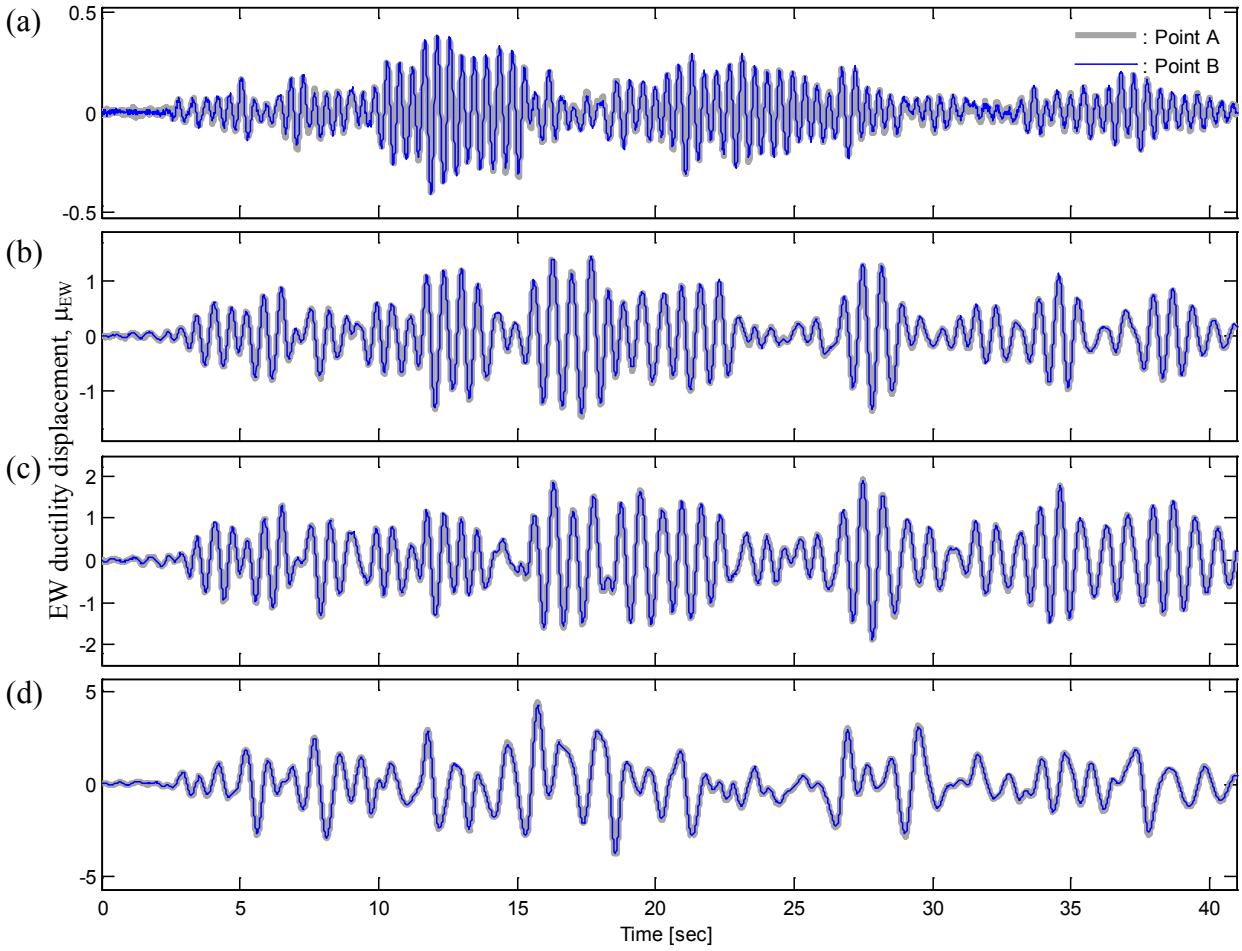

Figure 5-1: Experimental EW ductility displacement response of model A for: (a) EQ1, (b) EQ2, (c) EQ3, and (d) EQ4

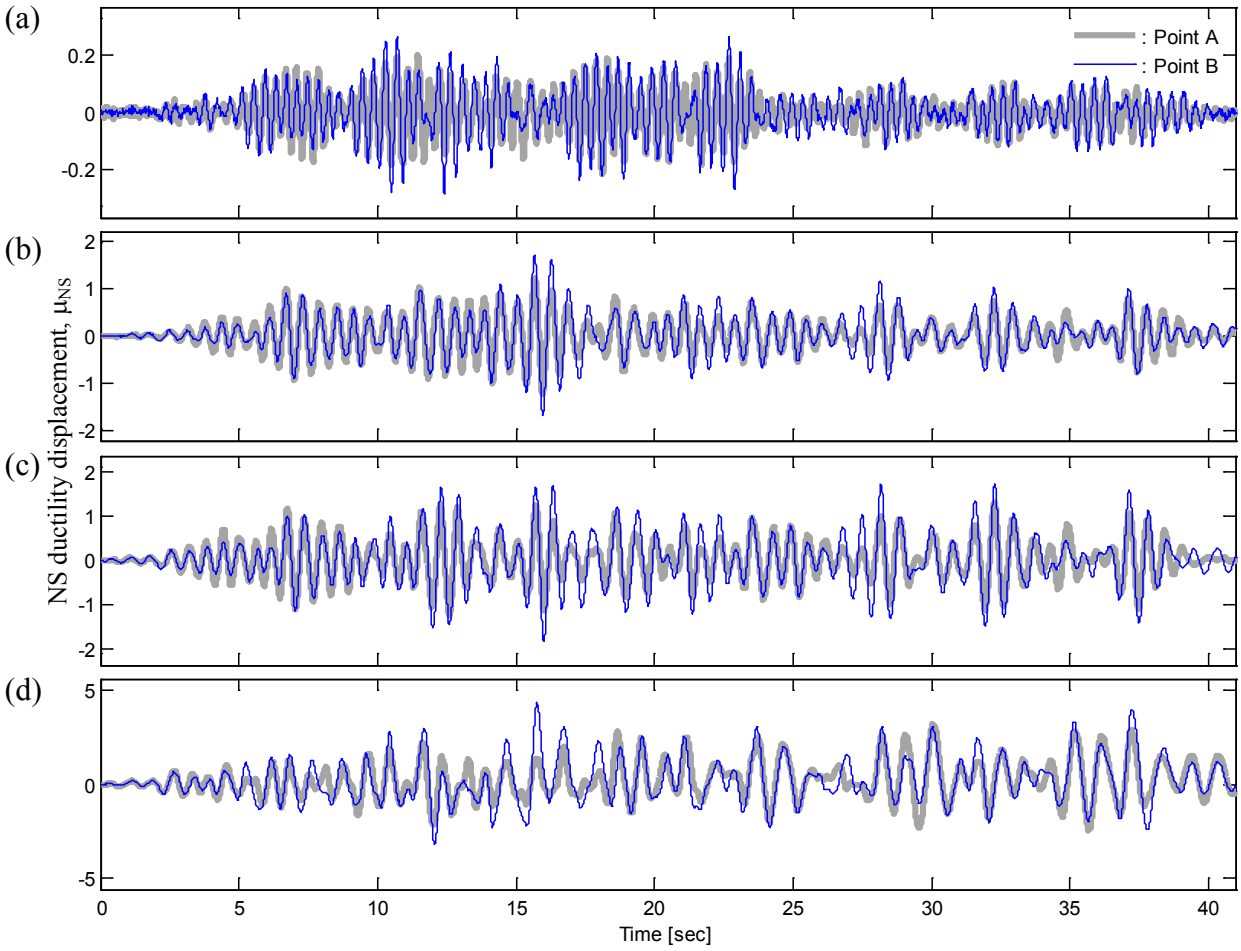

Figure 5-2: Experimental NS ductility displacement response of model A for: (a) EQ1, (b) EQ2, (c) EQ3, and (d) EQ4

5.2. Wavelet-Based Time-Frequency Analysis (Model A)

In order to recognize the range of frequencies of interest, the dominant frequencies in the response of the frame are identified via the Fourier and power spectra of the displacement response of point B to the different earthquake loads. Figure 5-3 and Figure 5-4 present and compare the results of both approaches for EW and NS directions, respectively. In the case of the Fourier spectrum (continuous gray lines), it was necessary to compute a smoothed version by using a 5 element window moving average (dashed blue lines). For the power spectrum, 600 points were used to define a Welch window and 580 points were used to overlap the segments for the averaging (windowing) process. The signal dominant frequencies (blue and cyan circle) are computed by locating the peak value on each spectrum. Notice that the results are quite

similar for both approaches. The frequency shift (using Fourier results) goes from 2.22Hz to 0.98Hz in the EW direction and from 2.51Hz to 0.93Hz in the NS direction. Table 5-1 presents a frequency shift summary for the EW and NS directions for both approaches. Also, notice that the shape of the normalized Fourier spectrum for the input earthquake accelerations (Figure 5-3a and Figure 5-4a), displays the expected features of a synthetic earthquake record (wide frequency content, not common for real earthquakes).

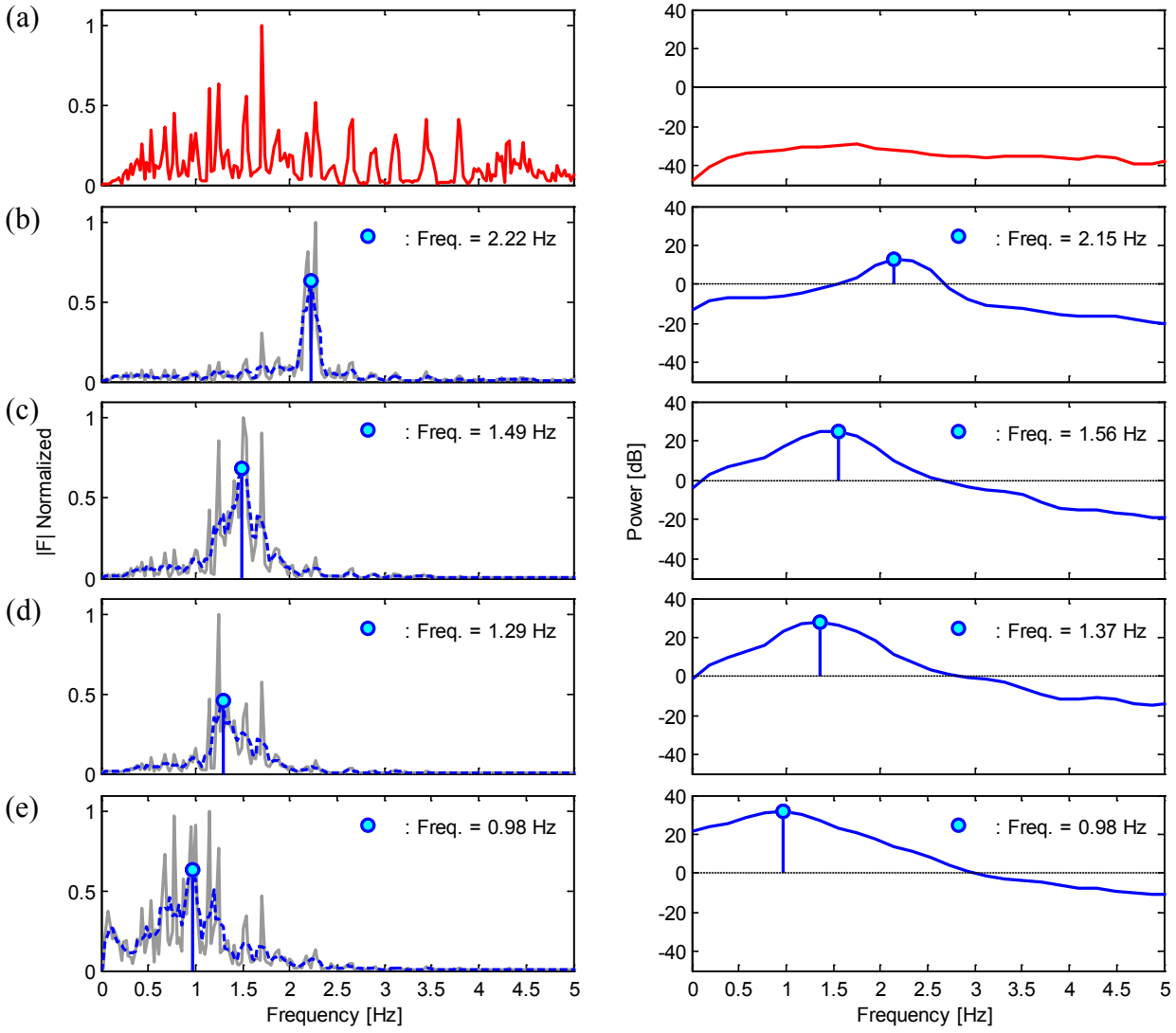

Figure 5-3: Normalized Fourier (left) and power (right) spectra (EW direction) of: (a) input earthquake acceleration; and Model A, point B displacement response for (b) EQ1, (c) EQ2, (d) EQ3, and (e) EQ4

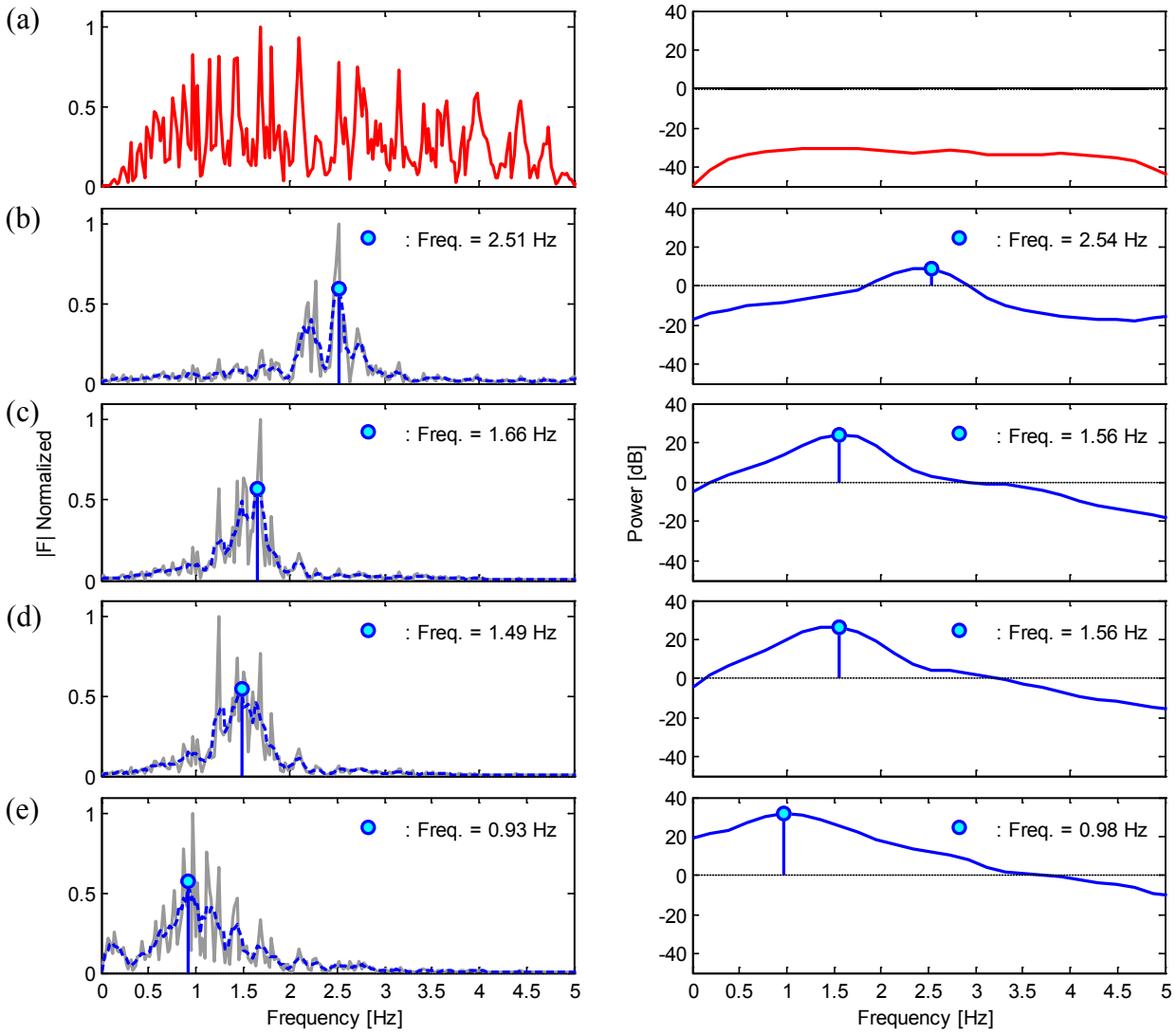

Figure 5-4: Normalized Fourier (left) and power (right) spectra (NS direction) of: (a) input earthquake acceleration; and Model A, point B displacement response for (b) EQ1, (c) EQ2, (d) EQ3, and (e) EQ4

Table 5-1: Summary of model A frequency shifts using the recorded displacements

During Test	EW Frequency (Hz)		NS Frequency (Hz)	
	Fourier	PSD	Fourier	PSD
EQ1	2.22	2.15	2.51	2.54
EQ2	1.49	1.56	1.66	1.56
EQ3	1.29	1.37	1.49	1.56
EQ4	0.98	0.98	0.93	0.98

5.2.1. Model A low frequency analysis (CWT)

Based on the identified range of signal frequencies, the parameters f_c and f_b required to define the modified Morlet wavelet were defined as 1 and 3, respectively. Figure 5-5 (blue thick lines) shows the time and frequency resolutions for the CWT analysis on the frequency range of interest (from 0.9Hz to 2.6Hz).

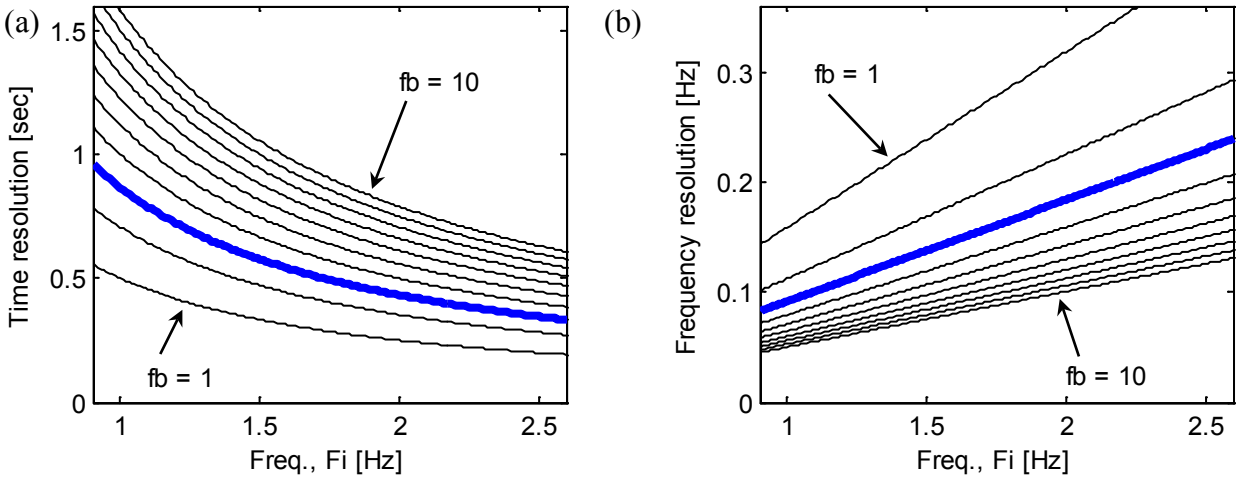

Figure 5-5: (a) Time and (b) frequency resolutions for the modified Morlet Wavelet for different values of f_b and using $f_c = 1$

Figure 5-6 to Figure 5-9 present the CWT results for the experimental and simulated (fiber-based model) data. Dotted lines on the sides of the figures denote the edge-effects zone (Equation (2-5)). The continuous gray line and dashed blue line represent the wavelet ridges and a smoothed version of them, respectively. This time, target frequency values at the beginning and the end of the motion are not illustrated since structural frequencies before and after earthquake loads application cannot be computed.

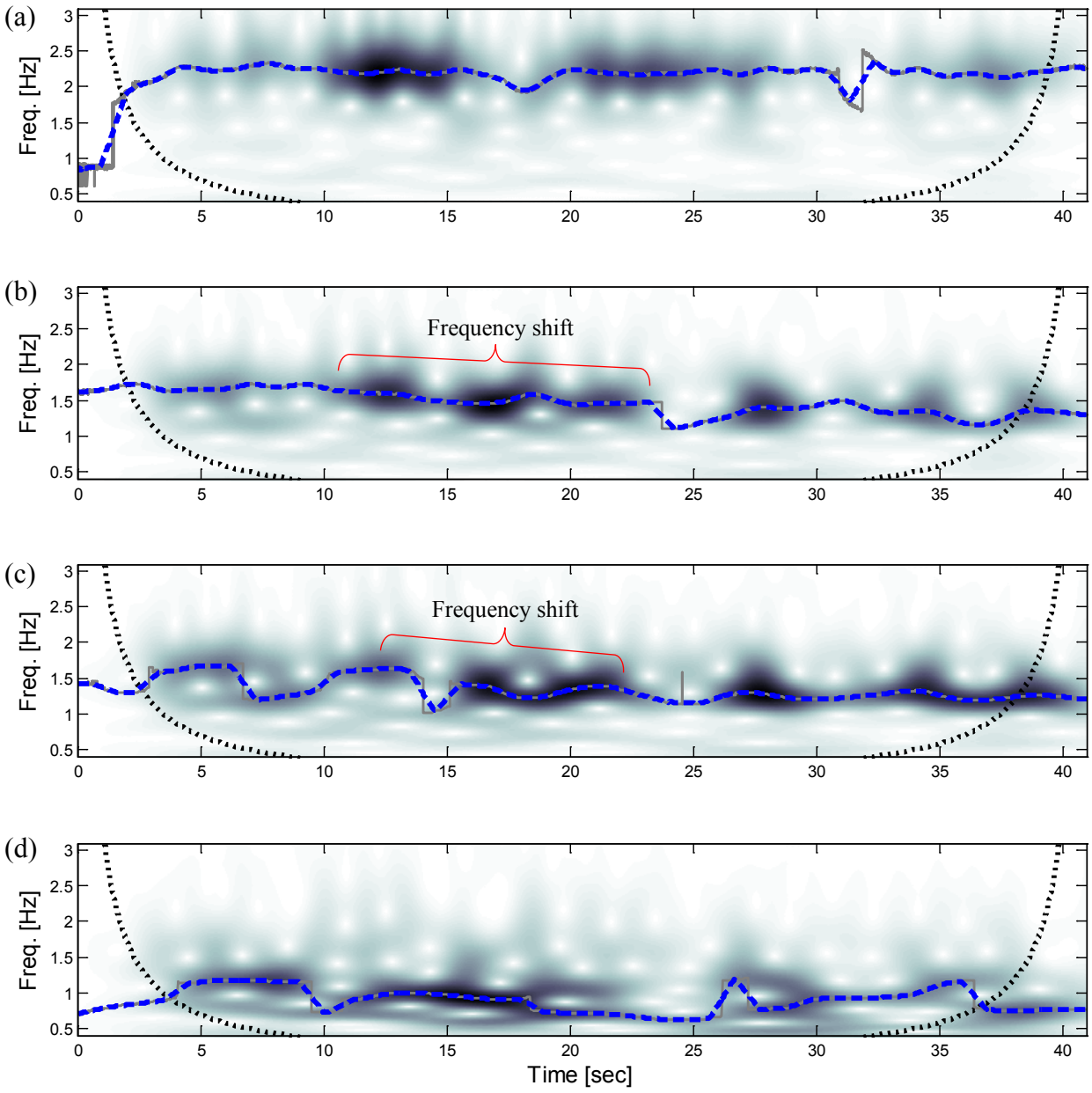

Figure 5-6: Low frequency CWT analysis results for the recorded model A, point B displacements (EW direction) for (a) EQ1, (b) EQ2, (c) EQ3, and (d) EQ4

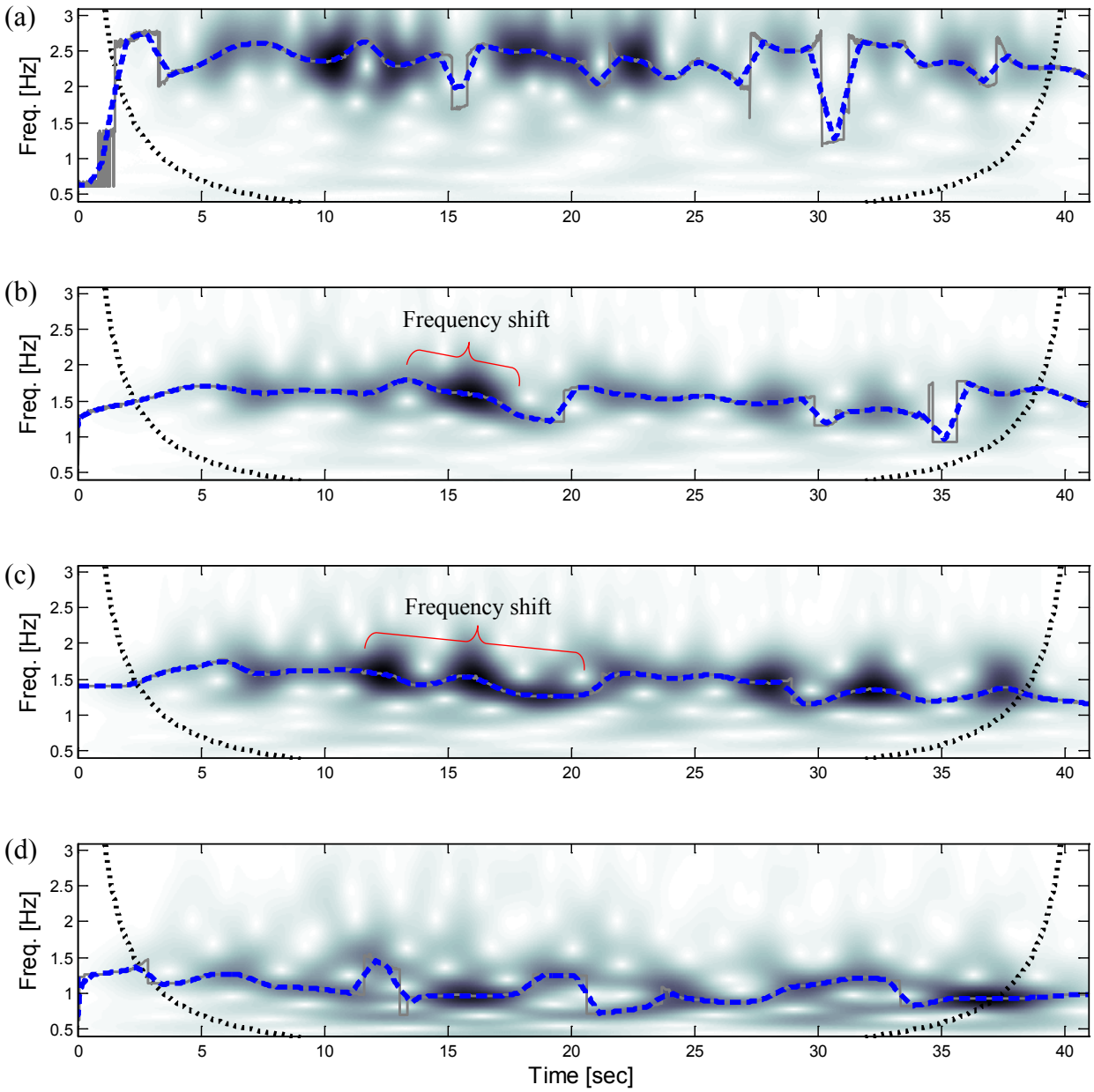

Figure 5-7: Low frequency CWT analysis results for the recorded model A, point B displacements (NS direction) for (a) EQ1, (b) EQ2, (c) EQ3, and (d) EQ4

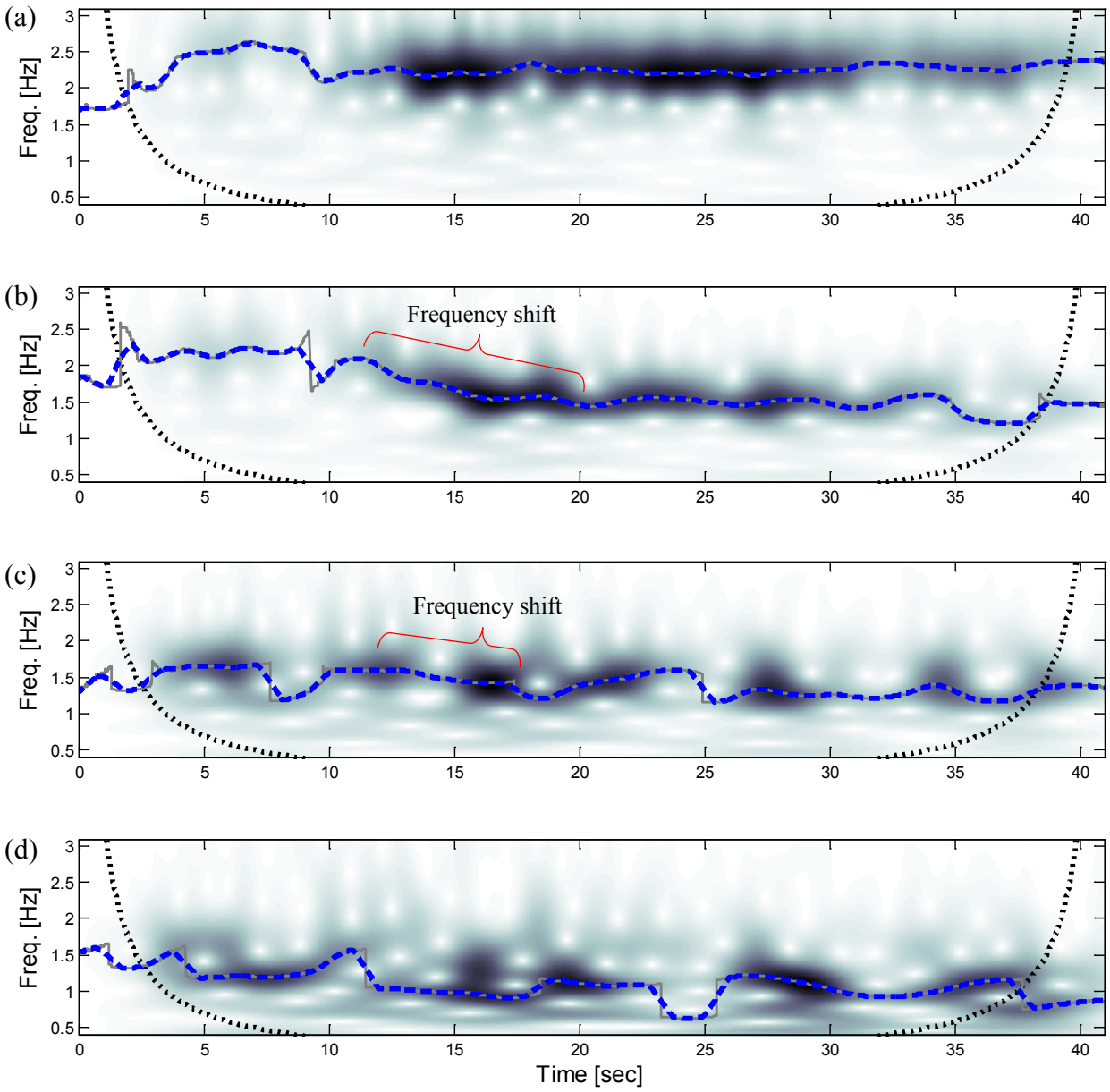

Figure 5-8: Low frequency CWT analysis results for the simulated model A, point B displacements (EW direction) for (a) EQ1, (b) EQ2, (c) EQ3, and (d) EQ4

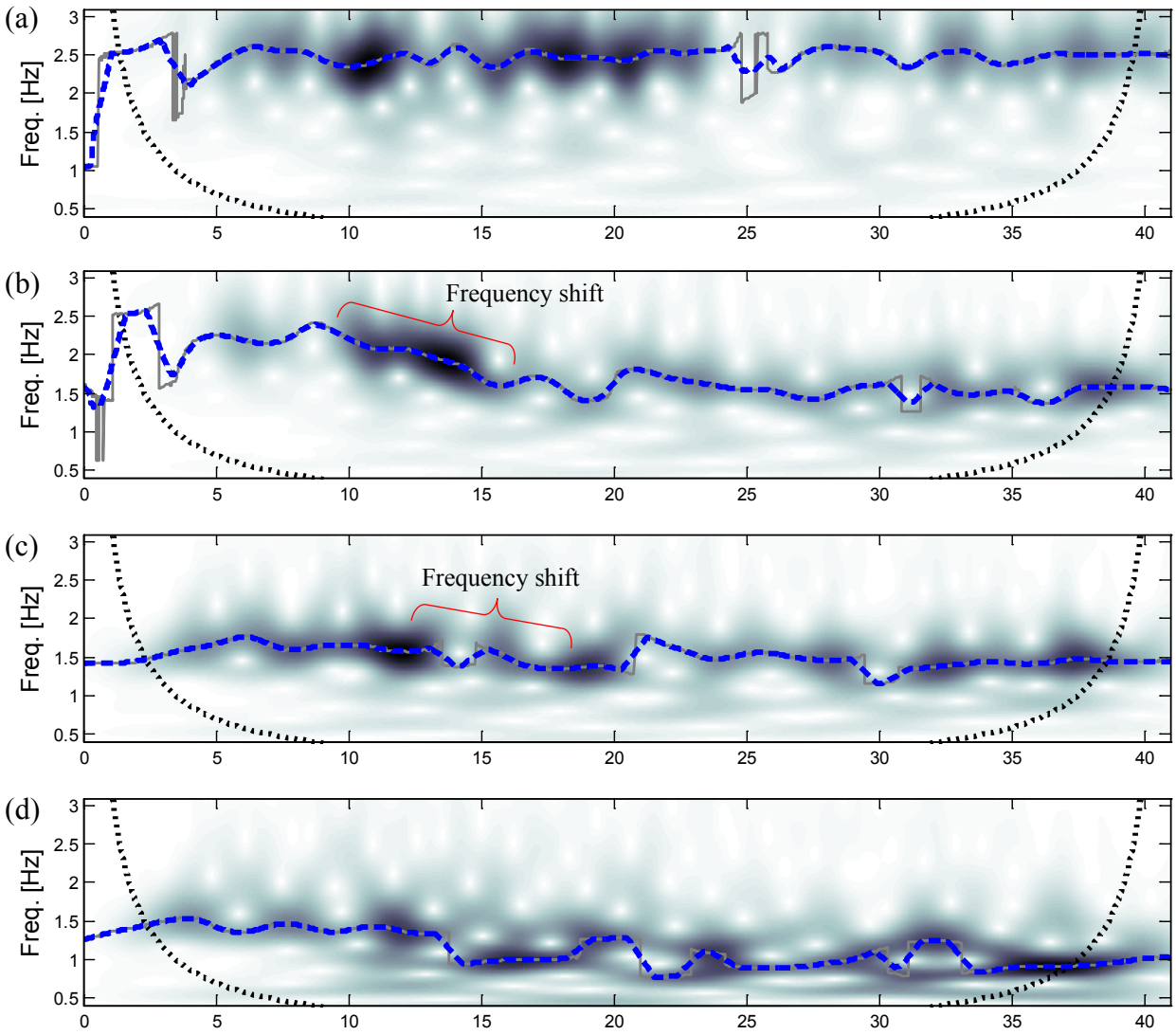

Figure 5-9: Low frequency CWT analysis results for the simulated model A, point B displacements (NS direction) for (a) EQ1, (b) EQ2, (c) EQ3, and (d) EQ4

The results obtained are quite similar in both directions for the two scenarios analyzed, that is, using experimental and simulated displacement response. The variation patterns, in terms of the vibration frequency shifts, are more evident for EQ2 and EQ3, where the frequencies decrease more than in the other EQ loads. Figure 5-10 displays the frequency exhibited after each ground motion for the numerical model (from an eigenvalue analysis) along with the experimental frequency identified during each EQ excitation (i.e., from the Fourier analysis in Figure 5-3 and Figure 5-4). For the simulated data, notice that the first frequencies correspond to the pristine structure, that is, before applying the earthquake loads. It is seen that the larger

changes occur after EQ2 and EQ4 for the simulated data, this is also reflected in the two larger values of relative frequency shifts in Table 5-2, which presents a relative and absolute simulated frequency shift summary for both directions. The relative frequency shift measures the frequency change after each EQ and the absolute frequency shift measures the cumulative change with respect to the initial frequency of vibration before applying any EQ. Similar results are presented in Table 5-3, this time using the recorded data to display a frequency shift summary in terms of the dominant frequencies presented in Figure 5-3 and Figure 5-4.

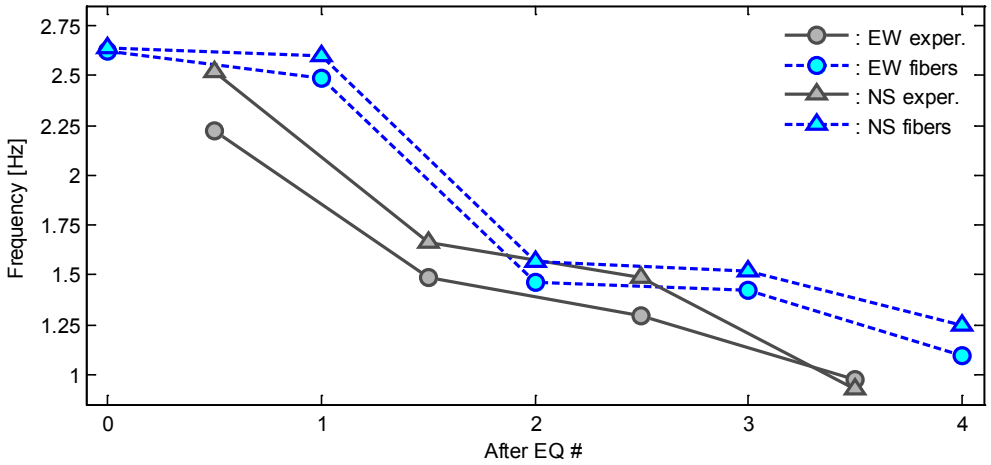

Figure 5-10: Frequency changes after each earthquake for both directions

Table 5-2: Summary of simulated model A frequency shifts

After Test	EW Direction		NS Direction	
	Relative Freq. Shift (%)	Absolute Freq. Shift (%)	Relative Freq. Shift (%)	Absolute Freq. Shift (%)
EQ1	5.03	5.03	1.44	1.44
EQ2	41.06	44.03	39.81	40.68
EQ3	2.77	45.58	2.84	42.37
EQ4	23.36	58.29	18.05	52.77

Table 5-3: Summary of experimental model A frequency shifts

Between Tests	EW Direction		NS Direction	
	Relative Freq. Shift (%)	Absolute Freq. Shift (%)	Relative Freq. Shift (%)	Absolute Freq. Shift (%)
EQ1 – EQ2	32.97	32.97	33.98	33.98
EQ2 – EQ3	13.11	41.76	10.29	40.78
EQ3 – EQ4	24.53	56.04	37.70	63.11

A detailed analysis of CWT results is presented in Figure 5-11 and Figure 5-12, where the wavelet ridges presented in Figure 5-6 to Figure 5-9 are presented again, but this time for comparison purposes for both scenarios (experimental and simulated data) for the EW and NS directions, respectively. The identified simulated frequencies at the beginning and end of the ground motions (horizontal continuous thin lines) are also included. In the cases where only one horizontal line is shown, it is because the frequency shift was minimum and the two lines cannot be distinguished. It is seen that for all cases, except for the edge zones and for the EQ2 up to 15 seconds, the instantaneous frequency (wavelet ridges) are in close agreement.

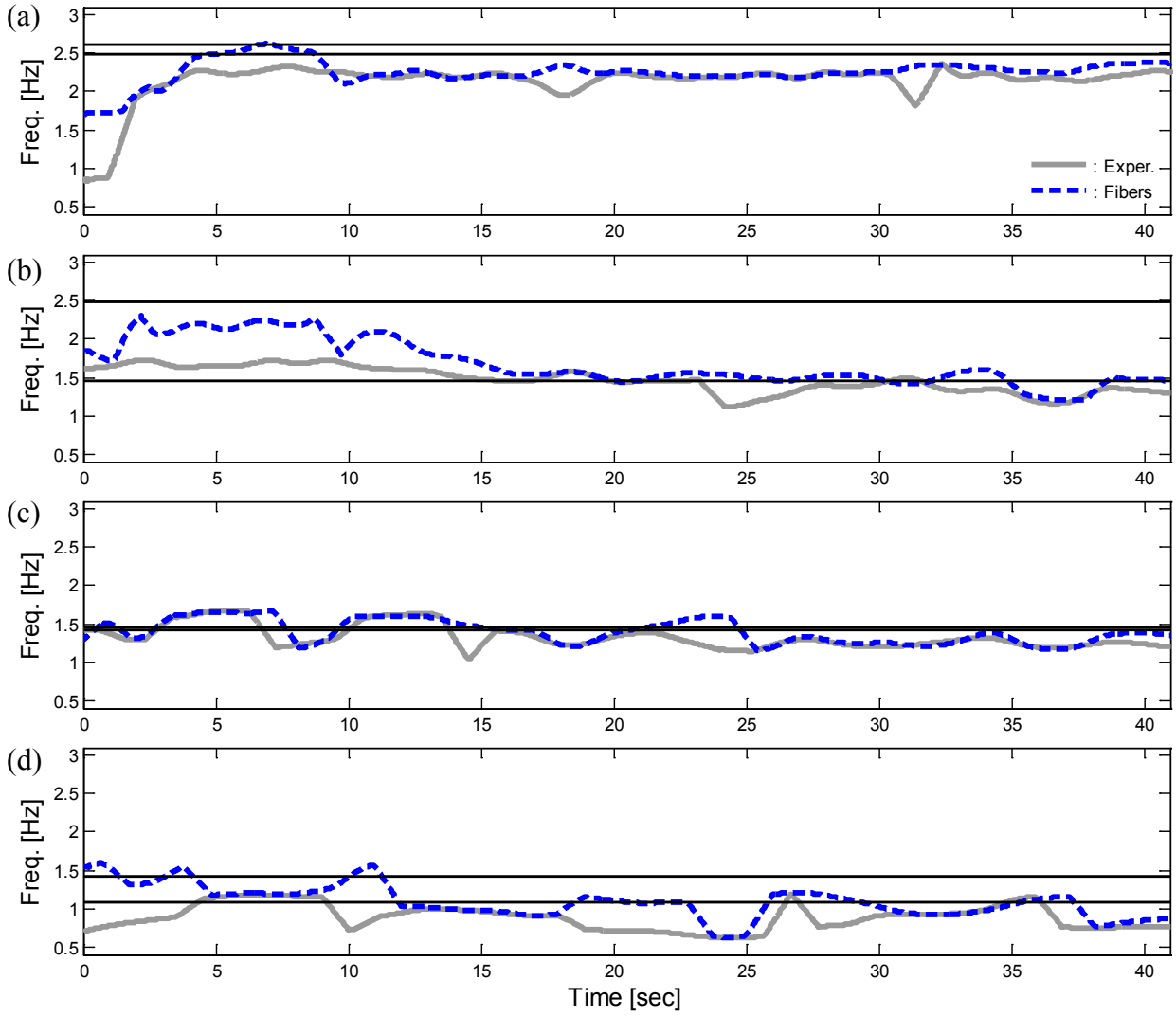

Figure 5-11: Comparison of wavelet ridges extracted from CWT analysis using experimental and simulated model A, point B displacements (EW direction) for (a) EQ1, (b) EQ2, (c) EQ3, and (d) EQ4

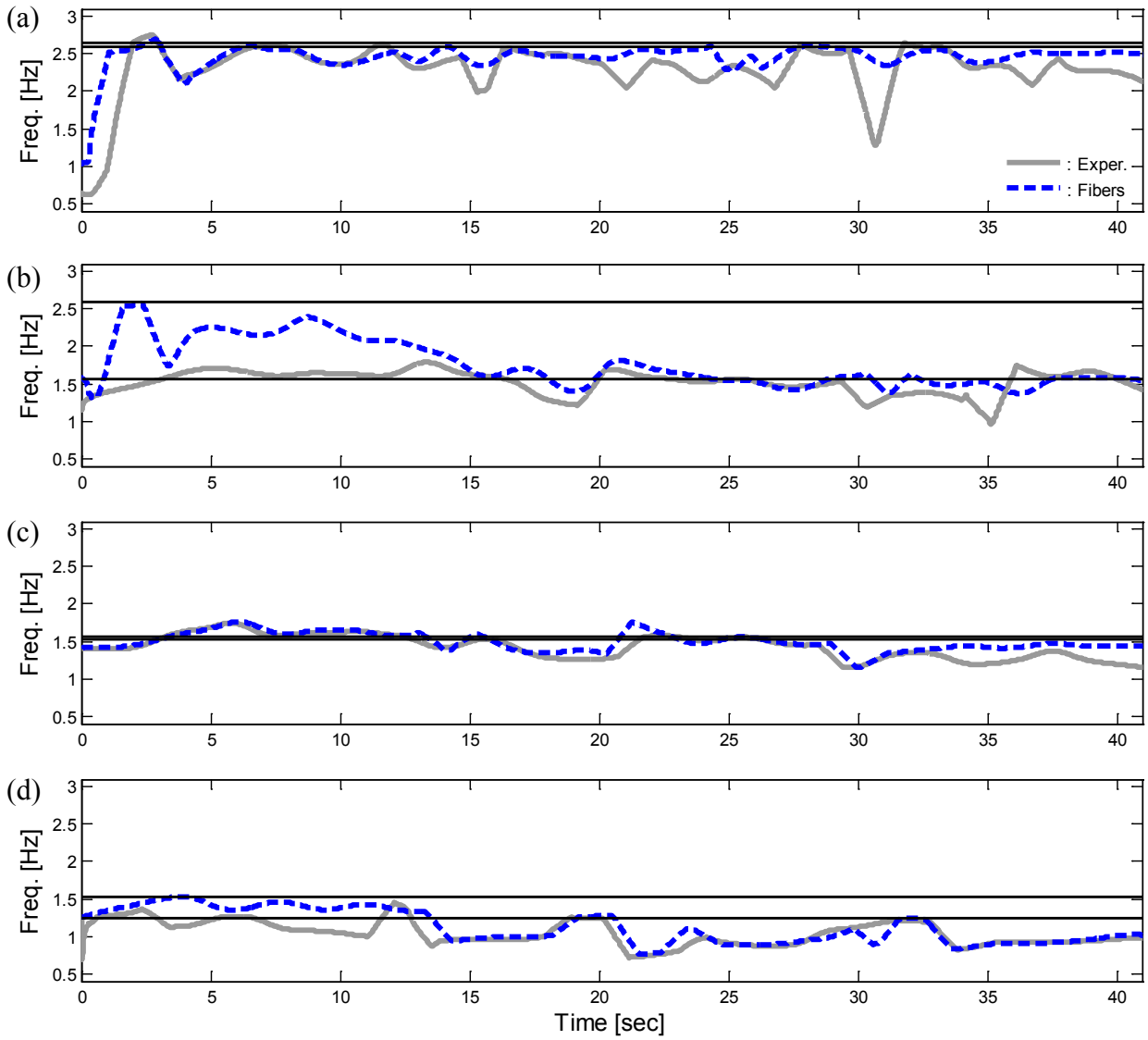

Figure 5-12: Comparison of wavelet ridges extracted from CWT analysis using experimental and simulated model A, point B displacements (NS direction) for (a) EQ1, (b) EQ2, (c) EQ3, and (d) EQ4

In order to better understand the frequency changes, the maximum simulated displacement is computed for both directions. Figure 5-13 presents the maximum responses extracted from the simulated model data. Based on these results and the yield displacements computed in Chapter III, Figure 5-14 and Figure 5-15 show again the frequency changes for EW and NS directions, respectively, but this time in terms of the ductility displacement. Notice that the larger frequency shift takes place just when the structure reaches ductility values slightly

larger than 1 while a medium intensity ground motion is applied (the registered PGAs are 0.19g and 0.16g for the EW and NS directions, respectively).

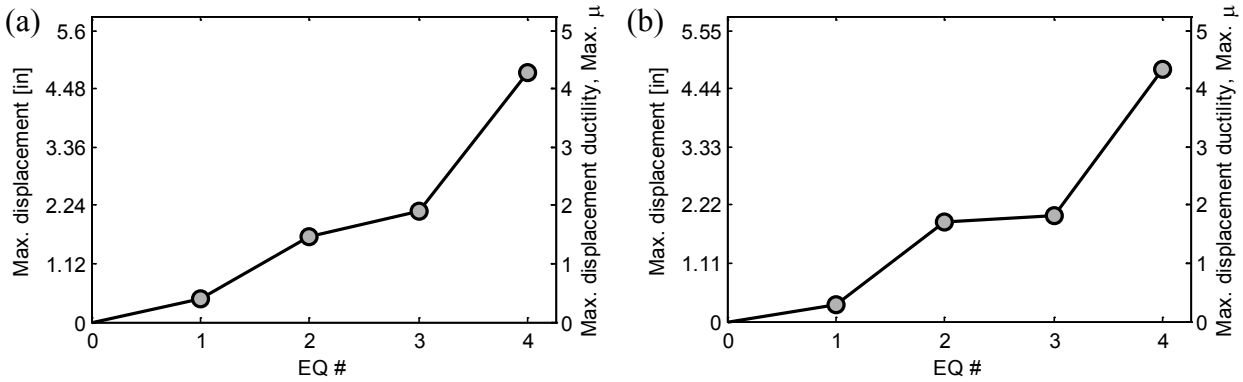

Figure 5-13: Maximum response during each earthquake for: (a) EW and (b) NS directions

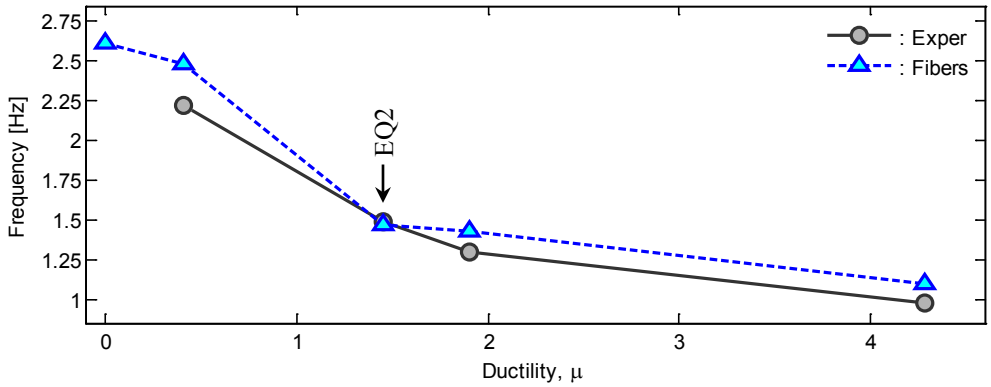

Figure 5-14: Frequency changes vs. ductility demand (EW direction)

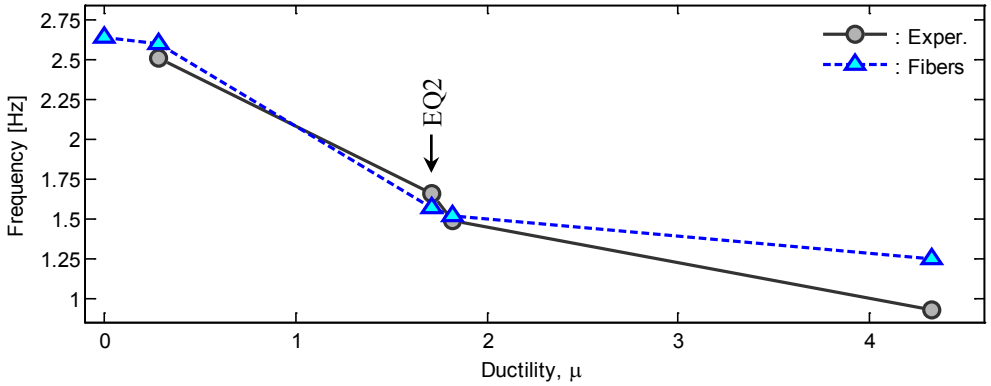

Figure 5-15: Frequency changes vs. ductility demand (NS direction)

5.2.2. Model A high frequency analysis (DWT)

Figure 5-16 to Figure 5-19 display the normalized absolute values of the detail functions from the experimental and fiber-based model displacements in both directions. The threshold criterion adopted (to avoid the identification of spurious spikes) is the same than for the UCSD column, that is, the values of the detail functions are normalized using Equation (4-1) and any time instant where the normalized absolute value (z) is larger than 6 is treated as a damage instant.

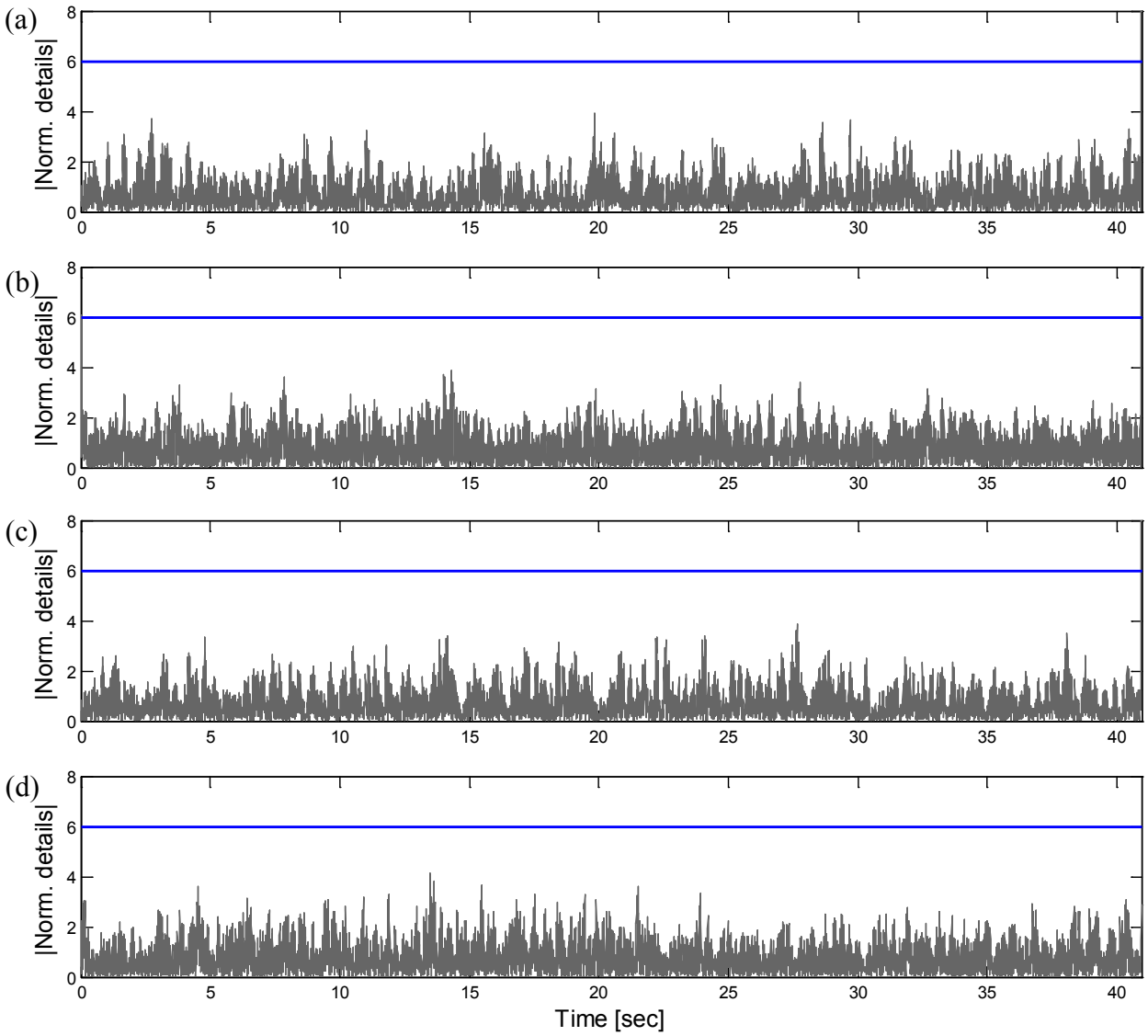

Figure 5-16: DWT analysis results (detail functions) for the recorded model A, point B displacements (EW direction) for (a) EQ1, (b) EQ2, (c) EQ3, and (d) EQ4

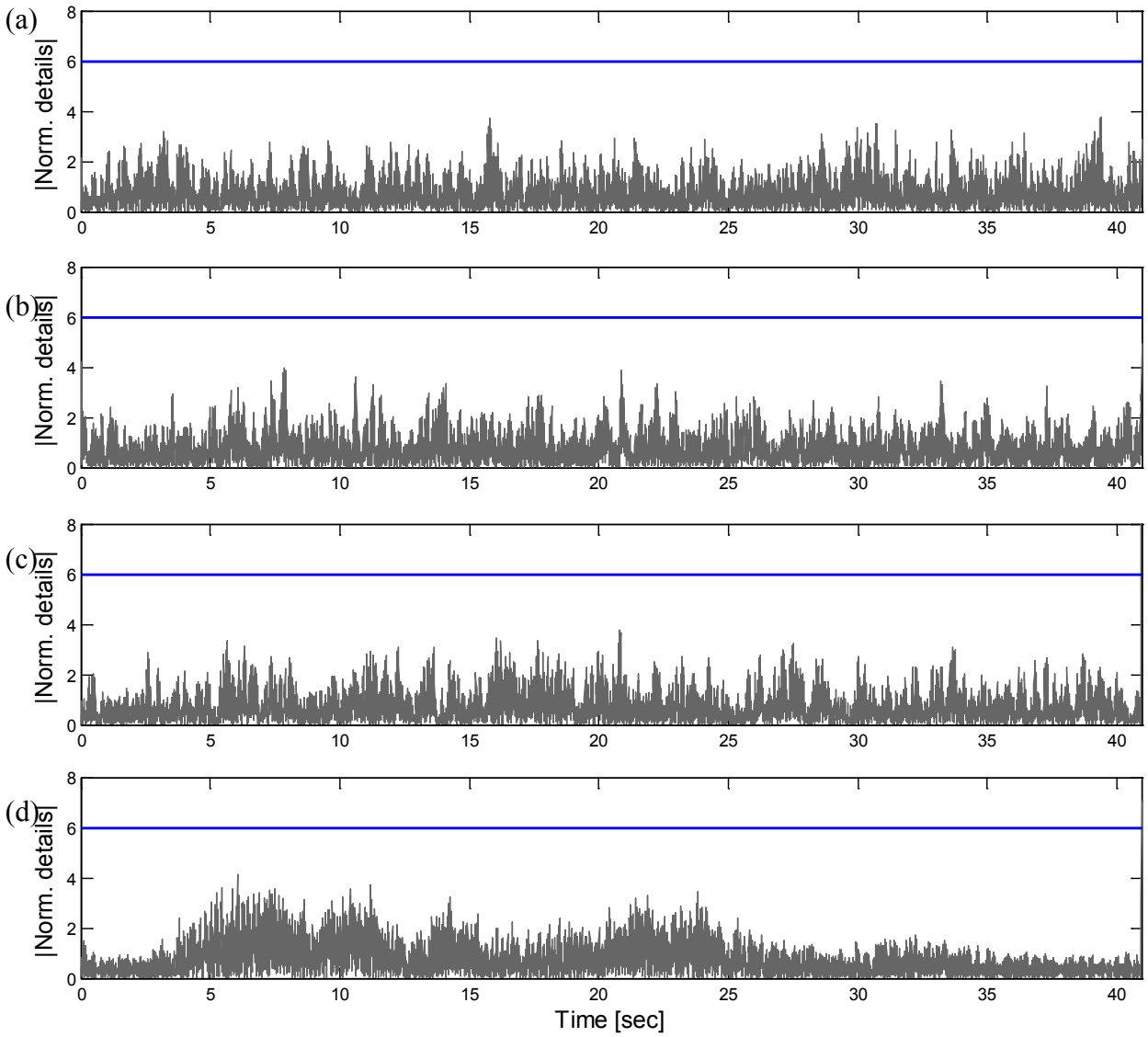

Figure 5-17: DWT analysis results (detail functions) for the recorded model A, point B displacements (NS direction) for (a) EQ1, (b) EQ2, (c) EQ3, and (d) EQ4

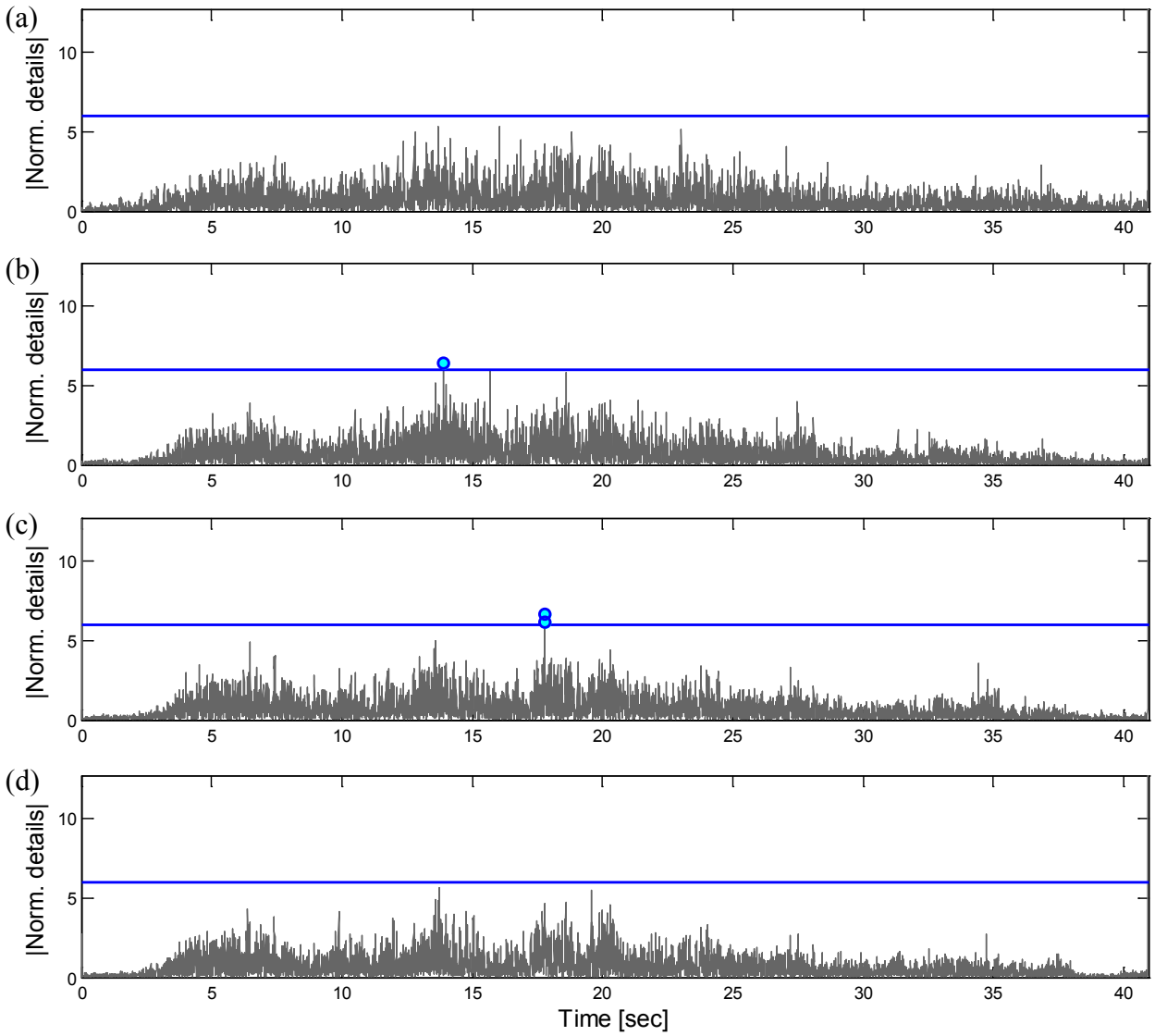

Figure 5-18: DWT analysis results (detail functions) for the simulated model A, point B displacements (EW direction) for (a) EQ1, (b) EQ2, (c) EQ3, and (d) EQ4

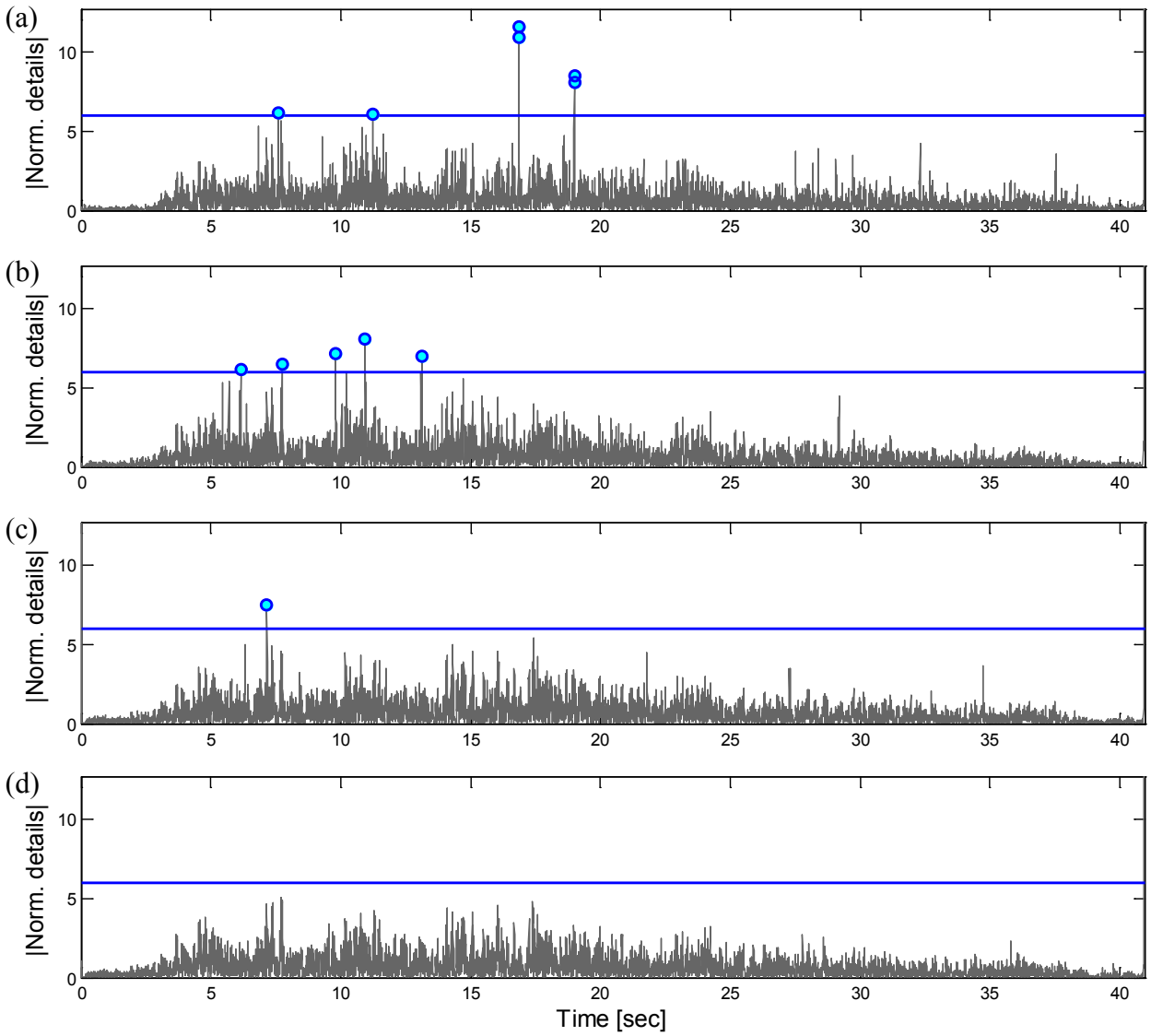

Figure 5-19: DWT analysis results (detail functions) for the simulated model A, point B displacements (NS direction) for (a) EQ1, (b) EQ2, (c) EQ3, and (d) EQ4

It is seen, from the results using the experimental data (Figure 5-16 and Figure 5-17), that no significant damage was induced to the 3D frame model A, that is, it can be inferred that no rebar fracture occurred in this structure. Different results were obtained from simulated data (Figure 5-18 and Figure 5-19) in which irregularities were detected for EW (EQ2 and EQ3) and NS (EQ1, EQ2, and EQ3) directions. It is seen that most of those irregularities are of low amplitude and could be related to limitations in the numerical models. DWT results for EQ1 in NS direction (Figure 5-19a) show two high amplitude spikes appear between 15 to 20 seconds, which seem to make no sense since the structure remained within the elastic range (Figure

5-13b). Moreover, the frequency detected after EQ1 is only 1.44% different than the pristine structures' frequency of vibration.

In order to go one step further in the analysis of this structure, one additional ground motion (EQ5) was applied to the FE model to analyze the results when rebar fracture episodes occur. The reference level earthquake load (EQ3) was repeated after EQ4 was applied. The selection of the additional excitation load was performed based not only on the need to produce rebar fracture, but also on the need of the model to remain stable along the application of the entire motion, that is, not to produce collapse. The FE model exhibited a total of four rebar fracture episodes during EQ5 (two of them in the column below control point B); this means that a large damage was induced to the structure during EQ4 because the intensity level of EQ5 (i.e., the same as EQ3) is just a half of EQ4, in other words, it is possible that the bars were taken up to near fracture conditions during EQ4. Analysis of the rebar stress time history revealed that failure of the four longitudinal bars took place at ~ 11.6, 13.2, 24.2, and 31.9 seconds. Figure 5-20 presents the CWT results for the model simulated (fiber-based model) data of EQ 5 for both directions. Vertical dashed red lines represent the instants of bars' failure.

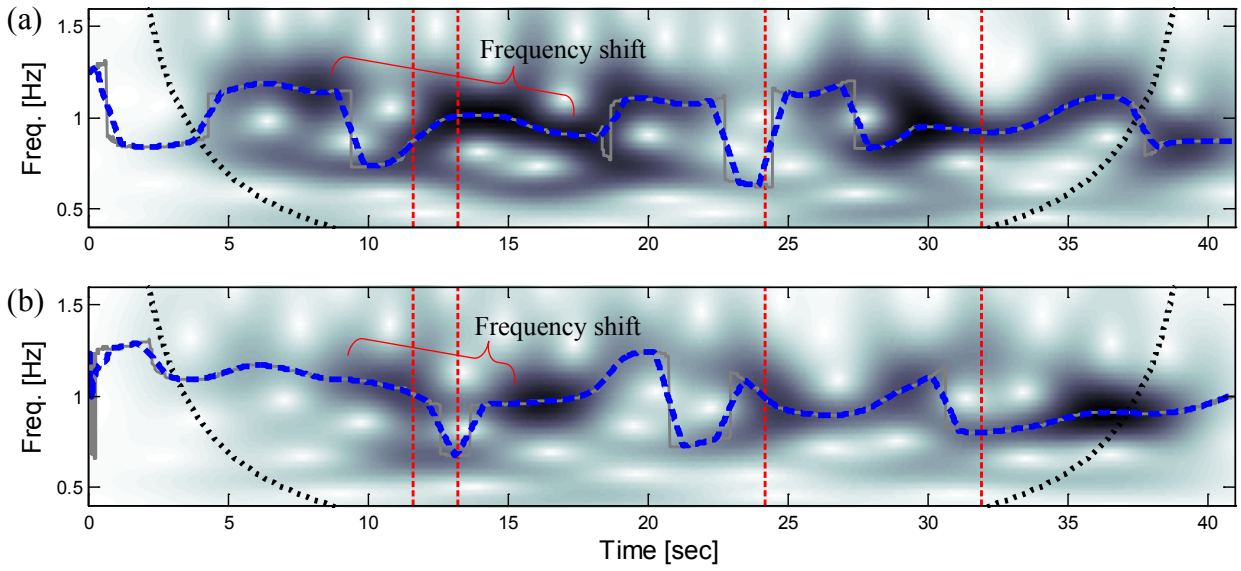

Figure 5-20: Low frequency CWT analysis results for the simulated model A, point B displacements for EQ5 on (a) EW and (b) NS directions

It is seen that the vibration frequency shifts are not that evident. The wavelet ridges seem to remain horizontal despite that a significant damage was induced in the structure (four rebar fracture episodes); however, a frequency drop is observed around 10 to 15 seconds just when two failure episodes took place. Figure 5-21 illustrates once more the frequency changes after each earthquake but this time including results from EQ 5. Notice that, even when a large damage was induced, the frequency shifts after EQ5 are not that large when compared to the changes after EQ2, which correlate well with the UCSD results where small frequency changes are detected even when rebar fracture occurs.

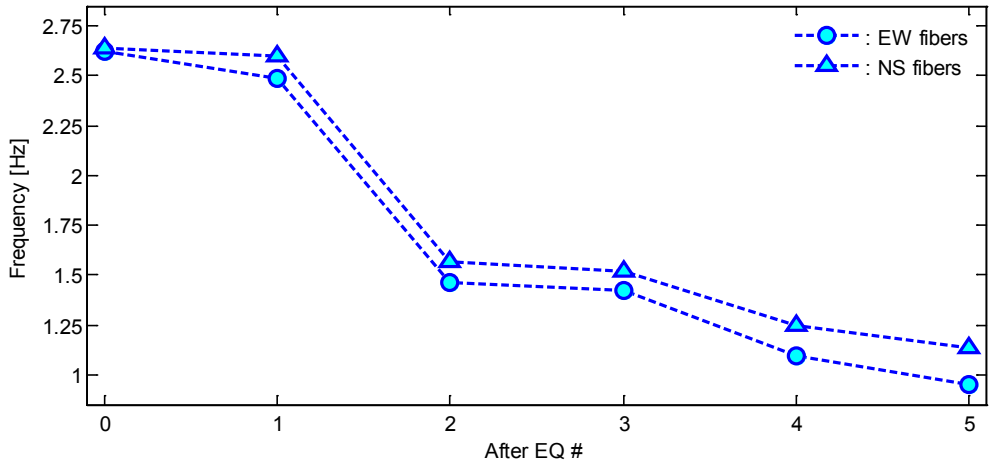

Figure 5-21: Frequency changes after each earthquake for both directions

Figure 5-22 displays the normalized absolute values of the detail functions from the fiber-based model displacements in both directions. Figure 5-23 present similar results but this time using the model accelerations in both directions. In both cases (Figure 5-22 and Figure 5-23) the threshold criterion is the same than in previous analyses. Notice the big difference between both results; while a DWT analysis using displacements does not detect any irregularity, spikes arise from the results using accelerations for the analysis. Vertical dashed red lines in Figure 5-23 represent the instants of bar's failure. Notice some of the irregularities detected during the analysis occurred near to two of the failure instants. Thus, a detailed analysis will be performed later to determine if those spikes are pinpointing a fracture episode.

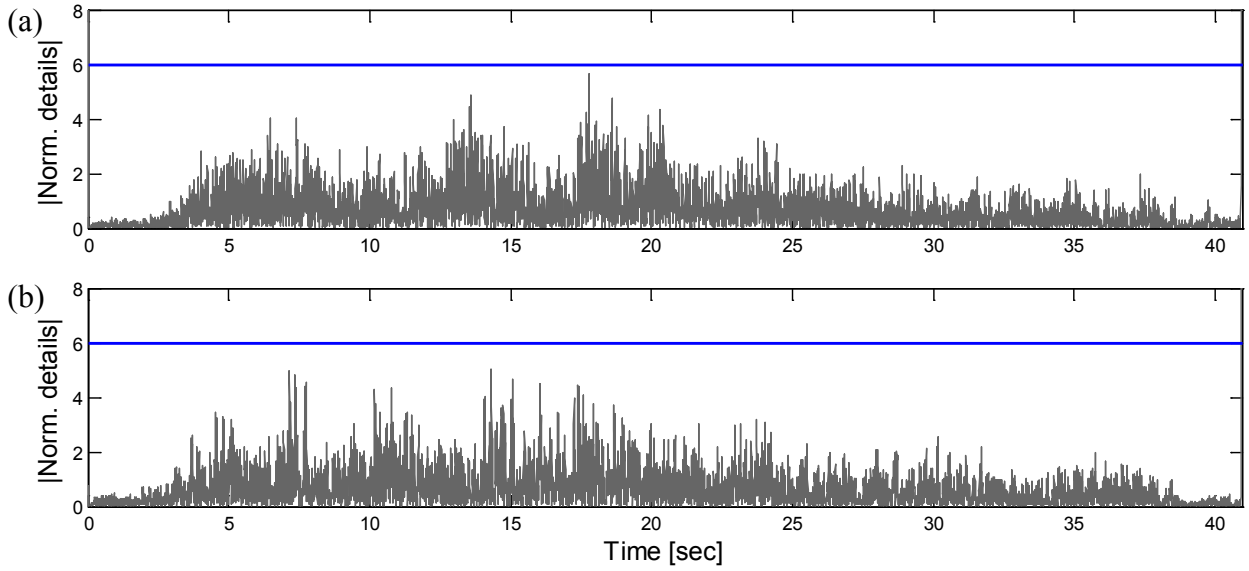

Figure 5-22: DWT analysis results (detail functions) for the simulated model A, point B displacements for EQ5 on (a) EW and (b) NS directions

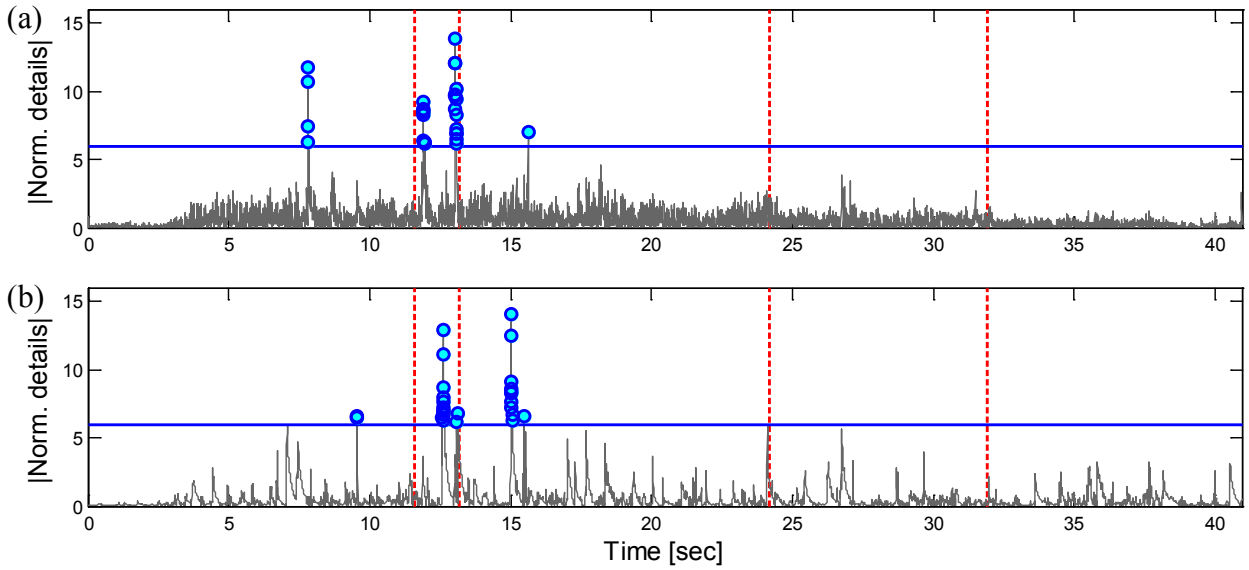

Figure 5-23: DWT analysis results (detail functions) for the simulated model A, point B accelerations for EQ5 on (a) EW and (b) NS directions

High amplitude irregularities were detected at 7.80, 11.89, and 13.04 seconds for EW direction (Figure 5-23a); and at 12.06 and 15.02 seconds for NS direction (Figure 5-23b). In order to determine if these irregularities are pinpointing a rebar fracture episode, Figure 5-24 presents a detailed analysis of the two bars, from the column below point B, that fracture during

EQ5. Notice that only one of the irregularities detected (i.e., at ~13.04 seconds for EW direction) arises at the instant when failure of bar 2 occurs (Figure 5-24e left) at ~ 13.2 seconds. Moreover, it is observed that bar 1 (Figure 5-24d) does not fracture at the instants where the irregularities are detected and besides no spikes arise beyond 18 seconds, which means that fracture episode of bar 1 is not identified from the DWT analysis.

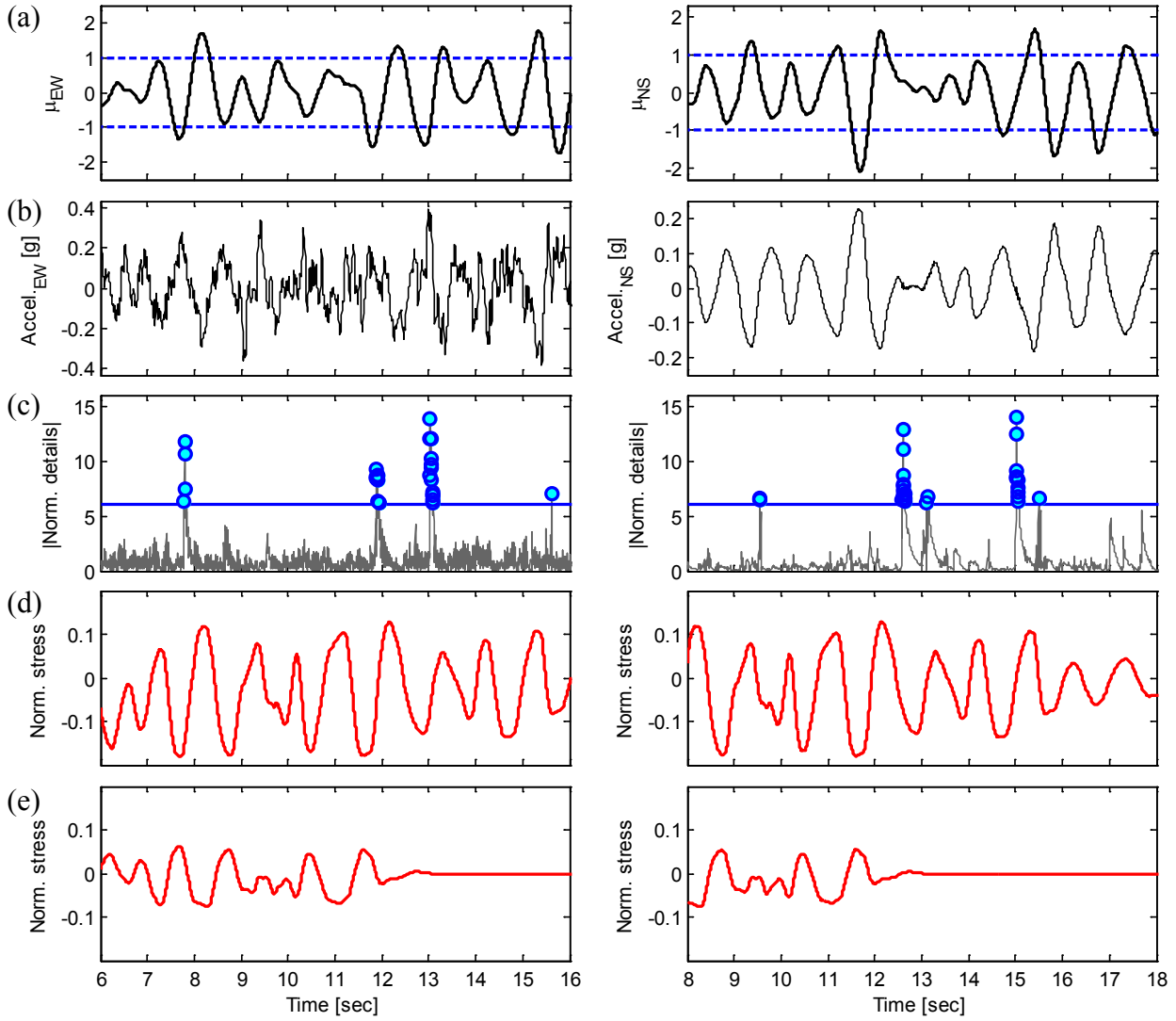

Figure 5-24: EW (left) and NS (right) detailed analysis of two rebar rupture episodes during EQ5. (a) Ductility displacement, (b) acceleration, (c) normalized absolute values from DWT, normalized stress (f/fy) of fractured (d) bar 1, and (e) bar 2

Notice that, although the structure is subjected to inelastic excursions, the normalized stress (f/fy) values are low near the rebar fracture episodes (Figure 5-24d and Figure 5-24e); this

means that the bars' rupture in this particular case occurs different than in the UCSD column, where bars fractured abruptly when subjected to high stresses. However, in terms of DWT results these are very similar to the ones obtained in Chapter IV using the fiber-based model, that is, some of the irregularities detected match the rebar fracture episodes and there are other spikes which could arise from numerical limitations in the FE model.

An analysis of four induced rebar fracture episodes was performed in order to evaluate the DWT results that one could obtain in a more realistic scenario. Using the acceleration disturbance (acceleration impulses) measured during the first rebar fracture episode in the UCSD column (Figure 4-30), the simulated acceleration response of EQ5 (in both directions) is modified so that an acceleration impulse is added at the instants where bar's failure are supposed to occur according to the FE model (i.e., at ~ 11.6, 13.2, 24.2, and 31.9 seconds). Thereby, induced fracture episodes are expected at the aforementioned instants. Figure 5-25 and Figure 5-26 display the modification to the acceleration response of EQ5.

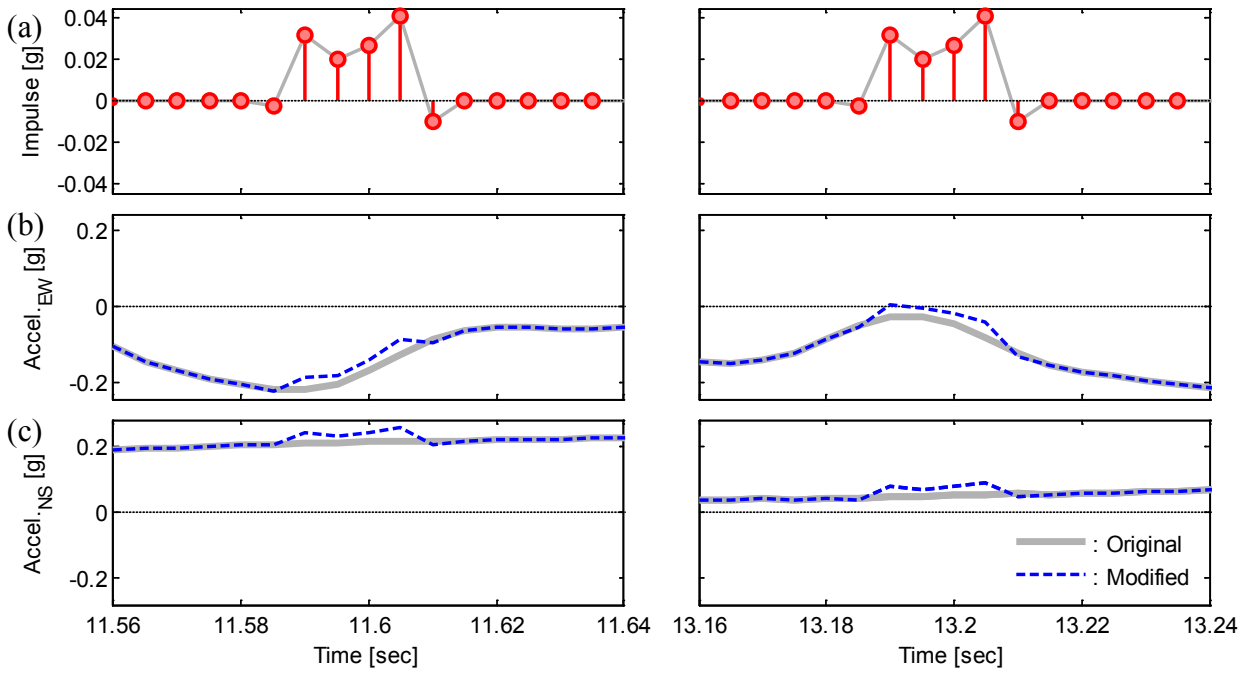

Figure 5-25: Simulated acceleration response modification of EQ5 to induce fracture episodes at 11.6 (left) and 13.2 seconds (right). (a) Added impulse accelerations, (b) EW acceleration, and (c) NS acceleration

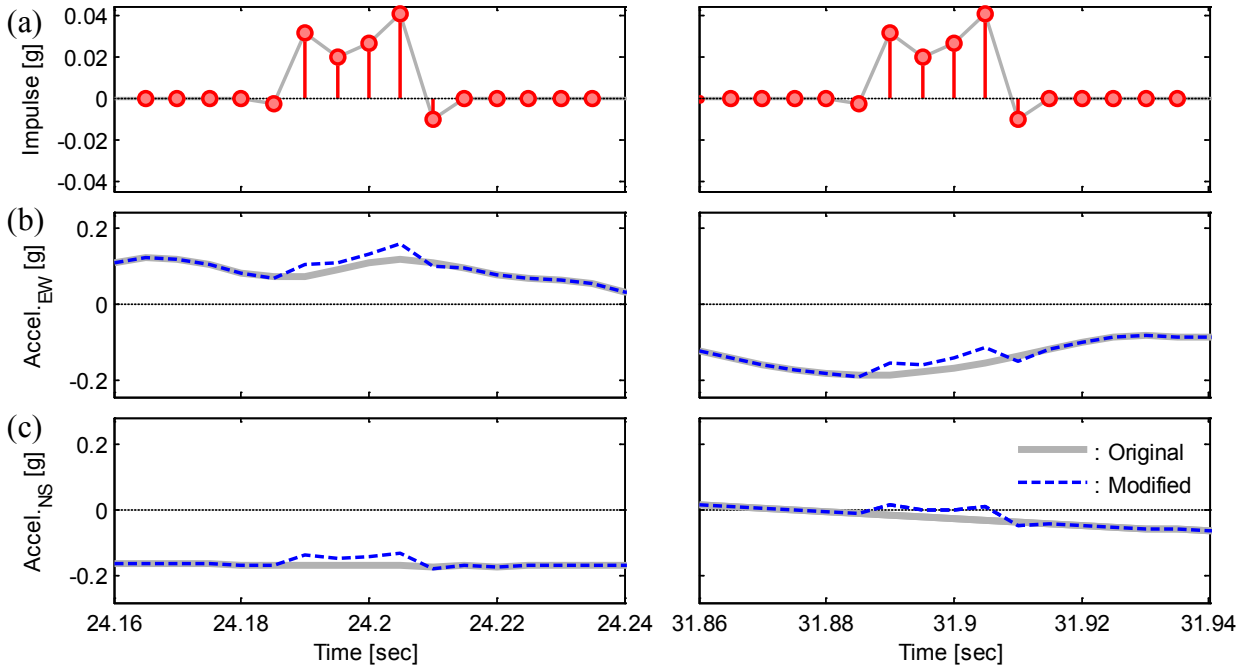

Figure 5-26: Simulated acceleration response modification of EQ5 to induce fracture episodes at 24.2 (left) and 31.9 seconds (right). (a) Added impulse accelerations, (b) EW acceleration, and (c) NS acceleration

Figure 5-27 and Figure 5-28 present the modified acceleration response of EQ5, the low frequency CWT analysis, and the normalized absolute values of the detail functions (DWT analysis) from the modified model accelerations on EW and NS directions, respectively. From the CWT analysis it is seen, as stated earlier from Figure 5-20, that the wavelet ridges seem to remain horizontal; however, near the induced fracture episodes (vertical dashed red lines) frequency drops are observed. Nevertheless, there are some instants where the frequency increase instead of decrease (see for example around 15 to 20 seconds in Figure 5-27b and Figure 5-28b), which could be related to the earthquake's frequency content instead to the structure's vibration frequency. It is observed that the numerically-induced effects of the rebar fracture episodes are clearly identified in the DWT analysis (Figure 5-27c and Figure 5-28c) at ~ 11.6, 13.2, 24.2, and 31.9 seconds. Notice that the amplitude of these spikes is about one and a half times larger than the amplitude of the irregularities detected previously, whose amplitude decreased with respect to the analysis previously performed (see Figure 5-23). In fact, some spikes disappear due to the magnitude of the new irregularities and the normalization process.

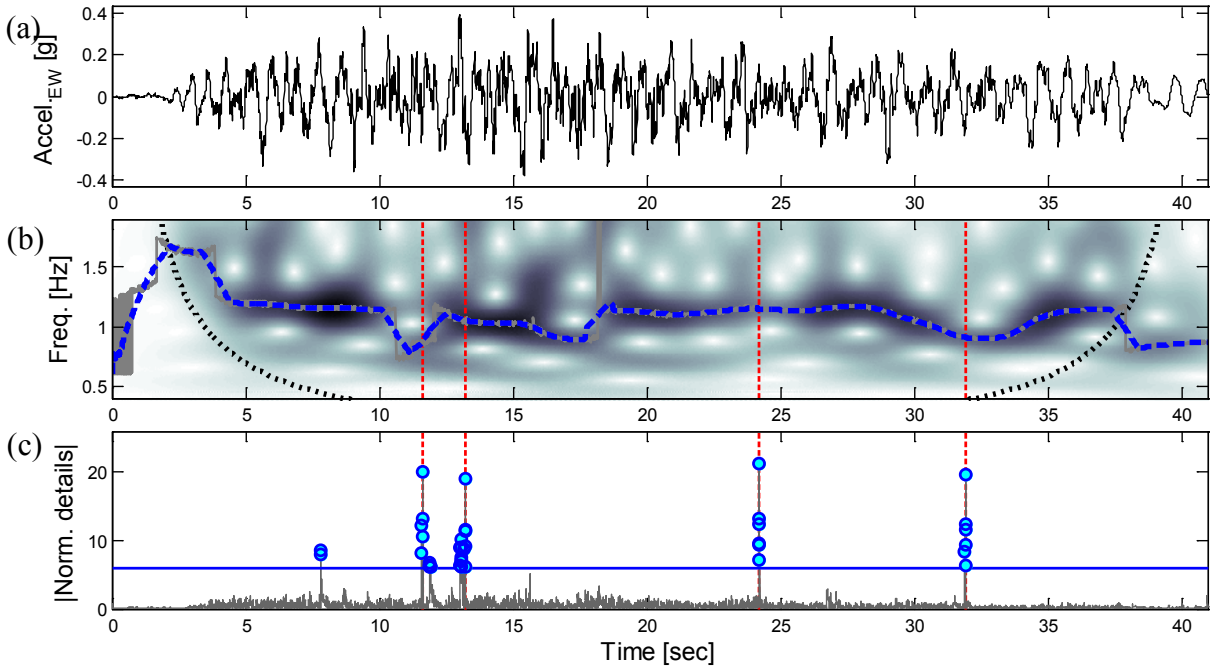

Figure 5-27: Analysis results for the simulated model A, point B, EW accelerations for EQ5 including impulsive acelerations to simulate four rebar fracture episodes. (a) Modified acceleration response, (b) CWT results, and (c) DWT results

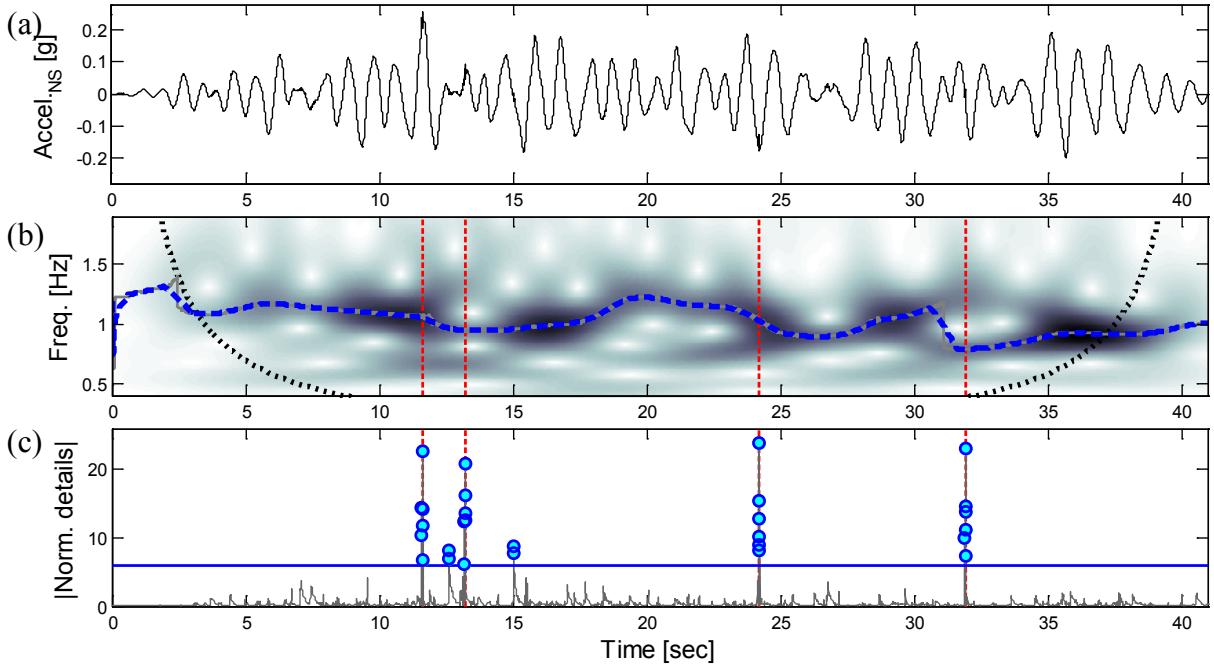

Figure 5-28: Analysis results for the simulated model A, point B, NS accelerations for EQ5 including impulsive acelerations to simulate four rebar fracture episodes. (a) Modified acceleration response, (b) CWT results, and (c) DWT results

5.3. Chapter Summary and Conclusions

- ✓ The CWT analysis in the low frequency range was more successful for the simulated than for the experimental model data. While in the first case decreasing frequency values are quite evident, the instantaneous frequency (wavelet ridges) seems to remain horizontal for the experimental data.
- ✓ The DWT analysis revealed that more accurate and realistic results are obtained when acceleration responses are used to perform the analyses. Numerically induced rebar fracture episodes were successfully identified during EQ5 for the simulated model A.
- ✓ Decreasing values of the structure's natural frequency were identified. Nevertheless, similar to UCSD results, the frequency shifts tend to saturate at large levels of ductility demand.

CHAPTER VI

6. CONCLUSIONS AND RECOMMENDATIONS

6.1. Conclusions

- ✓ CWT is a powerful tool to perform simultaneous time-frequency analysis in order to detect frequency shifts of a structure by using either the acceleration or displacement response. However, depending on the earthquake's frequency content, such changes could not be related to the structure's frequency and certainly they would not be an indicator of the stiffness degradation. Similar results and a decreasing trend of the instant frequency were observed for both simulated and experimental data.
- ✓ Irregularities related to structural damage such as inelastic excursions and rebar fracture episodes were successfully detected through the detail functions of the DWT analyses.
- ✓ For the UCSD column it was found that rebar fracture episodes can be detected by simply looking at the jerk response. However, in this is arguable because of the scarce number of episodes to compare.
- ✓ In both cases examined in this research, large frequency shifts were detected at low ductility demand values (~μ4) from this point forward frequency changes were less noticeable despite the increasing ductility demand. Small changes were detected, for instance, when some bars fractured which is considered as an irreparable damage. Perhaps this parameter can be used as damage indicator for moderate damage (e.g. cracking and concrete spalling); however, its ability to differentiate moderate to severe damage (e.g. rebar buckling or rupture) is arguable.
- ✓ Nonlinear FE models are a powerful tool to simulate the structural response of a structure. The results obtained in this research closely resemble the experimental results. Nevertheless, for SHM purposes FE models yet have limitations which do not allow, for example, replicate certain characteristics of the response (acceleration impulses) at the rebar fracture episodes. Moreover, fiber-based models seem better suited for validation of structural health monitoring algorithms as the local response is

better represented. Traditional multilinear hysteretic models should be avoided for such purposes since the abrupt changes in stiffness causes spurious irregularities in the high frequency response of the structure.

6.2. Recommendations for Future Studies

- ✓ All the results and conclusions presented in this work were obtained for the two particular examples presented. Thus, it is suggested to perform more analyses using different structural configurations. Although it is not easy to find information as complete as the UCSD column example. It would be even more interesting to be able to apply the methodologies presented in this research, using experimental data in which the soil-structure interaction can be taken into account. For instance, the Building Research Institute (BRI) strong motion network at Japan has earthquake records of several building instrumented (most of them) at the base and the top of the structures.
- ✓ It is also suggested to study more rebar fracture episodes since the results found here are only for one bar size, a specific cross section, and a structural configuration (cantilever column). Thus, different bar's size, cross section, and structural configurations should be explored. If a clear trend on the instant acceleration response (impulses) is observed, the possibility to generate a new type of wavelet could be explored. The shape of the impulses found would be the shape of the new wavelet type which could allow identifying fracture episodes on an easier and precise fashion.
- ✓ The occurrence of rebar buckling was one of the features that the nonlinear FE models did not detect. Thus, including rebar buckling on a nonlinear finite element model would be a very useful tool not only for SHM purposes but also for structural design.
- ✓ Jerk was shown to be more responsive to induce damage than acceleration. Nevertheless, jerk values were calculated based on the numerical differentiation of the recorded accelerations. It is recommended to explore the possibility of using/developing jerk sensors for health monitoring purposes.